論文 / 著書情報
Article / Book Information

題目(和文)	ナトリウム冷却高速炉の自然循環崩壊熱除去時の炉心熱流動現象に関する研究
Title(English)	Investigation on thermal hydraulics phenomena in a sodium-cooled fast reactor core during natural circulation decay heat removals
著者(和文)	上出英樹
Author(English)	Hideki Kamide
出典(和文)	学位:博士(工学), 学位授与機関:東京工業大学, 報告番号:乙第4034号, 授与年月日:2010年11月30日, 学位の種別:論文博士, 審査員:二ノ方 壽
Citation(English)	Degree:Doctor (Engineering), Conferring organization: Tokyo Institute of Technology, Report number:乙第4034号, Conferred date:2010/11/30, Degree Type:Thesis doctor, Examiner:
学位種別(和文)	博士論文
Type(English)	Doctoral Thesis

Investigation on Thermal Hydraulics Phenomena in a Sodium-Cooled Fast Reactor Core during Natural Circulation Decay Heat Removals

原子核工学専攻

上出　英樹

Abstract

A sodium-cooled fast reactor is a significant candidate for future power reactor systems. Decay heat removal is an essential function for the safety of reactor systems. Natural circulation can maintain this function in any situation, e.g., the failure of sodium pumps or air blowers, and total blackout, as long as the sodium level in the reactor vessel is maintained.

The pump and air blower are unnecessary for the natural circulation. However, the flow rate in the system and the temperature distribution along the circuit are both dependent on each other. This means that the flow rate cannot be decided beforehand and that it changes during transient. Flow rate uncertainty is one of the drawbacks of natural circulation.

As for the core, it consists of many flow channels that have different thermal powers and flow resistance coefficients according to the inner and outer core fuels, radial blanket fuels, and radial reflectors. Thus, buoyancy driven flow rates in these channels are also different. These channels are connected with one another via heat conduction through the wrapper tubes. This means that the temperatures (and the flow rate) in the multi-channels of the core are influenced by one another. Further, there is a sodium gap between the subassemblies in the core. This sodium produces a natural convection according to the temperature profile across the core and transports the heat in the core so as to flatten the temperature distribution.

There are several design variations for decay heat removal systems (DHRS). One well-used DHRS design has heat exchangers in a reactor upper plenum so as to use them in the case of sodium leakage accident in a main heat transport system. In this type of DHRS, cold sodium provided by the heat exchanger may stratify in lower part of the reactor upper plenum and cover the top of the high temperature core. This temperature distribution is the inverse of the point of buoyancy force.

These findings suggest that the core exhibits complex phenomena under natural circulation conditions. The following have been recognized as phenomena in the core during natural circulation to consider.

- Flow redistributions among the subassemblies and inside the subassembly
- Inter-subassembly heat transfer
- Penetration flow into subassemblies
- Inter-wrapper flow

These phenomena will influence the temperature profiles in the core, especially, the highest temperature during transient.

Evaluation of these thermal hydraulic phenomena in the core is important for the use of

natural circulation as a part of the decay heat removal system. Because heat removal in the subassembly and heat flux on the wrapper tube are the keys to these phenomena, sodium experiments were carried out using three-subassembly and seven-subassembly models. The inter-subassembly heat transfer and flow redistributions were examined in the three-subassembly model under steady state conditions. Transient characteristics of the flow redistributions and the inter-wrapper flow were investigated in the seven-subassembly model. A water experiment was performed to examine the natural convection in the gap region of an entire core. A basic water experiment and a sodium experiment using subassembly model were carried out on the penetration flow into an upward flow channel due to negative buoyancy force. These sodium and water experiments on core thermal hydraulics are described in this paper.

Transverse temperature distribution in a subassembly was characterized by a peaking factor and a wall subchannel factor with a buoyancy parameter of Gr/Re and heat flux of the inter-subassembly heat transfer. The peaking factor during a scram transient was also obtained as a function of the Gr/Re and the wall heat flux in order to estimate the peak temperature in the transition from forced to natural circulation. The seven-subassembly experiment revealed that the inter-wrapper flow had a significant reduction effect on the highest temperature in the subassembly through the wrapper tube. It was shown that this heat removal effect of the inter-wrapper flow was estimated by a non-dimensional parameter of $Gr^{4/7}/Re$.

Numerical simulation methods were developed for the thermal hydraulics in the core. A detailed prediction method in a subassembly with inter-subassembly heat transfer was verified via the three-subassembly and seven-subassembly experiments. Further, a simplified reactor scale simulation method was developed. This inter-wrapper flow model was verified by the water experimental results for natural convection in the entire core gap region.

A reactor core scale calculation was carried out using the simplified model to examine the core thermal hydraulic phenomena under natural circulation conditions. It was shown that the inter-wrapper flow had significant potential to remove the decay heat and also reduce the highest temperature in the core.

Further, feedbacks for a design study of 1,500 MWe class sodium-cooled reactor were discussed. Especially, utilization of inter-wrapper flow as a heat removal path was proposed for a beyond design-base event where a heat exchanger in a reactor vessel was solely used as the decay heat removal system. Finally, required features and functions of the evaluation methods to be applied to the core thermal hydraulic phenomena under a natural circulation condition were summarized.

要旨

ナトリウム冷却高速炉は将来の原子炉システムの重要な候補に挙げられている。安全上の重要な機能である炉停止後の崩壊熱除去に自然循環を用いることで、動的機器が使えない事態においても除熱機能を維持でき、信頼性を高めることができる。しかし自然循環では、強制循環と比較して循環流量は基本的に制御されず、流量が確保されるためには相対的に炉心温度が高くなることが避けられないこと、また浮力や熱伝導を介して温度分布の平坦化が生じることから、炉心の最高温度を合理的に評価するには浮力の効果を適切に考慮する必要がある。

本研究では、浮力による高温部への流量再配分、集合体間の温度差による熱移行現象、集合体間ギャップ部の自然対流など、炉心温度分布に影響が大きい熱流動現象をナトリウムおよび水実験により解明するとともに、多次元解析コードを用いた評価手法を開発した。これらにより、評価の指標となるパラメータを求め、最高温度への影響を定量的に明らかにした。さらに、機構論的に現象を模擬し、最高温度を評価できる手法を見出した。

第一章　Introduction（序論）では、高速炉崩壊熱除去系の設計の変遷とこれまでの自然循環に関する研究から、炉心熱流動現象に関する課題を設定し、本研究の方針、高速炉の実用化に向けた方向性を示した。

第二章　Inter-Subassembly Heat Transfer and Intra-Subassembly Flow Redistribution（集合体間熱移行と集合体内流量再配分）では、集合体内の浮力による流量再配分と集合体間熱移行による集合体内最高温度の低減について、複数の模擬集合体からなるナトリウム試験装置を用いて定常状態ならびにスクラム過渡時の現象を解明した。これにより、集合体内温度分布が浮力により平坦化する効果を表す指標として集合体の発熱長と水力等価直径の 2 つの代表長さを取り入れた新しい無次元パラメータを見出した。さらに集合体間熱移行の効果を含む自然循環時の集合体内無次元最高温度の特性を明らかにした。また、評価手法としてサブチャンネルベースのメッシュで複数の集合体を同時にモデル化する多次元解析により、集合体の壁サブチャンネルと内部サブチャンネル間の流量再配分を考慮し、上記の集合体内温度分布をよく模擬できることを示した。

第三章　Penetration Flow into Low Power Subassemblies（集合体内潜り込み現象）では、冷却器を炉容器上部プレナムに浸漬する崩壊熱除去型式（ＤＲＡＣＳ）において、低温ナトリウムが高温の集合体の上部を覆い浮力により集合体

内に潜り込む現象について、水試験と多次元解析の適用性評価を実施した。その結果、潜り込みの発生条件が浮力と慣性力の比により表せること、解析手法に求められる要件を明らかにした。

第四章　Inter-Wrapper Flow（集合体間ギャップ部自然対流現象）では、炉心の集合体間ギャップ部の自然対流（インターラッパーフロー、ＩＷＦ）に着目して、集合体の最高温度に与える影響を定常ならびに過渡試験により明らかにした。前述のＤＲＡＣＳ型式では、冷却器からの低温ナトリウムが高温の集合体間ギャップ部に潜り込み、ＩＷＦがより顕著となることが予測された。試験では、この潜り込み現象を確認するために、集合体間ギャップを含む７集合体からなる炉心、浸漬型冷却器、炉容器上部プレナム、過渡を可能とする 1 次、２次冷却系を有するナトリウム試験装置を製作した。試験により、ＩＷＦは集合体の側壁を通した除熱により定常状態ならびに過渡時に集合体内最高温度を低減する大きな効果を有することが明らかにするとともに、この効果が炉心槽内の浮力と集合体内の慣性力に関する無次元パラメータで表せることを示した。

第五章　Whole Core Analysis of NC/DHR（全炉心体系での自然循環崩壊熱除去解析）では、上述の炉心部熱流動現象に多次元熱流動解析を適用し、全炉心での現象について考察した。前述のサブチャンネルレベルで複数の集合体を同時にモデル化する手法を拡張し、内部サブチャンネルと壁サブチャンネルを区別した上で炉心部集合体、集合体間ギャップと炉容器上部プレナムを同時にモデル化し、実機に適用可能な簡素化手法を提案した。７集合体ナトリウム試験により集合体内外の温度分布の予測性を検証した。本手法を用いて６０万ｋＷｅ級高速炉の自然循環崩壊熱除去を対象に実規模解析を行い、全炉心での現象について知見を得た。その結果、ＩＷＦが炉心全体の流量再配分と相まって自然循環時の炉心最高温度低減に大きな効果を有することを明らかにした。

第六章　Discussions（考察）では、本研究で得られた自然循環時の複数集合体規模での熱流動現象の実験知見、解析知見を整理し、解析手法の要件をまとめた。特にＩＷＦを評価する上で、集合体内部の温度分布と集合体間ギャップ内流れ、さらには炉容器上部プレナムの温度成層化現象を一括して扱う必要性を示し、部分的な簡略化を施した多次元解析モデルが有効な評価手法であることを明らかにした。さらに、大型炉における全炉心体系での自然循環時の現象を考察してＩＷＦを活用した設計概念を提示し、その評価には前述の要件を備えた解析手法が必要かつ適用可能なことを示した。

第 7 章　Summary and Conclusions（結論）においては、本研究のまとめを行い、得られた結論を総括した。

Acknowledgements

The author is grateful to Mr. Kazuziro Sato and Dr. Katsuhisa Yamaguchi of Japan Atomic Energy Agency (JAEA) for giving a chance to study thermal hydraulics in sodium-cooled fast reactors using water and sodium test facilities. The author wishes to express his gratitude to Mr. Yoshiaki Ieda, Mr. Kenji Hayashi, Mr. Tadashi Isozaki, Mr. Hiroyuki Miyakoshi, Mr. Hiroyuki Ohshima, Mr. Jun Kobayashi, and Mr. Nobuyuki Kimura of JAEA for technical discussions, construction of test loops, and data analyses as well as helpful suggestions. It is the author's pleasure to acknowledge help of Professor Akira Yamaguchi of Osaka University for a system code development of long-term simulation. The author is very thankful to Dr. Isamu Maekawa, Mr. Shin-ichi Toda, and Dr. Nishimura Motohiko of Kawasaki Heavy Industries Ltd. for kind advices, detailed numerical simulations, and designs of test sections. The author also acknowledges the kind supports provided by Mr. Mitsuo Sumiya and Mr. Masami Ito of Joyo-Sangyo Ltd. for significant advances of test loop operations and measurement techniques. The author is very grateful to Dr. Helmut Hoffmann and Dr. Dietrich Weinberg of Forshungszentrum Karlsruhe (FzK) and also Dr. Denis Tenchine of Commissariata a l'energie atomique (CEA) for fruitful discussions of natural circulation in European Fast Reactor.

Lastly the author would like to express his sincere appreciations to Professor Hisashi Ninokata of the Tokyo Institute of Technology for his long-term supervision, encouragements, excellent guidance, and instructions. The author is very thankful to Professor Masanori Aritomi, Professor Minoru Takahashi, Professor Hiroshige Kikura, and Professor Takayuki Aoki of Tokyo Institute of Technology for their advices and comments provided during the review of this thesis.

Contents

Table List

Figure List

Chapter 1.

Chapter 2.

Acronyms

CFD	Computational Fluid Dynamics
DHRS	Decay Heat Removal System
DHX	Dipped Heat Exchanger
DRACS	Direct Reactor Auxiliary Cooling System
FBR	Fast Breeder Reactor
IC	Immersed Cooler, the same meaning as DHX
IHX	Intermediate Heat Exchanger
IRACS	Intermediate Reactor Auxiliary Cooling System
IWF	Inter-Wrapper Flow
JAEA	Japan Atomic Energy Agency
JSFR	Japan Sodium-cooled Fast Reactor
LDA	Laser Doppler Anemometer
NCDHRS	Natural Circulation Decay Heat Removal System
PAHR	Post Accident Heat Removal
PIV	Particle Image Velocimetry
PLANDTL	Plant Dynamics Test Loop
PRACS	Primary Reactor Auxiliary Cooling System
RVACS	Reactor Vessel Auxiliary Cooling System
SG	Steam Generator

Chapter 1. Introduction

Chapter 1. Introduction

1.1 Decay Heat Removal by Natural Circulation

A sodium-cooled fast reactor is a significant candidate for future power reactor systems. Decay heat removal is an essential function for the safety of nuclear reactors including the sodium-cooled reactors. An example of decay heat curve of a sodium-cooled reactor after a scram is shown in Fig. 1.1-1. The residual power just after the scram reaches ca. 6% of the initial power. It decays gradually, 2% at 1000s from the scram, 1% at 10,000s, still 0.6% at 100,000s (1.2 day). Thus, it is necessary to effectively remove the decay heat over a long period. The objective of the decay heat removal is to maintain the integrity of core fuels and also sodium boundary of the cooling systems.

In cases of normal and manual shutdown, decay heat is removed via the normal heat transport system and finally to a water-steam system which bypasses the turbine, according to the design. Such a system is referred to as an operational grade decay heat removal system. In case of emergency, the decay heat must be removed by a special system which has higher reliability; that is, a safety graded decay heat removal system (DHRS).

Recent fast reactors and design studies are equipped with a DHRS. Figure 1.1-2 shows a flow diagram of the Japanese prototype fast reactor, MONJU. A branch line connects an air cooler with the secondary cooling system as the DHRS in each cooling loop. The air cooler is usually used as a final heat sink because of the higher operational temperature of the sodium-cooled reactor compared with light water reactors.

The capacity of the DHRS depends on the design and 2.5% of the reactor full power, for example. The temperature course of the core outlet depends on the design of the heat transport system, e.g., the sodium inventory. Slow temperature increase due to a larger sodium inventory will permit a smaller DHRS capacity according to the decrease of the decay heat during transient.

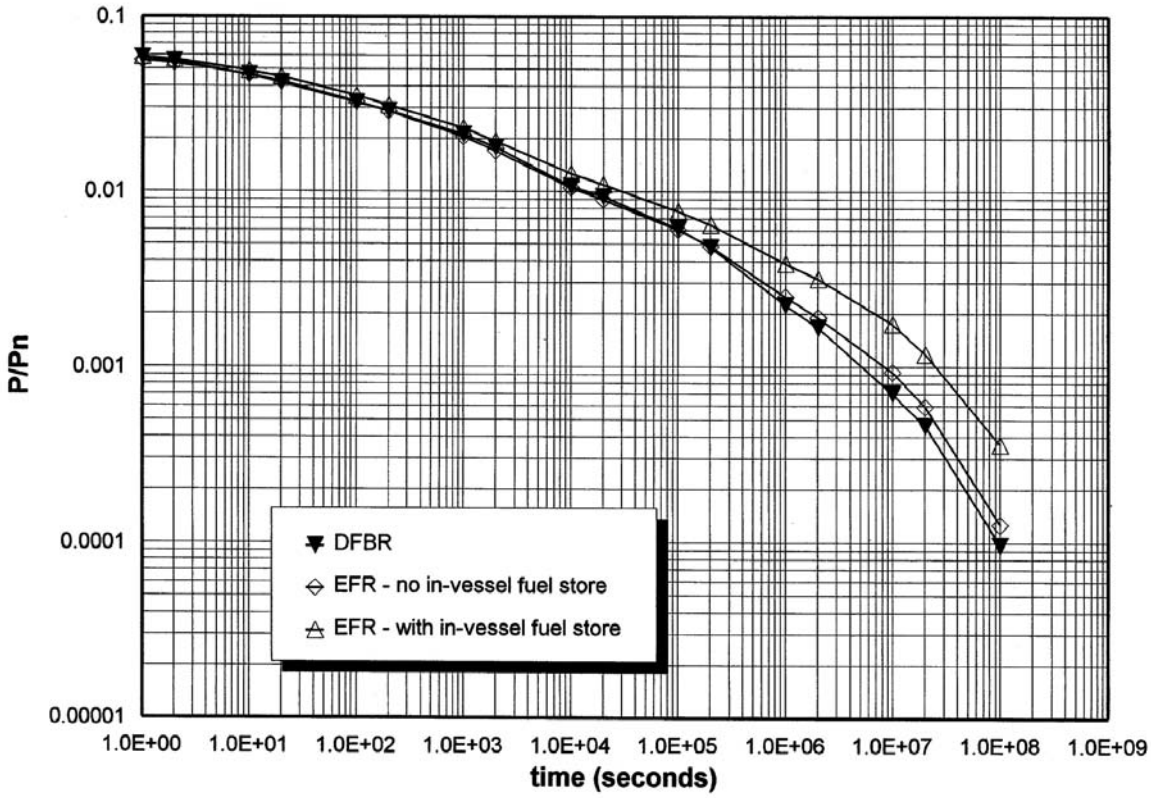

Fig. 8. Comparison of DFBR and EFR decay heat (without margins).

B. Farrar et al., Fast reactor decay heat removal: approach to the safety system design in Japan and Europe, Nuclear Engineering and Design 193 (1999) 45–54
Page 53, Fig. 8

Fig. 1.1-1 Decay Heat Curve in Sodium Cooled Fast Reactors

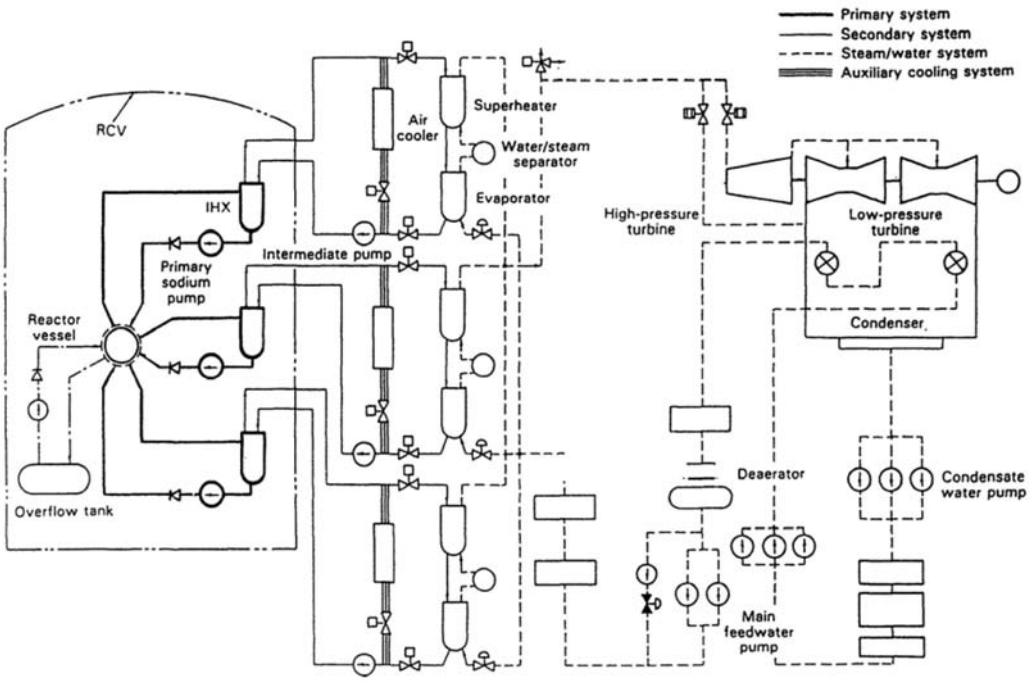

Flow diagram reactor plant.

IAEA Fast Reactor Database,
http://www.iaea.org/inisnkm/nkm/aws/frdb/index.html
13. FAST REACTOR DESIGNS, Page 356

Fig. 1.1-2 Flow Diagram of Main Cooling System in MONJU

Post accident heat removal (PAHR) is also a significant function of the DHRS in a core disruptive accident. It is obvious that the cooling of core fuel debris is crucial for in-vessel retention.

Higher reliability is needed in the DHRS than is required in normal cooling systems, and different design approaches to the DHRS are available depending on the plant design. One example is deterministic with probabilistic reinforcement. Independent and multiple heat transport loops are applied to the DHRS to increase redundancy. The number of loops is determined so as to satisfy the deterministic requirement for operation in event categories and to achieve the required reliability of the DHRS. Depending on the circumstances, diversity of the system is also required against common mode failures. For example, designs of heat exchangers and the driving force of fluid circulation are varied.

Passivity is also a significant feature in maintaining DHRS function. Natural circulation without the operation of active components extends the passivity of the DHRS. Natural circulation can maintain the function of the DHRS in any situation, e.g., failure of the sodium pumps, air blowers, and the total blackout issue as long as the sodium level is maintained in the reactor vessel.

As for the sodium reactors, the operation temperature is around 550 ˚C in a reactor upper plenum and much lower than the boiling point of the coolant, ca. 880 ˚C. Thus, a single phase flow condition can be expected in a wide range of accidents. It helps that the phenomena are simple under natural circulation conditions. Further, this wide coolant temperature range allows large temperature differences between the hot region in the core and the cold region in a heat exchanger, i.e., large natural circulation head. These facts suggest that sodium reactors are advantageous in terms of natural circulation (capability, or characteristic, or property).

Further, several recent designs of sodium-cooled fast reactors simplify the DHRS by using natural circulation. The DHRS has no sodium pump. This means that there is no need to consider pump failure or the failure of related equipment, e.g., control unit,

electrical power line, air conditioner in the control unit room. The load on emergency diesel generators is also reduced.

However, natural circulation also has certain drawbacks. The flow rate through the core is determined by pony motor pump operation in the forced circulation mode. In contrast to this, the core flow rate in natural circulation depends on temperature distribution along the primary circuit and changes over time according to the temperature. This temperature also depends on the flow rate. Therefore, it is impossible to decide the core flow rate in advance in the natural circulation mode. This creates difficulty in estimating the highest temperature in the core. A network code which models the entire heat transport system is needed determine the transient temperatures and flow rate courses.

One of the significant goals of the DHRS is to maintain the integrity of the core, i.e., to maintain the highest clad temperature of the fuel pin at less than the threshold value defined by safety evaluation. The core consists of hundreds of flow channels, i.e., driver core fuel subassemblies, radial blanket fuel subassemblies, and radial reflectors. These channels have different transient temperatures and flow rates. Each of the core fuel subassemblies consists of many fuel pins. Thus, the evaluation methods should cover plant-wide system response, the core of multi-channels, and fuel pins inside the subassemblies. Further, uncertainty should be considered in the physical models, e.g., correlations of the flow resistance coefficient in each component and the heat transfer coefficient in each heat exchanger in a wide region of the flow velocity, i.e., Re number.

Thus, it is essential to know the characteristics of natural circulation in a wide spectrum of the system. As for the plant-wide system, the natural circulation flow rate depends on the geometry of the heat transport system, especially the arrangement of the DHRS heat exchangers in the main heat transport system. There are several DHRS designs for sodium-cooled reactors. Such designs and the history of the DHRS are discussed in the next section.

1.2 History of Decay Heat Removal Systems and Natural Circulation

1.2.1 DHRS Design Options

The DHRS is designed to remove decay heat from the core after reactor shutdown. The operational coolant temperature of a sodium-cooled reactor is higher by 200˚C than a light water reactor. Then, the final heat sink in the sodium-cooled reactor is the atmospheric air, via the heat exchanger between the sodium and the air. Here, the heat transport path from the core to the sodium-air heat exchanger depends on the design. Figure 1.2-1 shows several DHRS design options that have been considered in the past. Here, four DHRS types are depicted,

1) IRACS: Intermediate Reactor Auxiliary Cooling System,
2) PRACS: Primary Reactor Auxiliary Cooling System,
3) DRACS: Direct Reactor Auxiliary Cooling System,
4) RVACS: Reactor Vessel Auxiliary Cooling System.

Most DHRS can be classified into these types of cooling systems. Each of the systems is described below.

1) IRACS

Sodium-sodium heat exchanger of the DHRS is installed in the secondary cooling system between the IHX and SG. In some designs, a branch line is connected between the secondary cooling system and the air cooler instead of the sodium-sodium heat exchanger. The integrity of the secondary cooling system is necessary for decay heat removal in this design. Thus, the secondary cooling system is also classified into the safety system.

2) PRACS

The sodium-sodium heat exchanger is set in the primary cooling system, mainly in the primary side inlet plenum of the IHX. There is no need for a secondary cooling system in this design in contrast to the IRACS.

3) DRACS

The sodium-sodium heat exchanger is immersed in the reactor upper plenum. The main cooling path uses the primary circuit; however, in case of sodium leak

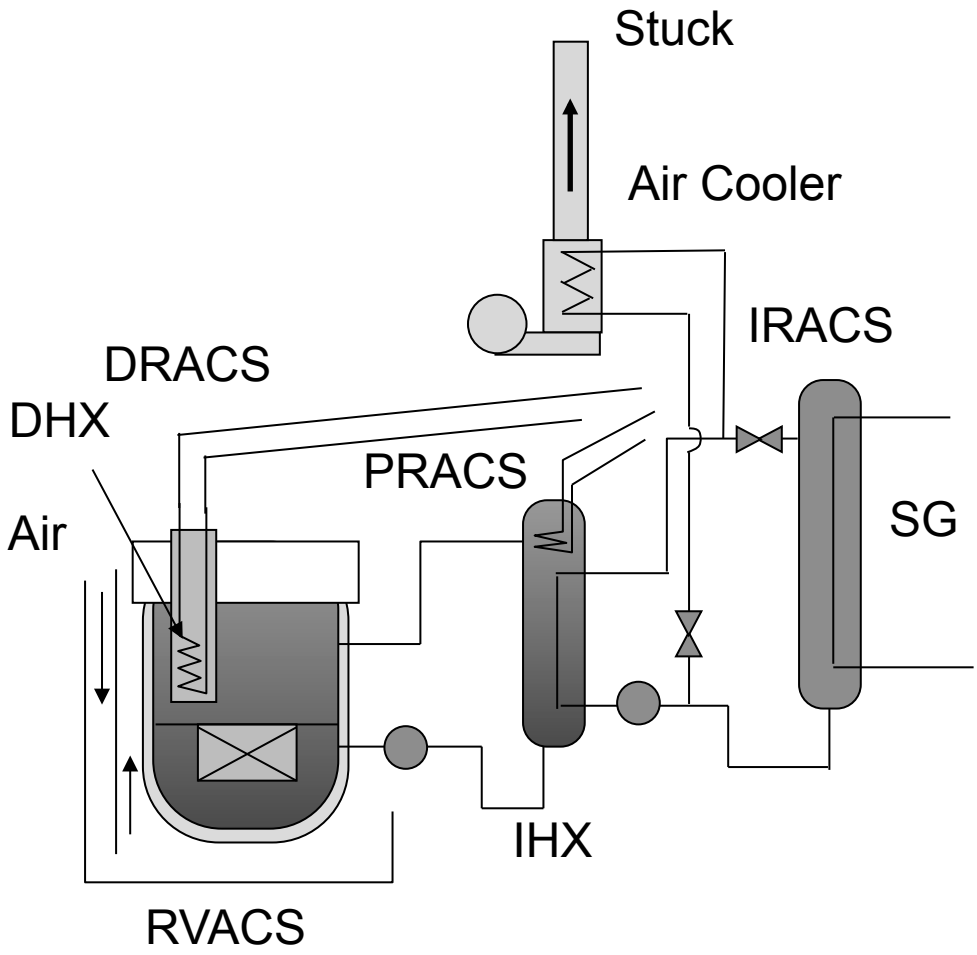

Fig. 1.2-1 Typical Design Options of DHRS

accident in the primary circuit, in-vessel natural circulation is also available. There is a design option to connect the upper and lower plenums in the reactor vessel directly using a flow diode to enhance the in-vessel cooling function.

4) RVACS

There is no sodium-sodium heat exchanger in this design. The reactor vessel wall is a heat transfer area between the primary circuit and the air. When the electric power output is increased, the heat transfer area of the reactor vessel is reduced relative to the decay heat. Thus, this concept is normally applied only to small or middle size reactors of less than 50MW at full electric power.

During the long history of sodium-cooled reactors, the DHRS has been modified according to country and safety requirements. Several DHRS designs for sodium-cooled reactors operated around the world are described in next section.

1.2.2 Sodium-Cooled Reactors around the World

Sodium-cooled reactors have been developed as shown in Table 1.2-1. A database of fast reactors around the world (IAEA, 2006) was summarized by the IAEA and updated in 2006. DHRS flow diagrams and components in several reactors are explained below by country and history.

(1) Experimental Reactors

Several experimental reactors reached criticality between 1950 and 1980 in the USA, Russia, UK, France, Germany, Japan, and India. EBR-II in the USA is one of the experimental reactors in the early phase. Figure 1.2-2 shows a schematic of the primary cooling system of EBR-II (Feldman, 1987). EBR-II is a pool type reactor, which has a large-capacity cold pool. This heat capacity helps moderate temperature increase in the core during long transient time after a scram. Shutdown coolers are installed as DHRS and connected with sodium-sodium heat exchangers that are immersed in the cold pool of the reactor vessel. Thus, type of DHRS is a DRACS in this plant. Such an estimated DHRS type is also shown in Table 1.2-1. There is no pump in the secondary loop of the DHRS in EBR-II.

Table 1.2-1 Sodium Cooled Fast Reactors around the World

Reactor	Country	Category*1	First Criticality	Power*2	Type*3	DHRS
Rapsodie	France	Exp.	1967	40th	Loop	
KNK-II	Germany		1972	20e	Loop	IRACS
FBTR	India		1985	13e	Loop	
PEC	Italy		Cancelled	120th	Loop	
JOYO	Japan		1977	140th	Loop	Main Air Cooler
(DFR)*4	UK		1959	15e	Loop	
BOR-60	Russia		1968	12e	Loop	IRACS
EBR-II	USA		1961	20e	Pool	DRACS
Fermi	USA		1963	60e	Loop	
FFTF	USA		1980	400th	Loop	Main Air Cooler
BR-10	Russia		1958	8th	Loop	PRACS
CEFR	China		2010	23.4e	Pool	
Phenix	France	Dem./Prot.	1973	250e	Pool	IRACS, RV
SNR-300	Germany		Cancelled	327e	Loop	DRACS
PFBR	India		Planning	500e	Pool	DRACS
MONJU	Japan		1995	280e	Loop	IRACS
PFR	UK		1974	250e	Pool	PRACS
CRBRP	USA		Cancelled	380e	Loop	
BN-350	Russia		1972	130e	Loop	
BN-600	Russia		1980	600e	Pool	
ALMR	USA		Planning	303e	Pool	RVACS+IRACS
Super-Phenix 1	France	Comm.	1985	1242e	Pool	IRACS
Super-Phenix 2	France		to EFR	1440e	Pool	
SNR-2	Germany		to EFR	1497e	Pool	DRACS
DFBR	Japan		Cancelled	660e	Loop	DRACS
CDFR	UK		to EFR	1500e	Pool	
BN-1600	Russia		Planning	1600e	Pool	
BN-800	Russia		Planning	800e	Pool	IRACS
EFR	Europe		Cancelled	1580e	Pool	DRACS
JSFR	Japan		Planning	1500e	Loop	PRACS+DRACS

*1: Experimental reactor/ Demonstration or Prototype reactor/ Commercial size reactor

*2: Nominal Power (MW), th: thermal power, e: electric power (gross)

*3: Configuration of primary circuit

*4: DFR: NaK was used as coolant in the primary and secondary circuits.

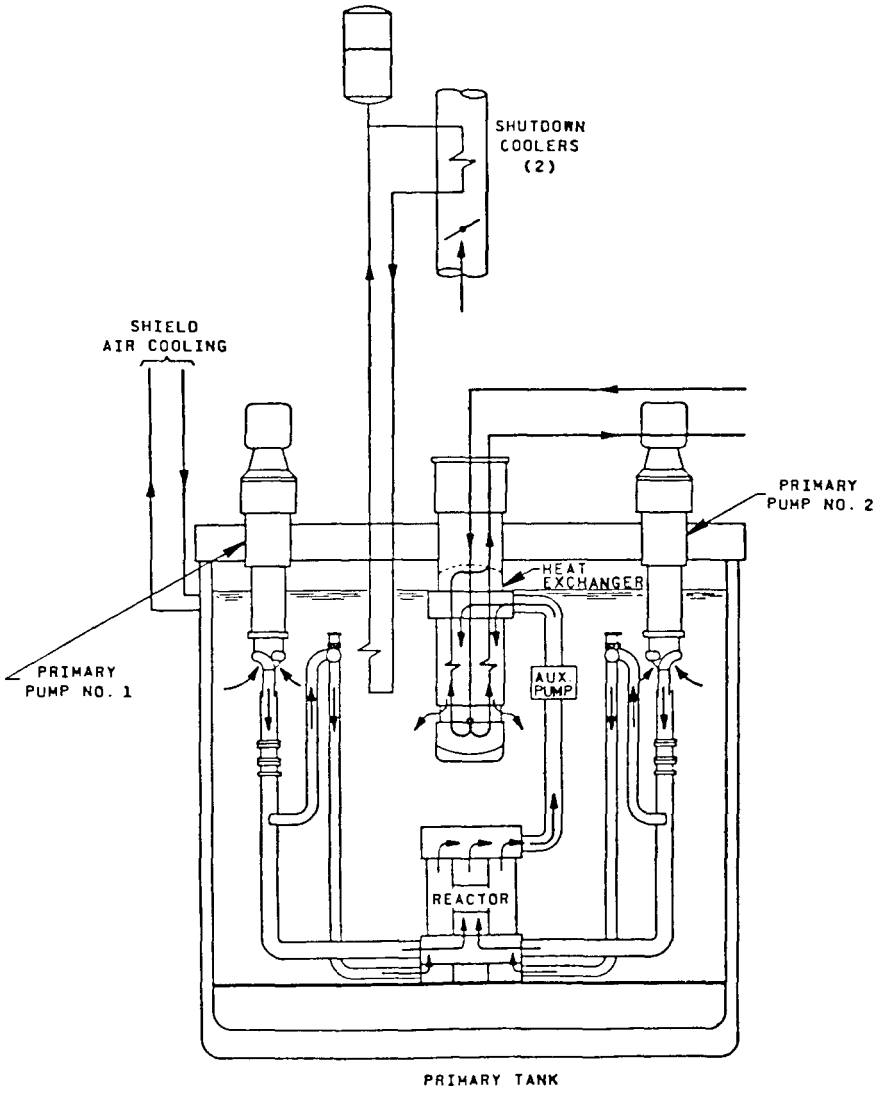

Fig. 1. EBR-II primary system.

E.E. FELDMAN, EBR-II UNPROTECTED LOSS-OF-HEAT-SINK PREDICTIONS AND PRELIMINARY TEST RESULTS, Nuclear Engineering and Design 101 (1987) 57-66
Page 58, Figure 1

Fig. 1.2-2 Schematic of Primary Cooling System of EBR-II

A flow diagram for BOR-60 in Russia is shown in Fig. 1.2-3. BOR-60 is a loop type reactor with sodium-air heat exchangers in the secondary cooling system. The DHRS type is an IRACS, and SG bypass lines connect with the sodium-air heat exchangers directly. There are several valves that switch the lines from the SG to the air coolers.

Figure 1.2-4 shows a flow diagram of the KNK-II cooling system. KNK-II is also a loop type reactor with sodium-air heat exchangers in the secondary cooling system (Schubert, 1984). The main cooling line passes through the SG and the air cooler in series connection. There is a bypass line; however, it merely bypasses the SG. The DHRS type is an IRACS.

Several DHRS types were used in the experimental reactors of this period. However, the IRACS was the most commonly applied. In case of the DRACS used in EBR-II, there is no pump in the secondary cooling system of the DHRS and natural circulation is used.

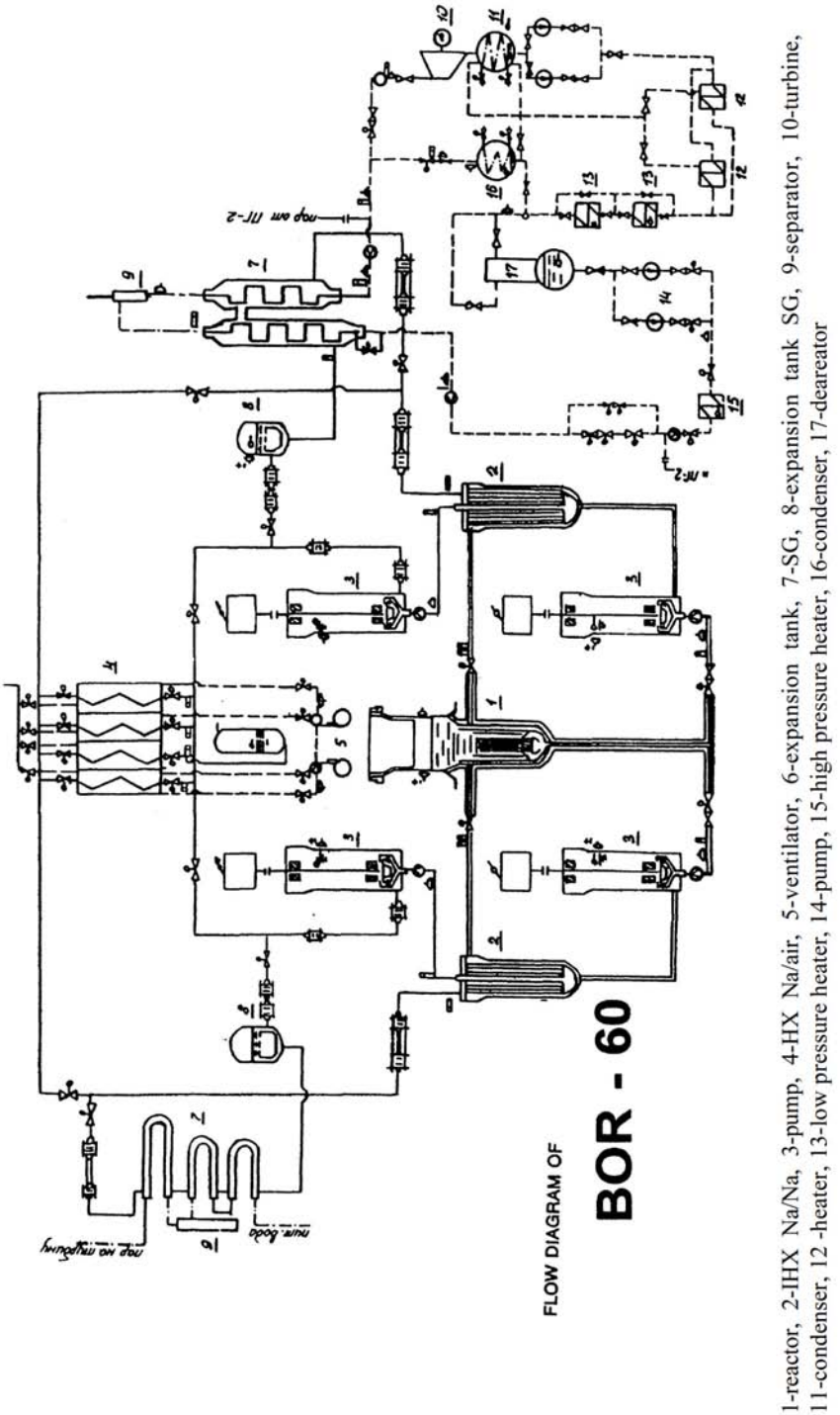

IAEA Fast Reactor Database,
http://www.iaea.org/inisnkm/nkm/aws/frdb/index.html
13. FAST REACTOR DESIGNS, Page 296

Fig. 1.2-3 Flow Diagram of Main Cooling System in BOR-60

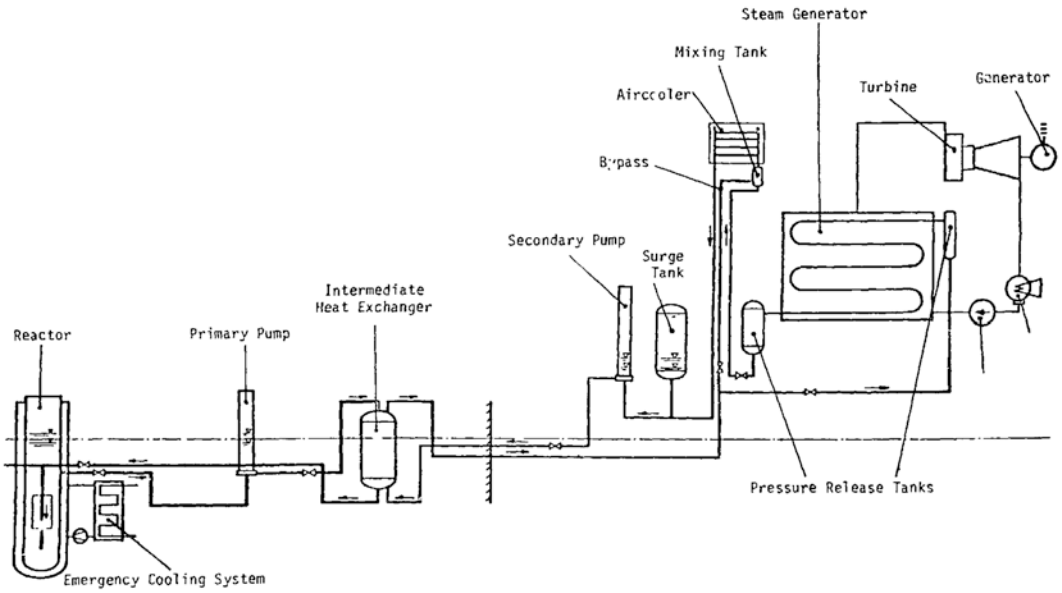

Figure 1.1 KNK-II Plant Layout

Schubert, B.K, Dynamic simulation of the air-cooled decay heat removal system of the German KNK-II experimental breeder reactor, Brookhaven National Lab., Upton, NY (USA), NUREG/CR—3910 (1984).
Page 11. Figure 1.1

Fig. 1.2-4 Flow Diagram of KNK-II Cooling System

(2) Prototype or Demonstration Reactors

Prototype or demonstration reactors were also built from the 1970 to the 1980's. Figure 1.2-5 (a) shows the primary system of the Phenix in France, which is a pool-type reactor. The DHRS is installed in the secondary cooling system as shown in Fig. 1.2-5 (b). The SG is covered by an air-cooling shroud. There is no separated sodium-air heat exchanger, and no line to bypass the SG. This is a simple DHRS system. The heat sink for air cooling is located in the secondary cooling system, meaning that this DHRS can be categorized as an IRACS.

SNR-300 was built in Germany; however, the reactor was not put into operation. The flow diagram of the DHRS in SNR-300 (Willrodt, 1989) is shown in Fig. 1.2-6(a). DHRS sodium-sodium heat exchangers (immersed coolers, ICs) are set in the reactor vessel. Three of the ICs are connected to one air cooler and a total of 6 ICs and two air coolers are used. This DHRS is categorized as a DRACS. Details of the IC and flow path in the reactor vessel are shown in Fig. 1.2-6(b). The ICs are immersed in the hot pool outer annulus. There are several flow diodes at the lower end of the annulus wall and the core support plate (grid plate) to make a flow path from the hot pool outer annulus to the lower plenum during the decay heat removal operation, i.e., in-vessel natural convection. An electromagnetic pump and a blower are installed in each sodium loop and air cooler intake, respectively.

The cooling system of MONJU is shown in Fig. 1.1-2. MONJU is a loop-type reactor. The air coolers of the DHRS are set in the lines to bypass the SGs. There are several valves which switch the lines from the SG to the air coolers when the DHRS is operated. This DHRS is categorized as an IRACS. The pony motors are installed in the primary and the secondary cooling systems and blowers are installed at the air inlets of the air coolers for the decay heat removal operation.

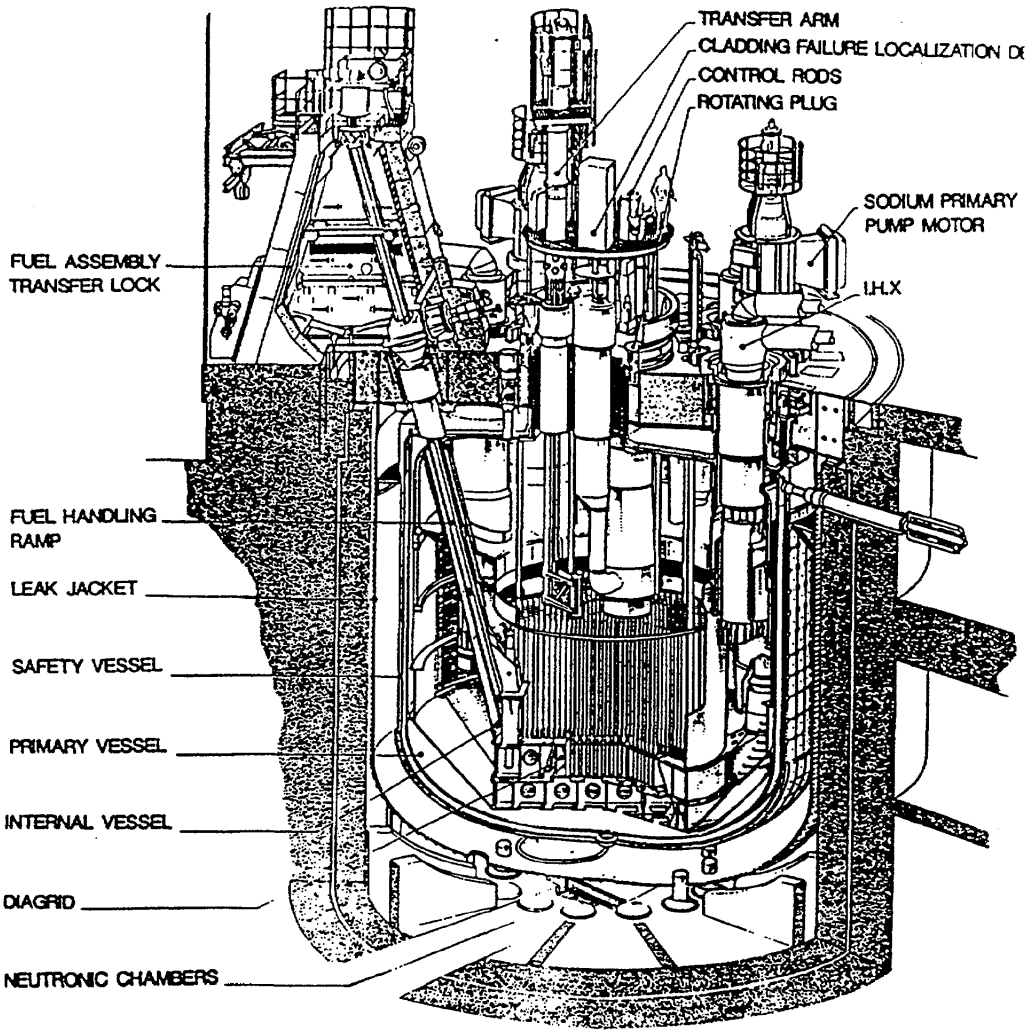

PHENIX REACTOR BLOCK

IAEA Fast Reactor Database,
http://www.iaea.org/inisnkm/nkm/aws/frdb/index.html
GRAPHIC MATERIAL, Page 163

Fig. 1.2-5(a) Schematic of Primary Cooling System in Phenix

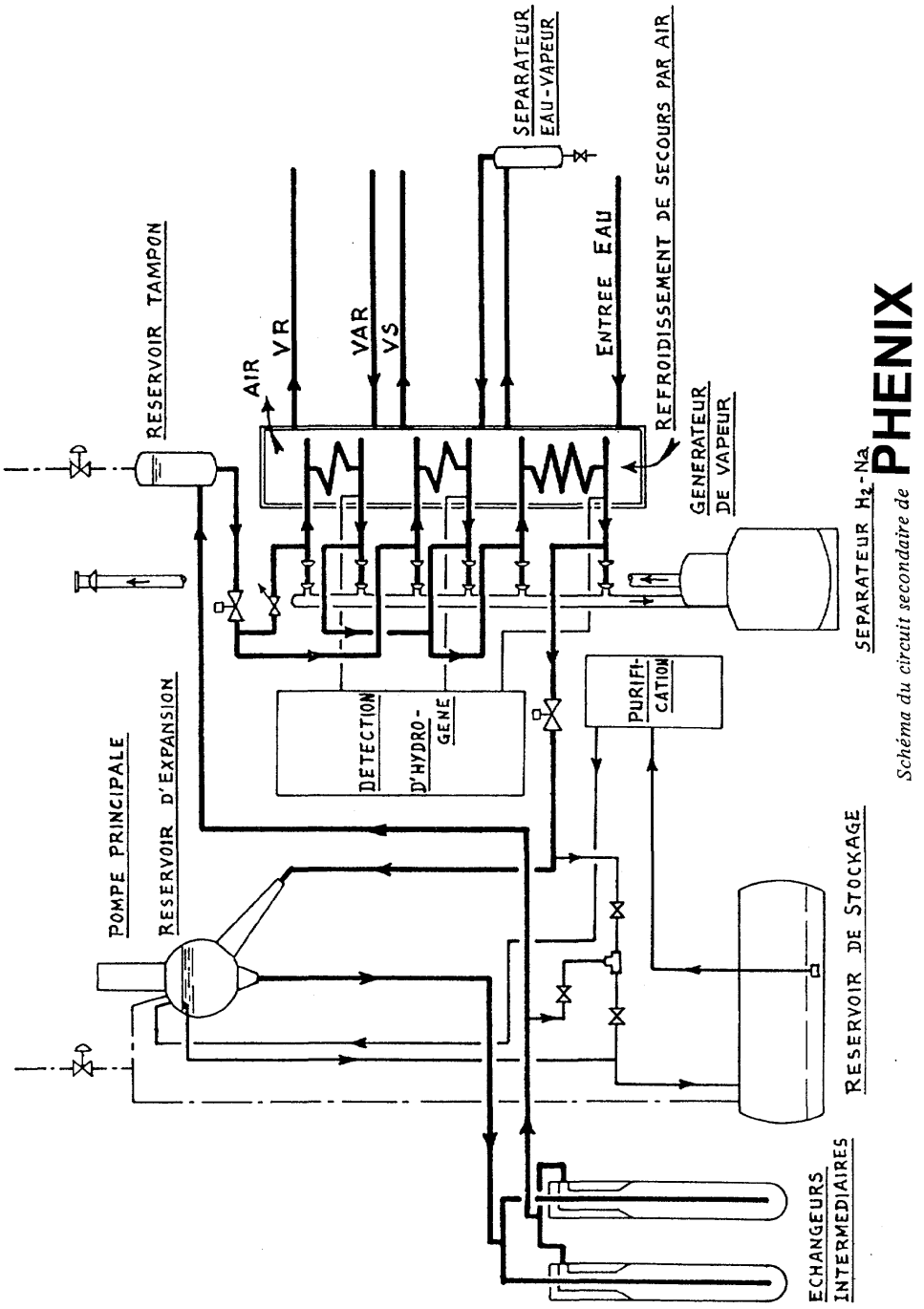

IAEA Fast Reactor Database,
http://www.iaea.org/inisnkm/nkm/aws/frdb/index.html
GRAPHIC MATERIAL, Page 164

Fig. 1.2-5(b) Flow Diagram of Secondary Cooling System in Phenix

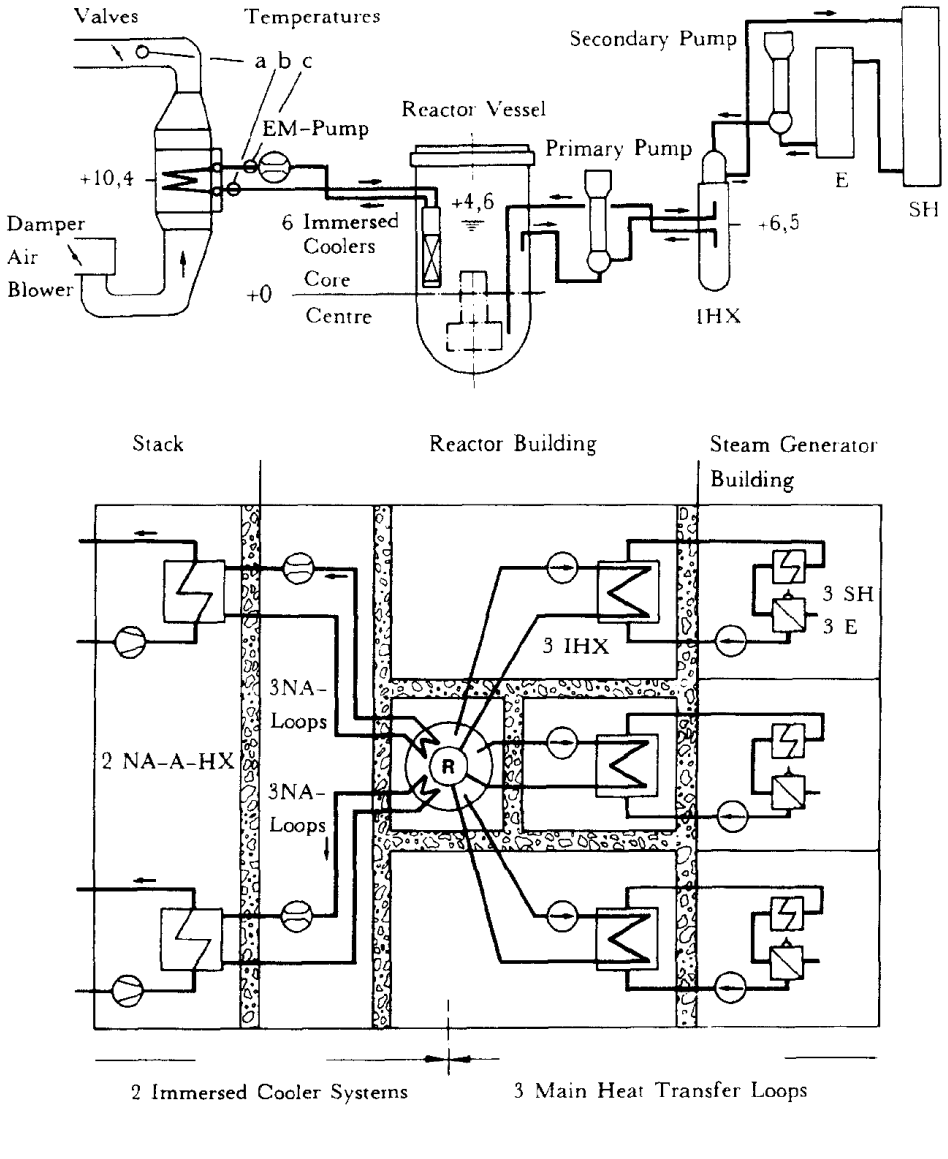

Fig. 1. SNR-300 decay heat removal plan.

U. WILLRODT, Verifications of The Design Calculations of The Immersed Cooler System During The Start-up Tests of SNR-300, Nuclear Engineering and Design 113 (1989) 121-130
Page 122, Fig. 1

Fig. 1.2-6(a) Flow Diagram of Cooling System and DHRS in SNR-300

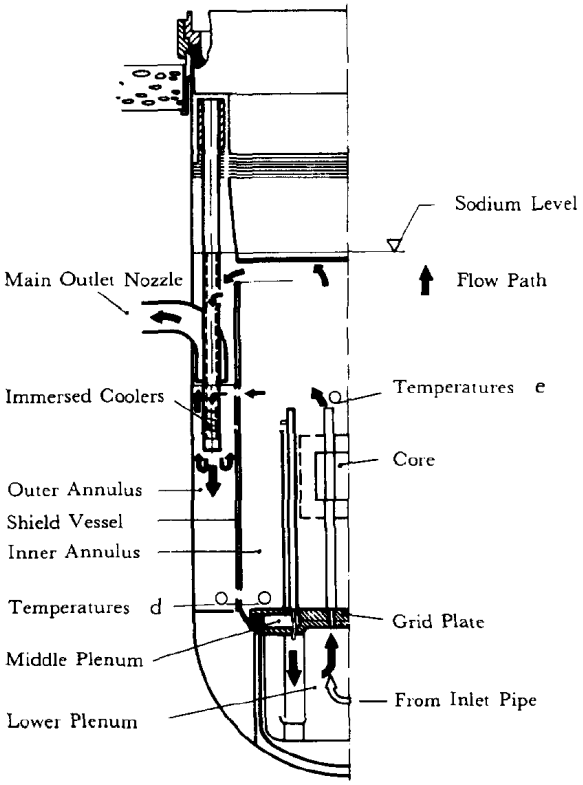

Fig. 2. In-vessel flow paths during emergency cooling.

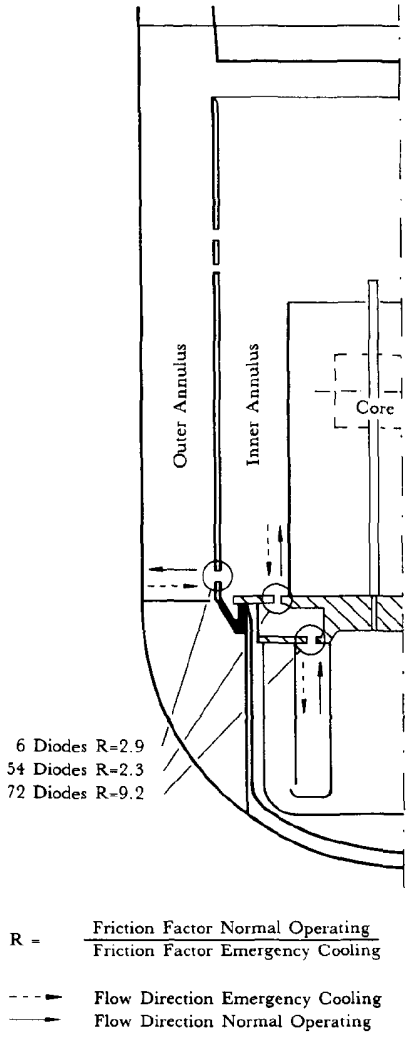

Fig. 3. Location and characteristics of the flow diodes.

U. WILLRODT, Verifications of The Design Calculations of The Immersed Cooler System During The Start-up Tests of SNR-300, Nuclear Engineering and Design 113 (1989) 121-130
Page 123, Fig. 2 and Fig. 3

Fig. 1.2-6(b) Detail of Immersion Cooler and Flow Path in SNR-300

Figure 1.2-7(a) shows the flow diagram of PFR in the UK. PFR is a pool-type reactor and has DHRS heat exchangers in the reactor vessel (Huebel, 1974). A close view of the reactor vessel is shown in Fig. 1.2-7(b). The left hand side of the figure shows PFR, and SNR-300 is shown in the right hand side. The DHRS heat exchanger is installed in each IHX upper plenum. Thus, this DHRS is classified as a PRACS. The DHRS secondary loop uses NaK as a coolant and there is no pump, as shown in Fig. 1.2-7(c). The melting point of NaK is lower than room temperature, and there is no need to consider solidification due to over cooling or too small flow rate in the air coolers. This design using NaK has the advantage of using natural circulation in the secondary loops of the DHRS.

Among the prototype or demonstration reactors between the 1970s and 1980s, the numbers of the loop- and pool-type reactors are comparable. The DRACS, which used heat exchangers in the hot pool, was selected as well as the PRACS for the pool-type reactor. The IRACS was also well used as a DHRS.

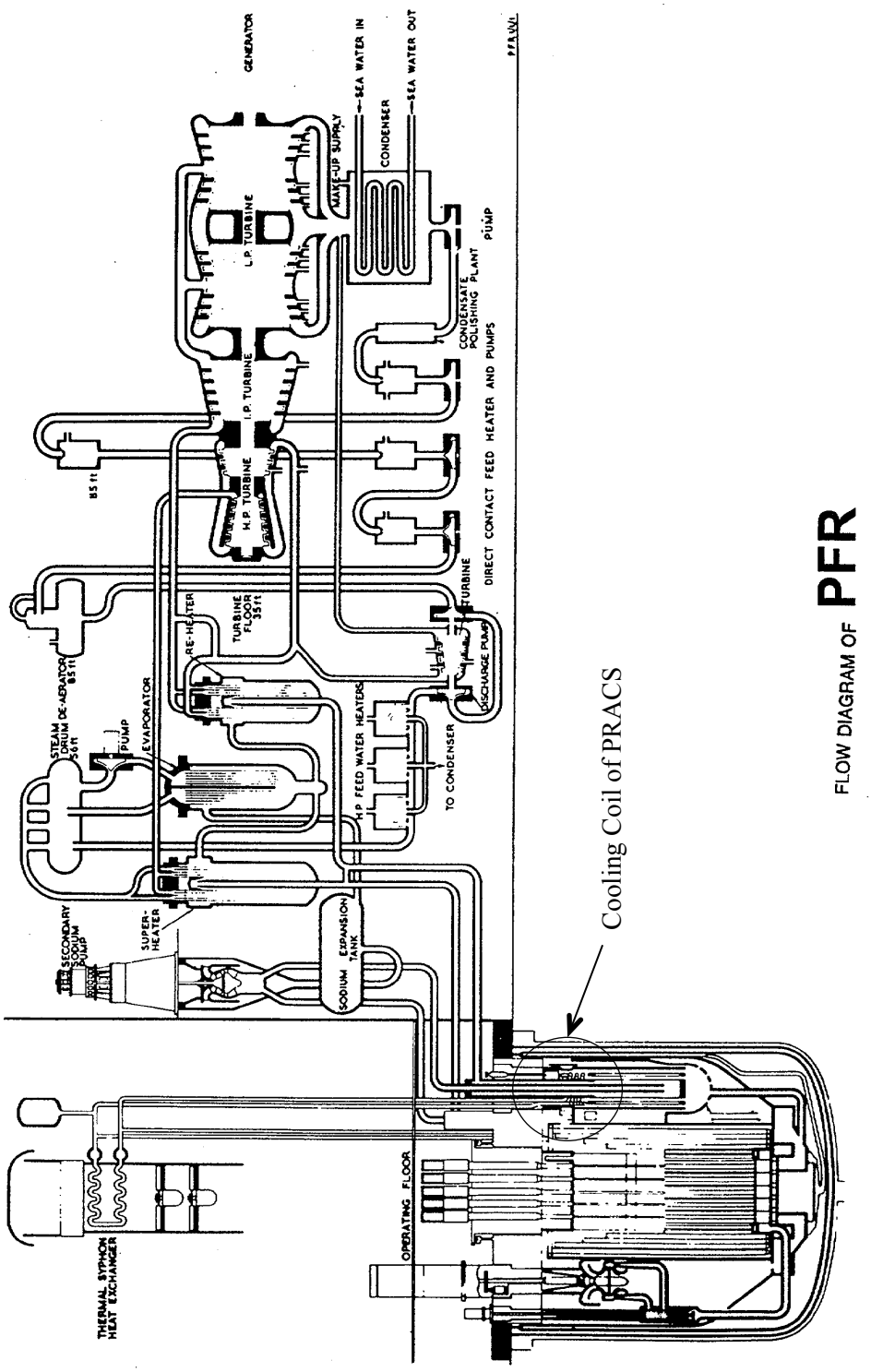

IAEA Fast Reactor Database,
http://www.iaea.org/inisnkm/nkm/aws/frdb/index.html
GRAPHIC MATERIAL, Page 167

Fig. 1.2-7(a) Flow Diagram of PFR Cooling System

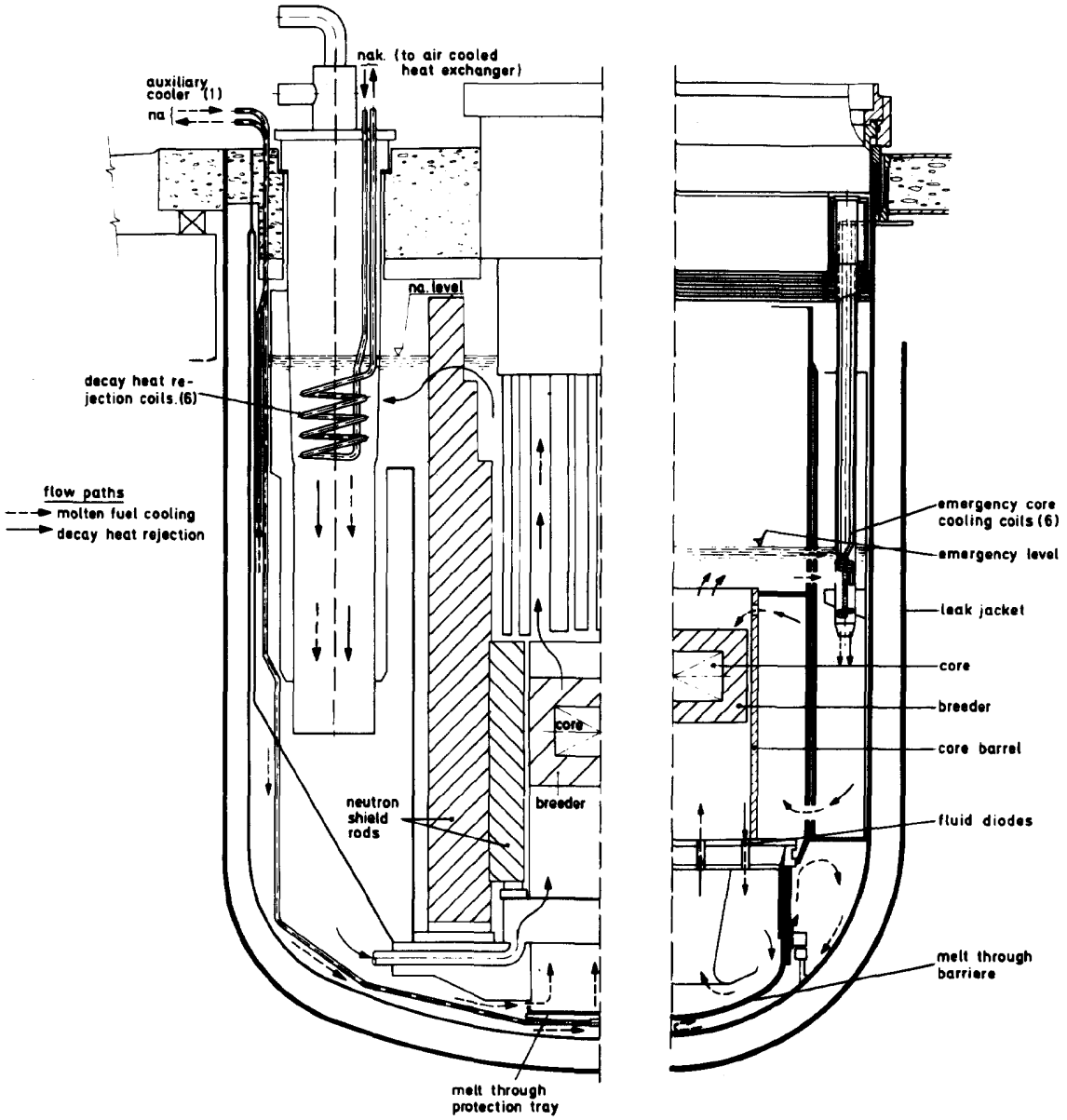

Fig. 11. Arrangements for decay heat removal and control of fuel debris in the PFR (left) and SNR-300 (right).

H. HUÉBEL, Design of The Primary Containment for Pool and Loop Arrangements of LMFBRS, Nuclear Engineering and Design 27 (1974) 139-154.
Page 150, Fig. 11

Fig. 1.2-7(b) Schematic of PRACS Heat Exchanger in PFR

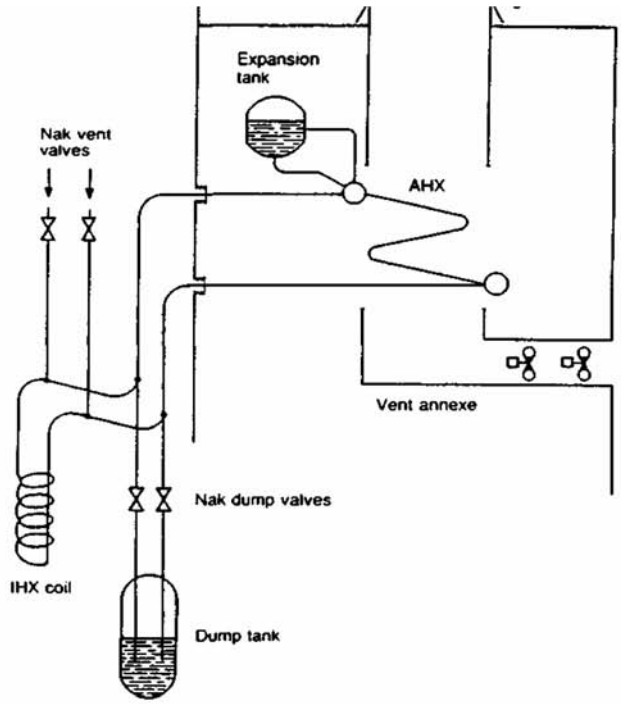

PFR thermal siphon decay heat rejection loop.

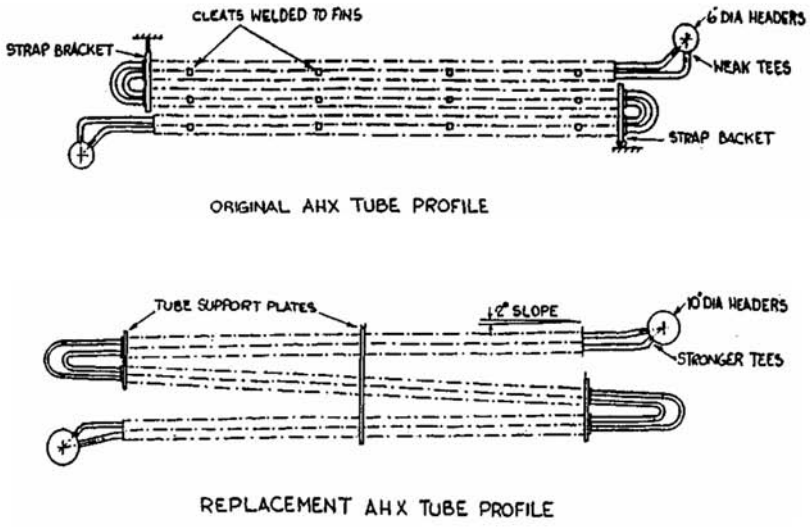

The original and replacement PFR thermal syphon air heat exchangers.[7]

IAEA Fast Reactor Database,
http://www.iaea.org/inisnkm/nkm/aws/frdb/index.html
13. FAST REACTOR DESIGNS, Page 336

Fig. 1.2-7(c) Schematic of PRACS secondary Loop in PFR

(3) Commercial Size Reactor

The Super-Phenix (Favet, 1990), at over 1200MWe, is a commercial-size reactor that was built and operated in France. Further, several commercial-size reactors have been designed in other countries, e.g., Germany, UK, Russia, and Japan. Figure 1.2-8(a) shows schematic of main heat transport systems and DHRS in the pool-type reactor of Super-Phenix. A bird's-eye view of the secondary cooling system is shown in Fig. 1.2-8(b). The air coolers of the DHRS are set in the lines to bypass SGs. There are valves which switch each line from the SG to the air cooler when the DHRS is operated. The cooling system consists of four primary pumps, 8 IHXs, four secondary pumps, four SGs, and four air coolers of the DHRS. This DHRS is categorized as an IRACS. Each of the air coolers has a blower in the air intake.

The 660 MWe DFBR (Ueta, 1995) was designed in Japan as a loop-type reactor with three IHX vessels and three pump vessels around the reactor vessel as shown in Fig. 1.2-9(a). Dipped heat exchangers are immersed in the reactor upper plenum. DFBR has three main cooling system loops and four DHRS loops, as shown in Fig. 1.2-9(b). The primary pump in each loop has a pony motor that is connected to the emergency power line of the diesel generator. An electromagnetic pump and an air blower are installed in each DHRS loop. The DHRS type in DFBR is a DRACS. There is no flow diode in the reactor vessel, as seen in the design of SNR-300. The main cooling path in the decay heat removal operation is the primary circuit through the IHX and pump vessels.

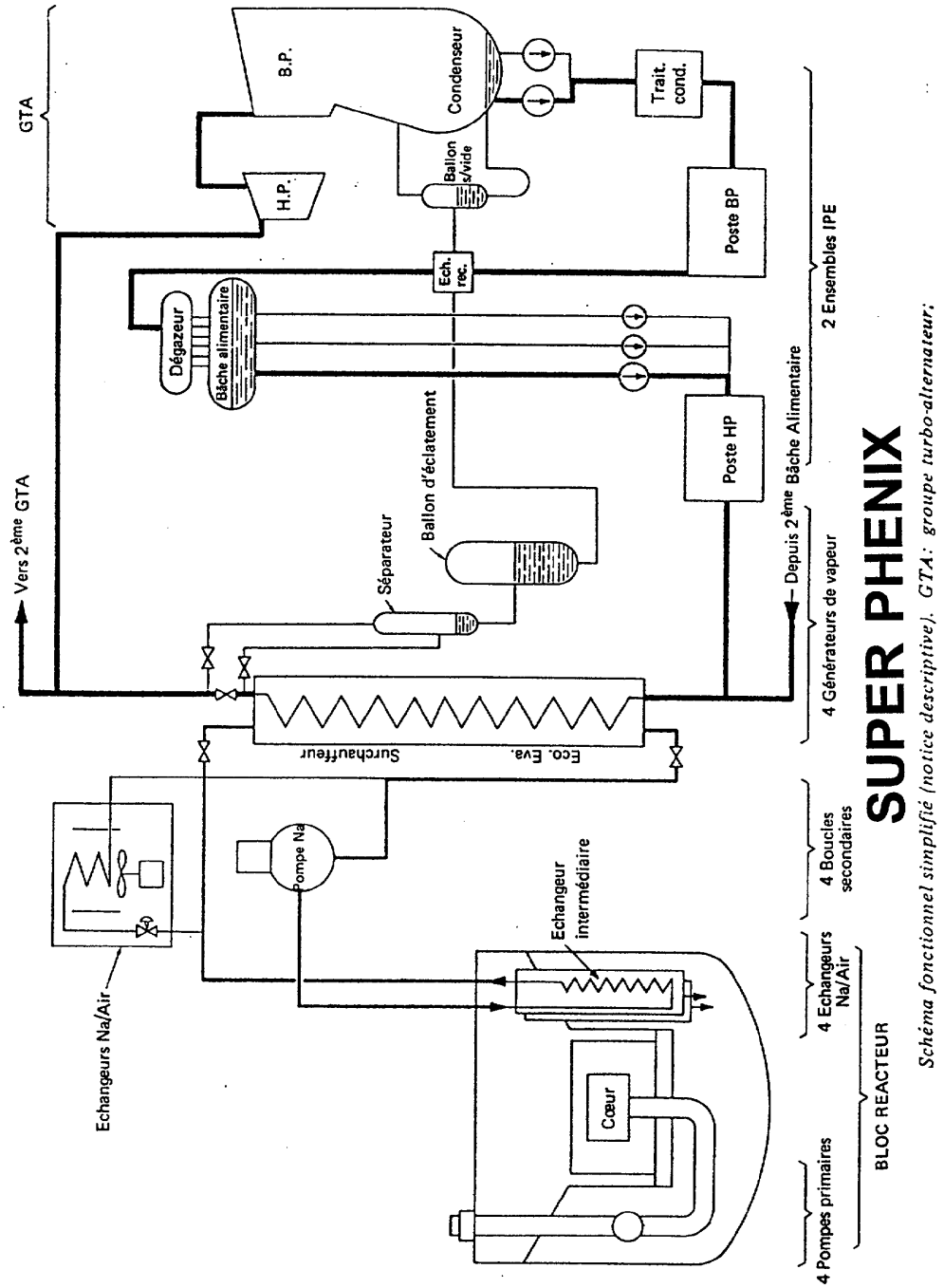

IAEA Fast Reactor Database,
http://www.iaea.org/inisnkm/nkm/aws/frdb/index.html
GRAPHIC MATERIAL, Page 157

Fig. 1.2-8(a) Flow Diagram of Cooling System and DHRS in Super-Phenix

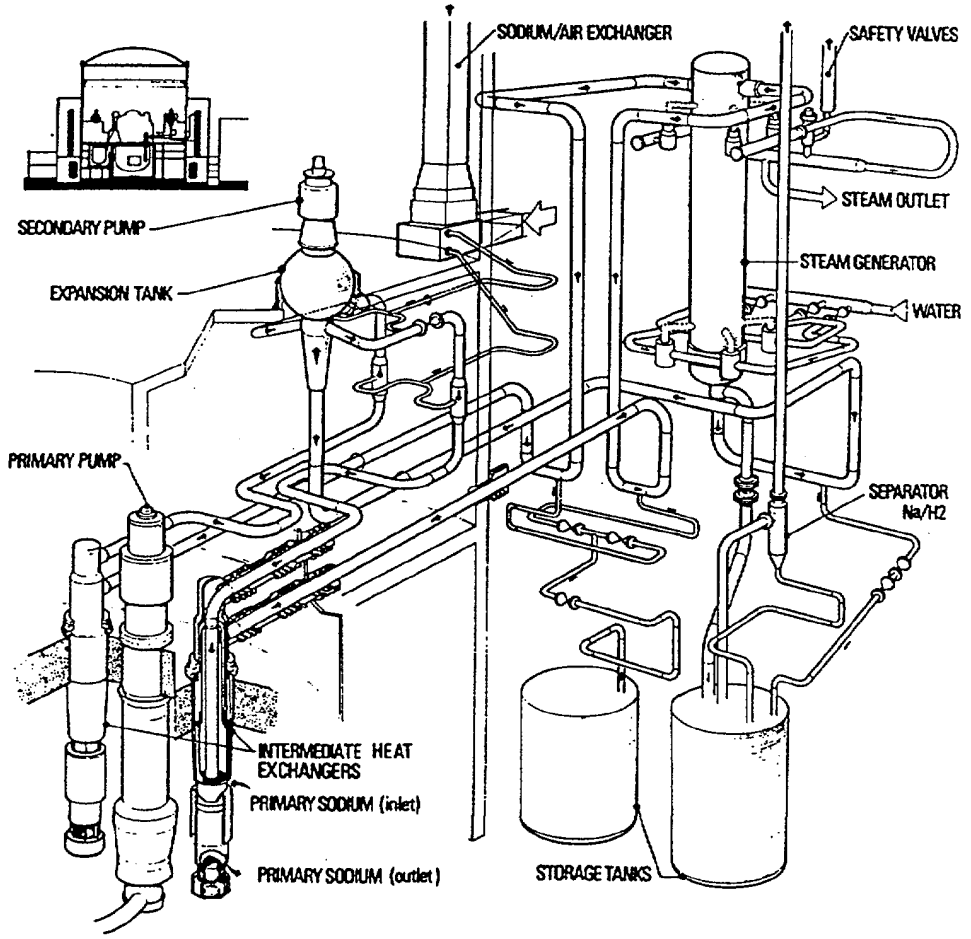

Main secondary sodium circuits and steam generators together with the decay heat removal system

SUPER PHENIX

IAEA Fast Reactor Database,
http://www.iaea.org/inisnkm/nkm/aws/frdb/index.html
GRAPHIC MATERIAL, Page 155

Fig. 1.2-8(b) Schematic of Secondary Cooling System in Super-Phenix

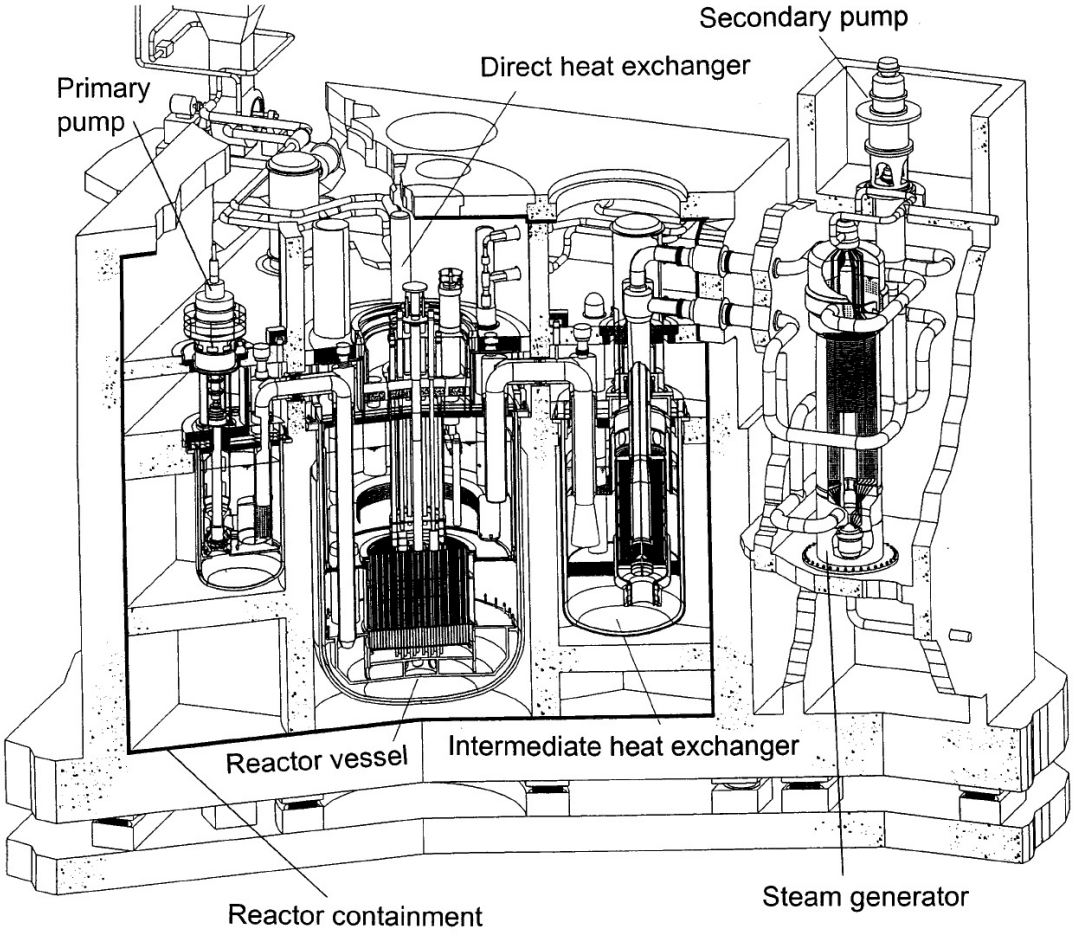

Fig. 4. DFBR primary and secondary systems.

B. Farrar et al., Fast reactor decay heat removal: approach to the safety system design in Japan and Europe, Nuclear Engineering and Design 193 (1999) 45–54
Page 48, Fig. 4

Fig. 1.2-9(a) Schematic of Cooling System in DFBR

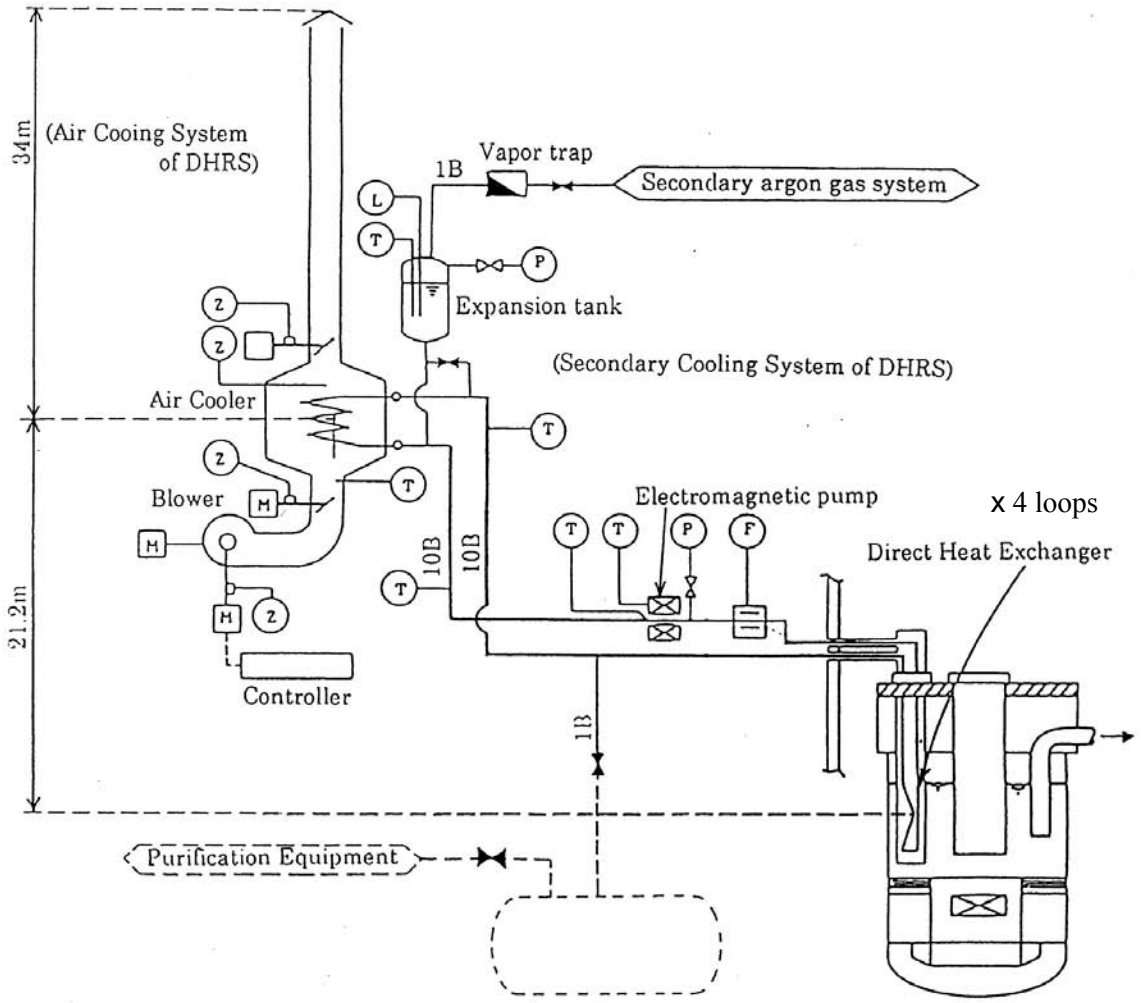

Fig. 7. DRACS of DFBR.

B. Farrar et al., Fast reactor decay heat removal: approach to the safety system design in Japan and Europe, Nuclear Engineering and Design 193 (1999) 45–54
Page 52, Fig. 7

Fig. 1.2-9(b) Flow Diagram of DHRS in DFBR

Several design studies were carried out in France, Germany, and the UK as Super-Phenix 2, SNR-2, (Weinberg, 1986) and CDFR, respectively. These projects were integrated into 1500 MWe EFR (Hennies, 1991). Figure 1.2-10(a) shows the primary circuit of EFR, where three pumps and 6 IHX are set. Six dipped heat exchangers are installed in the DRACS hot pool (Farrar, 1999). Here, diversity was considered as two types of cooling systems, including the dipped heat exchanger and the air cooler designs, the forced and natural circulations in the secondary loop and the air side of the air coolers. Three of the dipped heat exchangers are connected to natural circulation sodium loops and the air coolers use only natural draft in the air side, as shown in Fig. 1.2-10(b). Three residual DHRS loops use a forced circulation system, which is shown in Fig. 1.2-10(c).

As a next generation nuclear reactor, a JSFR (Japan Sodium-cooled Fast Reactor) design study (Kotake, 2010, 1500MWe) is being carried out in Japan together with an advanced and consistent fuel cycle system. Figure 1.2-11 shows the DHRS and main cooling system of JSFR. JSFR is a loop-type reactor with two main cooling system loops. A dipped heat exchanger is set in the reactor upper plenum as a DRACS, and a sodium-sodium heat exchanger is installed in the upper plenum of IHX as a PRACS in each of the two main cooling loops. Thus, JSFR has a combined DHRS using one DRACS and two PRACS units. Natural circulation is applied in offsite power loss events, i.e., design base events. Details of the cooling system are described in section 1.5.

In the designs of commercial size reactors from the 1980's, the pool-type reactor is often applied and a DRACS is selected as the DHRS. There are several designs in the category of design base accidents which use natural circulation for the DHRS.

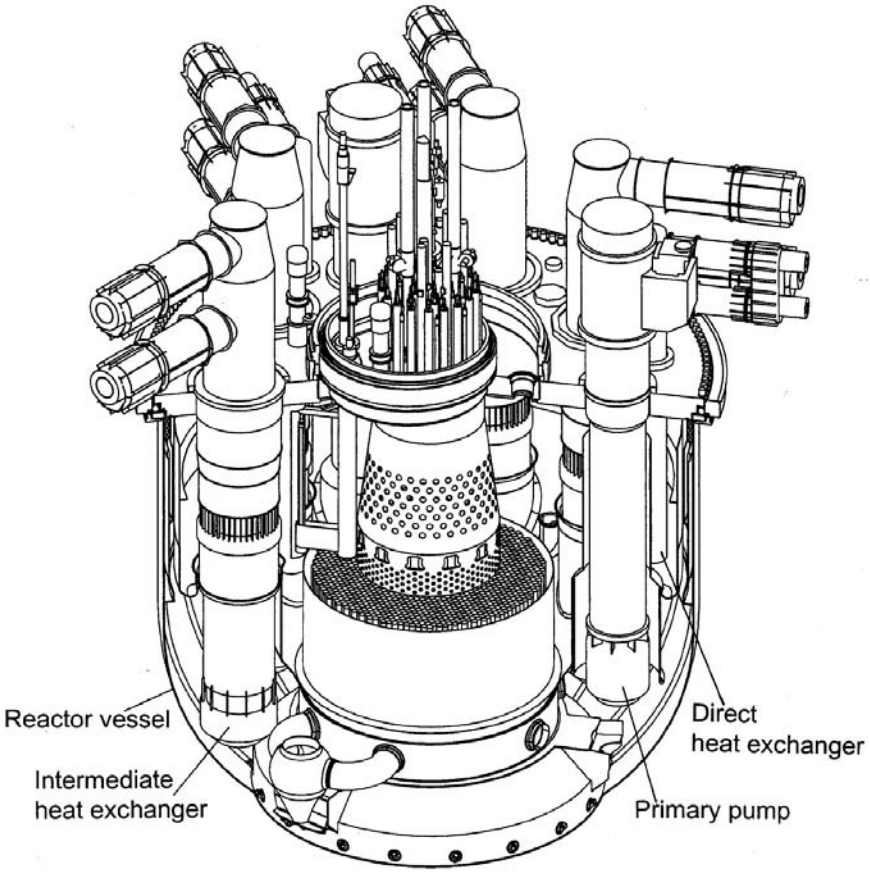

Fig. 2. EFR primary circuit.

B. Farrar et al., Fast reactor decay heat removal: approach to the safety system design in Japan and Europe, Nuclear Engineering and Design 193 (1999) 45–54
Page 47, Fig. 2

Fig. 1.2-10(a) Schematic of Primary Cooling System in EFR

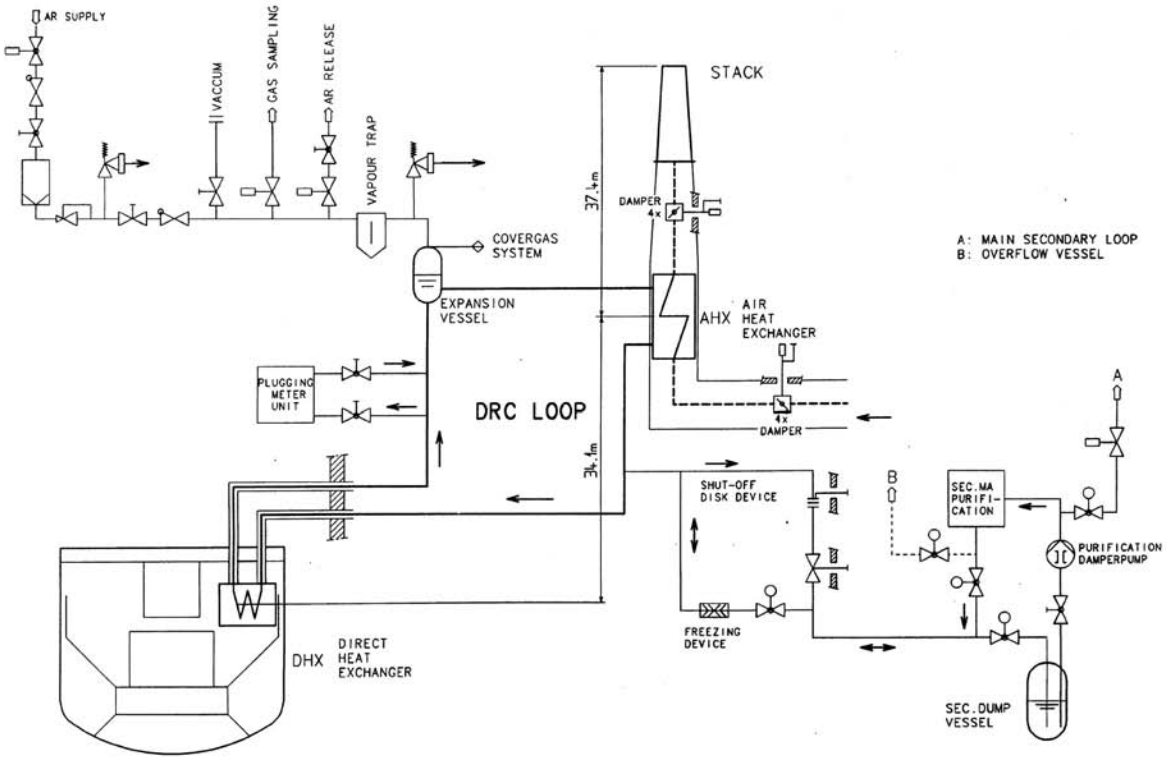

Fig. 6. DRC-1 of EFR.

B. Farrar et al., Fast reactor decay heat removal: approach to the safety system design in Japan and Europe, Nuclear Engineering and Design 193 (1999) 45–54
Page 50, Fig. 6

Fig. 1.2-10(b) Flow Diagram of Natural Circulation DHRS in EFR

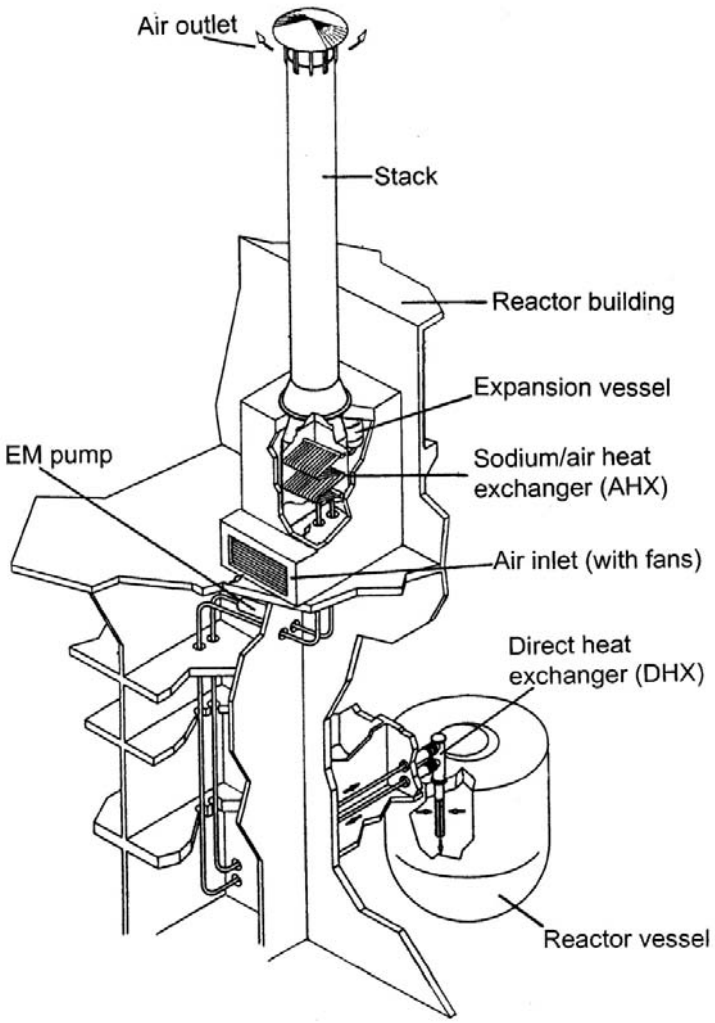

Fig. 5. Schematic DHR loop.

B. Farrar et al., Fast reactor decay heat removal: approach to the safety system design in Japan and Europe, Nuclear Engineering and Design 193 (1999) 45–54
Page 49, Fig. 5

Fig. 1.2-10(c) Schematic of Forced Circulation DHRS in EFR

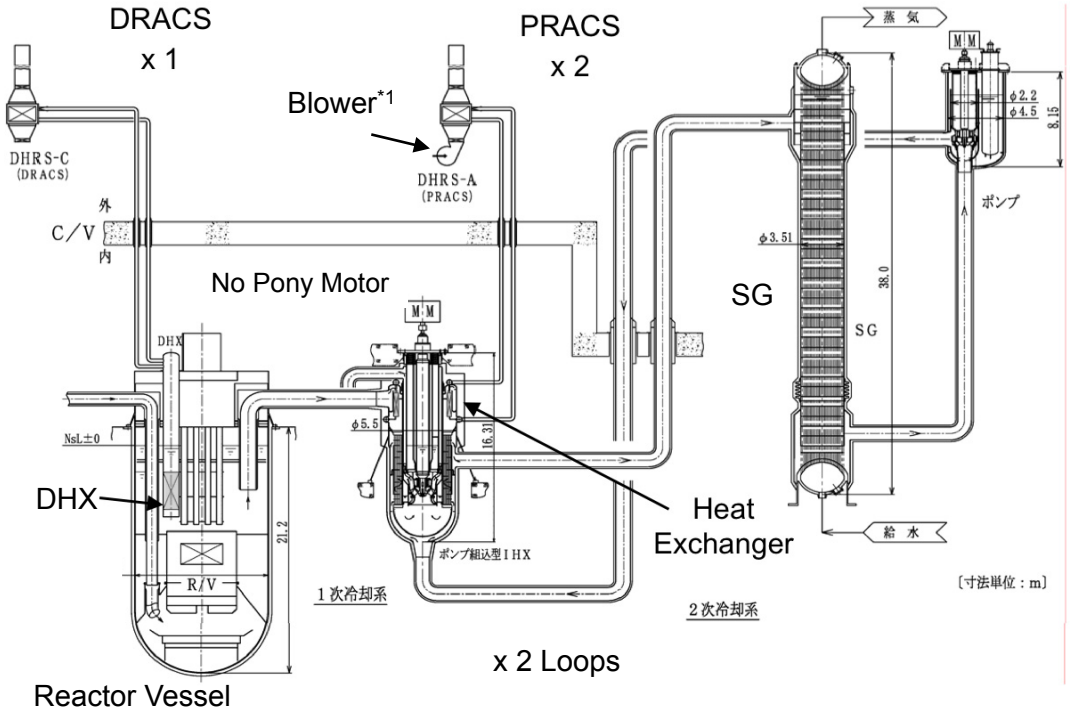

*1 Blowers are connected to normal power lines, not to emergency line.

Fig. 1.2-11 Schematic of Main Cooling System and DHRS in JSFR

1.2.3 Summary

Several types of DHRS have been applied to sodium-cooled fast reactor designs around the world. Recently, a DRACS is often used as the DHRS, and the IRACS is still one of the significant options. Further, natural circulation is considered as a decay heat removal operation in the design base accidents of offsite power loss. In such cases, there is no pump and no blower in the DHRS. There are several designs for which a PRACS is selected as the DHRS; however, the number of application examples is limited.

One of the reasons for the selection of the DRACS is that the system has heat exchangers in the reactor vessel and can function in case there is no flow path through the main primary circuits and also in the PAHR (Post Accident Heat Removal) phase during a severe accident.

1.3 Literature Survey

Natural circulation is a significant issue for the safety of sodium-cooled fast reactors. Therefore, many studies on natural circulation have been carried out. Here, experimental studies are selected to examine the phenomena during natural circulation according to the scale of the phenomena and system.

1.3.1 Reactor Tests

Demonstration experiments using actual reactors were performed around the world, e.g., SNR-300 in Germany (Willrodt, 1989), experimental fast reactor Joyo in Japan (Yamaguchi, 1989 and Sawada, 1990), and Super-Phenix (Favet, 1990). Natural circulation tests from the full power operation were carried out at Joyo. Subassembly outlet temperatures were measured during transient. Post analyses using a network code based on a multi-channel core model showed that the severest temperature course at a central fuel subassembly was significantly over-estimated. It was concluded that one of reasons for this was the heat transfer between the central subassemblies and surrounding low-temperature subassemblies.

1.3.2 Experiments on Primary System Behavior

Natural circulation depends on the geometry of the flow path, i.e., the height difference between the core and the heat exchangers of the DHRS, the mixing of hot and cold fluids from the core and the heat exchangers, and the height layout of the cooling circuits. The core outlet temperatures and the highest temperature in the core depend directly on the flow rate and temperature in the primary circuits. Thus, several model experiments were carried out to examine the dynamic behavior of natural circulation in the primary circuits using water as a working fluid. In these experiments the geometry of the primary circuits was well modeled to examine the time development of natural circulation in the primary circuits after the scram, which strongly depends on the layout of the flow path and the heat exchangers of the DHRS.

In Germany, RAMONA (Hoffmann, 1992) and NEPTUN (Weinberg, 1995) experiments were carried out to evaluate natural circulation characteristics for decay heat removal in SNR-2 and EFR, pool-type reactors and designed to use the immersed

coolers in the hot pool as DHRS, i.e., DRACS. RAMONA is a 1/20 scale model of the reactor vessel, where the core, IHXs, pumps, the immersed coolers, UIS, hot and cold pools are simulated. Ri number similarity and Pe number similarity were considered as scale law. The core is composed of ring-shaped heater blocks and annular flow channels between the rings. The subassemblies and fuel pins were not modeled because the model scale is too small. The secondary side loops of the IHXs and the immersed coolers are simulated as the only boundary conditions by the chilling units and pumps. It was shown by the RAMONA experiments that thermal stratification was formed in the hot pool due to the cold fluid provided by the immersed coolers and that the natural circulation flow rate decreased temporally due to the temperature decrease in the hot pool and the temperature increase in the IHX, which lost the heat sink of the secondary loop flow. NEPTUN is a 1/5 scale model of the reactor vessel. The Pe number was larger than that in the reactor by a factor of 10; however, Re number distortion was approximately 1/100 and significantly more advanced as compared with RAMONA. The core is composed of multi circular channels where electric heater pins are installed. The region between the core flow channels in the core barrel is filled with water. The steady state experiments showed that more than 40% of the decay heat in the core was removed by natural convection in the core barrel and the hot pool. It should be noted that the flow channel shape is circular and the gap area between the core flow channels (fuel subassemblies) is relatively larger than in the actual geometry. However it is suggested that the flow in the gap between the core fuel subassemblies exerts a significant influence on decay heat removal.

In Japan, DELTA experiments (Ieda, 1991) were performed to examine natural circulation in a pool-type reactor. DELTA is a 1/8 scale water test model and has cooling coils in the inlet plenums of the IHXs as a PRACS and dipped heat exchangers in the hot pool as a DRACS. Comparison of natural circulation behaviors between the DRACS and the PRACS was carried out in the DELTA experiment. The time trends of core temperatures and subassembly flow rate in transition from forced to natural circulation are shown in Fig. 1.3-1. It was shown that the natural circulation flow rate decreased due to the temperature increase in the downward flow paths of IHXs and also temperature decrease in the upward flow path of the reactor upper plenum in the case of

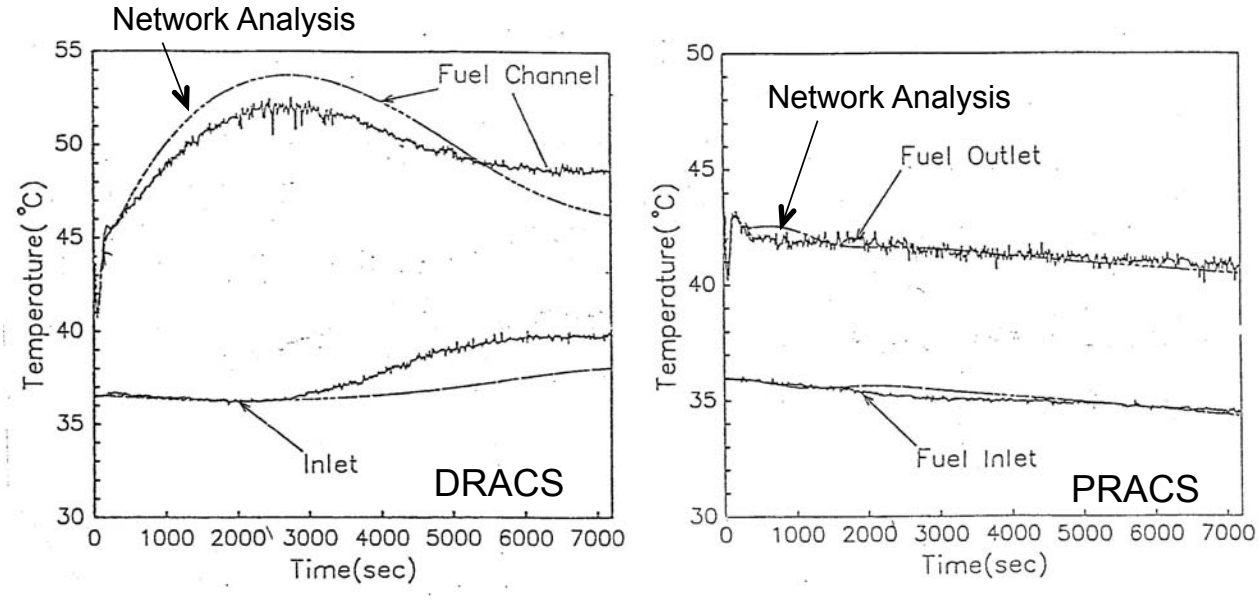

Core Inlet and Outlet Temperatures

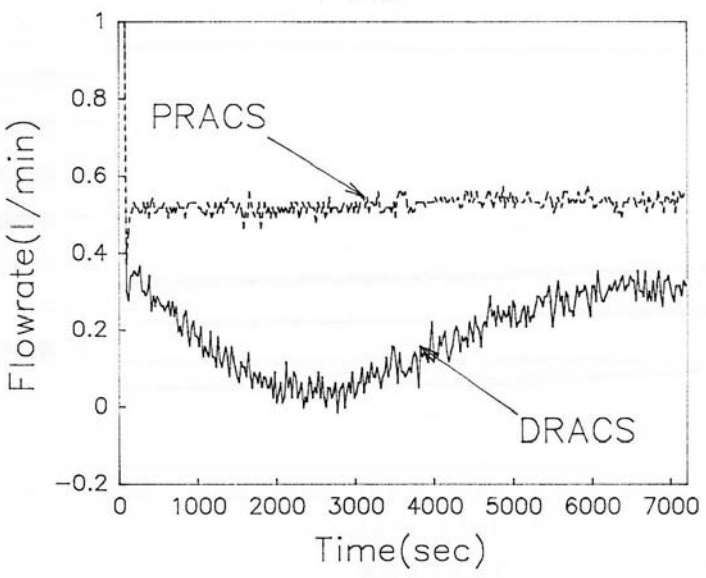

Flow Rate in a Subassembly

Fig. 1.3-1 Comparisons of Core Outlet Temperatures and Flow Rates between DRACS and PRACS obtained by DELTA Experiment

the DRACS as well as in the RAMONA experiment. The flow rate recovered when the cold fluid in the upper plenum entered the IHX inlet window and the IHX temperature decreased. In the case of the PRACS the core flow rate was maintained at a higher flow rate than in the case of the DRACS because of the low temperature in the entire length of the IHXs cooled by the PRACS cooling coils. During the period of low core flow rate in the case of the DRACS, temporal back flows were observed in the core channels due to the lower inertia force of the upward flow and negative buoyancy force of the stratified cold fluid in the upper plenum provided by the dipped heat exchangers.

As for the DFBR in Japan, a water test using a 1/8 scale model (Koga, 1993) was carried out. DFBR is a loop-type reactor using the dipped heat exchangers for the DHRS, i.e., a DRACS. A modified Bo number and a modified Gr number using the estimated flow velocity based on the balance of buoyancy force and pressure loss were used as indexes of model similarity. The similarity law for the water model experiment (Eguchi, 1997) was deduced for natural circulation in an LMFR. It was shown by the experiments that thermal stratification was formed in the reactor upper plenum due to the operation of the DRACS, excess capacity of the dipped heat exchanger reduced the natural circulation flow rate via the temperature decrease in the upward flow path of the upper plenum, and oscillation of the flow rates in the primary loops occurred during the low flow rate period.

1.3.3 Experiments on Core Thermal Hydraulics

Several model experiments were performed on the thermal hydraulics in subassemblies, e.g., a core fuel subassembly, a blanket fuel subassembly using water and air as working fluids, and using sodium in studies under steady state conditions. Flow resistance and Re dependency were investigated in the wide region of fuel pin and spacer wire geometry, e.g., Cheng and Todreas (1986). Detailed flow velocity profiles in the pin bundle were also investigated by enlarged air experiments (Rehme, 1980) and sodium experiments (IAEA by Russia, 1999). Temperature distributions in the fuel pin bundle were also of importance under not only full power conditions but natural circulation conditions.

Here, it is difficult to simulate the subassembly in detail in water experiments because of the 3 to 4 mm of the hydraulic diameter and Pe number distortion. Full scale of the water test model results in an excessively large Pe number as compared with that in sodium reactors due to the large difference of heat conductivity of the fluids. Therefore, several sodium experiments were carried out on the thermal hydraulics in the subassemblies under natural circulation conditions.

The core of a reactor consists of hundreds of subassemblies. These subassemblies are thermally connected to one another through the sodium gap between the wrapper tubes. Under natural circulation conditions, the flow rate through the subassemblies is only 1 to 3% of that under full power conditions. Thus, such thermal interaction between the subassemblies is of importance in the evaluation of the highest core temperature. Such temperature profiles, influenced by heat flux through the wrapper tube and also power skew in a subassembly, were investigated using a single subassembly.

Peak sodium temperature over a range of radial heat flux gradient under forced to natural circulation conditions was investigated using a 61-pin bundle which modeled a typical blanket subassembly (Engel and Markley, 1982) and a 37-pin bundle for a core fuel subassembly (Namekawa and Luangdilok, 1985). The influence of buoyancy force on the peak temperature correlated with non-dimensional parameters. Radial cooling effect was also studied in a grid-spaced 37-pin bundle with annular flow channel surrounding the wrapper tube and the axial cooling effect using a heat exchanger installed in the upper plenum (Weissenfluh, 1989). However, there is no experiment which models multiple subassemblies and the heat transfer between the subassemblies directly. Further, influences of natural convection in the core barrel on the thermal hydraulics in the subassemblies have not been investigated.

In the upper plenum of the reactor vessel where a DRACS is selected as the DHRS, cold sodium is provided from the dipped heat exchanger during decay heat removal operation. This cold sodium covers the top of the hot core, which consists of multi channels. Then, negative buoyancy force appears by this inverse temperature field.

One of the possibilities is reverse, or penetration flow into low-velocity subassemblies, e.g., the radial blanket subassemblies. Such temporal reverse flow was observed in a water experiment (Ieda, 1991) in which a scram transient and transition to natural circulation in a pool-type sodium reactor using a DRACS was simulated. This penetration flow is the result of a balance between the buoyancy force and the inertia force of upward flow. Then, flow rate through a subassembly may become low in the case of a fine balance, and local high temperature can be seen in the subassembly.

Several water experiments (e.g., Barakat, 1989, Jerng and Todreas, 1992) were carried out in cooperation with JAEA at MIT to examine such a core-plenum interaction. Estimation models for the onset and depth of the penetration flow were deduced from the experiments. A non-dimensional parameter of $Gr_{\Delta T}/Re$ was used as one of the significant factors of the penetration flow into a vertical hot flow channel. However, estimating the penetration flow remains difficult with the simulation method.

1.3.4 Experiments on the DHRS

There are several designs that adopt complete natural circulation in the secondary loop of the DHRS and natural draft in the air cooler, as shown in EFR and PFBR (Arul, 2006) in India, where no pump is set in the secondary loop and no blower is installed at the air intake. There is no need to consider the risk of pump and blower failure because the air dampers are the only active component. However, operation would be more difficult even in standby mode with the need to take care minimum flow rate in the secondary loop, freezing in the heat exchange tubes of the air coolers, and heat loss via the air cooler. As for the decay heat removal operation, a performance estimation of the air cooler and the sodium-sodium heat exchanger is needed, e.g., heat removal capacity, temperature difference between the heat exchanger tubes, wind influence, natural convection in the air stack, startup transient, and freezing in the air cooler parallel heat exchanger tubes.

The large scale sodium experiment, ILONA (Stehle, 1994), was carried out for the EFR DHRS. EFR has six dipped heat exchangers in the hot pool and air coolers as in the DRACS. Two types of air coolers were designed to achieve component diversity.

One is straight tube type and the other is a helical tube type. Functional diversity was also achieved through different operating conditions for the two groups during standby at reactor power operation, i.e., different air damper opening positions. Sodium experiments were performed to verify component design and to investigate the steady and transient behavior of the sodium and natural air convections, including meteorological influences such as frost and storm, and the risk of sodium freezing. The air cooler is modeled to a power scale of 1/3rd. The helical coiled heat exchanger tube bundle is scaled 1:1 in tube diameter and pitch, and scaled 1: (square root of 3) in height and diameter of the helical tube bundle and air stack to set the heat transfer area to 1/3rd. Heat removal capacity, temperature distribution of the heat exchange tube outlets, transient behavior at the tube outlets and in the air stack during the startup were confirmed to be within the permissible range.

1.3.5 Study on Heavy Liquid Metal Reactor

Natural circulation has been investigated in the field of heavy liquid metal reactors. Lead and Pb-Bi coolants have the significant advantages not only of nuclear characteristics but also thermal hydraulics, e.g., higher conductivity and higher specific heat. Several heavy liquid metal reactors designs adopt natural circulation under full power conditions, especially in the case of small or medium size reactors (Chang, 2000, Davis, 2002, Sakai, 2004, Sienicki, 2005). A Pb–Bi cooled direct contact boiling water small fast reactor also has no pump in the primary cooling system, where Pb–Bi coolant is circulated by means of the buoyancy of steam bubbles (e.g., Takahashi, 2005, 2008).

1.4 Problem Definition

As described above, natural circulation flow rates depend on temperature distribution in the entire system, and the temperature at each component depends on the flow rates. Such system behavior has been investigated utilizing the water experiments of the primary system and reactor demonstration experiments. Several system network codes (e.g., Hoffmann, 1991, Yamaguchi, 1989) were applied to predict natural circulation flow rates and temperature transients at the components, and high applicability was confirmed.

However, the reactor core has complex geometry with a wide variation of length scale, from 3mm for the subchannel in the fuel subassembly to 5m for the core radius. The core consists of hundreds of subassemblies. Further, each subassembly consists of hundreds of fuel pins spaced by wrapping wires. Thus, the core has two levels of multi-channel, i.e., subassemblies and subchannels surrounded by the fuel pins. Natural circulation is driven by temperature increases in these complicated flow channels. This means that the estimation of the highest fuel pin clad temperature should consider buoyancy effects on the two levels of the flow channel configuration.

The subassemblies have a wide variation of power and flow rate according to the regions of the inner and outer core, the radial blanket, the control rod and radial neutron shielding. The subchannels in a subassembly also have variations of flow velocity and power due to geometry differences between the inner subchannel and the wall or outer subchannel, as shown in Fig. 1.4-1.

Under full power conditions, the flow velocities in these flow channels are decided by the flow resistance coefficients in the channels. However, under natural circulation conditions the flow velocities are determined by the pressure loss and buoyancy force resulting from temperature distribution along the flow channels. Thus, the flow velocity distribution among the flow channels changes from forced flow conditions to natural circulation conditions. This flow redistribution reduces the peak temperature due to the higher flow velocity in the higher temperature channel. The wide variations of power and flow velocity in the core channels result in flow redistribution and

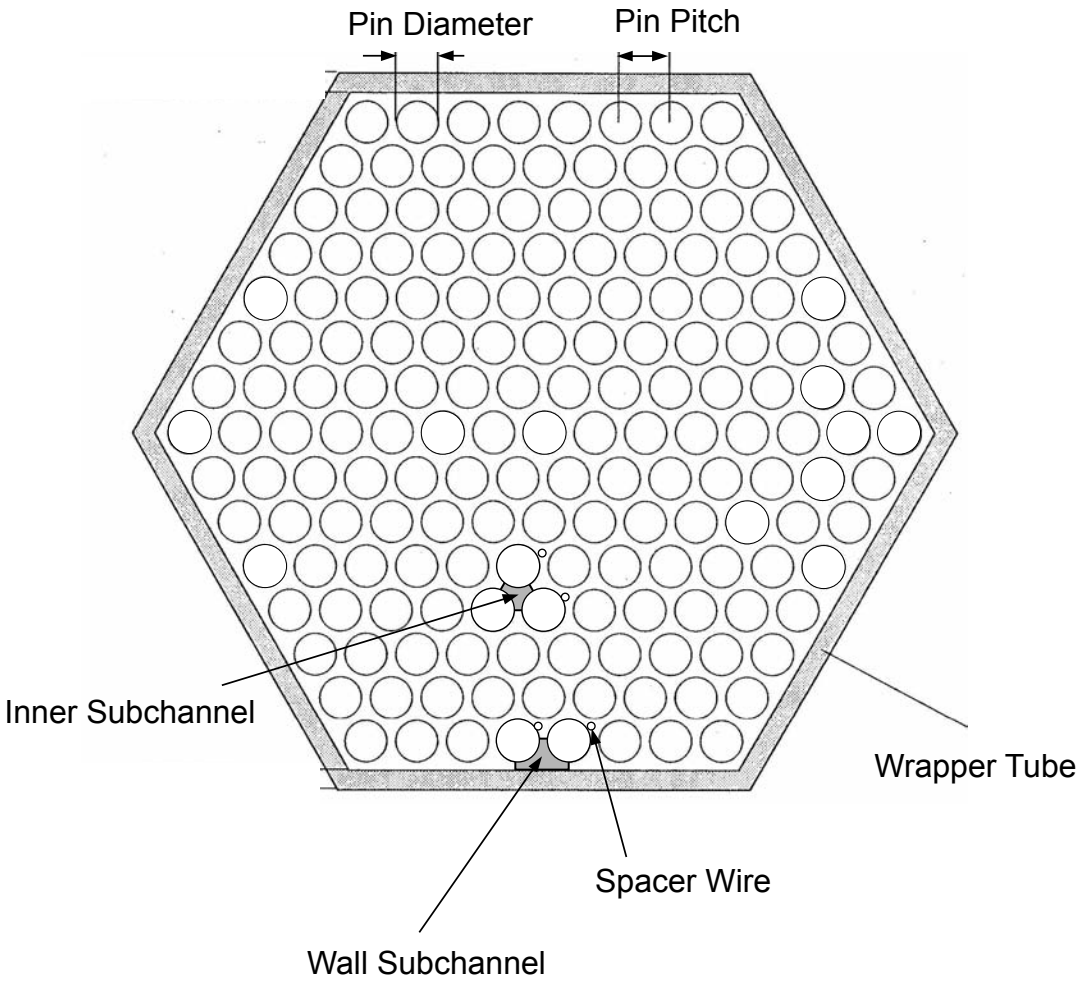

Fig. 1.4-1 Schematic of Subassembly Horizontal Cross Section

temperature flattening under natural circulation conditions, as shown in the single subassembly sodium tests (e.g., Namekawa, 1985). Further, temperature difference between adjacent subassemblies leads to heat transfer between the subassemblies. This inter-subassembly heat transfer also decreases the peak temperature among the subassemblies, as shown in the reactor experiment in JOYO.

Here, the heat flux through the wrapper tube wall due to the inter-subassembly heat transfer will influence the temperature distributions in the higher temperature subassembly and the lower temperature subassembly under low-flow velocity conditions, i.e., natural circulation. These temperature distributions in the subassemblies will also influence inter-subassembly heat transfer. Thus, it is necessary to consider inter-subassembly heat transfer and flow redistribution in the subassemblies simultaneously in order to estimate the highest temperature in the core. However, there is no experimental data to simulate such interaction between the subassemblies.

Such influences of buoyancy force on flow velocity distribution, heat transfer between the subassemblies and consequent flattening of temperature distribution are significant under natural circulation conditions. However, such effects, especially inside the subassembly, were not considered in the highest temperature evaluations for reactor safety. One reason for this is the limited information on thermal hydraulics in the core, which consists of multiple subassemblies.

As described in the previous section, a DRACS is often installed as the DHRS in middle to large size reactors. In the case of a DRACS, the core flow rate decreases temporally due to the temperature increase in the IHXs of the downward flow path, as shown in the RAMONA and DELTA experiments. Further, cold sodium provided by the dipped heat exchangers of a DRACS stratifies in the reactor upper plenum and covers the top of the core. In this situation the negative buoyancy force of the cold sodium may result in partial reverse flow in a low temperature subassembly and natural convection in the gap region between the subassemblies, as shown in the DELTA and NEPTUN experiments. Such cold flows from the reactor upper plenum into the core also influence the highest temperature in the core.

In this study such core thermal hydraulics are investigated in order to estimate the highest temperature in the core during the natural circulation decay heat removal including the transients from forced to natural circulation.

The phenomena to be estimated are illustrated in Fig. 1.4-2 and listed below;

1) Intra-subassembly flow redistribution: Flow redistribution among the subchannels in a subassembly and resulting temperature flattening,
2) Inter-subassembly heat transfer: Heat transfer between adjacent subassemblies,
3) Penetration flow into subassemblies: Partial reverse flow into subassemblies from the reactor upper plenum,
4) Inter-wrapper flow: Natural convection in the gap region between the subassemblies.

As can be seen, these phenomena occur in multi-subassembly systems. Thus, multi-subassembly sodium experiments were carried out in this study. The three-subassembly and seven-subassembly models were used in the experiments. As for the inter-wrapper flow phenomena of the entire core, a water experiment was applied to examine the flow fields in the core scale.

Numerical simulations have been applied to mixed convection in a wire wrapped subassembly, thermal stratification in a reactor upper plenum and in-vessel natural circulation (e.g., Ninokata, 1985). In this study, a multi-dimensional thermal hydraulic analysis code was applied to the experimental analyses of the multi-subassembly system in order to clarify the phenomena and to develop a tool for the investigation of whole core thermal hydraulics.

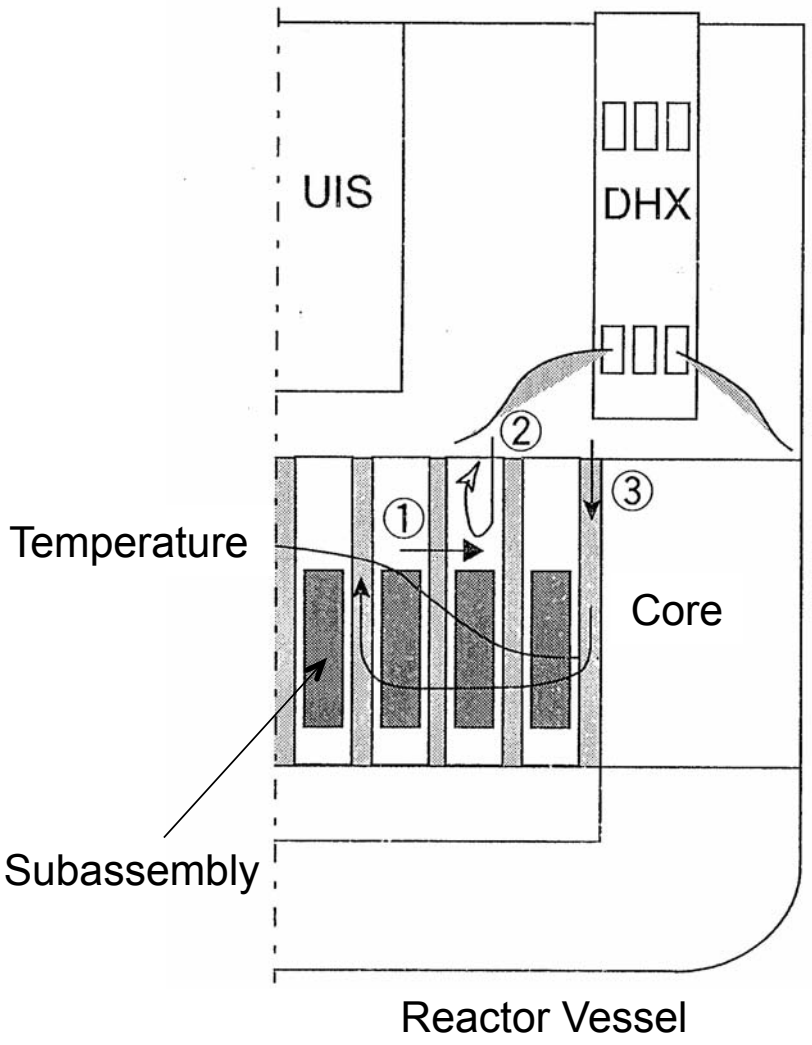

1) Flow redistribution in a subassembly,

2) Inter-subassembly heat transfer: ①,

3) Penetration flow into low power subassembly: ②

4) Inter-wrapper flow: ③

Fig. 1.4-2 Core Thermal Hydraulics during Natural Circulation Decay Heat Removal

1.5 Current JSFR Design at JAEA and Feedbacks from This Study

1.5.1 DHRS of JSFR

A feasibility study on the fast breeder reactor (FBR) and related fuel cycle system (Noda, 2000) has been carried out at the Japan Atomic Energy Agency (JAEA). A design study on an advanced sodium-cooled reactor was performed as one of the significant candidates for FBR in the feasibility study. One design issue is higher cost performance, and several innovative design concepts were incorporated (Shimakawa, 2002). Following the feasibility study, the reactor design and related research on the advanced loop-type sodium-cooled fast reactor, designated as the JSFR (Japan Sodium-cooled Fast Reactor, Kotake, 2010), were carried out at the JAEA.

A flow diagram of the JSFR cooling system is shown in Fig. 1.2-11. The primary cooling system has only two loops in order to reduce the number of components and the reactor building space. The two hot leg and four cold leg pipes are inserted vertically through the upper deck into the reactor vessel. Thus, there is no nozzle in the reactor vessel. The intermediate heat exchanger (IHX) and the primary pump are integrated into one component to reduce the component number and middle leg of the primary cooling system. The steam generator (SG) is a straight tube type.

With respect to the DHRS, a dipped heat exchanger is installed in the reactor upper plenum as a DRACS. Further, a sodium-sodium heat exchanger is installed in an inlet plenum of each IHX as a PRACS (see Fig. 1.5-1). Thus, the JSFR DHRS is a combined system using one DRACS and two PRACS. There is no pony motor in the primary pumps. No pump is installed in the secondary loops of the DRACS and PRACS. The DRACS air cooler has no blower. Each of the PRACS air coolers has a blower; however, the blower is connected only to a normal power line. Thus, this DHRS is a fully natural circulation system and natural circulation decay heat removal is demanded after a scram accompanied by loss of power incidents. In terms of diversity and redundancy, two independent dampers are installed at the inlet of each air cooler. Each of the dampers is driven by a motor, hence is an active component and connected to an independent emergency power line.

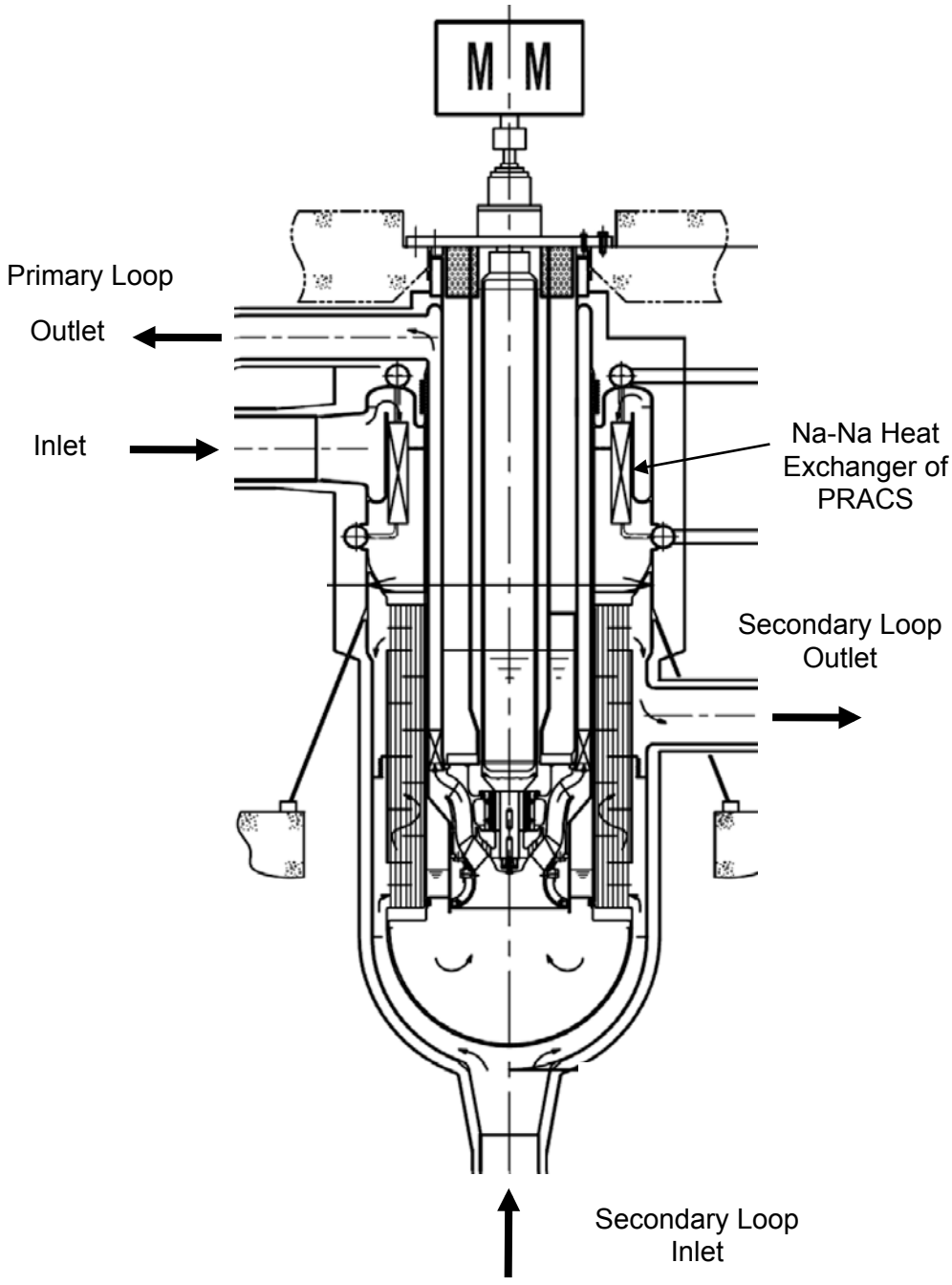

Schematic of Pump-IHX Integrated Component and PRACS heat exchanger

Fig. 1.5-1 Schematic of Pump-IHX Integrated Component and PRACS heat exchanger in JSFR

When the reactor is shut down by a scram, the dampers of air cooler are opened and several natural circulations are activated in the reactor system for the decay heat removal. Figure 1.5-2 shows such natural circulation paths in the reactor system. The main flow path through the core is the primary circuit cooled by the PRACS. The natural circulation in the secondary loop also contributes the cooling of the primary circuit in the first 1,000s from the scram. Natural drat in the air cooler stack is the final heat sink of the DHRS and induce the natural circulation in the DHRS sodium loop. The PRACS heat exchangers are installed in the top of IHX and enhanced the natural circulation in the primary circuit via the larger height difference between the core and the PRACS heat exchanger. Natural convection along the PRACS heat exchanger is also developed in parallel to the natural circulation through the primary circuit, which has larger flow area beside the PRACS heat exchange tubes. As for the DRACS, the sodium-sodium heat exchanger (DHX) is installed in the reactor upper plenum. A natural circulation path through the DHX is formed in the upper plenum in parallel to the primary circuit. The flow resistance coefficient in the DHX primary side is a significant parameter for this natural circulation through the DHX. The cold sodium provided by the DHX forms a stratified cold layer in the lower part of the upper plenum. This cold sodium above the hot core causes several core phenomena discussed in the section 1.4, i.e., the penetration flow into low power subassemblies and the inter wrapper flow. Further, inter-subassembly flow redistribution is a significant phenomenon for the core cooling. When the natural circulation head in the primary circuit is so low, some cold channels in the core have reverse flows. This inter-subassembly flow redistribution including the recirculation flow through the cold channels contribute the increase of flow rate through the hottest subassembly in the core, especially in case of the cold sodium layer above the core. However, such the inter-subassembly flow redistribution can be predicted by a flow network code based on a balance between the buoyancy force and the flow resistance.

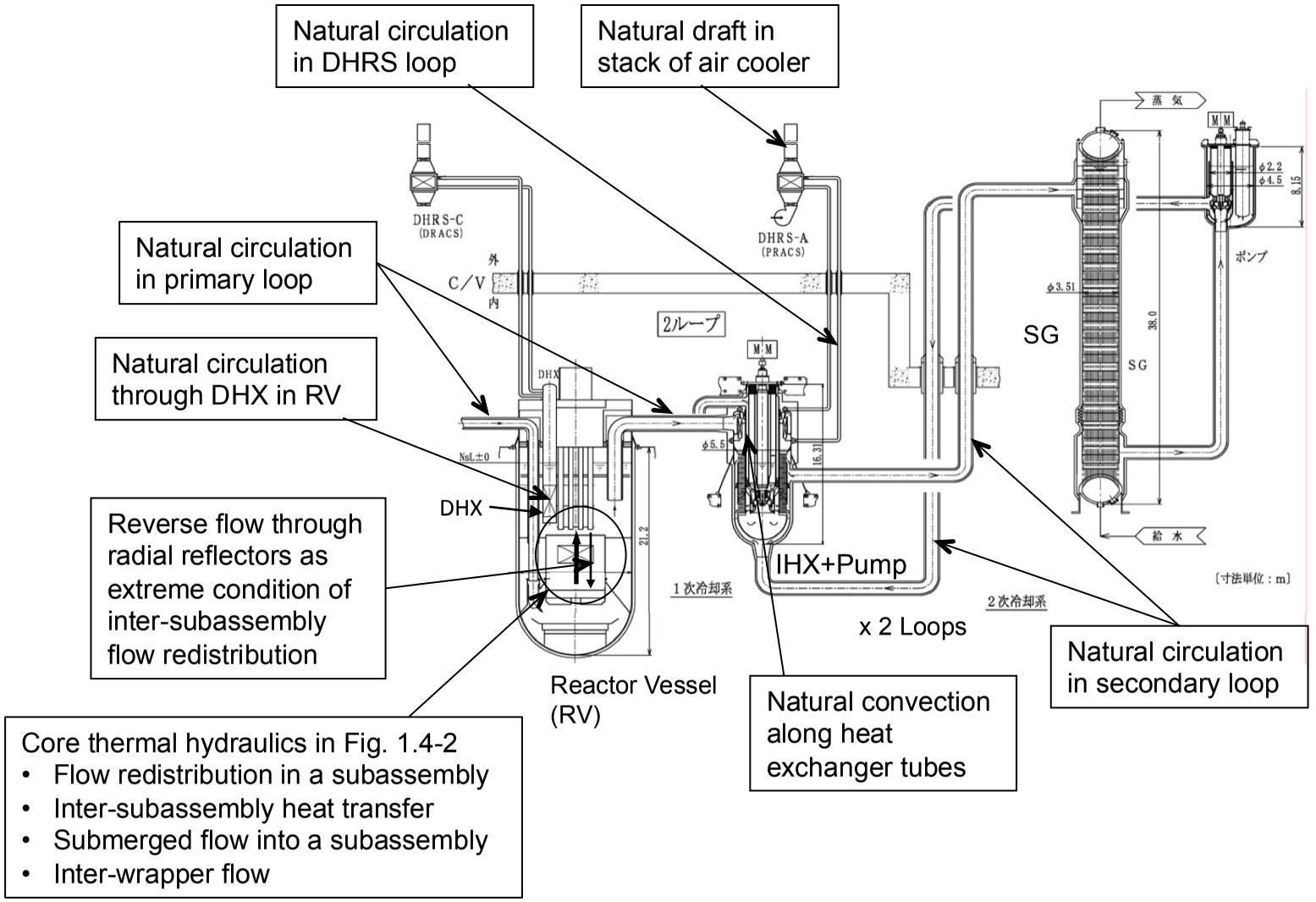

Fig. 1.5-2 Schematic of Flow Paths in Natural Circulation Decay Heat Removal

1.5.2 Feedbacks to JSFR

The highest temperature of the fuel pin clad in the core is a significant index of the integrity of the core. It is evaluated based on temperature increase in the hottest channel in the core and a hot spot factor, which includes space distribution of the temperature in the subassembly, uncertainties of power, flow rate, deformation of the fuel pin, etc. under forced flow conditions of the pony motor operation as well as full power operation. However, it is difficult to determine the temperature increase in the hottest channel under natural circulation conditions because of uncertainty about the flow rate, which depends on the temperature itself, and changes in time. On the other hand, the transverse temperature distribution in the subassembly should be flatter than under full power conditions due to buoyancy force and flow redistribution. If such a flattening effect is considered, the hot spot factor would be decreased. There is no authorized guideline for the hot spot factor under natural circulation conditions at this moment. However, natural circulation is demanded in design base events, e.g., loss of offsite power, in JSFR. Thus, core temperature evaluation should be carried out in consideration of the characteristics of natural circulation.

An understanding of core thermal hydraulics under natural circulation conditions is significant for the establishment such a guideline to estimate the highest temperature of the core fuel pin clad. The combination of DRACS and PRACS is used in JSFR. Further, in a hypothetical case of sodium leak accident at one of the PRACS secondary circuits, the role of DRACS in JSFR is still large. Therefore, the influences of cold sodium provided by the DRACS and stratified in the reactor upper plenum are also significant themes.

1.6 Objectives of This Study

The objective of this study are summarized below according to the problem definition and the feedback to reactor design:

1) To clarify the thermal hydraulic phenomena in a fast reactor core, which influence the highest temperature in the core (e.g., fluid temperature in the central part of core matrix and at the upper end of active core) during natural circulation decay heat removal based on sodium and water experiments

   Following phenomena are depicted as the significant issues in Chapter 1 based on literature survey and reactor conditions.

   (a) Intra-subassembly flow redistribution: Flow redistribution among the subchannels in a subassembly and resulting temperature flattening,
   (b) Inter-subassembly heat transfer: Heat transfer between adjacent subassemblies,
   (c) Penetration flow into subassemblies: Partial reverse flow into subassemblies from the reactor upper plenum,
   (d) Inter-wrapper flow: Natural convection in the gap region between the subassemblies.

2) To identify and model key phenomena that are to be considered in numerical simulation methods to simulate these phenomena in a multi-subassembly system based on their mechanisms which are obtained by the experiments

3) To predict thermal hydraulic phenomena in an entire core and to develop a whole core simulation method

4) Feedback to a reactor design from the findings obtained from the experiments and prediction analyses of whole core phenomena during natural circulation decay heat removal

1.7 Structure of the Dissertation

1.7.1 Contents

Chapters 2, 3 and 4 show several water and sodium experiments that were planned to examine the characteristic phenomena in the core introduced in section 1.4 and to establish estimation methods based on non-dimensional parameters and/or numerical simulations. A schematic of a thesis structure is shown in Fig. 1.7-1.

The inter-subassembly heat transfer and flow redistribution in subassemblies are investigated utilizing the multi-subassembly sodium experiments in chapter 2. Penetration flow into subassemblies due to negative buoyancy force is discussed in chapter 3 based on water and sodium experiments. The inter-wrapper flow is investigated utilizing a seven-subassembly sodium experiment and a 1/12 sector water model of the entire core in chapter 4.

The multi-dimensional analysis method was applied to the thermal hydraulics in the subassemblies affected by the inter-subassembly heat transfer. Verifications were carried out for the multi-subassembly experiments, where each of the subassemblies was modeled by a staggered half-pin mesh scheme.

Chapter 5 shows a multi-dimensional analysis method to simulate whole-core thermal hydraulics using a brick subassembly model and verifications based on the sodium and water experiments described in the previous chapters. The application analysis to the reactor size problem was carried out to predict whole core phenomena during natural circulation decay heat removal.

Chapter 6 summarized the obtained findings in this study in the categories of experiments and simulation methods. Then, core thermal hydraulics in a reactor of design study is predicted based on these findings. Further, feedback to the reactor design and requirements of the evaluation method are discussed. Concluding remarks are provided in chapter 7.

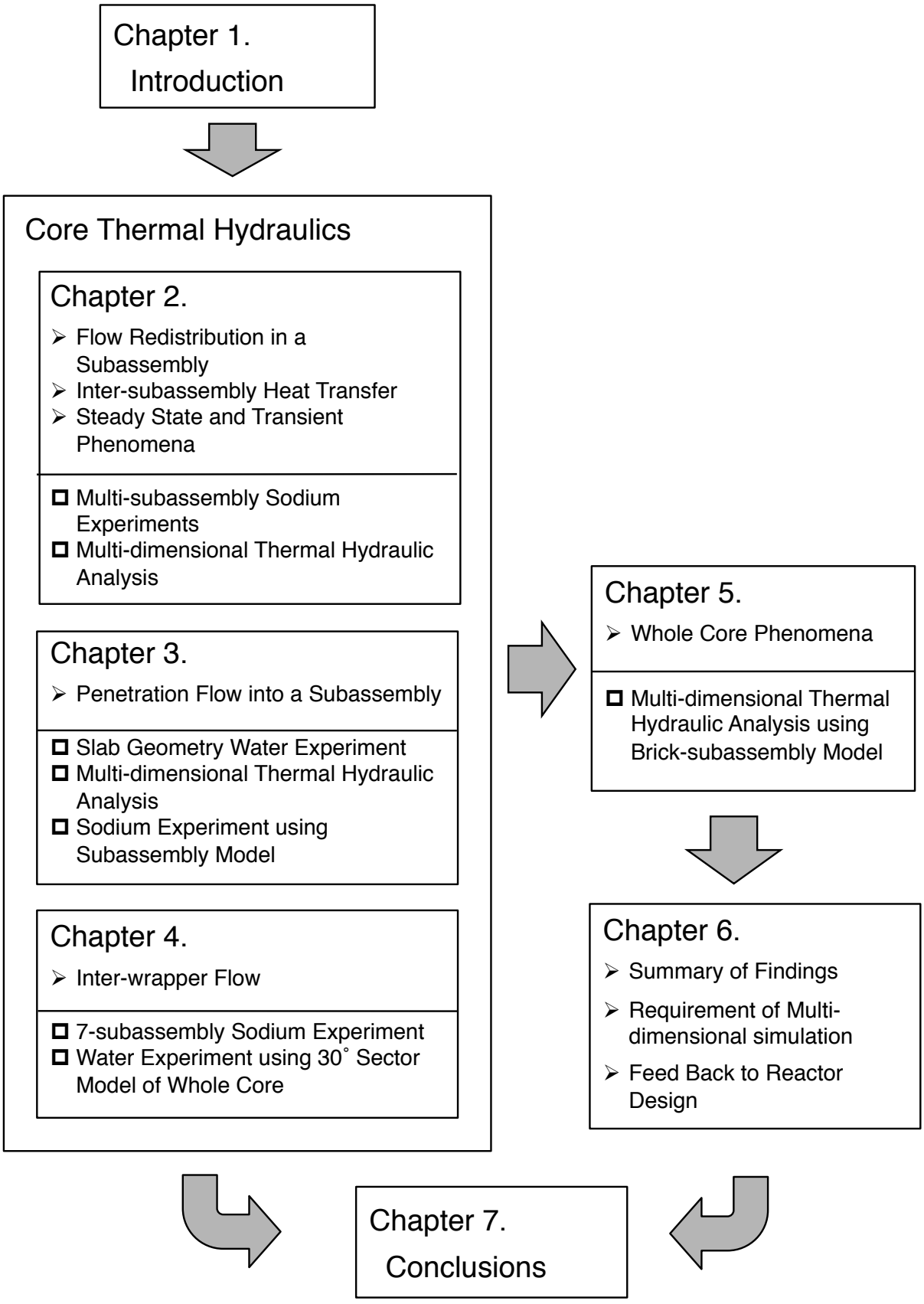

Fig. 1.7-1 Schematic of Thesis Structure

1.7.2 Approaches to the Experiments and Analyses in Each Chapter

(1) Inter-Subassembly Heat Transfer and Flow Redistribution in Subassemblies

Several sodium experiments were performed to examine the temperature profile influenced by buoyancy force under low flow conditions in a single subassembly using a heater panel and/or a cooling channel along the wrapper tube, e.g., Namekawa (1985) as described in section 1.3.3).

However, the heat flux in the axial direction is not constant and depends on subchannel temperatures near the subassembly wall. Investigation of the phenomena in a subassembly surrounded by actual subassemblies was desired. In chapter 2, a three-subassembly experiment using sodium as working fluid and seven-subassembly experiment are introduced. These two sodium experiments were carried out at the Oarai Research and Development Center of the JAEA. Influences of the heat transfer from the adjacent subassemblies on the maximum temperature in the pin bundle will depend upon the bundle size on the point of heat flux in the transverse direction. Therefore, a reactor size subassembly was simulated in the three subassembly experiment by using a 61-pin bundle in which a slightly enlarged blanket fuel pin was modeled. Further, the gap region between the wrapper tube was filled with stainless steel in order to simplify the phenomena and to measure the heat flux through the wrapper tube based on the thermocouples graved on the inside surfaces of each wrapper tube. As for the sodium gap between the wrapper tubes, natural convection occurs due to the temperature distribution across the whole core. Such phenomena were considered in the seven subassembly model.

The highest temperature after the scram appeared in the transient phase, the second peak following the pump stop and the third peak during long transient. As for the second peak, balance of buoyancy force and forced convection during the pump flow coast down is of interest. A transient experiment was carried out in the seven subassembly model, where a scram transient and transition to natural circulation were simulated.

Numerical simulation is also significant in the estimation of the highest temperature in an actual reactor core. Subchannel analysis is often used to simulate the temperature

and velocity field in a subassembly. CFD analyses using a detailed mesh scheme are also seen in recent applications. However, the majority of these analyses were applied to a single subassembly, and heat transfer between the subassemblies was beyond the scope. In chapter 2, multi-dimensional analyses were carried out for the three-subassembly model to estimate the influences of the heat transfer between the subassemblies on the thermal hydraulics inside the subassemblies. The analyses were based on a finite difference method, and a staggered half-pin mesh arrangement was applied in each of the subassemblies.

(2) Penetration Flow into Subassemblies

In case of the DRACS, it was shown that thermal stratification was formed in the reactor upper plenum. Temporal reverse flow in a blanket fuel subassembly channel or a low power channel was also observed in several water experiments (e.g., Sato, 1989 and Ieda, 1991) simulating natural circulation in a reactor. Such reverse flow was investigated using centrally heated annular channels connected to a cold upper plenum (Barakat, 1989). Several prediction models were deduced based on the water experiments.

Chapter 3 describes a water experiment carried out on a point of verification of the numerical simulation and also a sodium experiment to obtain the onset condition of the penetration flow. The experimental setup of the water test modeled a vertical square channel and an upper plenum of the reactor vessel in slab geometry. As for the penetration flow, the source of the cold flow, which covers the top of the channel, is of importance. Then, the upper plenum had a cooling panel, which simulated the dipped heat exchanger of the DRACS. Thermal stratification was formed in the plenum by the cold fluid from the cooling panel and the hot upward flow through the square channel. This vertical temperature distribution is of interest for the numerical simulations. The cold water penetrated into the channel under the low flow velocity and high temperature difference conditions. The phenomena were not steady, and the penetration occurred intermittently. The onset of the penetration flow was defined as a certain probability of low temperature spike measured by thermocouple. The onset and penetration depth in the square channel were predicted by a numerical simulation

code. The turbulence model in the code was of interest to simulate the thermal stratification and the penetration flow because of the importance of mixing between the hot and cold flows.

According to the penetration flow phenomena observed in the water experiment a sodium experiment was carried out in order to obtain the onset condition of the penetration. A subassembly model with an upper plenum was applied to the sodium experiment. The cold penetration flow was detected by the thermocouples at the neutron shielding above the pin bundle. The criteria of the penetration flow and penetration depth were obtained by the sodium experiments.

(3) Inter-Wrapper Flow

The sodium gap between the core subassemblies also permits the penetration flow from the upper plenum. There is no forced flow in the gap under the natural circulation conditions of the decay heat removal. Then, fully natural convection develops in the gap region according to the temperature distribution across the core and the cold penetration flow. This gap flow is called the inter-wrapper flow (IWF).

As described in section 1.3.2, a water experiment, NEPTUN (Weinberg, 1995), was carried out on FzK for a pool-type fast reactor, EFR (European Fast Reactor), which featured a DRACS. The NEPTUN model simulated the core by using electrical heater rods housed in hundreds of circular tubes instead of hexagonal wrapper tubes. The space between the simulated subassembly tubes, i.e., the gap region, was filled with water and connected to the hot pool in the reactor vessel. The NEPTUN experiment showed that a large amount of heat in the core was removed by the IWF. The estimated heat removal ratio of the IWF to the total heat in the core reached 40% in some cases. However, the geometry of the gap region was different from that in a reactor. In particular, the heat flow from the subassembly to the gap region will depend on the temperature distribution in the subassembly. Then, geometric similarity of the gap and subassembly inside is significant in the simulation of the IWF.

Two types of experiments were carried out at the JAEA concerning the IWF during

natural circulation decay heat removal. One is a sodium experiment, which models seven subassemblies, including the gap region and the fuel pin arrangement. The other is a water experiment for the IWF in the whole core, where only the gap region is modeled using a 30-degree sector model. The chapter 4 shows these experiments on the IWF. In the seven-subassembly sodium experiment, heat flow between the gap region and fuel pin bundle is of interest. The temperature distribution in the fuel pin bundle interacted with the heat flow through the wrapper tube. Transient phenomena are also a key point in relation to the time constant of the heat removal via the IWF in the estimation of highest temperature. Then, transient experiments were also carried out.

Here, the seven-subassembly model covered a limited area in the core. However, the IWF is developed according to temperature distributions across the whole core. The high temperature region of the inner core will have upward flow and downward flow in the low temperature region of the radial reflectors. Thus, a 30-degree sector water test model of the core and the reactor upper plenum was applied to examine the IWF in the whole core region. The experiment focused on the IWF itself and not on the thermal hydraulics inside the subassemblies. Then, only the heat flux on the wrapper tube was simulated by using transparent heater panels. This enabled transparent empty wrapper tube and flow velocity measurement based on flow visualization in the small width and zigzag flow paths of the gap region. The temperature distributions in the gap region across the core model and the flow velocity fields were measured in order to examine the natural convection phenomena of the IWF.

(4) Whole Core Analysis of NC/DHR

Previously mentioned phenomena, i.e., the inter-subassembly heat transfer, the penetration flow, and the inter-wrapper flow were connected with one another. Thus, numerical simulation methods are needed to estimate these complex phenomena simultaneously. Chapter 5 shows a simulation method for the inter-wrapper flow with the inter-subassembly heat transfer. The staggered half-pin mesh arrangement is an effective means of resolving the multi-subassembly system, excluding the gap region. However, it is difficult to apply this model to the whole core due to computational

resource limitations, even if the gap region is omitted. Then, a brick subassembly mesh scheme was developed by the author to simulate the multi subassemblies and the gap, simultaneously. This mesh structure is based on Cartesian coordinates and models the subassembly by inner subchannel region, wall subchannel region, and the wrapper tube in square shape. This two-layer model can represent the velocity and temperature profiles in the subassembly. Further, the gap region is set between the subassemblies that are allocated in a staggered half-subassembly arrangement. The peripheral length of the wrapper tube of the square subassembly model is set equal to that in an actual geometry to simulate the heat transfer between the subassembly and the gap region. Chapter 5 shows also verification of the brick subassembly model based on the sodium and water experiments described in the previous chapters.

Finally, the application to the reactor size problem was carried out to investigate thermal hydraulic phenomena in the entire core during natural circulation decay heat removal.

(5) Summary of Findings and Feedbacks to Reactor Design

Chapter 6 summarizes, several significant insights obtained in this study and needs of a multi-dimensional simulation method are discussed as an evaluation method of the core thermal hydraulic phenomena under natural circulation conditions. Further, feedbacks to a design study of 1,500MWe class reactor from this study are discussed. Especially, utilization of IWF is proposed as a heat removal path in case of beyond design event. Finally, required features and functions of an evaluation method to be applied to the core thermal hydraulic phenomena under natural circulation are confirmed.

Chapter 2. Inter-Subassembly Heat Transfer and Intra-Subassembly Flow Redistribution

Chapter 2. Inter-Subassembly Heat Transfer and Intra-Subassembly Flow Redistribution

2.1 Introduction

Analyses of the natural circulation test conducted in the Japanese experimental reactor JOYO revealed that the inter-subassembly heat transfer reduced subassembly outlet temperatures at the inner rows of the core (Yamaguchi, 1989). Under low flow conditions, radial heat transfer through wrapper tubes, i.e. inter-subassembly heat transfer, will significantly modify the flow and temperature distribution in the subassemblies due to the decrease of flow rate and axial heat transportation. The core thermal hydraulics, especially inter-subassembly heat transfer, should be investigated to accurately estimate the highest temperature in the core.

Thermohydraulics in the subassemblies under a mixed or natural convection flow regime has been studied using single subassembly models. Peak sodium temperature over a range of radial heat flux gradient under forced to natural circulation conditions was investigated using a 61-pin bundle which modeled a typical blanket subassembly (Engel and Markley, 1982) and also using a 37-pin bundle for a core fuel subassembly (Namekawa and Luangdilok, 1985). The influence of buoyancy force on the peak temperature was correlated with non-dimensional parameters. Radial cooling effect was studied in a grid-spaced 37-pin bundle with annular flow channel surrounding the wrapper tube, and axial cooling effect was studied using a heat exchanger installed in an upper plenum (Weissenfluh, 1989).

As mentioned above, the highest temperature in the core during natural circulation is strongly dependant on the thermal hydraulics in the subassemblies, i.e., flow redistribution caused by the buoyancy force. The inter-subassembly heat transfer also influences the temperature and flow redistribution in subassemblies via heat removal or

heat input through the wrapper tube. Thus, these two phenomena were studied together. Inter-subassembly heat transfer is heat flow across the subassemblies. It suggests that the following parameters are of importance as thermal resistance across the subassembly: 1) bundle size or flat to flat distance of a hexagonal wrapper tube; 2) number of pin layers in the subassembly; and 3) pin pitch by diameter (P/D). Further, there is a sodium gap in between the subassemblies and a portion of the heat is transported by the natural convection in that gap. This inter-wrapper flow and the inter-subassembly heat transfer are combined phenomena in the core. Here, it is considered to simplify the phenomena and to eliminate the inter-wrapper flow.

Two types of sodium experiments were carried out to study the flow redistribution in subassemblies and interaction with inter-subassembly heat transfer. First, a larger bundle size was selected to simulate the heat resistance across the subassembly. Then, a blanket subassembly was selected at a point of larger temperature gradient across the core. Since the pin diameter of blanket subassembly is larger than that of fuel subassembly, the simulated pin number can be reduced when the blanket subassembly undergoes experiment. As for inter-subassembly heat transfer, it is necessary to know the precise heat flux on the wrapper wall. Further, the inter-wrapper flow should be eliminated as a first step to create a simplified condition. Then, a three-subassembly model with a Y-shape wrapper tube wall and a seven-subassembly model were applied to the sodium experiments for a blanket subassembly and a core fuel subassembly, respectively. Figure 2.1-1 shows schematics of the horizontal cross sections of the subassembly models. The three-subassembly model simulates a blanket subassembly where 61 pins are installed (Kamide, 1995, 1998). The other two subassemblies provide heat to the 61-pin subassembly. The gap region between the subassemblies is ignored and a Y-shape wall connects the three subassemblies directly. Several thermocouples are embedded on the surface of the Y-shape wall to estimate the heat flux through the wall. The seven-subassembly model simulates a core fuel

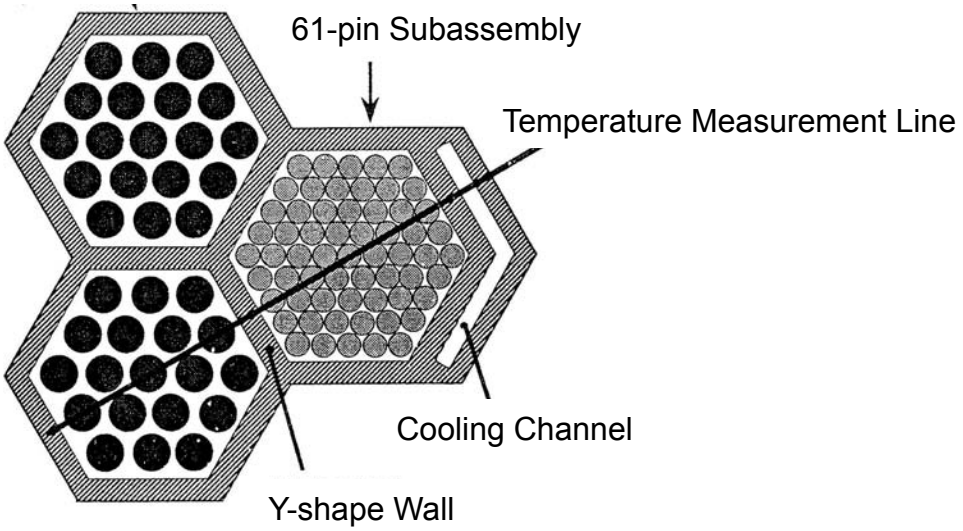

(1) Three-Subassembly Model

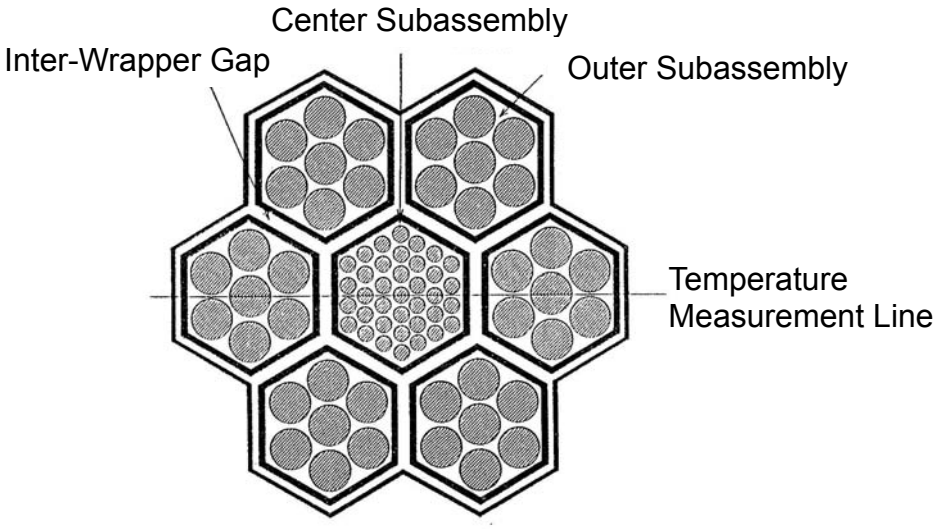

(2) Seven-Subassembly Model

Fig. 2.1-1 Multi-subassembly Models

subassembly where 37 pins are installed (Kamide, 1994, Nishimura, 2000). The six peripheral subassemblies provide heat to the center subassembly of 37-pin through the sodium gap between the subassemblies.

Flow redistribution occurs in the transition from a forced convection condition to a mixed or natural convection condition. However, steady state experiments were carried out as the first step under a wide range of flow velocity and pin surface heat flux conditions so as to cover mixed and natural convection conditions in a reactor using both multi-subassembly models. Next, transient experiments to simulate scram, flow coast down and natural circulation were performed in the seven-subassembly model, which was installed in a plant dynamics test loop (PLANDTL-DHX).

An analytical approach was investigated to simulate the highest temperature in a subassembly resulted from the flow redistribution in a subassembly and the inter-subassembly heat transfer. A three-dimensional thermohydraulics code, AQUA (Maekawa, 1990), was applied to the experimental analyses in a porous-body approach. A simulation method was developed and applicability to the inter-subassembly heat transfer in the multi-bundle system was examined.

2.2 Multi-Bundle Sodium Experiments under Steady State Conditions

2.2.1 61-Pin Blanket Subassembly Experiment

(1) Experimental Setup

Figure 2.2-1 shows a horizontal cross section of a core model in the experimental setup. The simulated core consists of three subassemblies: a 61-pin bundle and two 19-pin bundles. Fuel pins are simulated by electrical heater rods. The inter-subassembly heat transfer occurs particularly in the radial blanket region of the core as a steep radial temperature distribution exists in this region. Hence the 61-pin bundle simulates a blanket subassembly. Since subassembly size is considered to be an important factor in estimating the influences of heat transfer on the thermal hydraulics in a subassembly, the flat-to-flat distance of the 61-pin bundle is made approximately equal to that of large size FBRs, e.g., DFBR (Ueta, 1995), by slightly increasing the diameter of the heater rods. Here, DFBR is considered a typical example of an actual reactor for the purposes of this chapter. The 19-pin bundles model the flows in the core fuel subassemblies in order to simulate boundary between the blanket subassemblies and the core fuel subassemblies. The pin number in each subassembly is limited, however, the ratio of the flow to decay heat can be set so as to simulate the core fuel subassemblies. In an actual reactor core, there is a sodium gap between the subassemblies (inter-wrapper gap). In the simulated core, a stainless plate is installed in place of the sodium gap between the pin bundles to simplify the thermal boundary conditions surrounding the pin bundles. This modification enables the accurate estimation of heat flux on the wrapper tube wall through the temperature difference across the wall that is measured with embedded thermocouples on both side of the stainless plate. The influences of sodium gap flow between the subassemblies are examined in the seven-subassembly model. A cooling channel is also installed adjacent to the 61-pin bundle (the opposite side of the two 19-pin bundles). The 61-pin bundle is cooled by sodium flow through the channel, which simulates outer and colder subassemblies, i.e. radial reflectors or neutron shields. Hence, the 61-pin bundle can be simultaneously heated

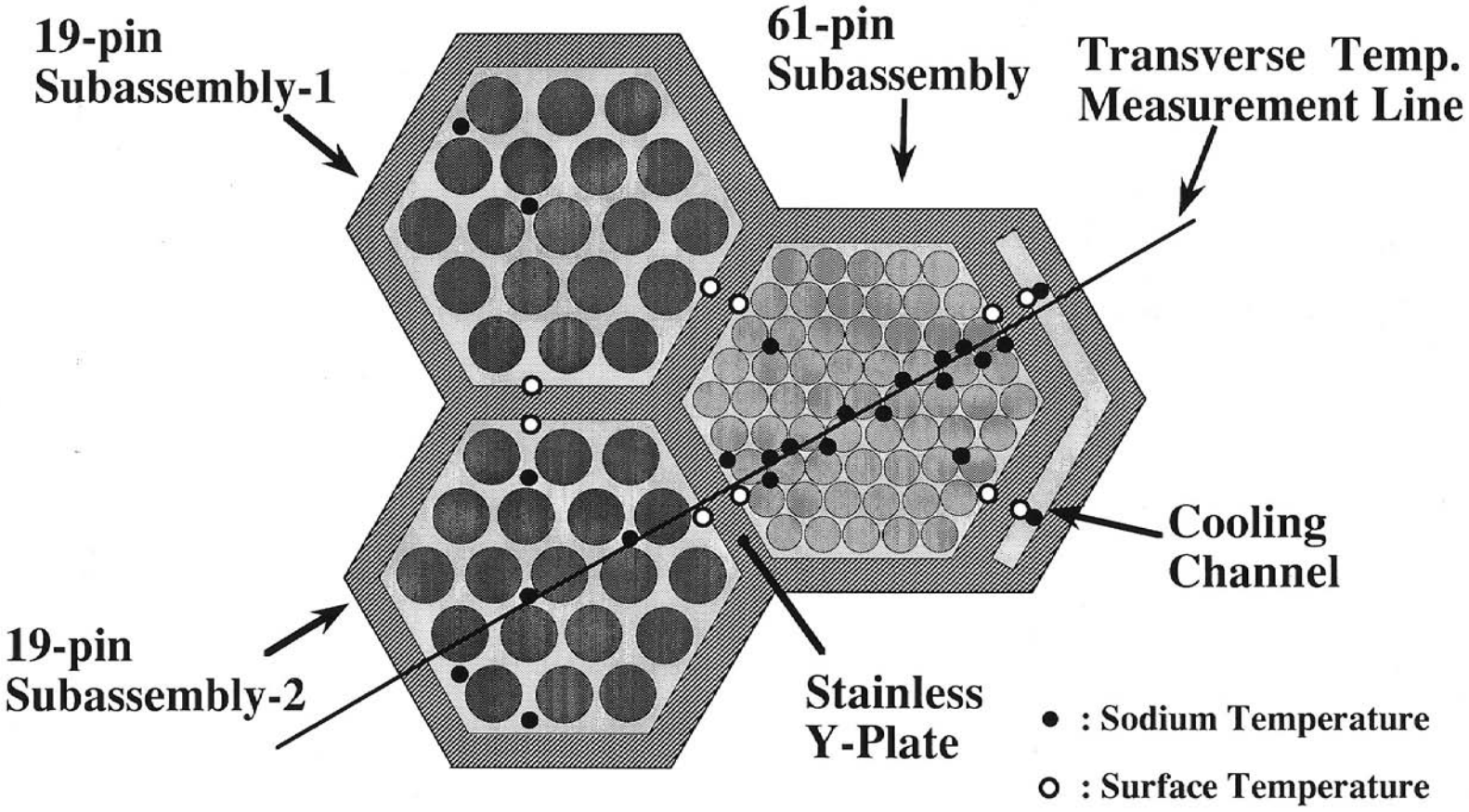

Fig. 2.2-1 Horizontal Cross Section of Three-Subassembly Model

and cooled by the 19-pin bundles and the cooling channel as a blanket subassembly is in a reactor.

Figure 2.2-2 shows a vertical cross section of the simulated core and a flow diagram of the experimental setup. The heated length of the heater rods measures 1.7 m. Sodium is pumped into the lower plenum and flows into each subassembly through connector pipes. The sodium flowing up in the subassemblies ascends to the upper plenum and returns to the pump. The inlet temperature to the subassemblies is kept constant by a heater and air cooler in the loop. Flow distribution among the three subassemblies can be controlled by valves and measured by electro-magnetic flow meters. The major specifications of the experimental setup are listed in Table 2.2-1. The heater power and flow rate in the subassemblies were kept constant during experimental cases, typically for 20 hours and set within the range of natural circulation conditions.

The sodium temperatures are measured by chromel-alumel thermocouples, 0.5 mm in diameter, at the center of subchannels in the pin bundles, and the surface temperatures of wrapper wall (the stainless plate) are measured by buried thermocouples, as shown in Fig. 2.2-1. Relative calibration of the temperature measurement was carried out based on homogeneous temperature condition data in the simulated core at five temperature levels between 250 °C and 450 °C. The estimated deviation in the temperature measurement was less than 0.5 °C.

(2) Experimental Parameters

Main concern is the relation between inter-subassembly heat transfer and intra-subassembly thermohydraulics, e.g., transverse temperature distributions in the pin bundles. Thus, the heat flux through the wrapper tube wall is a key parameter. Under natural circulation conditions, the flow velocity in the bundle is sufficiently low

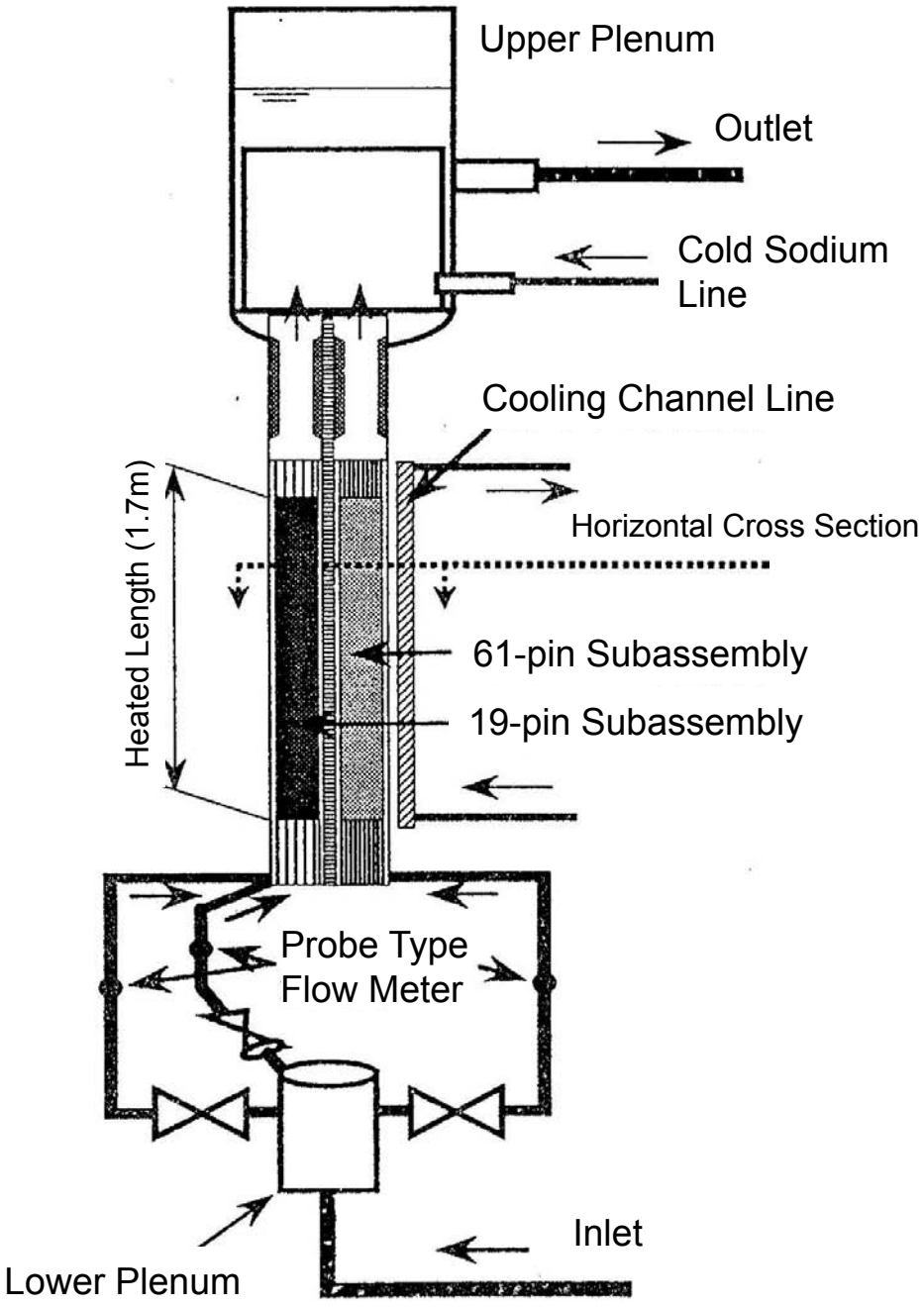

Fig. 2.2-2 Schematic of Three-Subassembly Model

Table 2.2-1 Specifications of Three-Subassembly Model

Number of subassemblies	3
Number of heater pins in a subassembly	61
Pin diameter	16 mm (Blanket fuel)
Wire spacer diameter	1.4 mm
Pin pitch/ Pin diameter	1.09
Hydraulic equivalent dia.	4.8 mm
Wire spacer lead	200 mm
Wire spacer lead/ Pin dia.	12.5
Maximum heater power /Subassembly	50 kW
Axial power distribution	Flat
Heated length	1.7 m
Flat to flat distance of pin bundle	140 mm
Inter-wrapper gap	No-gap, Stainless plate (15 mm thickness)

for the buoyancy force to influence the velocity distribution in the pin bundle. The buoyancy force is, therefore, an important factor.

A buoyancy parameter, Gr/Re, has been used as an index of buoyancy effect by Engel and Markley (1982) and by Namekawa and Luangdilok (1985). Engel used the hydraulic equivalent diameter in a pin bundle, D, in the definition of Gr. Namekawa used axial length from the heated lower end, L. In both studies, D is used in the definition of Re. In these studies, dependency on Gr/Re had unique characteristics at each height in the heated length. Here, a modified Grashof number (Gr*) is introduced to consider the influence of axial position (L) in the subassemblies on the buoyancy force. The definitions of Gr* and Re are as follows:

$$Gr^* = \frac{g\beta\Delta T L D^2}{\nu^2} \qquad (2\text{-}1),$$

$$\mathrm{Re} = \frac{DV}{\nu} \qquad (2\text{-}2).$$

Two representative lengths, L and D in Eq. (2-1), are used in the definition of Gr* to estimate buoyancy force and shear stress, respectively. ΔT is temperature increase from the inlet of the subassembly. The buoyancy force related to the intra-subassembly flow redistribution is resulted from the temperature difference between the subchannels. This temperature difference will increase when ΔT is large. Thus, ΔT will be one of representative quantities of the buoyancy force.

A modified buoyancy parameter, Gr*/Re was examined based on parameter experiments, where the power and flow rate in the 61-pin bundle were varied around the conditions of natural circulation decay heat removal (NC/DHR): 3 and 5% of actual reactor rated conditions for pin surface heat flux and 1 to 15 % for flow velocity in the blanket subassembly. The Re number in the 61-pin subassembly was varied from 230

to 3460. The main condition in the parameter experiments was V=3.7 cm/s and Re=460.

Further, a wall heat flux ratio, $q''_{w/p}$, is introduced as an index of inter-subassembly heat transfer. This parameter is a ratio of the heat flux through the wrapper wall (a plus sign is used for flux from wall to the 61-pin bundle) to the average heat flux on the heater pin surface. The temperature difference between the adjacent subassemblies was varied to control the wall heat flux ratio, $q''_{w/p}$.

$q''_{w/p}$ is defined on the wrapper wall beside the 19-pin bundles and also on the wall adjacent to the cooling channel. Since two 19-pin bundles are operated with identical heater power and flow rate, the heat flux on the wall adjacent to each 19-pin bundle is the same. The asymmetric condition of the heat flux ratios on walls adjacent to the 19-pin bundles ($q''_{w/p(19)}$) and the cooling channel ($q''_{w/p(cc)}$) is represented as an absolute ratio of wall heat flux: $|q''_{cc/19}|$.

(3) Experimental Results

<Influence of buoyancy force>

Transverse temperature distributions in the subassemblies were measured along the line at the top of heated length shown in Fig. 2.2-1. Figure 2.2-3 shows normalized temperature distributions in the 61-pin subassembly in three cases where the flow rate was varied at three levels and the heater power was kept constant at 3% of full power condition in a reactor. The normalized temperature is defined as follows:

$$T^* = \frac{T - T_{in}}{T_{ave} - T_{in}} \qquad (2\text{-}3),$$

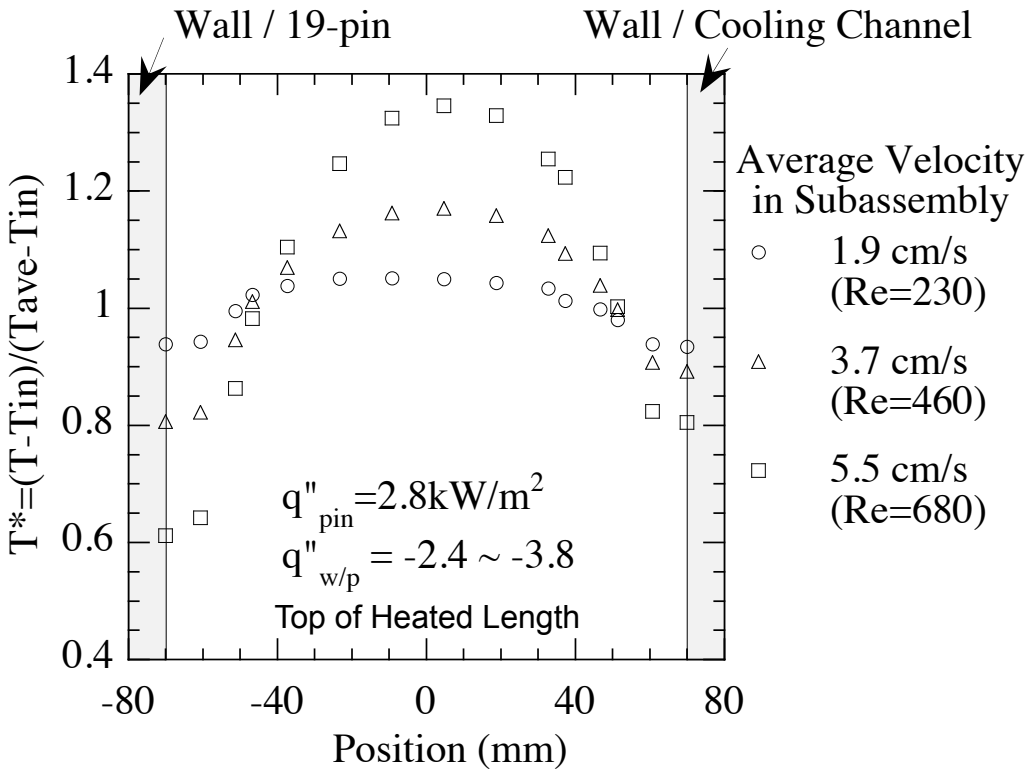

Fig. 2.2-3 Influence of Flow Velocity on Non-Dimensional Transverse Temperature Distributions in 61-pin Bundle

$$T_{ave} = \frac{\sum_{i=1}^{N} A_i T_i}{\sum_{i=1}^{N} A_i} \qquad (2\text{-}4).$$

Here T_{ave} is the average cross section temperature based on flow area weighted temperatures in 50 subchannels. The value of $q''_{w/p(19)}$ was set at -2.4 to -3.8, and $|q''_{cc/19}|$ was set at unity. It was seen that the lower flow rate resulted in a flatter temperature distribution, even if the pin bundle was cooled through the wrapper wall. This is because of intra-subassembly flow redistribution.

In order to consider such temperature flattening, a peaking factor and a wall subchannel factor are introduced. The peaking factor, P_f, means a normalized highest temperature at cross sections. The temperature at the wall subchannel is also of importance in estimating heat transfer between the subassembly and the inter-wrapper gap. A wall subchannel factor, W_f, is introduced as a normalized temperature at the wall subchannel. The definitions are as follows:

$$P_f = \frac{T_{peak} - T_{in}}{T_{ave} - T_{in}} \qquad (2\text{-}5),$$

$$W_f = \frac{T_{wall\,sub} - T_{in}}{T_{ave} - T_{in}} \qquad (2\text{-}6).$$

The values of P_f and W_f in the 61-pin bundle are shown in Figs. 2.2-4 and 2.2-5, respectively. The W_f was obtained at the left side wall subchannel next to the 19-pin bundle. The influence of the intra-subassembly flow redistribution on P_f and W_f was well correlated by Gr*/Re not only for cases in which no inter-subassembly heat transfer occurred ($q''_{w/p(19)}$ = -0.2 ~ 0.3) but also in cases where inter-subassembly heat transfer did occur ($q''_{w/p(19)}$ = -1.7 ~ -3.8).

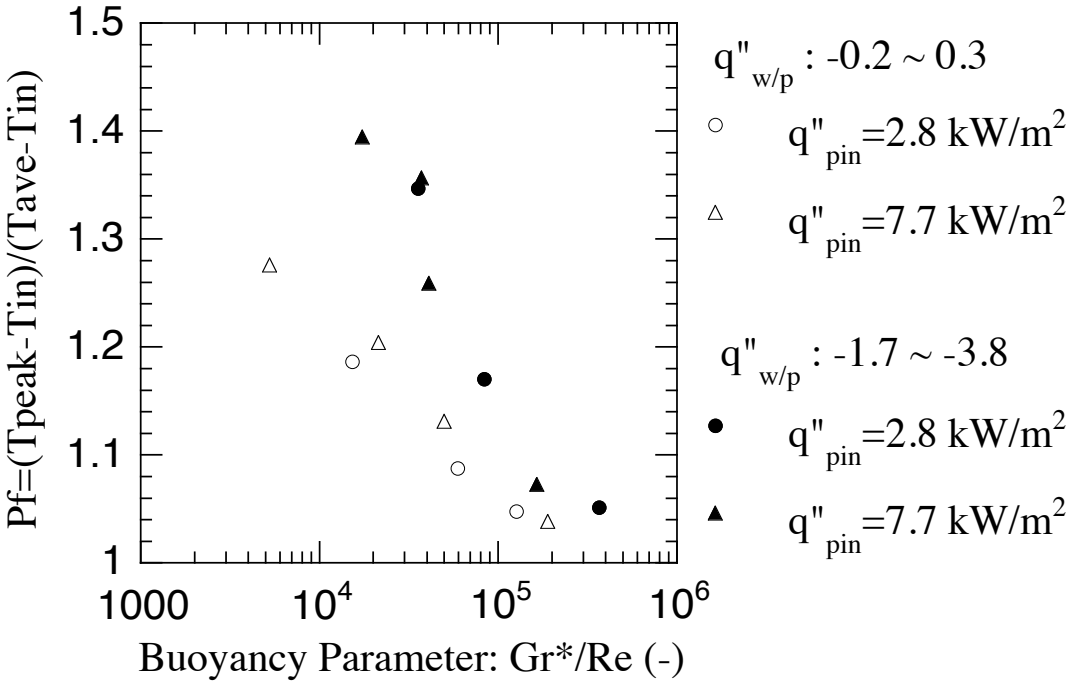

Fig. 2.2-4 Influence of Buoyancy Force on P_f in 61-pin Bundle

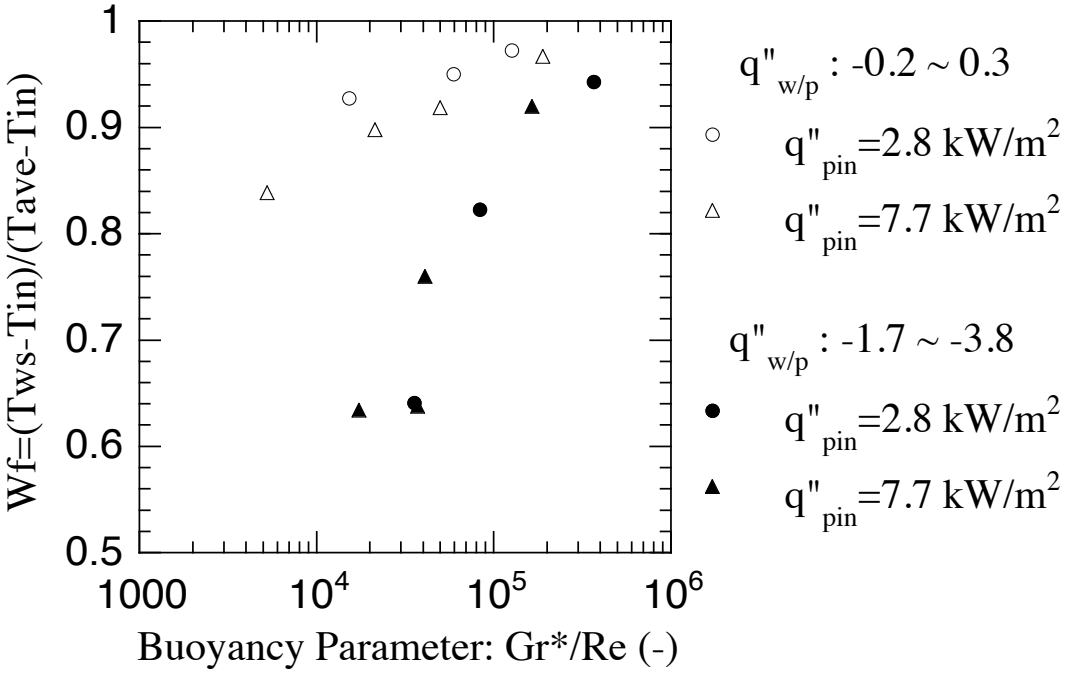

Fig. 2.2-5 Influence of Buoyancy Force on W_f in 61-pin Bundle

<Influence of wall heat flux>

The normalized transverse temperature distributions in the 61-pin bundle are shown in Fig. 2.2-6 for cases of cooled conditions at both walls adjacent to the 19-pin bundles and the cooling channel. In the case where $q''_{w/p}$ was nearly zero, a flat temperature distribution was registered due to the strong flow redistribution at $Gr^*/Re = 1.3 \times 10^5$. The inter-subassembly heat transfer caused drastic changes in the temperature distributions. The higher heat flux through the wall resulted in steeper temperature distribution, especially near the wall. This local temperature decrease near the wall suppresses the heat transfer from the pin bundle to the wrapper wall. If the temperature distribution were flatter, the temperature difference between the wall subchannels and the inter-wrapper gap would be larger and the heat flux through the wall would increase. The relation between $q''_{w/p}$ and W_f is significant in the evaluation of overall heat transfer in the subassembly.

The normalized temperature distributions in the cases of simultaneously heated and cooled conditions by the 19-pin bundles and the cooling channel are shown in Fig. 2.2-7. The values of $|q''_{cc/19}|$ were set at near unity in the experiments. The sodium temperature decreased from the left side to the right side monotonously. The cases of higher wall heat flux showed local temperature increase or decrease near the walls as compared with the cases of lower heat flux; temperature distributions across the internal part in the bundle were nearly equal between the two cases of $q''_{w/p}$=5.6 and 8.0. These experiments showed the obvious dependence of wall subchannel temperatures on wall heat flux.

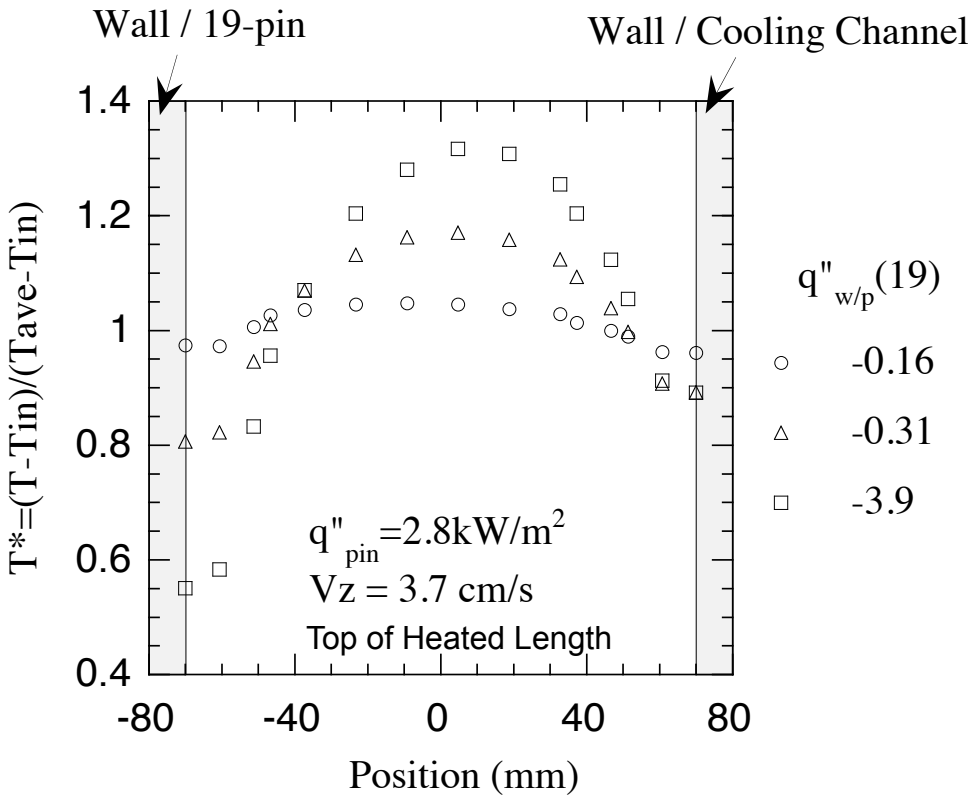

Fig. 2.2-6 Influence of Wall Heat Flux on Non-Dimensional Transverse Temperature Distributions in 61-pin Bundle under Cooled Conditions at Both Walls

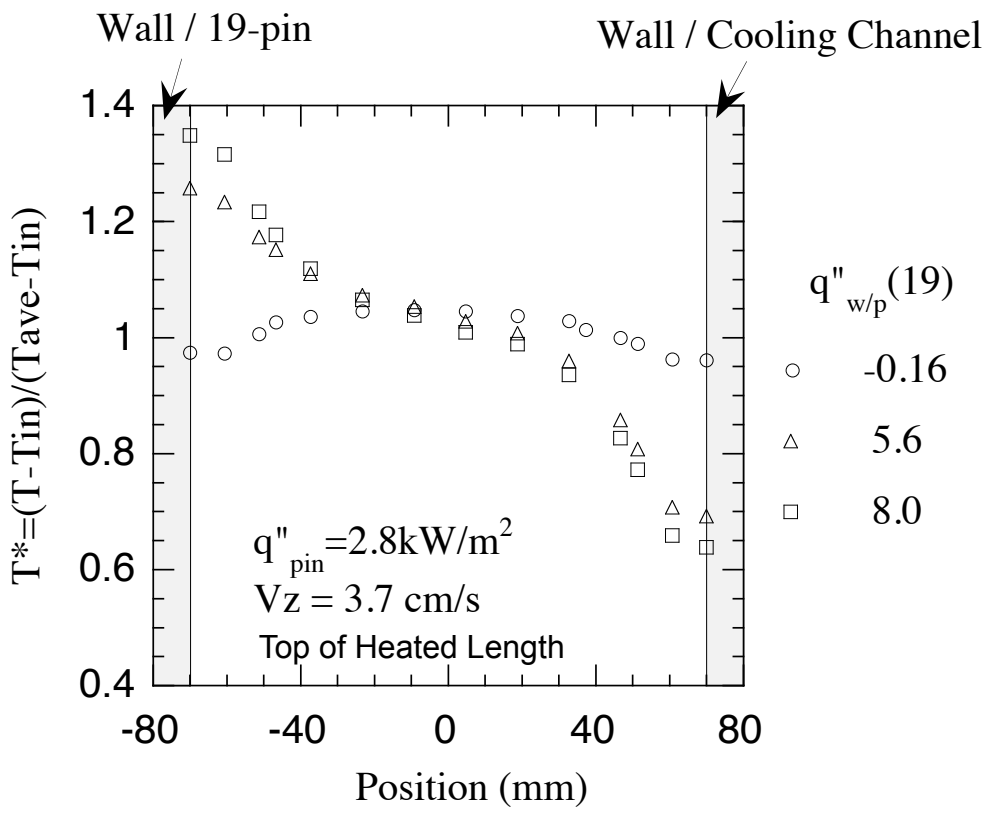

Fig. 2.2-7 Influence of Wall Heat Flux on Non-Dimensional Transverse Temperature Distributions in 61-pin Bundle under Simultaneously Heated and Cooled Conditions

Figure 2.2-8 indicates the influence of the wall heat flux ratio, $q''_{w/p(19)}$, on the wall subchannel factor (W_f) at the wall adjacent to the 19-pin bundles. Under the cooled condition ($q''_{w/p} < 0$), W_f decreased linearly with the decrease of $q''_{w/p}$ under low Gr*/Re conditions. In contrast to this, W_f fell steeply at a large negative $q''_{w/p}$ under high Gr*/Re conditions. When $q''_{w/p}$ was within -3, W_f under high Gr*/Re conditions was closer to unity than under low Gr*/Re conditions mainly due to intra-subassembly flow redistribution. However, when $q''_{w/p}$ was less than -3.0, W_f fell extremely and became comparable to low Gr*/Re cases. In other words, higher Gr*/Re resulted in smaller absolute W_f values under the weakly cooled condition ($q''_{w/p} > -3$); however, strong cooling caused a steep decrease in W_f even under higher Gr*/Re conditions. Figure 2.2-9 shows the peaking factors under cooling conditions through the wall and higher Gr*/Re conditions (> 220,000). As the absolute value of $q''_{w/p}$ increased, the peaking factor increased, when the pin bundle was cooled by adjacent subassembly. The peaking factor reached 1.32 when the wall heat flux ratio, $q''_{w/p}$ was -5.

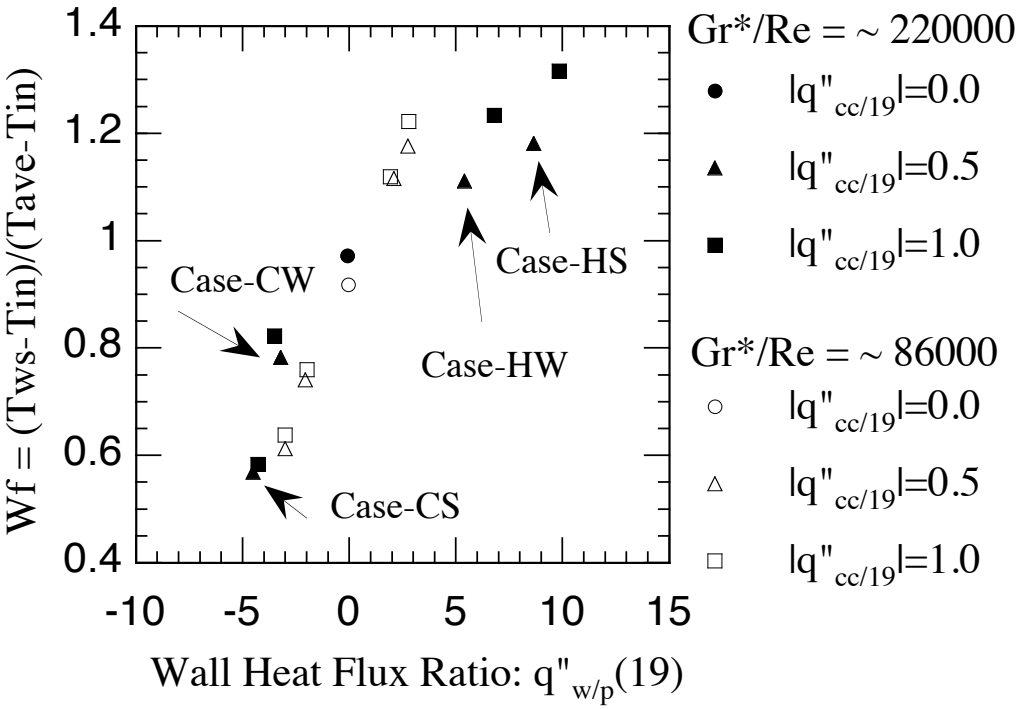

Fig. 2.2-8 Influence of Wall Heat Flux on Wall Subchannel Factor (at Left Wall) in 61-pin Bundle

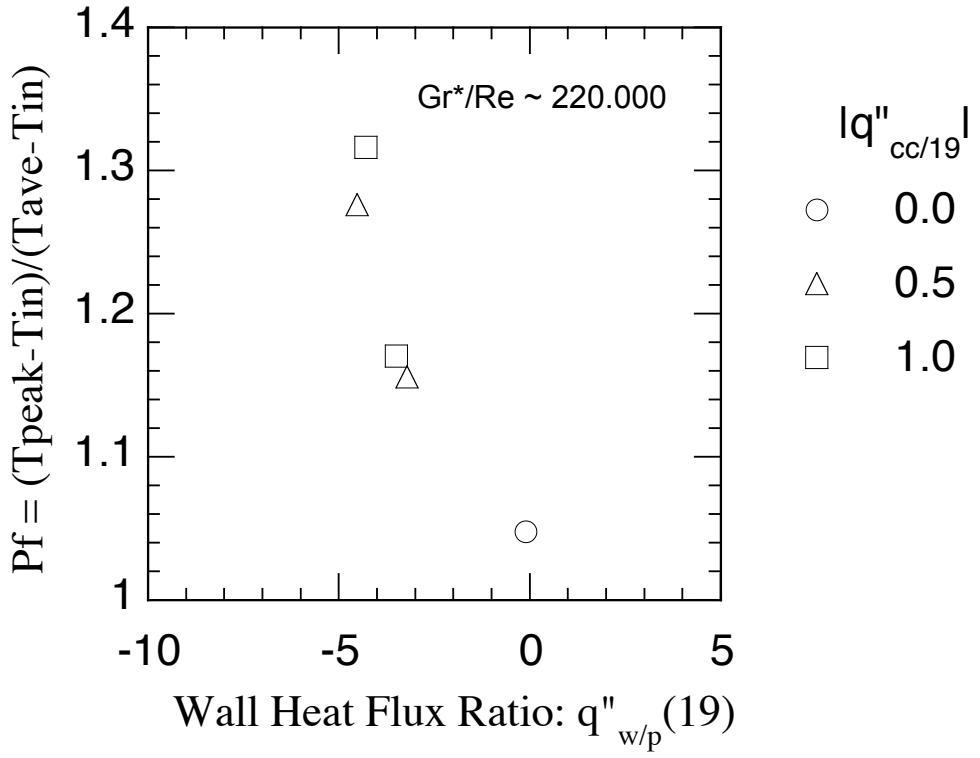

Fig. 2.2-9 Influence of Wall Heat Flux on Peaking Factor in 61-pin Bundle

2.2.2 37-Pin Core Fuel Subassembly Experiments

(1) Experimental Setup

To study the intra-subassembly flow redistribution in a core fuel subassembly combined with the heat transfer through the wrapper tubes and natural convection in gaps between the subassemblies, a core model composed of seven subassemblies was installed in the PLANDTL-DHX facility. Figure 2.2-10 shows a horizontal cross section of the core model. The center subassembly had 37 heater pins measuring 8.3 mm in diameter, and the 6 peripheral subassemblies had 7 pins each. The inter-wrapper gap filled with sodium was connected to an upper plenum. The heater pins of the center subassembly simulated a core fuel pin of a large FBR in full scale. The flat-to-flat distance of the subassembly was approximately 1/2 of an actual subassembly, which consists of 217 or 271 fuel pins. The heater power of each subassembly can be controlled individually. The major specifications of the core model are listed in Table 2.2-2.

The sodium temperatures in the core were measured by thermocouples of 0.3 or 0.5 mm diameter (see Fig. 2.2-10). Measurement accuracy was maintained by relative calibrations. A maximum flow rate of 1200 l/min was provided through the test section at constant temperature to maintain all thermocouples at identical temperature. Such homogeneous temperature data were recorded at seven temperature levels from 250 to 550˚C. Calibration constants were obtained from the least square method based on reference thermocouples, previously calibrated by hot bath. The maximum error among all thermocouples was 0.5˚C after calibration. The signals from the thermocouples, flow meters, and the electric power input of heater pins were recorded by 16-bit A/D converters at a sampling interval of 0.096s (~10 Hz).

(2) Influences of Inter-Subassembly Heat Transfer

Eight steady state experiments were carried out to investigate the influences of inter-subassembly heat transfer on temperature distributions. Conditions in the center subassembly were kept constant in the parameter experiments; the flow velocity and the

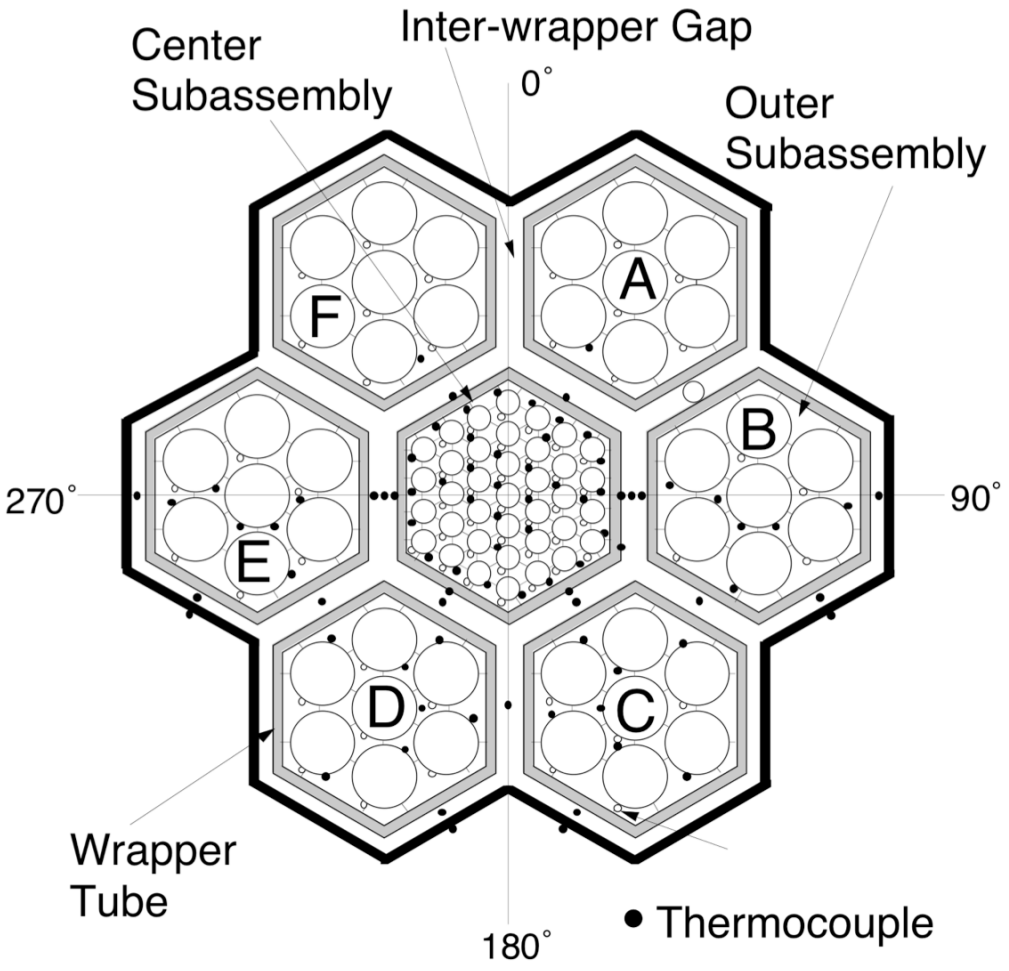

Fig. 2.2-10 Schematic of Horizontal Cross Section of Seven-Subassembly Model

Table 2.2-2 Specifications of Seven-Subassembly Model

Parameters	Center Subassembly	Outer Subassemblies
Flat to flat distance of wrapper tube	71.0 mm	71.0
Wrapper tube thickness	4 mm	4
Inter-wrapper gap	7.0 mm	7.0
Number of pins	37	7
Pin diameter	8.3 mm	20.8
Pin pitch/ Pin diameter	1.19	1.08
Hydraulic equivalent diameter	4.2 mm	5.9
Spacer wire diameter	1.5 mm	1.5
Wire wrap pitch/ Pin diameter	19.3	7.9
Heated length	1.0 m	1.0
Power profile	Chopped cosine	Chopped cosine

pin surface heat flux were set to the 2% level of the rated conditions of FBRs. The Re number in the 37-pin bundle is around 1,200. The conditions of all peripheral subassemblies were set to be equal. The outlet temperature difference between the center subassembly and the peripheral subassemblies were varied from -70˚C to +70˚C, which were estimated using flow rates and heater powers in the subassemblies and assuming an adiabatic condition between the subassemblies.

The wall heat flux ratio was used as a main parameter for effects of the inter-subassembly heat transfer on the temperature distributions as described in section 2.2.1. The heat flux through the wrapper tube ($q"_{wall}$) was estimated using the measured temperatures as follows:

$$q"_{wall} = H\left(T_{wall\,sub} - T_{gap}\right) \qquad (2\text{-}7),$$

$$\frac{1}{H} = \frac{1}{Nu\lambda/D} + \frac{1}{\lambda_{SUS}/d_{wall}} + \frac{1}{Nu\lambda/D_{gap}} \qquad (2\text{-}8).$$

$$Nu = 5 + 0.025Pe^{0.8}$$

The measured transverse temperature profiles at the top of the heated length in the center subassembly are shown in Fig. 2.2-11. The larger wall heat flux ratio resulted in the steeper temperature distribution.

The spatial peaking and wall subchannel factors were calculated from measured temperatures at several horizontal cross sections in the center subassembly. Average temperatures at certain cross sections were obtained from temperatures weighted by the subchannel flow areas instead of the mixed mean temperature. The spatial peaking factors and wall subchannel factors versus the wall heat flux ratio are shown in Fig. 2.2-12. The buoyancy parameter, Gr*/Re, at the top of heated length was less than 75,000. The spatial peaking factor at each height increased linearly with the wall heat flux ratio. This increase of the spatial peaking factor should be counted as along with the cooling

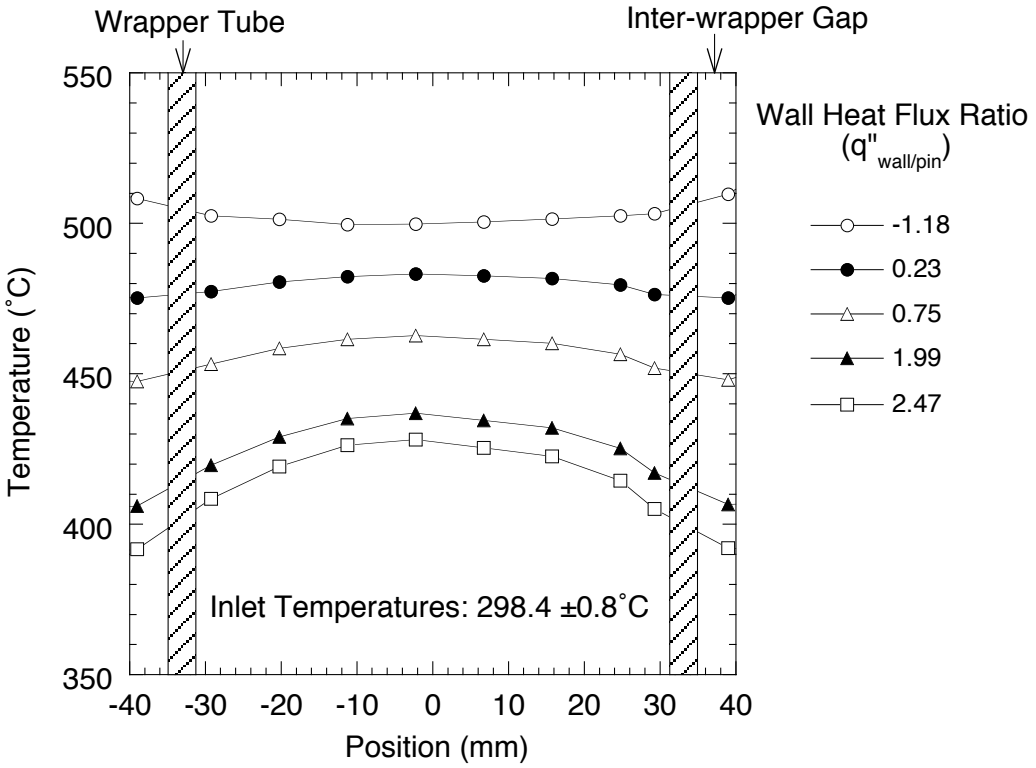

Fig. 2.2-11 Influence of Inter-subassembly Heat Transfer on Transverse Temperature Distributions at Top of Heated Length in Center Subassembly

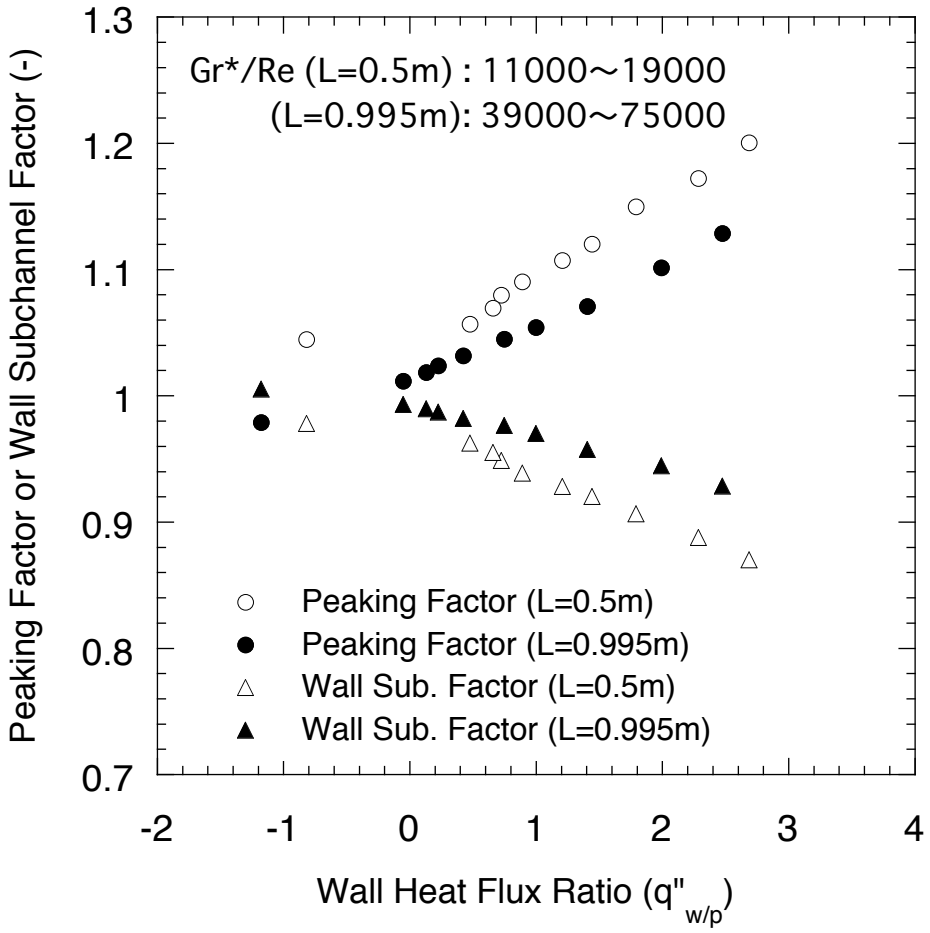

Fig. 2.2-12 Influences of Inter-subassembly Heat Transfer on Peaking Factor and Wall Subchannel Factor

effects through the wrapper tubes. The wall subchannel factor at each height reduced linearly with the increase of the wall heat flux ratio under cooled conditions ($q''_{w/p} > 0$). The decrease of the wall subchannel temperatures from the subassembly average temperature became larger as the wall heat flux ratio increased. This relation was clearly seen using the wall subchannel factor. The obtained linear correlation between W_f and $q''_{w/p}$ indicates that the wall subchannel temperatures did not significantly fall below the average temperature, even in the case of high a wall heat flux ratio.

This linear correlation was obtained under the conditions of Gr*/Re < 75,000 and consistent with the data of the 61-pin blanket subassembly in cases of Gr*/Re ~ 86,000 (see Fig. 2.2-8). On the other hand, the flow areas of the wall subchannels reached 40% of the total flow area in the pin bundle. Thus, the contribution of the wall subchannels to the average temperature was larger than that in the 61-pin bundle in the previous section and in an actual 217- or 271-pin bundle. The influence of pin bundle size on the spatial peaking and wall subchannel factors will be estimated by multi-dimensional analysis code.

(3) Influence of Intra-Subassembly Flow Redistribution

A modified Grashof number, Gr*, as shown in Eq. (2-1), was defined so as to consider the height in the bundle and to make it easier to estimate heat transfer through the wrapper tubes along the full height of the bundle.

The experiments were carried out for two parameters; the flow rate and the heater pin power in the center subassembly. The average velocity in the pin bundle of the center subassembly varied from 0.06 to 0.30 m/s (1 to 5% of the full flow in a reactor). The Re number in the 37-pin bundle ranges from 700 to 3,500. The pin surface heat flux varied from 1.5 to 3% of the full power. The inter-subassembly temperature difference at the outlet was 30˚C (assuming an adiabatic condition between the subassemblies), and kept constant in all cases.

Figure 2.2-13 shows the peaking factors at three levels (L=0.5, 0.83, and 0.995 m) in the center subassembly versus the buoyancy parameter, Gr*/Re. The wall heat flux ratios were kept at 1.3 to 2.4 in all cases. The peaking factors at all levels decreased linearly with the increase of Gr*/Re. The 95% confidence band of the linear least squares fit is also shown in Fig. 2.2-13. The peaking factor at any level could be estimated by a least squares fitted line versus Gr*/Re even in cases of inter-subassembly heat transfer influence.

As mentioned in section 2.2.1 (2), the buoyancy parameters, Gr/Re, have been used as an index of buoyancy effect by Engel and Markley (1982) and by Namekawa and Luangdilok (1985). Engel used the hydraulic equivalent diameter in a pin bundle, D, in the definition of Gr. Namekawa used axial length from the heated lower end, L, in the definition of Gr_L as shown below,

$$Gr_L = \frac{g\beta\Delta T_{mix} L^3}{\nu^2}$$
$$\mathrm{Re}_D = \frac{V D}{\nu} \qquad (2\text{-}9).$$

In this case, dependency of the peaking factor on Gr_L/Re_D had unique characteristics at each height in the heated length as shown in Fig. 2.2-14. The comparison of Gr/Re dependencies between Figs. 13 and 14 revealed that the influence of axial length, L, should be considered as a linear correlation shown in Eq. (2-1).

The wall subchannel factors at three levels in the center subassembly are shown in Fig. 2.2-15. These wall subchannel factors approached unity as Gr*/Re increased due to the effect of intra-subassembly flow redistribution. Tendencies of the wall subchannel factors versus Gr*/Re agreed on all three levels. The peaking factors and wall subchannel factors at any level could be predicted by a function of Gr*/Re in cases of inter-subassembly heat transfer influence.

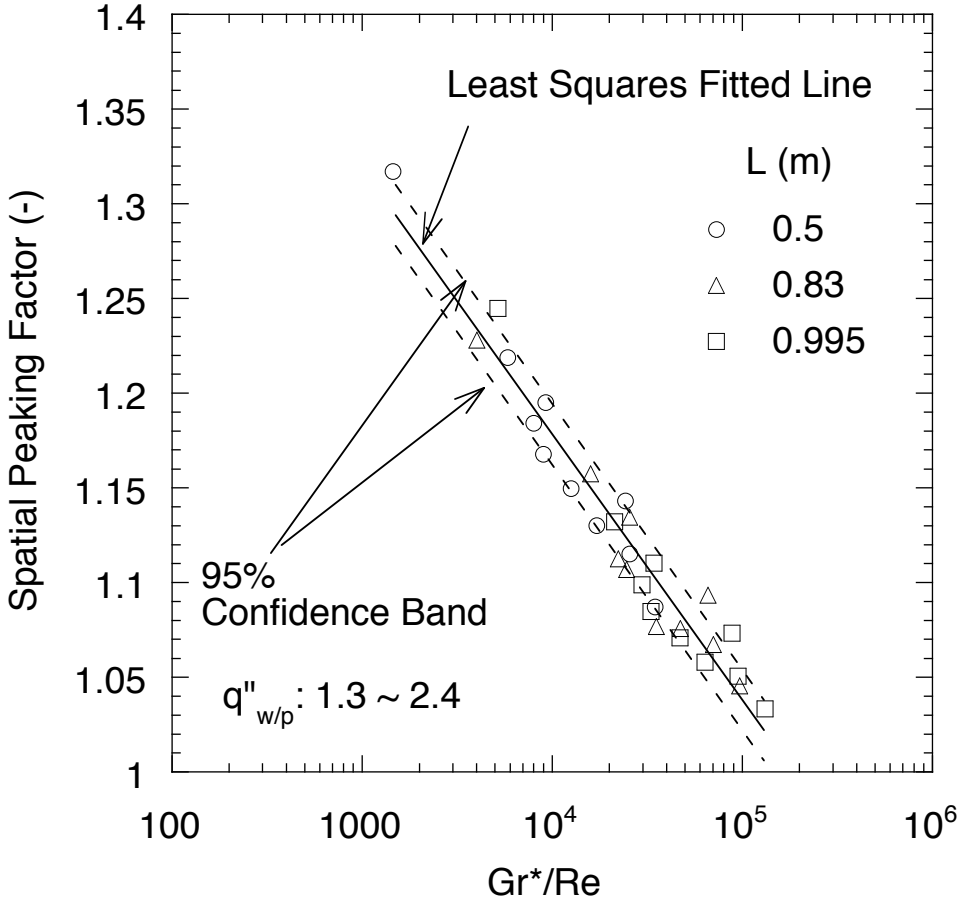

Fig. 2.2-13 Effect of Intra-subassembly Flow Redistribution on Peaking Factor under Inter-subassembly Heat Transfer

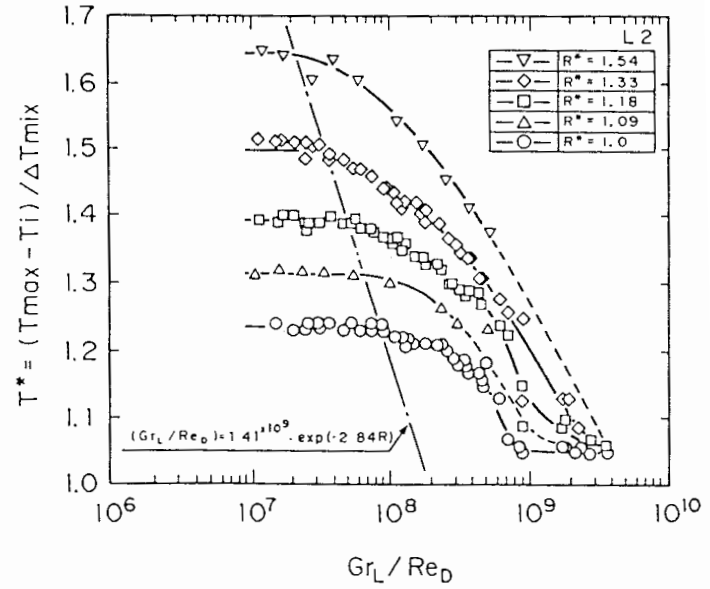

Fig.6 Temperature peaking factors as a function of buoyancy parameter at L2(Heated outlet)

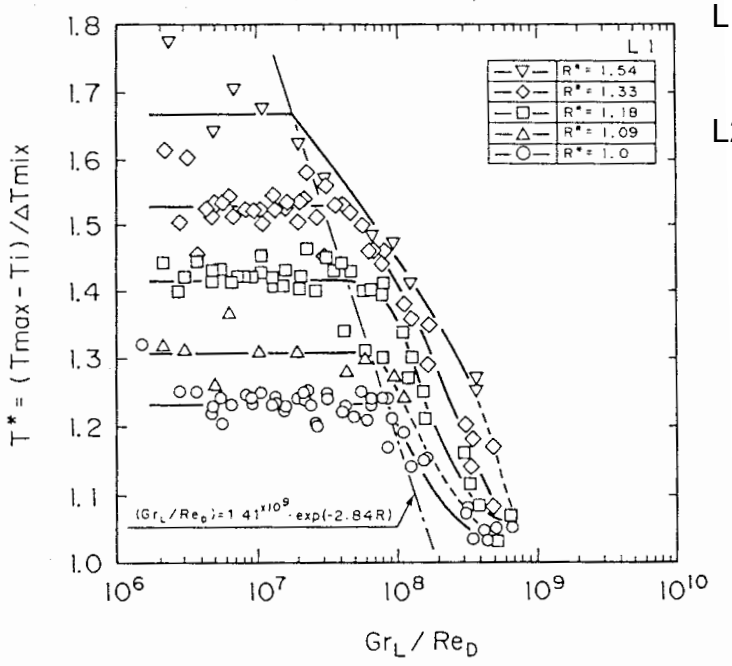

Fig.7 Temperature peaking factors as a function of buoyancy parameter at L1

Heated length: 930mm

L1: 608mm from the lower heated end

L2: 915 mm from the lower heated end

Namekawa, F., Luangdilok, W., et al., Buoyancy and radial power skew effects on wire-wrapped rod bundle thermal hydraulics in an LMFBR fuel assembly, Proc. 3rd Int. Top. Mtg. on Reactor Thermal Hydraulics, Vol.2 16.J-1 (1985).
Page 16.J-4, Figures 6 and 7

Fig. 2.2-14 Peaking Factors at Two Heights as a Function of Conventional Buoyancy Parameter

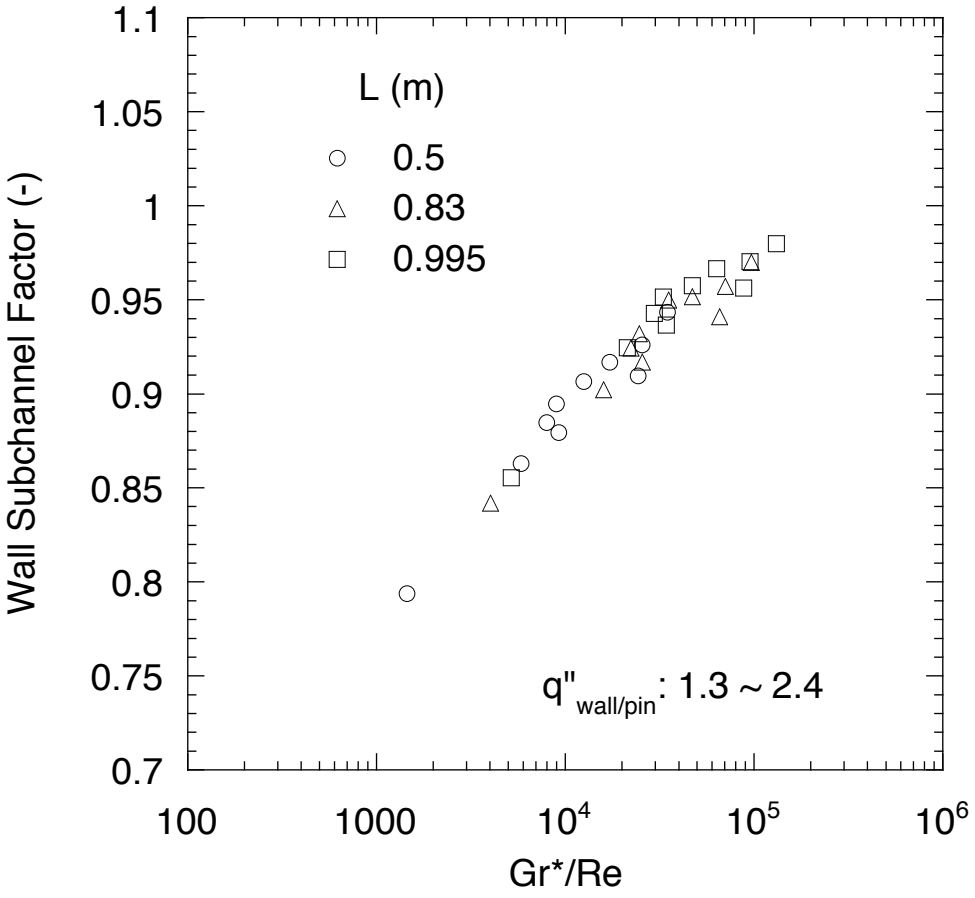

Fig. 2.2-15 Effect of Intra-subassembly Flow Redistribution on Wall Subchannel Factor with Inter-subassembly Heat Transfer

2.2.3 Summary of Steady State Experiments

The subassembly thermal hydraulics were investigated by the three-subassembly model and the seven-subassembly model using sodium as a working fluid under NC/DHR conditions. The experiments focused on flow redistribution and inter-subassembly heat transfer. The three-subassembly model simulated a blanket fuel subassembly of 61-pin bundle in real dimensions and also the boundary between the blanket fuel subassemblies and the core fuel subassemblies. The seven-subassembly model simulated the core fuel subassembly of 37-pin bundle as a partial model.

The peaking factor (P_f), normalized highest temperature at a cross section, was obtained in the experiments where the flow rate, the heater pin power, and the temperature difference between the subassemblies were varied.

Radial heat transfer between subassemblies was coupled with intra-subassembly thermohydraulics, especially with wall subchannel temperatures. For a one-dimensional network code, representative temperatures should be employed in the radial heat transfer calculation. The wall subchannel factor (W_f) was defined to estimate the wall subchannel temperature from the average cross section temperature by using the analogy of the peaking factor (P_f). Characteristics of intra-subassembly thermal hydraulics were grasped under mixed convection conditions as follows:

1) Influence of intra-subassembly flow redistribution
   - The transverse temperature distribution was flattened by intra-subassembly flow redistribution, even if inter-subassembly heat transfer occurred.
   - The influences on P_f and W_f correlated well by a modified buoyancy parameter, Gr*/Re, in the blanket and also core fuel pin bundles. The obtained correlation with Gr*/Re was independent of the axial position in the subassembly.

2) Influence of inter-subassembly heat transfer

- The inter-subassembly heat transfer reduced the highest temperature, even in a full size pin bundle of the blanket core fuel subassembly.
- Influence of inter-subassembly heat transfer on W_f and P_f correlated well using the wall heat flux ratio ($q''_{w/p}$).
- Under the conditions of a large negative $q''_{w/p}$ and high Gr*/Re, W_f decreased extremely.

2.3 Transient Experiments on the Second Peak after Scram

2.3.1 Concept of Highest Temperature Evaluation

An example of core outlet temperature course is shown in Fig. 2.3-1 during transition from forced to natural circulation for a case in which dipped heat exchangers (DHXs) are used as a decay heat removal system. The first peak results from a delay of the power shutdown from the flow coast down, which is generally assumed in safety evaluation analyses. Low flow rate due to natural circulation and relatively higher decay heat in the early period from a scram (order of 100s) causes the second peak. In the case of decay heat removal by the DHX, natural circulation flow decreases temporally due to cooling in the upper plenum, which reduces the natural circulation head, as shown in experimental and analytical investigations (Naohara, 1990, Gry, 1990, Hoffmann, 1992). The third peak is formed by this temporary decrease of the core flow at several thousand seconds from the scram. The second and the third peaks are of importance in the evaluation of core thermal hydraulics in NC/DHR.

The highest sodium temperature (T_{max}) in the core is one of the most important features of core thermal hydraulics. It has been evaluated under forced flow conditions as follows:

$$T_{\max} = T_{in} + P_f F \Delta T \qquad (2\text{-}10),$$

$$\Delta T = \frac{Q}{C_p W} \qquad (2\text{-}11).$$

P_f: Spatial peaking factor in the subassembly,

F: Safety margin including estimation error or uncertainty in power, flow, material property, and geometry in the subassembly.

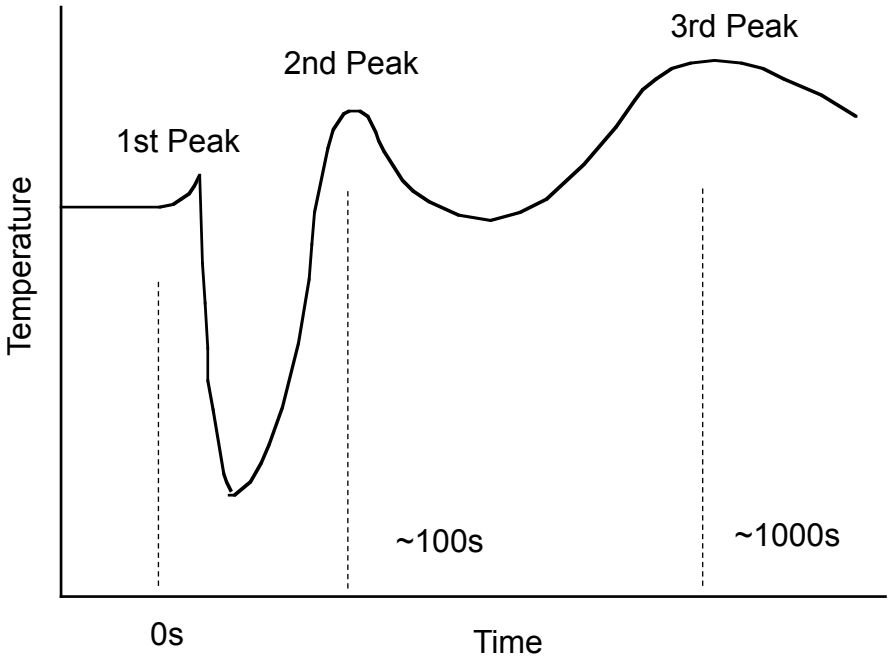

Fig. 2.3-1 Example of Core Outlet Temperature Course during Transition from Forced to Natural Circulation

To obtain T_{max} during transition from forced to natural circulation as illustrated in Fig. 2.3-1, T_{in} and ΔT in Eq. (2-10) can be estimated dynamically by a system simulation code based on network models. The network code models the entire core as several flow channels simulating the subassemblies in one-dimension. It is significant to consider the following three effects for the evaluation of ΔT during NC/DHR.

- Since the core flow is low, the buoyancy force influences flow distribution among the subassemblies. This inter-subassembly flow redistribution flattens the temperature distribution across the core.
- The temperature difference between the subassemblies causes inter-subassembly heat transfer, and this flattens the temperature distribution.
- The DHXs produce cold sodium in the upper plenum. This cold sodium penetrates into the inter-wrapper gap and causes natural convection in the core barrel. This inter-wrapper flow from the DHXs cools the subassemblies through the wrapper tubes, as shown in water and sodium experiments (Hoffmann, 1993, Kamide, 1993).

The inter-subassembly flow redistribution can be considered in the system simulation code using the multi-flow channel model of the core. Inter-subassembly heat transfer and cold inter-wrapper flow are categorized as heat transfer through the wrapper tubes and can be evaluated by the same method. The inter-wrapper flow and its thermal influences on the subassembly temperatures should be modeled in the code. The steady state experiments in the previous section show that in considering such heat transfer through the wrapper tubes, the wall subchannel temperatures (adjacent to the wrapper tube) should be used due to the large temperature differences between the average subassembly temperature and the wall subchannel temperatures. The flow network model generally treats only the average subassembly temperatures . Here, a wall subchannel factor, W_f, was introduced in Eq. (2-6). The wall subchannel temperature can be estimated using the average subassembly temperature and the wall subchannel factor. The thermal interaction between the subassemblies and the inter-

wrapper gap can be understood well via the relation between the wall subchannel factor and the thermal hydraulic condition.

The peaking factor, P_f in Eq. (2-10), decreases during transition from forced to natural circulation due to intra-subassembly flow redistribution caused by the buoyancy force. Thus, the estimation of P_f during the transitions is significant in predicting the highest temperature in the core. This spatial peaking factor at a certain height in the subassembly was defined in Eq. (2-5). The highest temperature in the core can be predicted by P_f, and the hottest average subassembly temperature at a certain height can be obtained from the system simulation code, where the inter-subassembly heat transfer is accounted.

Consideration of heat transfer through the wrapper tube and the decrease of P_f will reduce the estimated hottest temperature with physical rationality. To use this concept, the characteristics of W_f and P_f must be known in any condition during transition from forced to NC/DHR. The following two parameters were introduced in the previous section to represent the conditions in the subassemblies, a buoyancy parameter, Gr*/Re, and a wall heat flux ratio (a heat flux ratio of the wrapper tube surface to the pin surface), $q''_{w/p}$. The buoyancy parameter was introduced to take into account the effect of intra-subassembly flow redistribution. The wall heat flux ratio was for the cooling effect through the wrapper tubes.

2.3.2 Plant Dynamics Test Loop (PLANDTL-DHX)

Figure 2.3-2 shows a flow diagram of the sodium test loop, PLANDTL-DHX. The seven subassemblies are connected to the upper plenum, which has a dipped heat exchanger, DHX, of the decay heat removal system. The primary loop has an intermediate heat exchanger (IHX), a pump, and a lower plenum. Sodium flow is provided by three lines to the center subassembly, the three peripheral subassemblies in

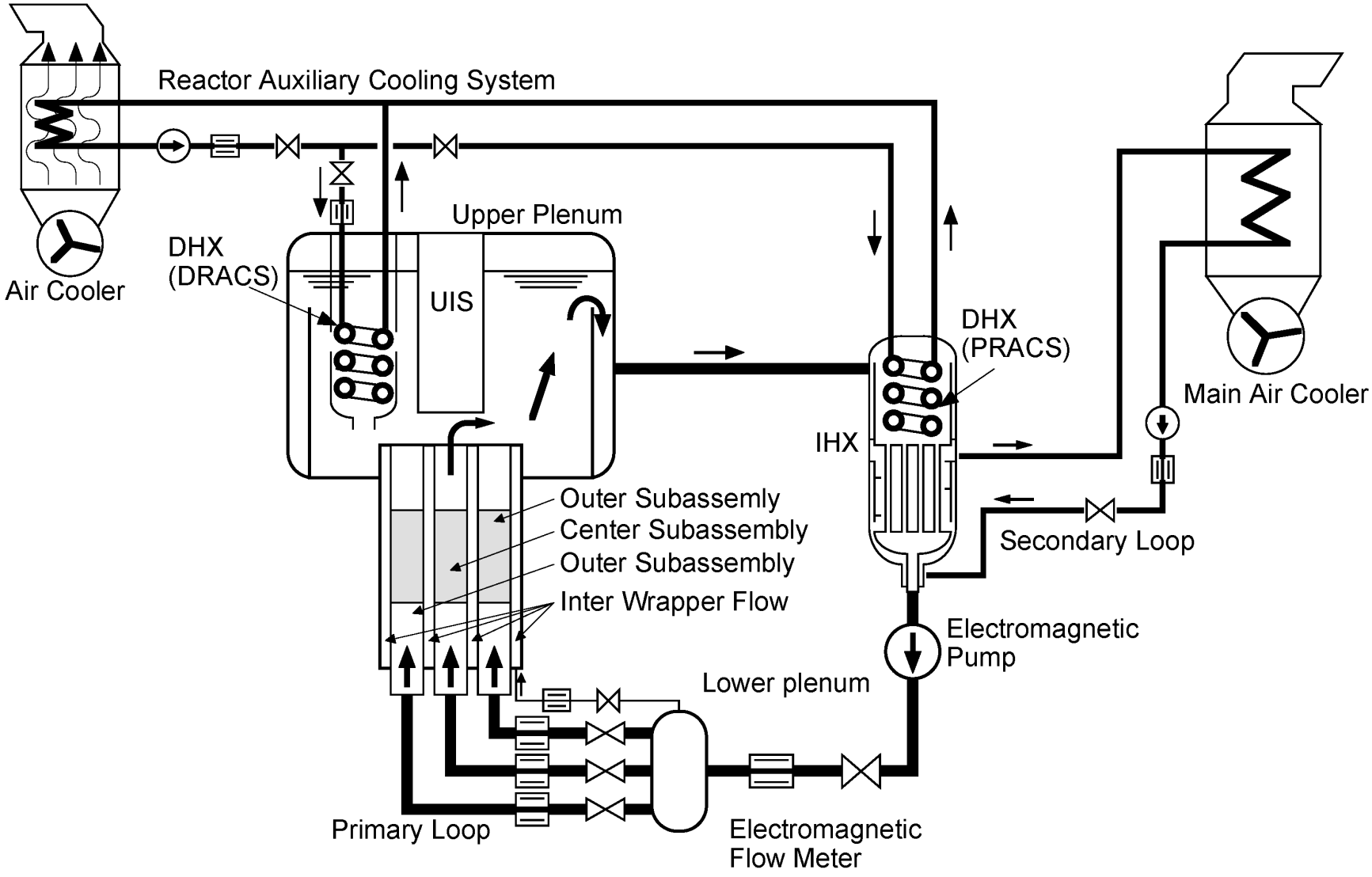

Fig. 2.3-2 Flow Diagram of the PLANDTL-DHX test facility

right side, and the other three subassemblies in left side, respectively (see Fig. 2.2-10). The flow rates of the three lines can be controlled individually. The secondary loops of the IHX and DHX have air coolers and pumps. PLANDTL-DHX can simulate the transition from forced to NC/DHR in the primary system and the decay heat removal system of FBRs.

The sodium temperatures of the core model were measured by thermocouples of 0.3 or 0.5 mm in diameter (see Fig. 2.2-10). Measurement accuracy was maintained by the relative calibrations as well as in the steady state experiments (See the section 2.2.2). Signals from thermocouples, flow meters, and electric power of the heater pins were recorded at a sampling interval of 0.017s (1/60 s) using a mini-computer system.

2.3.3 Transient Experiments

The prediction of the second peak temperature in a subassembly is of importance in the early phase (within 500s) of transition from forced to natural circulation. Then, the transient behavior of the peaking factor was investigated along with inter-subassembly heat transfer. Two cases of transient experiments were carried out. In Case-HM, the heater powers and the flow rates were identical in all subassemblies. This indicates that inter-subassembly heat transfer did not occur during transition. In Case-CL, the flow rates in all subassemblies were identical, as they were in Case-HM. The power in the center subassembly was also identical to that of Case-HM. However, the power of the 6 peripheral subassemblies was reduced so as to set their outlet temperatures lower by 30°C than the center subassembly at initial conditions. The power ratio of the center subassembly to the other subassemblies was kept constant during transition. The temperature difference between the center and peripheral subassemblies due to the difference of subassembly powers resulted in inter-subassembly heat transfer in Case-CL.

The power and flow courses in the center subassembly are shown in Fig. 2.3-3. These curves simulated transition from forced to natural circulation in FBRs and were identical in the two cases. At the initial condition, the flow velocity and the average pin surface heat flux in the center subassembly were 0.6 m/s and 15 W/cm^2, respectively. They corresponded to approximately 12% of full flow and full power in a core fuel subassembly of an FBR. The representative curves from rated conditions in an FBR are also shown in Fig. 2.3-3. The power course was obtained based on a decay heat curve. The flow was reduced by halving time of 7s and then maintained at a natural circulation flow level (2%). The Re number in the 37-pin bundle was changed from 7,000 to 1,100 in this transient. The flow course in the experiment traced this representative flow curve that was started at 18s. The power transient in the experiment started at 0s and was controlled to simulate a power-to-flow ratio in the representative curves within 30s. Hereafter the power curve in the experiment traced the decay heat curve.

Figure 2.3-4 shows comparisons of the temperature courses in the center subassembly between Case-HM and Case-CL. The compared positions were the center subchannel at the top of the heated length and the outlet center. The hottest temperature in the subassembly during the transition was registered at the top of the heated length in each case. The hottest temperature in Case-CL was lower by 20°C than in Case-HM. This indicates that the inter-subassembly heat transfer reduced not only the outlet temperature but the hottest temperature in the subassembly during the early phase (< 500s) of transition. The transverse temperature distributions in Case-HM at the top of the heated length are shown in Fig. 2.3-5. The temperature gradient around the center changed extremely in the transition. In the transient experiments, the peaking factor was defined as a non-dimensional temperature at the center subchannel using instant temperatures in the subassembly.

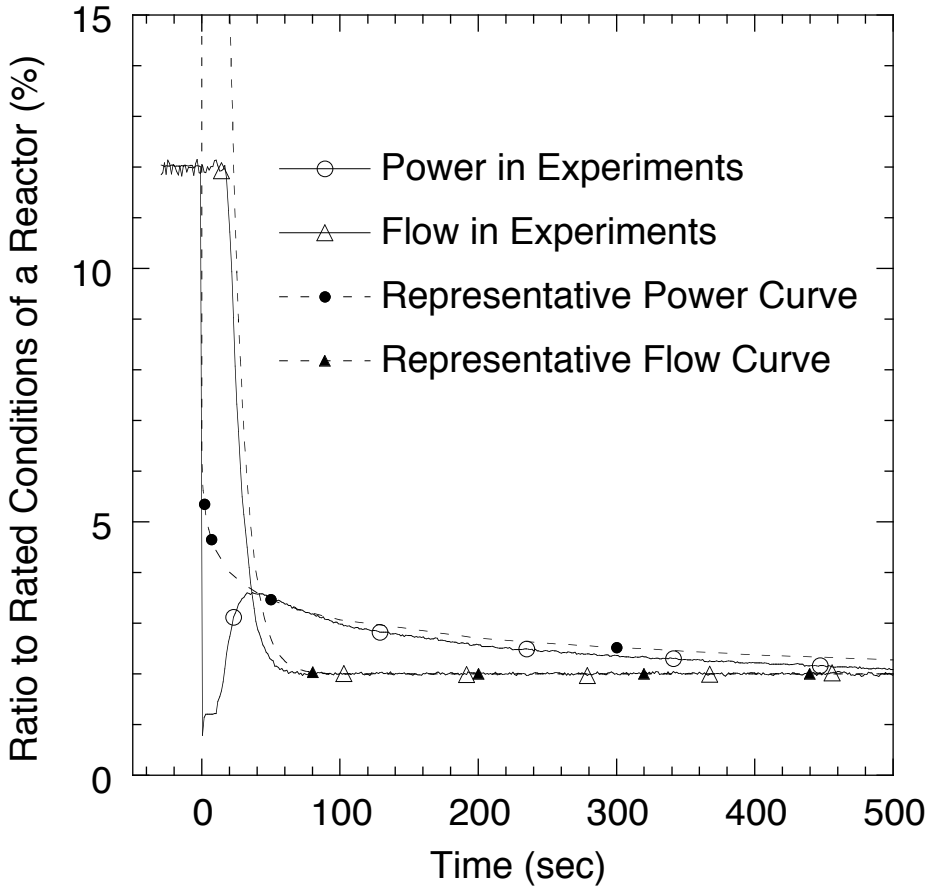

Fig. 2.3-3 Power and Flow Courses in Transient Experiments

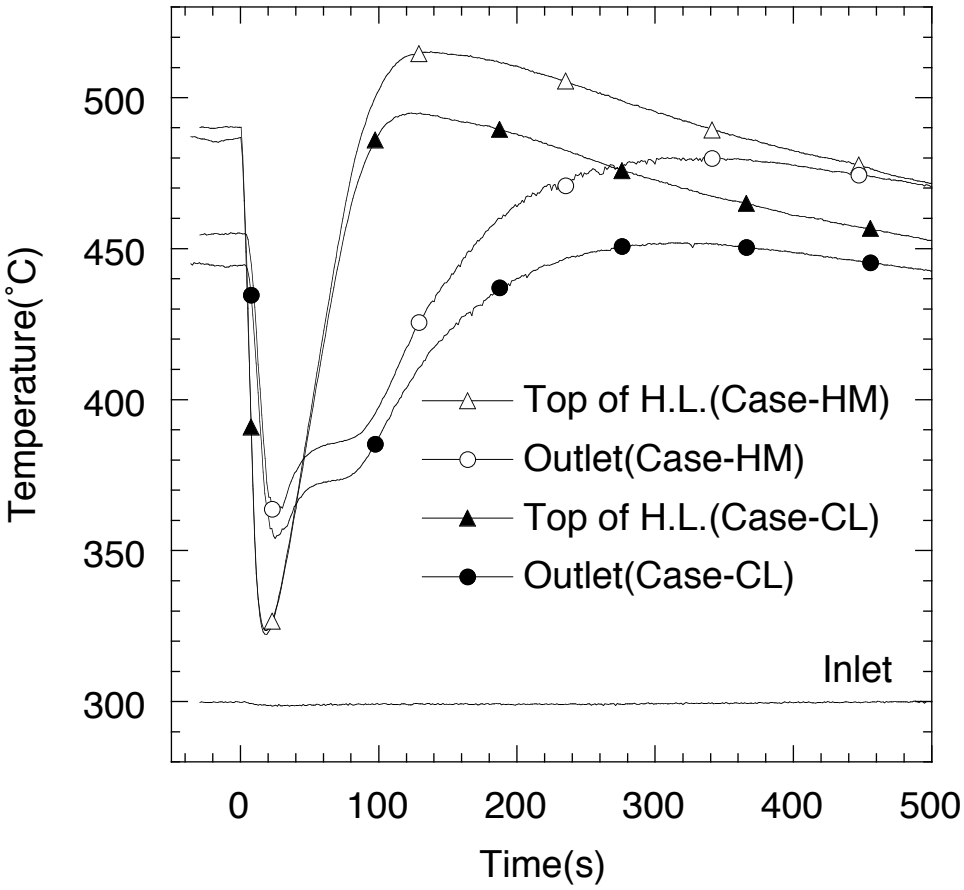

Case-HM: Homogeneous Temperature Condition
Outlet temperatures of all subassemblies are the same under initial forced flow condition.
Case-CL: Cooled Condition
Outlet temperature at the center subassemblies is higher by 30˚C than those at other 6 subassemblies under initial condition.

Fig. 2.3-4 Temperature Histories in Center Subassembly in Case-HM and Case-CL

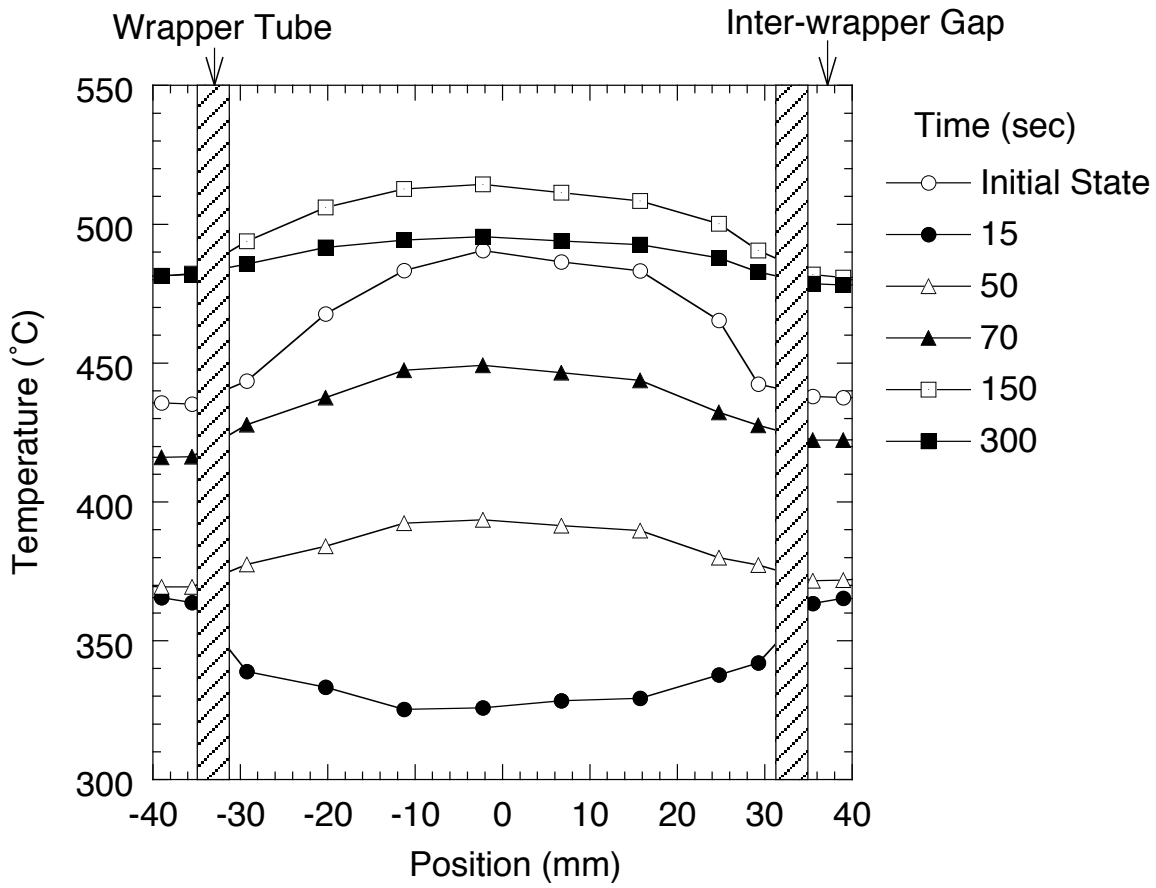

Fig. 2.3-5 Transverse Temperature Distributions at Top of Heated Length in Center Subassembly in Case-HM

Figure 2.3-6 shows the time histories of the peaking factor, i.e., non-dimensional center subchannel temperature in Case-HM and Case-CL. The peaking factors under the initial conditions were approximately 1.2 in Case-HM and Case-CL. A steep decrease and recovery of the peaking factor was registered just after power shutdown. This decrease was caused by the fact that the peripheral subchannels in the center subassembly received heat from the wrapper tubes and the sodium in the inter-wrapper gap remained at higher temperatures and, therefore, the center subchannel temperatures became lower than the average, as shown in Fig. 2.3-5 (at 15s). Except for this steep dip, the peaking factor decreased steadily from 1.2 to 1.05 during transitions. When the highest temperature was recorded in Case-HM, the peaking factor was nearly 1.08. It was clearly indicated from these results that the reduction of the peaking factor was significant in the evaluation of the highest temperature.

The correlation between the peaking factor and the buoyancy parameter, Gr*/Re, is shown in Fig. 2.3-7. The solid and dotted lines are the linear least squares fit and the 95% confidence band of the peaking factor obtained from the steady state experiments (see Fig. 2.2-13), respectively. The peaking factors during transitions decreased along the least squares fitted line except for the early phase (within 40s). In other words, this linear correlation of P_f versus Gr*/Re can be applied to the estimation of P_f during transient.

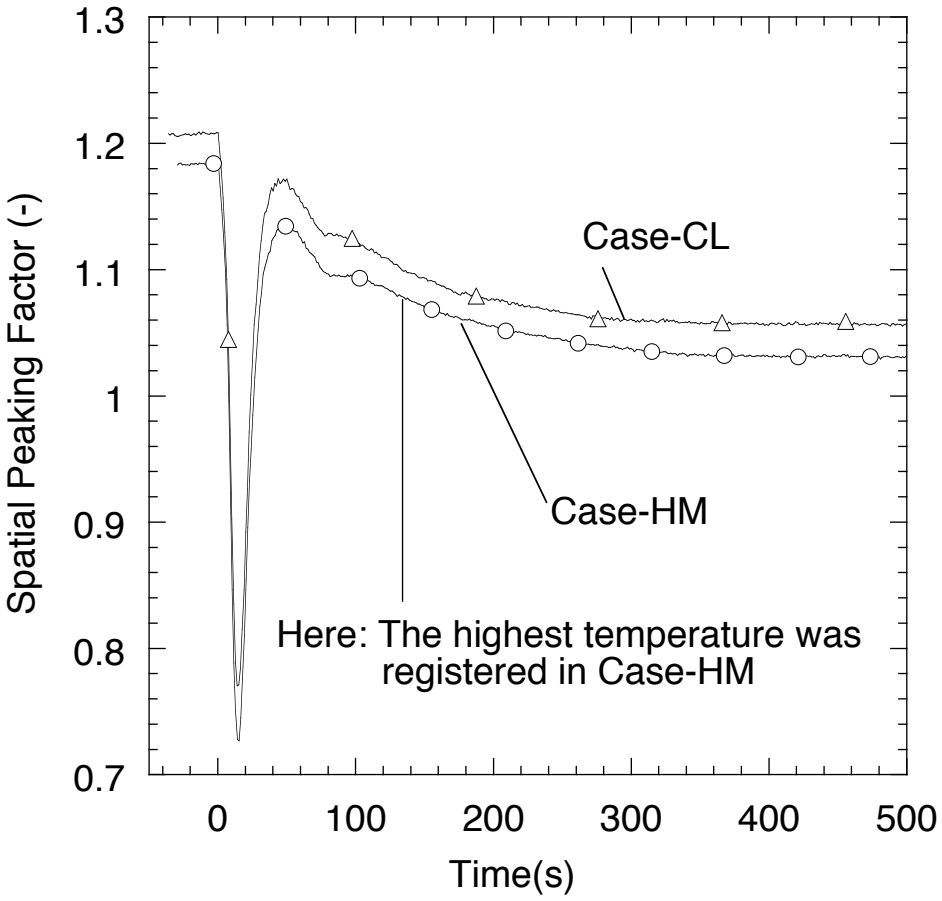

Fig. 2.3-6 Time Histories of Spatial Peaking Factor
in Case-HM and Case-CL

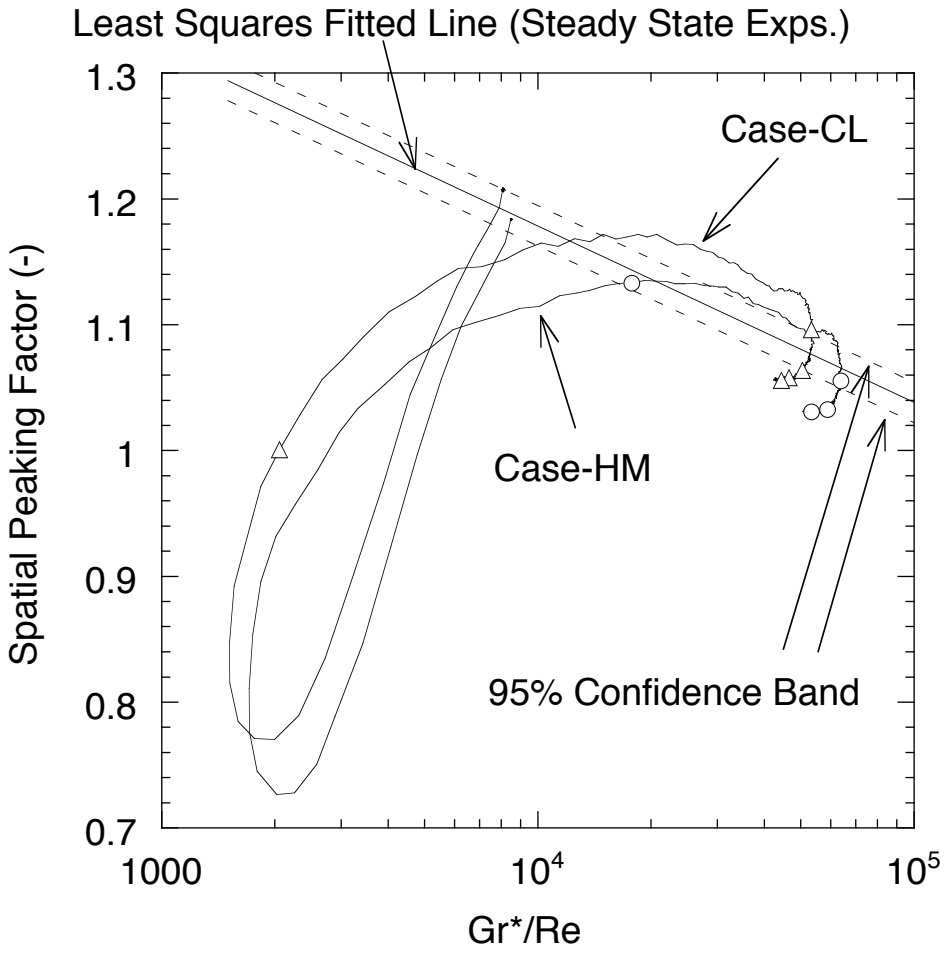

Fig. 2.3-7 Spatial Peaking Factors versus Buoyancy Parameter, Gr*/Re, in Transitions

2.3.4 Summary of Transient Experiment

Influences of the intra-subassembly flow redistribution and the inter-subassembly heat transfer on the second peak temperature during a scram transient were investigated in the transient experiments using the 37-pin core fuel subassembly model surrounded by six subassemblies. The following findings were obtained:

- The peaking factor decreased from 1.2 to 1.05 during the transitions from the 12% velocity condition to 2% of the full power condition in a core fuel subassembly. When the highest temperature was recorded, the peaking factor was nearly 1.08.
- The inter-subassembly heat transfer had significant effect on the reduction of the hottest temperature in a subassembly during the transition including the second peak.
- The peaking factor correlation obtained from the steady state experiments could be applied to the estimation of the transient behavior.

2.4 Multi-Dimensional Analyses of Inter-Subassembly Heat Transfer

2.4.1 Simulation Method

The three-dimensional thermohydraulic analysis code, AQUA (Maekawa, 1995), was applied to the analyses of the multi-subassembly experiment in a porous-body approach. The AQUA code is based on a finite difference method in Cartesian coordinates or cylindrical coordinates. Numerical methods of the code are listed in Table 2.4-1. The main purposes of the experimental analyses were to establish an extrapolation method from the experiments to the actual reactors and to obtain information about velocity fields in the subassemblies. The multi-region model incorporated in the AQUA code was applied to simulate the three-subassembly model. The 61-pin bundle and the adjacent 19-pin bundle were modeled in individual two-mesh schemes. The mesh arrangements are shown in Fig. 2.4-1. Half of the three-subassembly model was modeled because of a symmetry assumption where two 19-pin subassemblies were operated under the same conditions. The staggered half-pin mesh arrangement proposed by Ro and Todreas (1988) was applied to the 61-pin bundle and the 19-pin bundle. In this mesh arrangement, each subchannel in a subassembly can be represented by one control volume in calculations. The heat transfer through the wall between the pin bundles was simulated by thermal structure model connecting the two-mesh regions. The correlations of axial flow resistance were set separately at wall, corner, and internal subchannels based on the study by Cheng and Todreas (1986). The axial permeability was also set separately at each subchannel. The permeabilities in the horizontal (x and y) directions were set based on the real flow area at the mesh boundaries. The boundary conditions of the analyses were the heater pin power, the flow rates, and the inlet temperatures in each subassembly and in the cooling channel.

Table 2.4-1 Numerical Methods of AQUA Code

Numerical Scheme	Finite Difference Method
Coordinates	Cartesian* Cylindrical
Convection Terms	1st order upwind* QUICK+FRAM
Turbulence Model	Laminar (No turbulence model)* k-ε
Complicated Geometry	Porous Body Model* Multi-region Model*

* These options were selected in this study

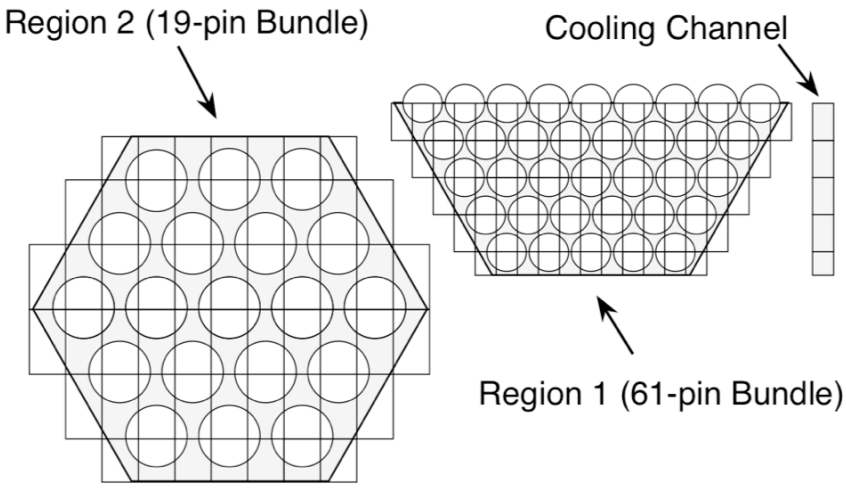

Fig. 2.4-1 Mesh Arrangement for Three-Subassembly Model

2.4.2 Calculated Results

As examples of the experimental analyses, the transverse temperature distributions at the end of the heated length are shown in Fig. 2.4-2 for Cases CW and CS in Fig. 2.2-8, where the 61-pin bundle was cooled through both walls. The experimental conditions are listed in Table 2.4-2. The character "C" of the case names indicates that the 61-pin subassembly is cooled and the character "H" indicates that it is heated. The character "W" means that the 61-pin subassembly is weakly cooled or heated and the character "S" that it is strongly cooled or heated. The calculations accurately predicted the increase of sharpness of the temperature distribution in the 61-pin bundle due to the cooling through the walls. The temperature distributions are shown in Fig. 2.4-3 for Cases HW and HS under the simultaneously heated and cooled conditions. The local increase of temperature near the heated wall (left side) in the 61-pin bundle was accurately predicted by the calculations.

The relation between the wall subchannel factor, W_f, and the wall heat flux ratio, $q''_{w/p}$, is compared between experiments and calculations in Fig. 2.4-4. The calculations could accurately predict the experimental results, especially the steep fall of W_f at negative large $q''_{w/p}$. The peaking factor, P_f, was also accurately predicted, as shown in Fig. 2.4-5. Figure 2.4-6 shows the calculated flow velocity fields in Cases CS and CW. Development of the intra-subassembly flow redistribution due to the buoyancy force is clearly seen in the figure. In the lower non-heated pin bundle, velocity near the wall is larger than in the central subchannels due to lower flow resistance coefficient at the wall subchannel. However, the transverse velocity profile shows convex shape due to the flow redistribution accompanied by the buoyancy force at the middle height of heated bundle and the velocity near the wall is much lower than at the center subchannel. Negative velocities were seen at the upper left side of the heated bundle in Case CS and the magnitudes of the downward velocities were much larger than those in Case CW.

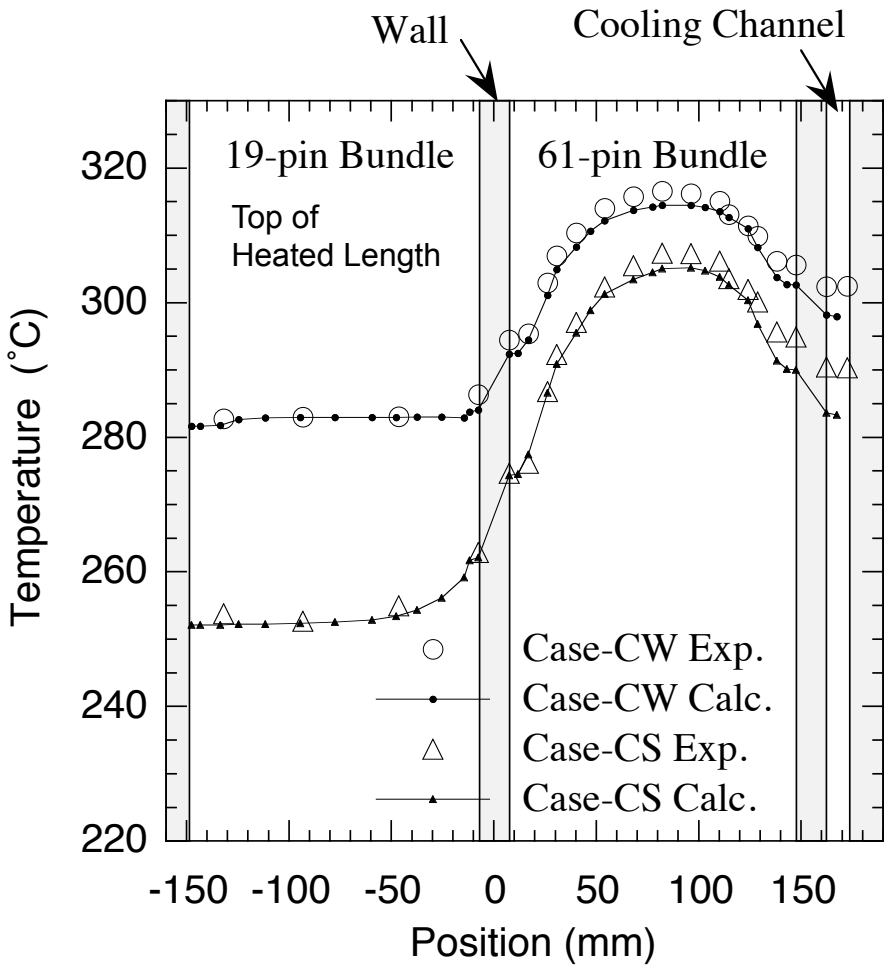

Fig. 2.4-2 Comparison of Temperature Distributions between Experiments and Calculations under Cooled Conditions at Both Walls

Table 2.4-2 Experimental Conditions of Three-Subassembly Experiment

	Case-CW	Case-CS	Case-HW	Case-HS
Flow Rate	10.3 l/min*	10.4	10.3	10.3
Heater Power in 61-pin Bundle	14.5 kW	14.5	14.5	14.5
Flow Rate	13.1 l/min	13.2	13.1	13.1
Heater Power in 19-pin Bundles	6.9 kW	0.0	33.5	40.2
Flow Rate in Cooling Channel	0.9 l/min	1.7	1.0	1.7
Inlet Temperature	247 ˚C	248	247	249

C: Cooled condition for the 61-pin bundle
H: Heated condition
W: Weakly cooled or heated condition
S: Strongly cooled or heated condition

*: Re Number in 61-pin bundle = ~ 460

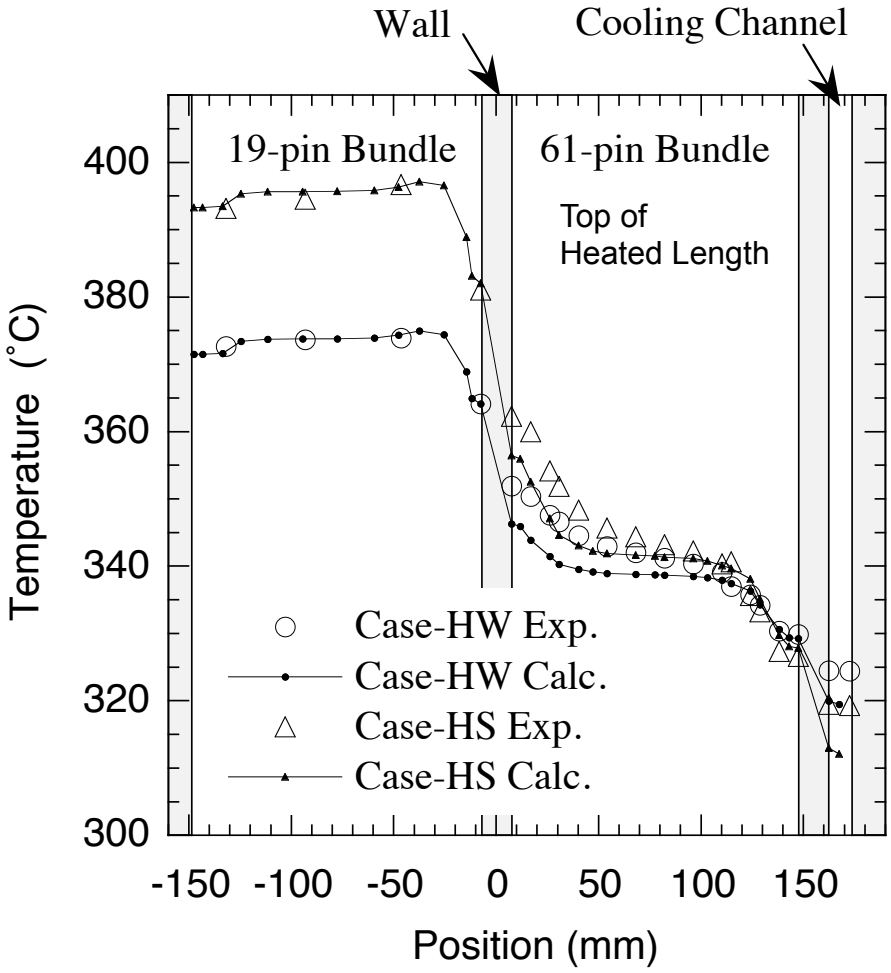

Fig. 2.4-3 Comparison of Temperature Distributions between Experiments and Calculations under Simultaneously Heated and Cooled Conditions

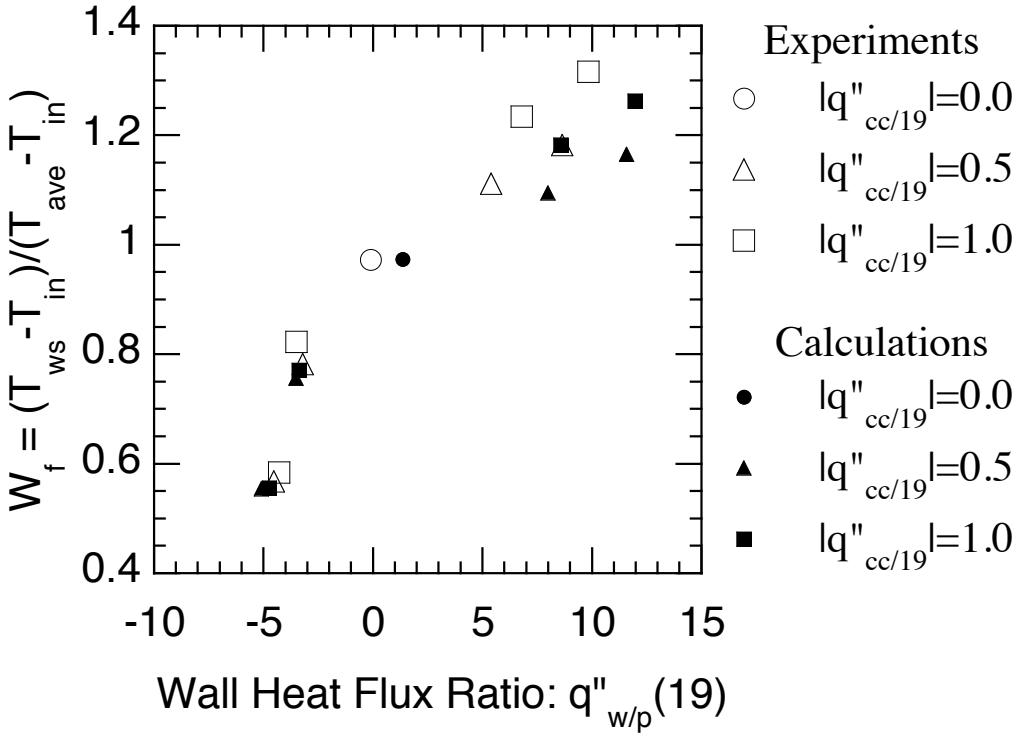

Fig. 2.4-4 Comparison of Wall Subchannel Factor (W_f) between Experiments and Calculations

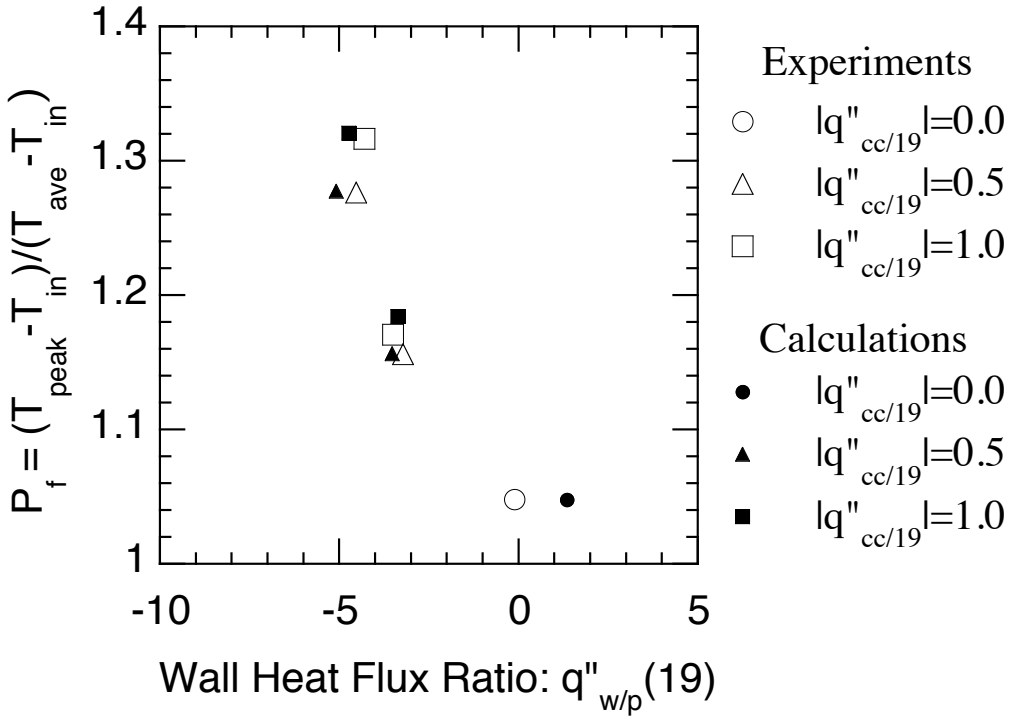

Fig. 2.4-5 Comparison of Peaking Factor (P_f) between Experiments and Calculations

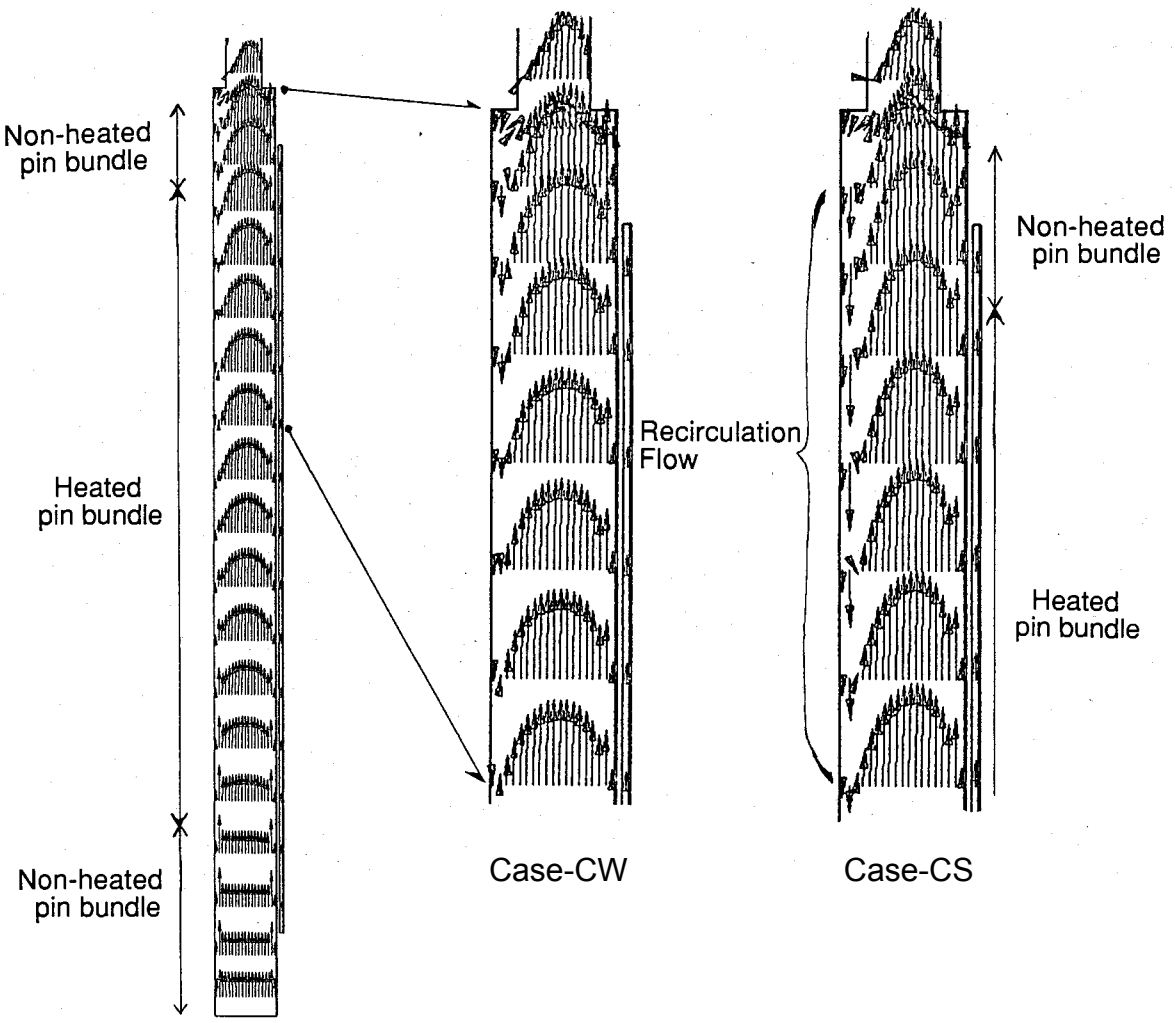

Fig. 2.4-6 Calculated Velocity Fields in 61-pin Subassembly

This strong recirculation flow results from the extreme intra-subassembly flow redistribution influenced by cooling through the wall. The asymmetric and lower temperatures in the 61-pin bundle near the 19-pin side wall (see Fig. 2.4-2) are developed by the heat flux toward the 19-pin bundle and also these recirculation flows.

The characteristics of the transverse temperature distribution in the 61-pin bundle was accurately estimated by the calculations using the staggered half pin mesh arrangement under varied conditions of inter-subassembly heat transfer, including recirculation flow in the subassembly. The characteristics of P_f and W_f in actual reactor pin bundles, for example, the 271-pin core fuel subassembly and the 91-pin blanket fuel subassembly, are intended to be predicted by this method.

2.4.3 Summary of Multi-Dimensional Analyses

The three-dimensional thermohydraulics code, AQUA, was applied to the experimental analyses of the three-subassembly model tests. The multi-region model and the staggered half pin mesh arrangement were used. The correlations of axial flow resistance developed for subchannel analysis codes were applied in the wall subchannel region and the inner subchannel region separately.

The AQUA code could accurately simulate the transverse temperature distributions in the multi-subassembly system, including P_f and W_f under mixed convection conditions influenced by inter-subassembly heat transfer. The intra-subassembly flow redistribution caused by buoyancy force was clearly calculated from the lower non-heated part to the heated end, especially local reverse flow near the wrapper tube wall cooled by the adjacent subassembly. These facts showed that the applied modeling of the staggered half pin mesh arrangement and the axial flow resistance coefficients at the wall subchannel and the inner subchannel regions was adequate for the simulation of subassembly thermal hydraulics under natural circulation conditions.

2.5 Conclusions

The subassembly thermal hydraulics were investigated by the three-subassembly model and the seven-subassembly model using sodium as a working fluid. The experiments focused on flow redistribution and inter-subassembly heat transfer under NC/DHR conditions including transient from forced to natural circulation. The three-subassembly model simulated a blanket fuel subassembly of 61-pin bundle in real dimensions and also the boundary between the blanket fuel subassemblies and the core fuel subassemblies. The seven-subassembly model simulated the core fuel subassembly of 37-pin bundle as a partial model under the steady state conditions and the scram transient conditions.

The peaking factor (P_f), normalized highest temperature at a cross section, was obtained in the steady state experiments where the flow rate, the heater pin power, and the temperature difference between the subassemblies were varied.

Radial heat transfer between subassemblies was coupled with intra-subassembly thermohydraulics, especially with wall subchannel temperatures. Thus, it is of importance to know the behavior of the wall subhcannel temperature. The wall subchannel factor (W_f) was defined to estimate the wall subchannel temperature from the average cross section temperature by using the analogy of the peaking factor (P_f). Characteristics of intra-subassembly thermal hydraulics were grasped under mixed convection conditions as follows:

1) Influence of intra-subassembly flow redistribution
   - The transverse temperature distribution was flattened by intra-subassembly flow redistribution, even if inter-subassembly heat transfer occurred.
   - The influences on P_f and W_f correlated well by a modified buoyancy parameter, Gr*/Re, in the blanket and also core fuel pin bundles. The obtained correlation with Gr*/Re was independent of the axial position in the subassembly.

2) Influence of inter-subassembly heat transfer

- The inter-subassembly heat transfer reduced the highest temperature, even in a full size pin bundle of the blanket core fuel subassembly.
- Influence of inter-subassembly heat transfer on W_f and P_f correlated well using the wall heat flux ratio ($q"_{w/p}$).
- Under the conditions of a large negative $q"_{w/p}$ and high Gr*/Re, W_f decreased extremely.

The transient phenomena were investigated using the 37-pin core fuel subassembly model surrounded by six subassemblies. The influences of buoyancy force on the second peak were examined. The following findings were obtained:

- The temperature flattening effect of the intra-flow redistribution was observed obviously in the transient experiments. The peaking factor decreased from 1.2 to 1.05 during the transitions from the 12% velocity condition to 2% of the full power condition in a core fuel subassembly. The peaking factor was nearly 1.08 at the second peak during the scram transition.
- The inter-subassembly heat transfer had significant effect on the reduction of the hottest temperature in a subassembly during the transition including the second peak.
- The peaking factor correlation using Gr*/Re obtained from the steady state experiments could be applied to the estimation of the transient behavior.

The three-dimensional calculation method was applied to the experimental analyses of the three-subassembly model tests. The multi-region model and the staggered half pin mesh arrangement were used. The correlations of axial flow resistance developed for subchannel analysis codes were applied in the wall subchannel region and the inner subchannel region separately.

The applied method could accurately simulate the transverse temperature distributions in the multi-subassembly system, including P_f and W_f under mixed convection conditions influenced by inter-subassembly heat transfer. The intra-subassembly flow redistribution caused by buoyancy force was clearly calculated from the lower non-heated part to the heated end, especially local reverse flow near the wrapper tube wall cooled by the adjacent subassembly.

These facts showed that the modeling of the staggered half pin mesh arrangement and the axial flow resistance coefficients at the wall subchannel and the inner subchannel regions was adequate for the simulation of subassembly thermal hydraulics under natural circulation conditions.

Nomenclature

d_{wall}: Thickness of wrapper tube wall,

D : Hydraulic equivalent diameter of pin bundle,

g : Gravitational acceleration,

Gr : Grashof number,

L : Height from the bottom of the heated region,

Pe: Peclet number,

P_f: Peaking factor,

$q''_{cc/19}$ Ratio of heat flux values on the wall beside the 19-pin bundle and on the wall adjacent to the cooling channel,

q''_{pin} Heat flux on heater pin surface,

$q''_{w/p}$: Ratio of the heat flux on wall (wrapper tube) to on pin surface,

Re : Reynolds number,

T*: Normalized temperature,

T_{ave} : Average temperature in a horizontal cross section of a subassembly,

T_{in}: Inlet temperature,

T_{peak}: Peak temperature in the subassembly,

T_{ws}: Wall subchannel temperature,

V : Subassembly average axial flow velocity,

P_f : Peaking factor,

W_f : Wall subchannel factor,

Greek letters

β : Volumetric expansion coefficient of sodium,

ΔT : $T_{ave} - T_{in}$,

ν : Kinematic viscosity of sodium,

λ: Heat conductivity,

Subscripts

(19): Side toward the 19-pin bundles,

(cc): Side toward the cooling channel,

sus: Stainless steel,

gap: Inter-wrapper gap.

Chapter 3. Penetration Flow into Low Power Subassemblies

Chapter 3. Penetration Flow into Low Power Subassemblies

3.1 Introduction

When the DRACS is operated during natural circulation decay heat removal, cold sodium is provided to an upper plenum of the reactor vessel by the dipped heat exchanger. The cold sodium will be stratified in a lower part of the upper plenum. At the core outlet, the hot fluid from the core mixes with the cold sodium and moderate temperature fluid fills the upper part of the plenum and flows out through the plenum outlets.

The cold sodium stratified in the bottom of the upper plenum covers the top of the core, especially the peripheral regions, e.g., blanket subassemblies and radial neutron shielding assemblies. In such low-power subassemblies, upward flow velocity is lower than in the core fuel subassemblies under natural circulation conditions. This low flow velocity may result in a partial backflow from the upper plenum, where the cold sodium exists. Consequently, the cold sodium in the upper plenum bottom can penetrate into the low power subassemblies due to the buoyancy force. The cold penetration flow mixes with the hot upward flow in the subassembly, causing the temperature difference between the downward flow and the upward flow to decrease, after which the penetration flow turns upward. In such cases, the upward flow area is decreased in the region of the partial backflow and the pressure loss coefficient will increase, resulting in a further reduction of the upward flow velocity.

Such phenomena were observed in water experiments (Satoh, 1989 and Ieda, 1991) simulating the scram transients of a loop-type and a pool-type reactor and were investigated using centrally heated annular channels connected to a cold upper plenum (Barakat, 1989). Several prediction models were deduced from the water experiments.

Here, a simple water experiment was carried out on the buoyancy driven phenomena in order to develop and verify a multi-dimensional analysis method (Kamide, 1996). In the experiment, the reactor core, the upper plenum, and the dipped heat exchanger were modeled in a simple apparatus. The cold fluid penetration into the simulated core was

observed under certain conditions. A number of parameter experiments were carried out to determine the onset condition of this penetration flow. Four cases were selected among these parameter experiments for use in code verification.

According to the penetration flow phenomena observed in the water experiment a sodium experiment was carried out in order to obtain the onset condition of the penetration (Kamide, 2009). A subassembly model with an upper plenum was applied to the sodium experiment. The cold penetration flow was detected by the thermocouples at the neutron shielding above the pin bundle. The onset condition map and criteria of the penetration flow were obtained by the sodium experiments.

3.2 Water Experiment on Buoyancy Driven Penetration flow

(1) Experimental Setup

The experimental model, named COPIES, was composed of an abstract of the upper neutron shielding part of a reactor core and an upper plenum. Figure 3.2-1 shows the test section, which is a slab geometry model 150 mm in depth with water as the working fluid. In the experimental model, the upper neutron shield of a fuel subassembly was represented by a simple rectangular inlet channel, and a hot plenum and a dipped heat exchanger were represented by the plenum and the cold wall. The ceiling of the plenum section was inclined intentionally to check for adequate boundary treatment in the computational procedure.

Hot fluid was supplied to the plenum from the inlet channel and allowed to flow through the plenum toward the outlet. The flow rate and the inlet temperature were kept constant. The lower part of the inlet channel had a flow straightener 500 mm in length. The velocity distribution was found to be nearly uniform at the outlet of the flow straightener. Velocity distribution developed in a 1500 mm long plain rectangular channel situated after the flow straightener.

A cooling box was attached to the cold wall of the plenum test section. The cold wall was made of a copper plate 5 mm thick. Cold water of the secondary loop flowed upward in the cooling box; the flow rate and the inlet temperature were kept constant.

The Cartesian coordinates are defined in Fig. 3.2-2. The x-, y-, and z-components of velocity are v_X, v_Y, and v_Z, respectively. Gravity acts in the z-direction.

Figure 3.2-3 shows the temperature measurement points in the test section. Four vertical traverse lines were set in the plenum: P1, P2, P3, and P4. A traverse thermocouple set was installed in the inlet channel. Temperatures were measured in the x-z plane (y = 0 mm) by Copper-Constantan thermocouples measuring 1 mm in diameter. The data sampling time was 300s with a sampling interval of 0.5s. The averaged temperatures for each 300s sample were used as the measured results. The measurement accuracy was within 0.15 ˚C.

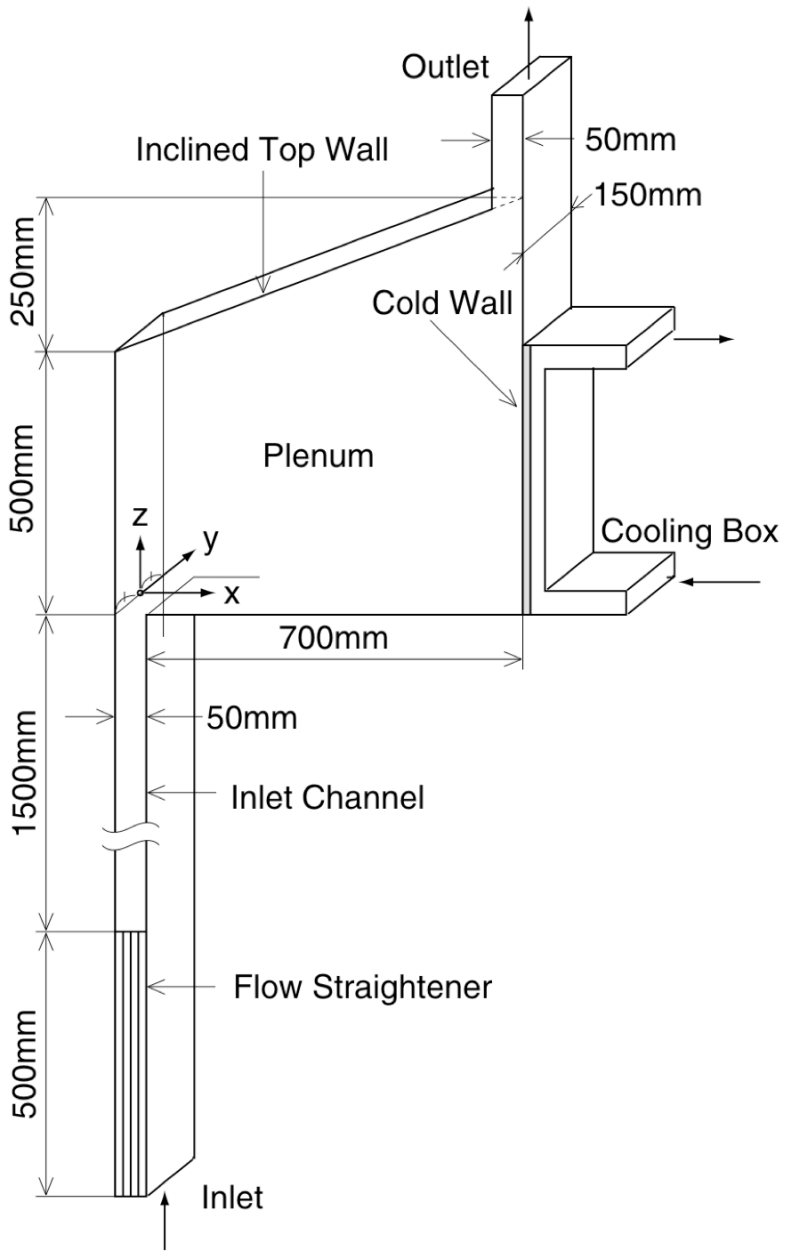

Fig. 3.2-1 Test Section of Penetration Flow Experimental Setup

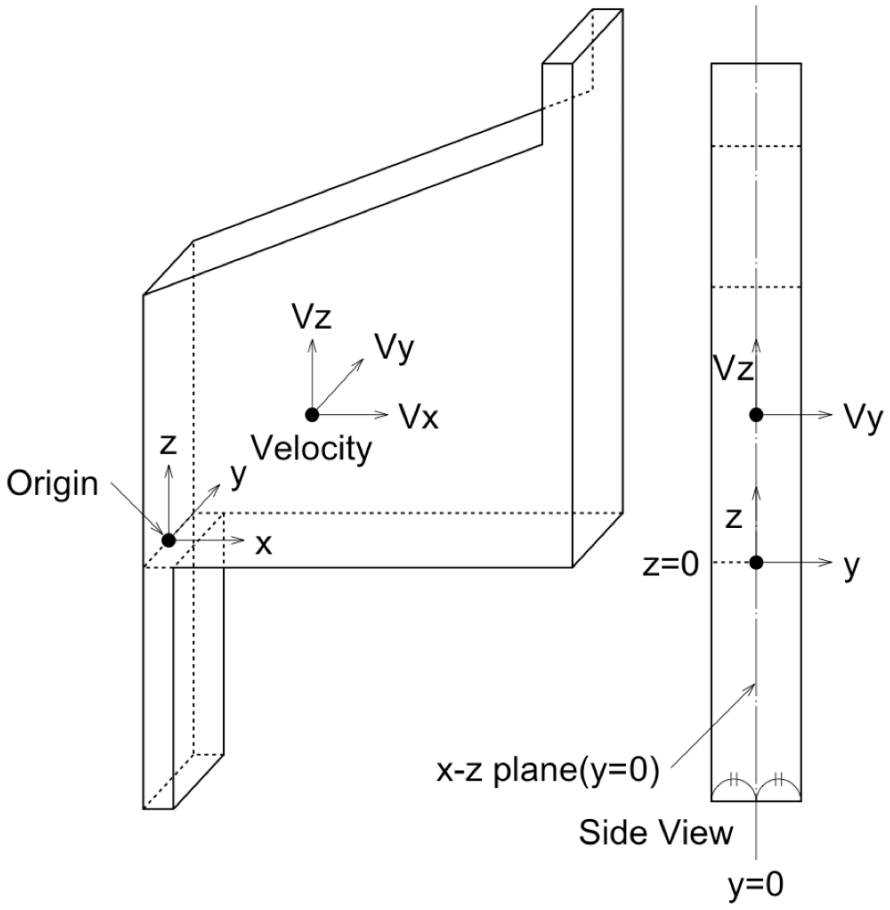

Fig. 3.2-2 Coordinates in Test Section

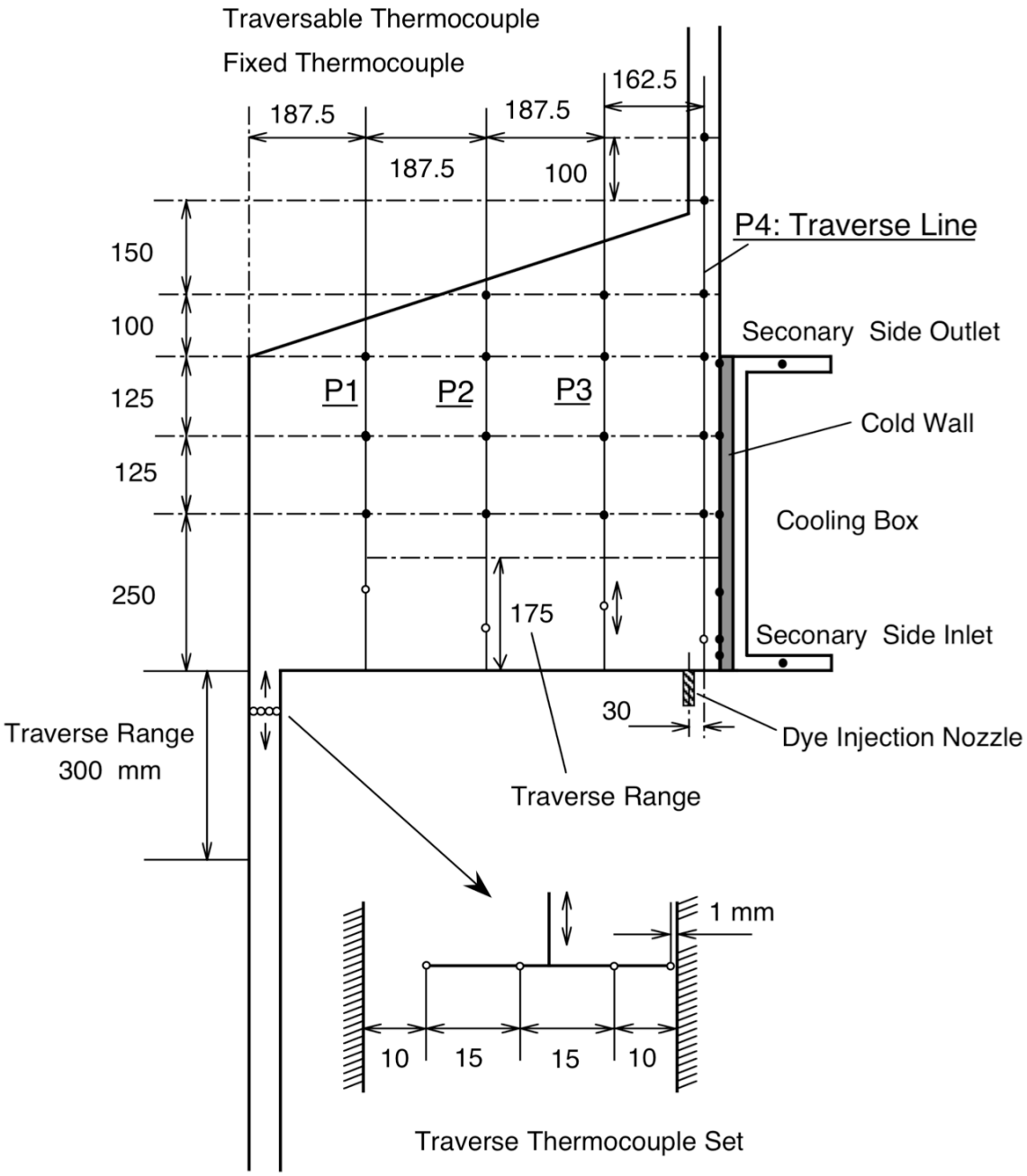

Fig. 3.2-3 Temperature Measurement Positions

The velocity distribution was measured by a probe-type two-dimensional Laser Doppler Anemometer (LDA). The probe of the LDA was set in front of the plenum and traversed by a computer controlled x-y-z traverse unit. The traverse position was accurate to within 0.2 mm. Average velocities of 500 sampled data per position were used.

(2) Experimental Parameters

It is thought that the cold penetration phenomenon into the inlet channel depends on the local temperature difference between the upward hot flow in the channel and the cold fluid in the plenum, and on the upward flow velocity in the channel. Thus, the following three parameters were varied to determine the onset and depth of the penetration flow:

- Inlet temperature of the test section: from 20 to 50 ˚C;
- Flow rate into the test section: from 13.5 to 45 l/min; and
- Inlet temperature of the cooling box: from 10 to 30 ˚C.

The Re number was determined in the inlet channel with a hydraulic equivalent diameter of 0.075m and channel averaged velocity. The Re number was varied from 2,200 (20˚C) to 13,000 (50˚C). The temperature deviations of the inlet flow into the test section and the cooling box were both within 0.2 ˚C. The deviation of the inlet flow rate of the test section was below 0.1 l/min. The heat loss from the surrounding walls was no more than 5% of the removal heat of the cooling box (the test section was insulated using a styrene foam plate measuring 5 cm in thickness).

Four test cases, Cases 1, 2, 3, and 4, were selected as the code verifications from the parameter experiments. The flow rate into the inlet channel was increased in ascending order from Case 1 to Case 4 while all other conditions were kept constant. In Case 1, penetration flow was observed. In Case 4, the forced flow into the test section was 2.5 times larger than that in Case 1 and no penetration flow was observed. The experimental conditions of Cases 1 to 4 are shown in Table 3.2-1. In the next section, the experimental results for these four cases are discussed.

Table 3.2-1 Experimental Parameters of Penetration Flow

	Case 1	Case 2	Case3	Case 4
Inlet temperature of the test section	48.9 ˚C	49.0	49.1	49.1
Flow rate into the test section	18.0 l/min	22.5	27.0	45.0
Inlet temperature of the cooling box	12.6 ˚C	11.9	12.1	13.1
Flow rate in the cooling box	25.0 l/min			

(3) Results of Plenum Thermal Hydraulics

Figure 3.2-4 shows the measured velocity fields in the plenum in the x-z plane (y = 0 mm) for Cases 1 and 4. In Case 1, a main flow path was seen along the left wall and the inclined top walls. A large clockwise recirculating flow appeared at the upper right section. A thin film (< 1 cm) downflow stream was observed along the cold wall and a thin flow toward the exit of the inlet channel along the bottom plate. This is a stratified flow from the cold wall. The flow pattern in Case 4 was almost the same as the pattern in Case 1. However, the recirculating flow region in Case 4 was shifted to the lower part of the plenum as compared with Case 1 due to the larger inertia force of recirculation flow from the inlet channel.

Vertical distributions of the x-component flow velocity (v_X) and the temperature in Case 1 are shown in Fig. 3.2-5 along the traverse line P1. The temperature profile shows a constant temperature region above 250 mm and thermal stratification below this level. A leftward flow (negative value) was observed below 150 mm (in the stratified layer).

The temperature distributions across the stratified layer indicated a point at approximately 60 mm where the temperature gradient changed from low to high. This change in the temperature gradient resulted from mixing at the stratification interface. The standard deviation of the temperatures is shown in Fig. 3.2-6 based on the data registered over the 300s sampling time along the P1 line with the temperature and velocity profiles. The temperature deviation increased above the height of the point where the gradient changed (z=60 to 80 mm), indicating that greater mixing occurred in this region. The velocity profile showed a larger gradient in this region than in the lower region. These data suggest that turbulence mixing due to shear stress would influence the velocity and temperature profiles.

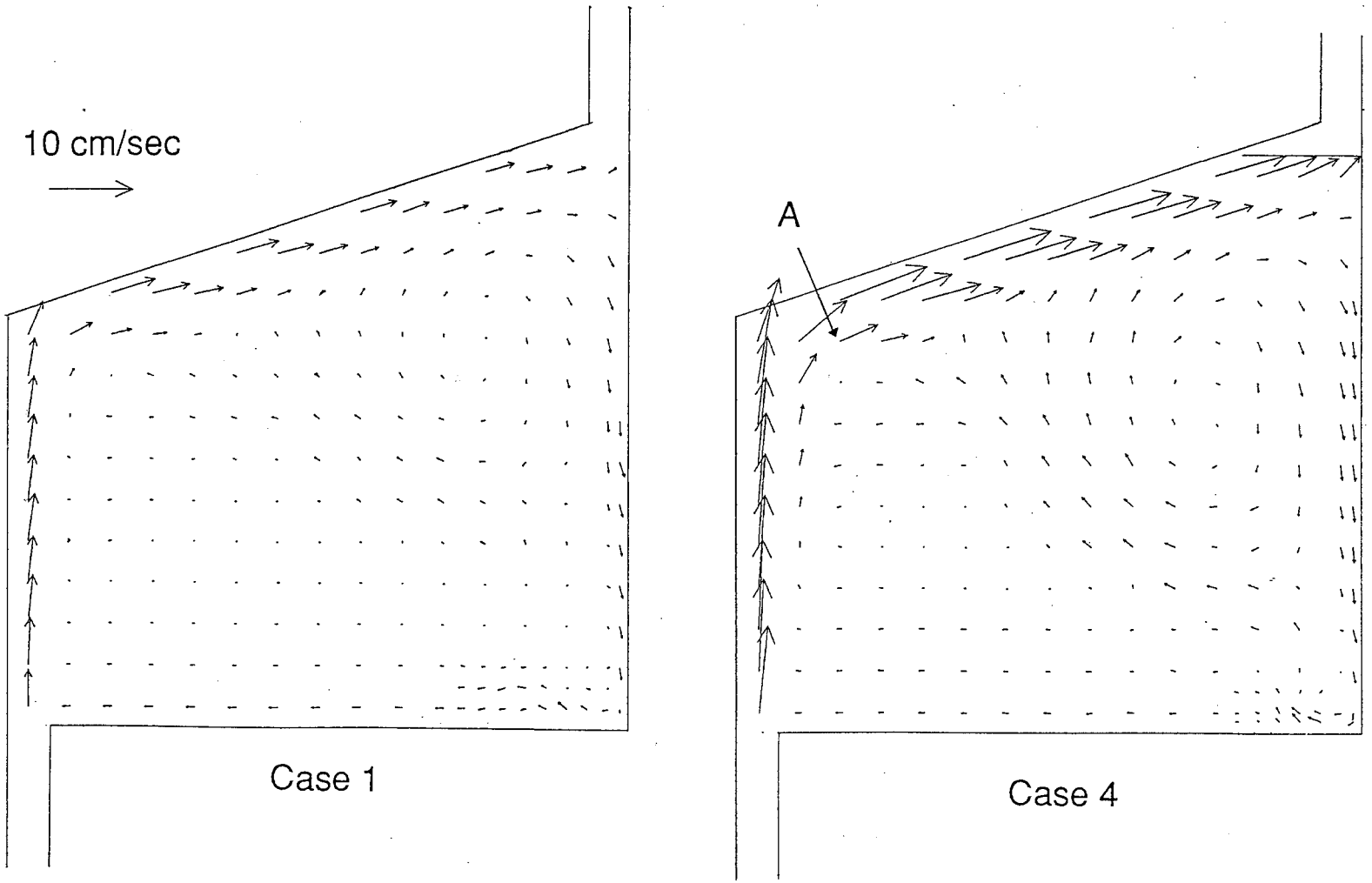

Fig. 3.2-4 Measured Velocity Fields in Cases 1 and 4

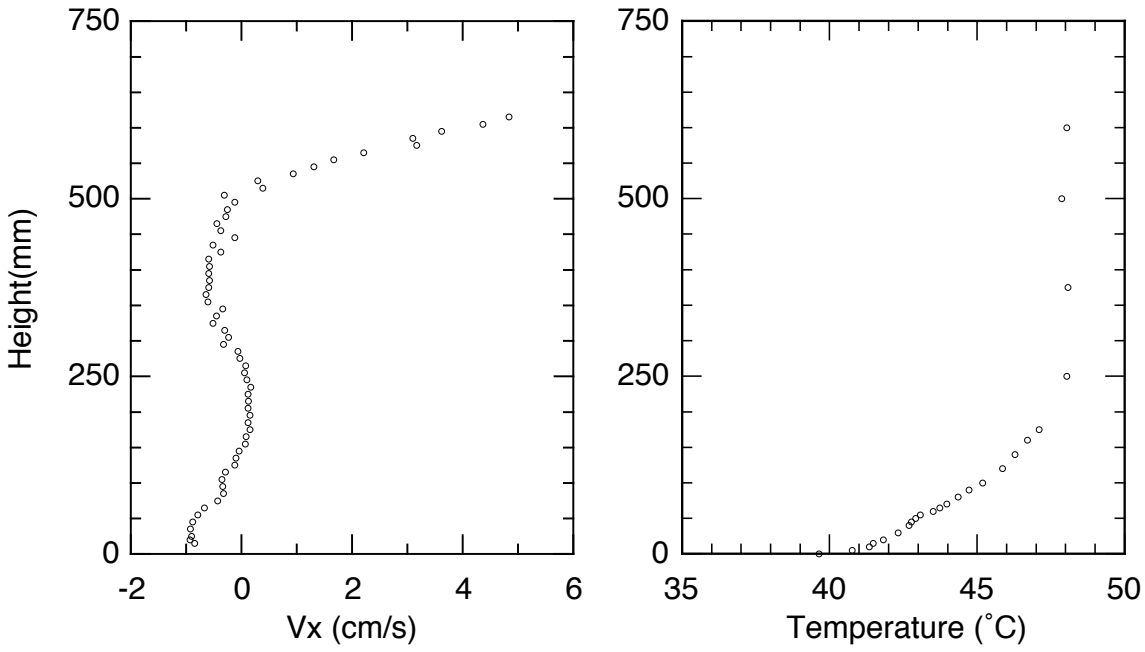

Fig. 3.2-5 Vertical Distributions of Horizontal Velocity Component and Temperature in Case 1

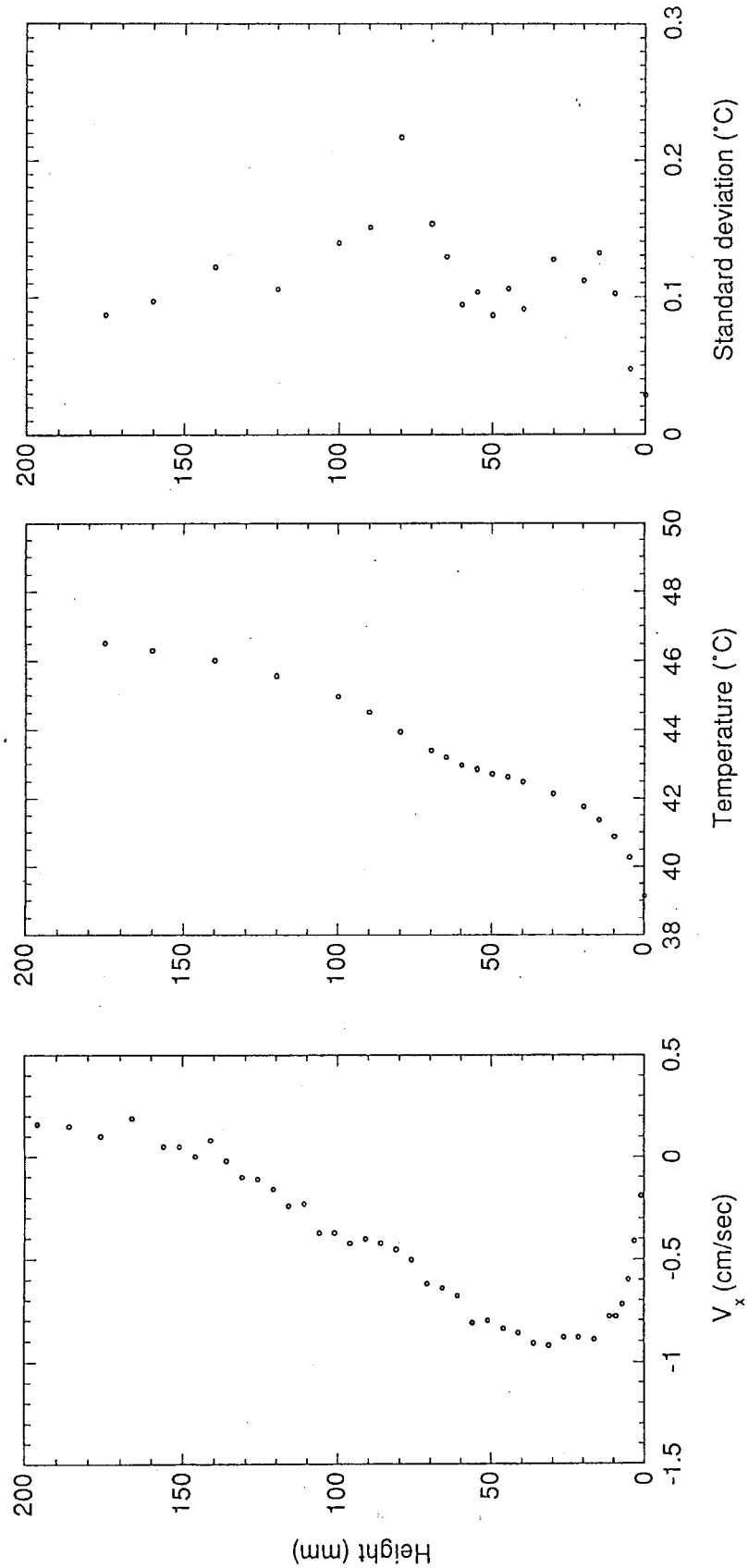

Fig. 3.2-6 Vertical Distributions of Temperature Fluctuation Intensity, Temperature and Horizontal Velocity Component along P1 line in Case 1

(4) Results of Penetration Flow

Buoyancy driven penetration flow into the inlet channel was detected in Cases 1, 2, and 3. No penetration flow was observed in Case 4. The lower flow rate in the inlet channel resulted in the penetration flow. It is easily predicted that the velocity profile in the channel is important for the penetration flow. In Fig. 3.2-7, velocity profiles (v_Z-component) in the x-direction are shown at a depth of 200 mm (z= -200 mm) for Cases 1 to 4 without any flow in the cooling box (homogeneous temperature condition). The resultant velocity profiles showed characteristics of the turbulent flow described by the logarithmic law.

The penetration flow in Case 1 was visualized by a laser light sheet and neutrally buoyant dye injection. Figure 3.2-8 illustrates the flow pattern. Photo A is a front view and B is a left-sided view. Photo A shows a typical penetration flow and photo B shows several falling flows observed along the bottom plate, indicating that the film flows tended to traverse down along the specific flow paths from the corner edge once penetration was triggered. The flow in each path was in a thin film measuring approximately 10 mm wide in the y-direction and typically a few mm thick in the x-direction. The penetration phenomena were not stable; i.e., the penetration depth varied with time from 0 cm to a few cm and back to 0 cm, and this cycle was repeated. The time period of each penetration cycle was typically a few seconds.

Penetration was detected by changes in temperature in the inlet channel using a thermocouple set (see Fig. 3.2-3). The thermocouple set could traverse in the z-direction in the x-z plane (y = 0 mm). The measured temperatures are shown in Fig. 3.2-9 for Case 1 at a depth of 10 mm (z = -10 mm). The temperature at the right end position (x = 49 mm) showed the largest fluctuations. This is consistent with the visualized flow pattern, that is, the penetration flow forming thin films along the right side wall of the inlet channel.

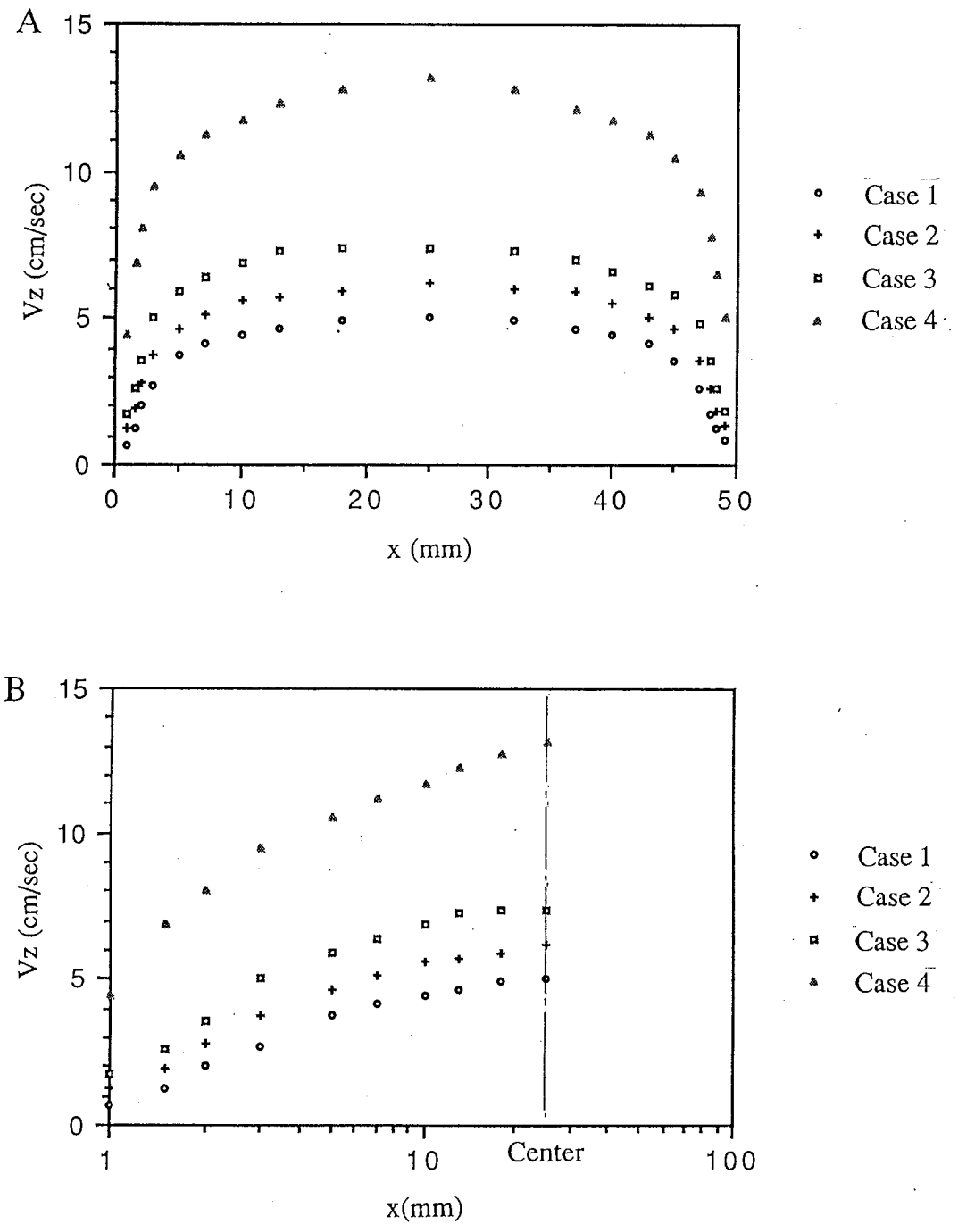

Fig. 3.2-7 Horizontal Distributions of Vertical Velocity Components in Cases 1 to 4

A

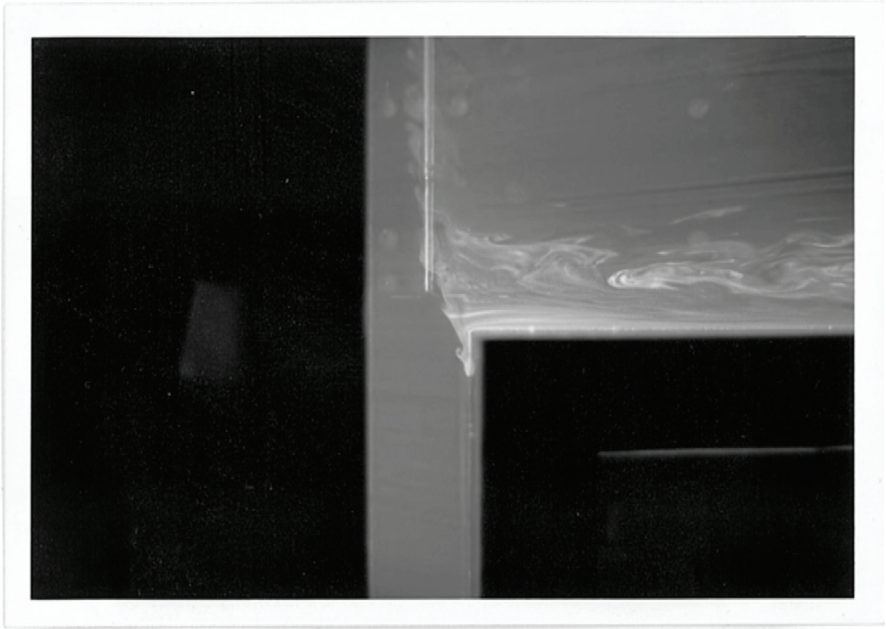

B

Fig. 3.2-8 Photos of Penetration Flow

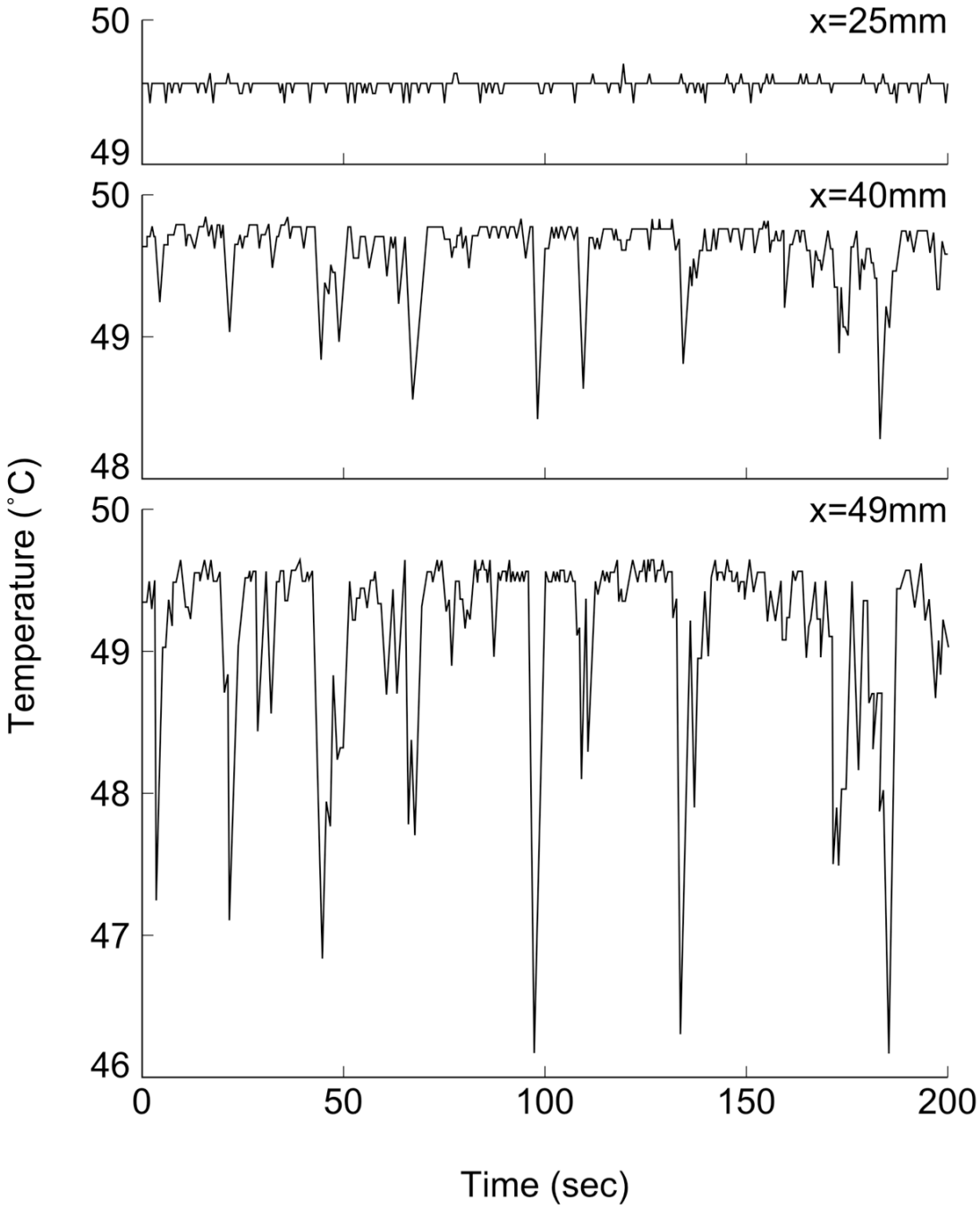

Fig. 3.2-9 Temperature Histories in Flow Channel at z= -10mm in Case 1

The frequency of penetration flow was obtained by evaluating the temperature history of the right-end thermocouple; there were steep spiked-shaped dips descending from the temperature at the channel inlet (48.9 ˚C). Each spike corresponded to one penetration flow. The obtained frequency of the penetration flow in Case 1 is shown in Fig. 3.2-10. The frequency decreased as the thermocouple was moved deeper into the inlet channel. From this figure, we defined the maximum penetration depth and the occurrence of penetration flow as follows:

> Penetration flow was considered to have occurred when the flow was detected with at least a frequency of 1/1000 cps at z= -1 cm and,
>
> maximum penetration depth is the deepest position where the penetration flow was detected with at least a frequency of 1/1000 cps.

Here the frequency of 1/1000 cps was defined as the minimum cps which could be detected (>100 counts) over a 24-hour period. Counts detected at a lower frequency were not included in the statistical analysis.

Measurements were carried out on a total of 30 cases to obtain the onset condition of the penetration flow and the maximum depth. Figure 3.2-11 shows an occurrence map of the penetration flow with respect to the Reynolds number, Re, and the Grashof number, Gr. The circles and crosses in the figure represent cases where the penetration flow did and did not occur, respectively. The definitions of Re and Gr numbers are:

$$\mathrm{Re} = \frac{v_z D}{\nu} \qquad (3\text{-}1),$$

$$Gr = \frac{g\beta\Delta T D^3}{\nu^2} \qquad (3\text{-}2).$$

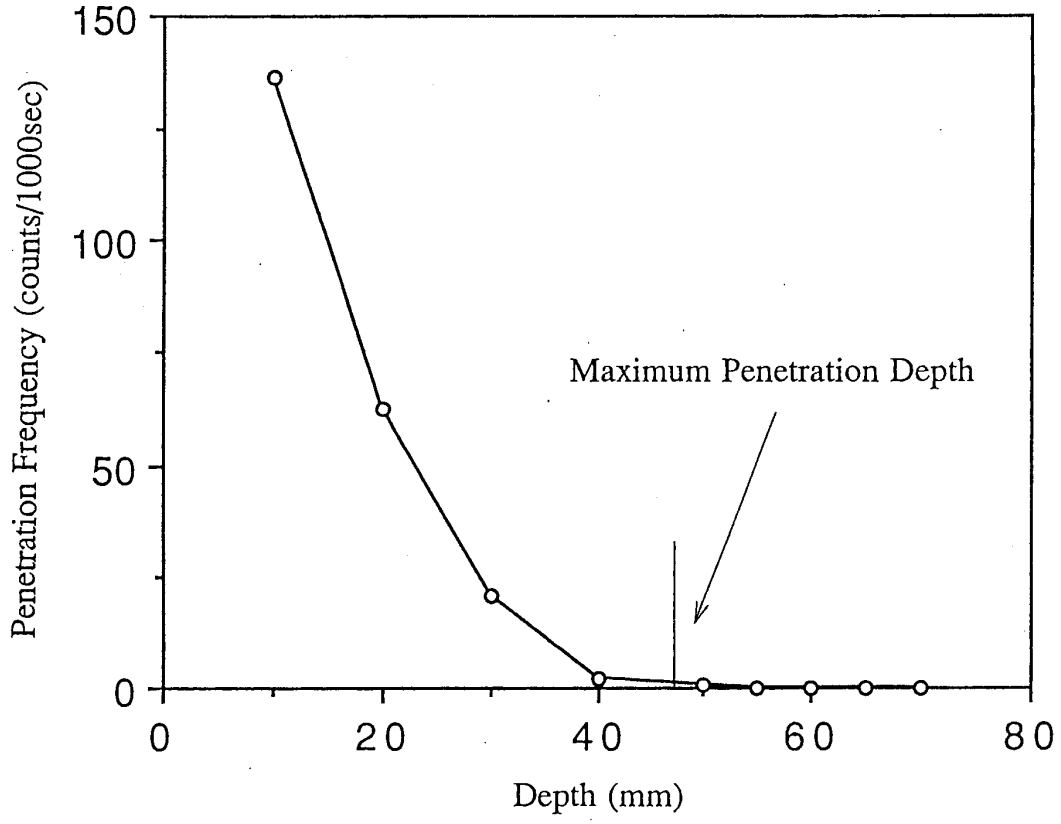

Fig. 3.2-10 Frequency of Penetration Flow and Penetration Depth

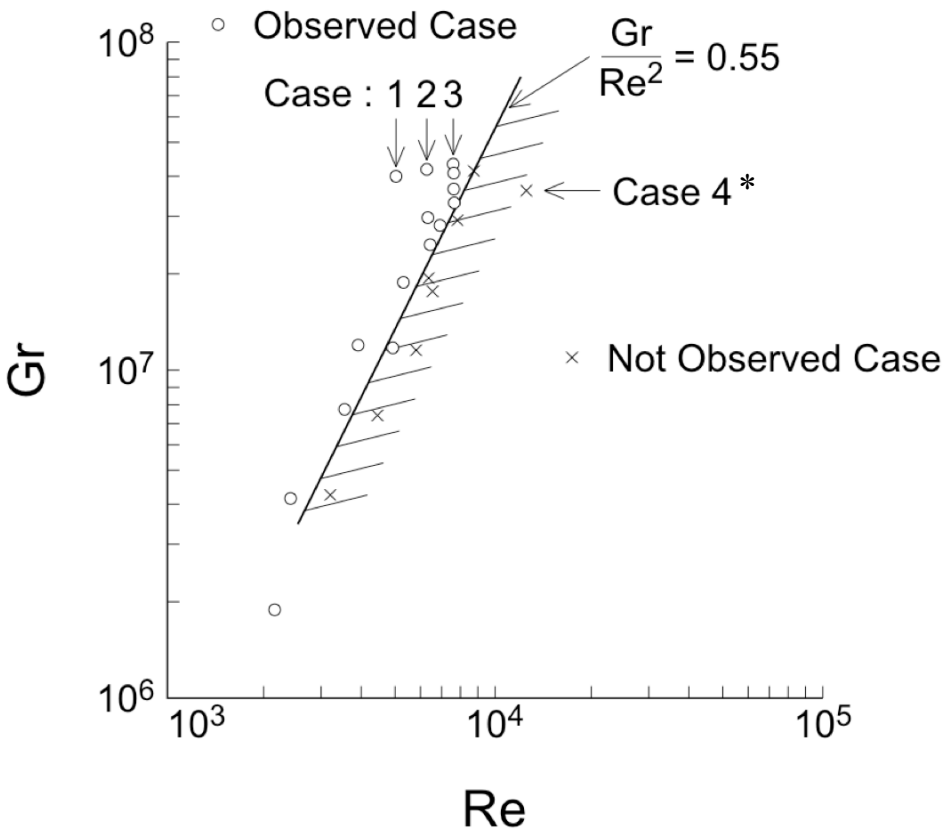

* Cases 1 to 4 were applied to experimental analyses in Section 3.3.

Fig. 3.2-11 Onset Condition Map of Penetration Flow

Figure 3.2-11 depicts the two regions separated by the straight line $Gr/Re^2 = 0.55$: Penetration flows were observed in the upper left region but not in the lower right. Thus, the onset condition of the penetration flow was a Gr/Re^2 larger than a critical value, which was constant in a turbulent flow regime in the channel ($3000 < Re < 8000$). The positions of Cases 1 to 4 are also shown in this figure.

Modi and Torrance (1987) examined the flow penetration process in a vertical duct with air both experimentally and numerically. They reported that the onset of penetration flow was represented as a Gr/Re^2 over a critical value (between 0.50 and 0.71) in a turbulent flow regime ($Re \approx 3000$). The results of our experiment using water were in good agreement with this air experiment.

Jerng and Todreas (1992) examined the penetration flow into vertical heater pin bundles below a non-heated shield section using water as a working fluid both experimentally and numerically. They reported that Gr/Re^2 was related both to onset and depth of penetration. The energy exchange between the penetrating and forced flow was identified as a key mechanism controlling the depth of penetration.

The maximum penetration depths with respect to Gr/Re^2 in the present study are shown in Fig. 3.2-12. The penetration depth increased according to the increase of buoyancy force represented by Gr/Re^2. However, some scattered data were seen. Figure 3.2-13 shows the maximum depth as the contour on the Gr/Re^2 and $1/Re$ axes. The penetration depth formed a smooth surface; when the Gr/Re^2 value remained constant, the penetration depth increased with the value of $1/Re$. This Re dependency is the result of turbulent mixing and shear flow mixing between cold penetration flow and hot upflow, and higher mixing (higher Re) remains at a shallow depth due to a decrease in the negative buoyancy force and an increase in shear stress.

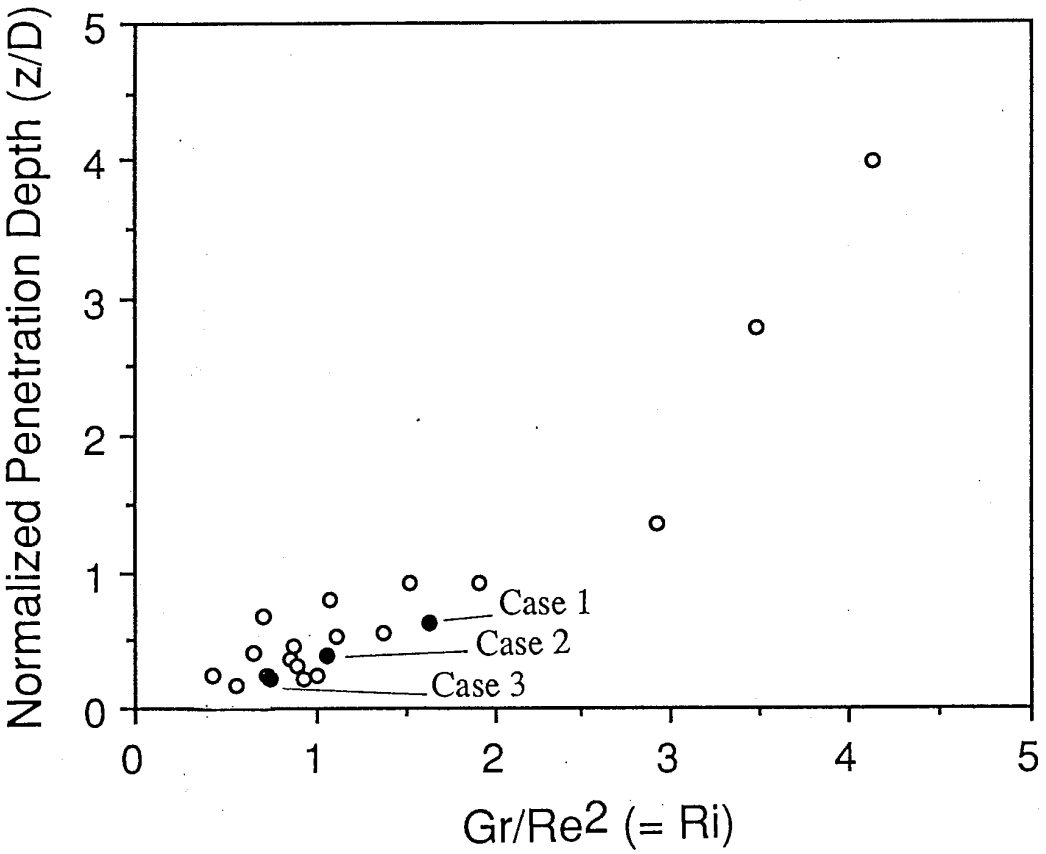

Fig. 3.2-12 Relation between Penetration Depth and Gr/Re^2

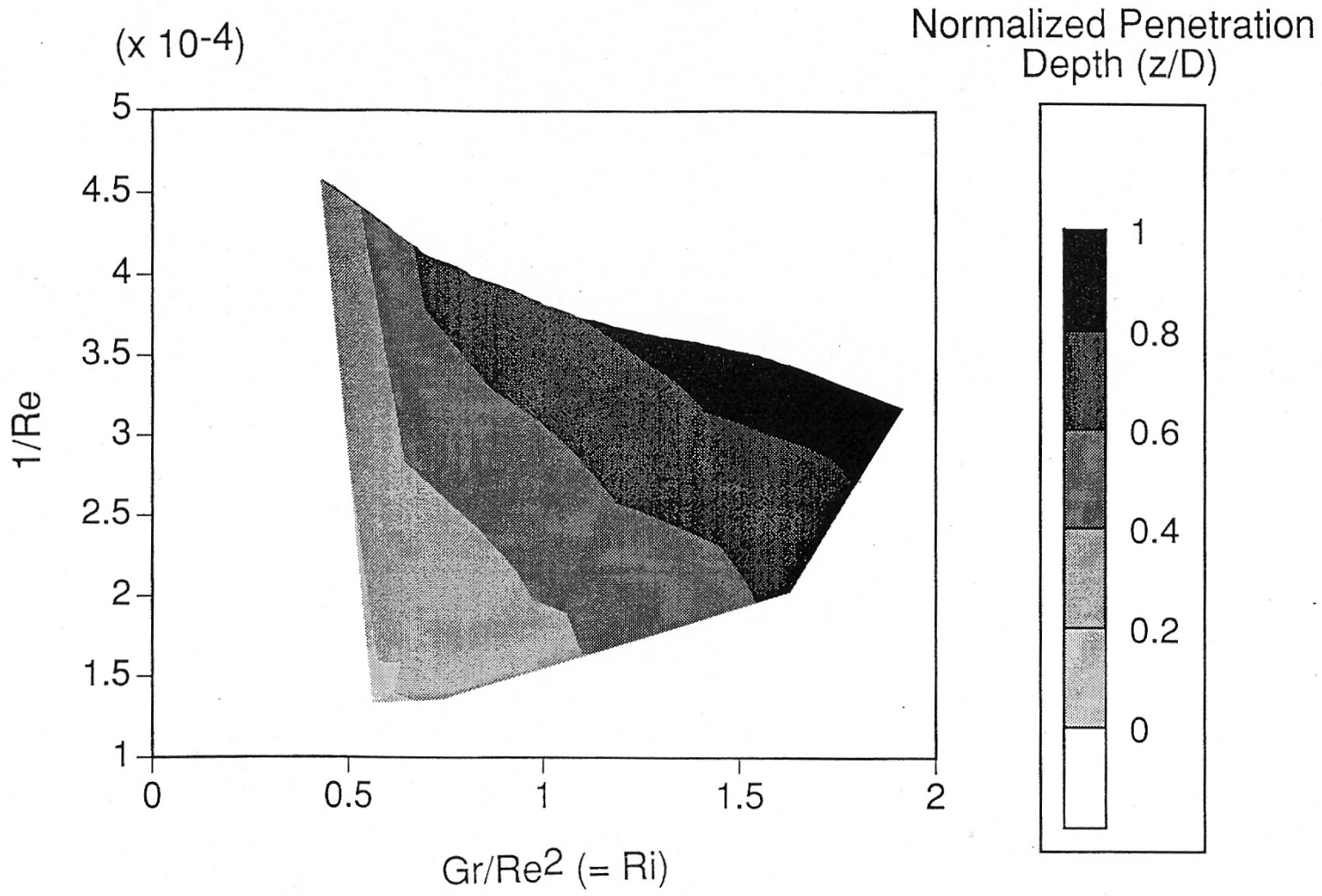

Fig. 3.2-13 Contour of Penetration Depth on axes of Ri and 1/Re

From the present study and the current literature, the onset condition of the buoyancy induced penetration flow which occurs when Gr/Re^2 exceeds a critical value applies not only to air but to water under a wide range of Re values. This means that the penetration flow occurs when the buoyancy force due to temperature difference exceeds the inertia force of upward flow. The penetration depth was correlated not only to Gr/Re^2 but also to Re.

3.3 Multi-dimensional Analysis on Penetration Flow

(1) Problem Description

The penetration flow into subassemblies from stratified cold fluid in the upper plenum is a complex phenomenon. It depends on upward flow velocity in the subassembly and temperature difference between the hot upward flow and the cold stratified fluid. Further, partial backflow is a multi-dimensional phenomenon in the flow channel. Precise predictions of the stratification in the upper plenum and counter flows in the channel together are necessary. Thus, multi-dimensional analysis has a significant role in estimating the penetration flow.

A numerical simulation was carried out to clarify applicability to thermal stratification in the plenum and buoyancy induced penetration flow into the inlet channel. Comparisons between the experiments and analyses were done with respect to the profiles of the temperature and v_x in the plenum along the P1 to P4 lines, occurrence of the penetration flow, and its maximum depth in Cases 1 to 4.

The simulation geometry was set in two dimensions. In reality, the thermal hydraulic phenomena occurring in the test section showed three-dimensional behavior if examined closely. However, only two dimensions in a limited mid-region in the y-direction were targeted. The profile of v_z in the y-direction in the inlet channel was nearly flat in the mid-region near y = 0 mm extending to a comparably broad region while the velocities near the wall decreased due to the effect of wall friction. Therefore, the effect of the wall friction on the velocity field in the mid-region of the inlet channel can be assumed to be negligible in the following discussions. In the same way, the velocity profile in the y-direction was flat in the mid-region near y = 0 mm in the plenum. The temperature distribution in the y-direction was flat both in the inlet channel and in the plenum. Therefore, we analyzed only the velocity and temperature fields on the x-z plane at y = 0 mm.

(2) Boundary Conditions

Inlet velocity profile

A uniform velocity profile at the outlet of the flow straightener was given as the inlet boundary condition and the development of the velocity profile along the inlet channel was calculated by an analysis code. The 1500 mm inlet channel should be sufficiently long to attain a nearly fully developed turbulent flow field in the channel for the experiment and for the calculation. Additionally, the measured profile of velocity component v_Z in the x-direction was provided at y = 0 mm, z = -200 mm as a control result in Fig. 3.2-7.

Inlet temperature

The temperature distribution in the inlet channel was uniform in the region where the cold penetration did not take place. Therefore, the point data were given as the inlet temperature.

Heat transfer on the surrounding walls

The heat loss to the ambiance, i.e., the difference between the heat removed from the test section and the heat removed by the cooling box, was no more than 5%. Therefore the surrounding walls, except for the cold wall, were treated as the adiabatic boundaries.

Heat transfer on the cold wall

The temperatures on the surface of the cold wall were measured and total heat removed by the cooling box was calculated based on the inlet and outlet temperatures and the flow rate in the cooling box. The heat flux through the cold wall was given as the boundary condition. The average heat flux through the cold wall was obtained as the total heat removed by the cooling box divided by the surface area of the cold wall. In this description, two-dimensional thermal hydraulic phenomena were assumed in the test section based on the temperature and velocity field in the x-z plane (y = 0 mm). It is noted that the velocities in the x-z plane are not equal to the averaged velocities because the velocity distribution in the y-direction was not accounted for. The heat removed from the cold wall, if we limit ourselves in the x-z plane and are consistent with the two-dimensional assumption, is not same as the actual average heat flux of the

cold wall. The heat flux for the boundary condition, therefore, is approximated and given by the following equation:

$$q'' = \frac{Q}{A_c}\frac{v_{av}}{W / A_{in}} \qquad (3\text{-}3).$$

Boundary conditions used in the analyses of Cases 1, 2, 3, and 4 are shown in Table 3.3-1.

(3) Methods Applied

AQUA (Maekawa, 1990), which is based on the finite difference method, was used as a multi-dimensional analysis code. Several analysis methods were applied to the experiments in order to clarify influences on the prediction of the penetration flow. One is a combination of the first-order upwind scheme and the no turbulence model (Method-DL1), the other is a combination of the QUICK and k-ε model (Method-DKQ). As for the k-ε model, the constant C_1 of the production term in the dissipation rate equation was also a parameter. It is increased by 15% from the standard value, which was proposed by Launder and Spalding (1974), in order to apply it to low Re flows.

(4) Calculated Results for Plenum Thermohydraulics

The calculated velocity fields in Case 4, obtained from Method-DL1 and -DKQ, are shown in Figs. 3.3-1(a) and (b), respectively. Method-DL1 gave a stable flow field using the first-order upwind scheme without turbulence models. The flow field calculated by Method-DKQ was also stable, in which the second-order scheme, QUICK, and the modified k-ε model were incorporated.

The flow pattern in the experiment, based on flow visualization, was almost stable. The angle of the measured velocity vectors at each point in Fig. 3.2-4 was nearly constant over time, e.g., the standard deviation of the velocity angle was only 2.9° at point A in Case 4.

Table 3.3-1 Boundary Conditions for Numerical Simulations

Conditions	Case 1	Case 2	Case 3	Case 4
Inlet Temperature (°C)	48.9	49.0	49.1	49.1
Average Inlet Velocity (cm/s)	4.15	5.16	6.34	11.4
Outlet Boundary Pressure (Pa)	Constant ($P=1.013 \times 10^5$)			
Cold Wall Temperature (°C)	14.8	14.4	14.5	15.4
Heat Flux (W/m^2) on the Cold Wall	-2.13×10^4	-2.24×10^4	-2.34×10^4	-2.40×10^4
Bottom Wall Temperature (˚C)*	37.0	36.7	36.4	38.5

* Temperature at the bottom of the traverse line P4

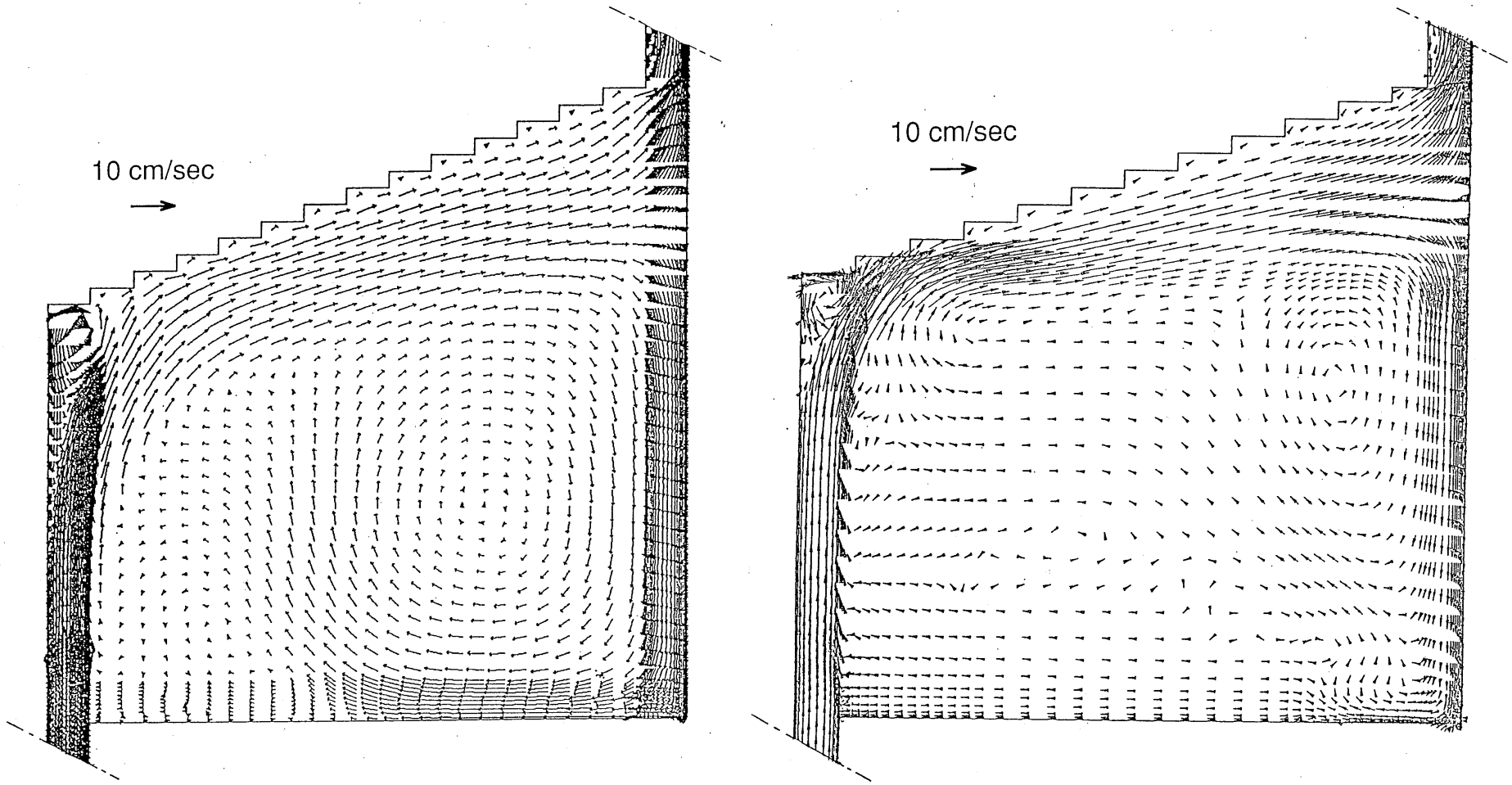

(a) Method DL1

(b) Method DKQ

Fig. 3.3-1 Calculated Velocity Fields in Case 1

The first-order upwind scheme gave stable flow without any turbulence models. It produced unphysical numerical viscosity, which provided a damping source and stabilized the flow. In Case 4, the Re number was 13,000 in the inlet channel based on the cross section averaged velocity. Therefore, the flow in the channel was in a turbulent regime. In other words, the flow field in the plenum had a strong turbulence source at the exit of the inlet channel. To see the effect of the turbulence model on the flow pattern or flow stability, an additional calculation was carried out by a method with the QUICK scheme and without any turbulence models. Here, the same code with Method-DKQ was used. The calculated velocity field in Case 4 is shown in Fig. 3.3-2. The flow pattern was unstable. This indicated that the stabilizing effect of the k-ε turbulence model was significant on the flow field.

Figure 3.3-3 shows the distributions of the horizontal component of velocity (v_x) and temperature along the P1 line in Case 1 obtained from Methods-DL1 and DKQ. The maximum velocity at the upper side was well predicted by Method-DKQ. The first order upwind resulted in smaller velocity due to the numerical viscosity. In the temperature distribution, Method-DL1 showed steep distributions in the lower half region. The temperature distribution obtained from Method-DKQ was in good agreement with the experimental data. The mixing between the hot layer and the cold flow at the bottom seen in the left graph could be well estimated by the combination of the k-ε model and QUICK.

Figure 3.3-4 shows the same distributions of the v_x and temperature in Case 1 obtained from Method-DKQ using a modified k-ε model and the standard model. Here, the effect of this modification is revealed by comparison with the distributions obtained by an additional calculation using the standard constants of the k-ε model. In the modified k-ε model, the width of the stratified flow region was half that of the experiment. The temperature distribution agreed well with the measured data. However, in the original k-ε model, the velocity distribution was broad in the stratified flow region and the temperature gradient in the stratified layer was smaller than the experimental result.

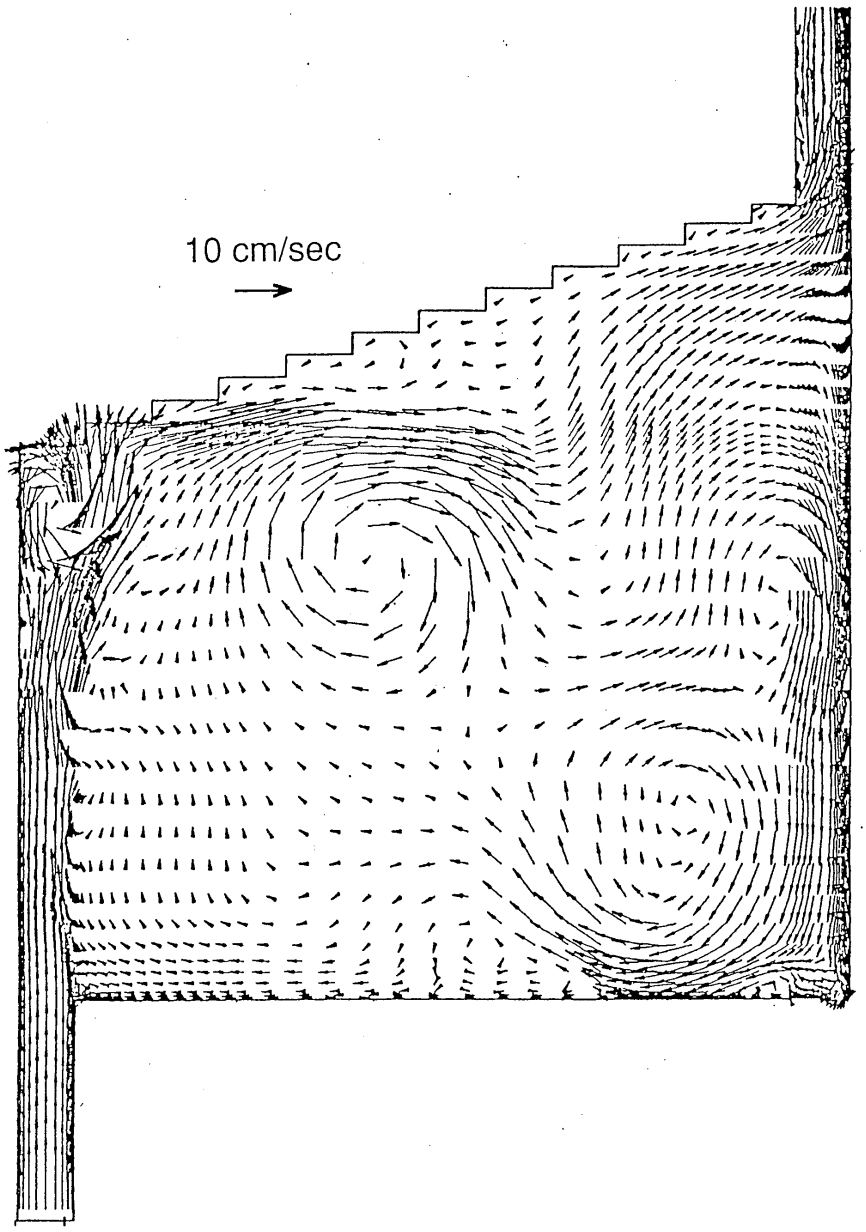

Fig. 3.3-2 Velocity Field calculated by Method of No Turbulence Model and QUICK

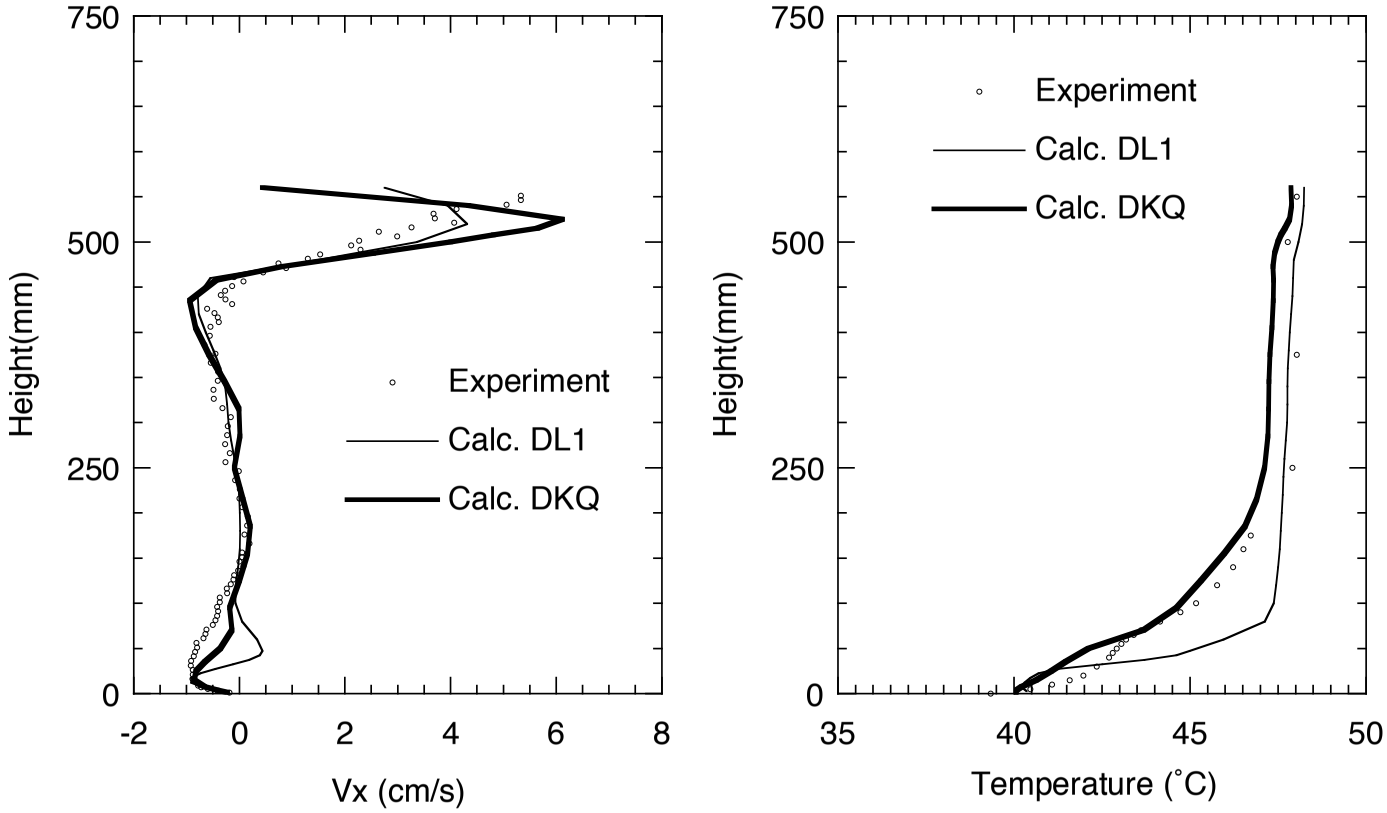

Fig. 3.3-3 Comparisons of Velocity and Temperature Distributions along P1 Line in Case 1 between Calculations of DL1 and DKQ

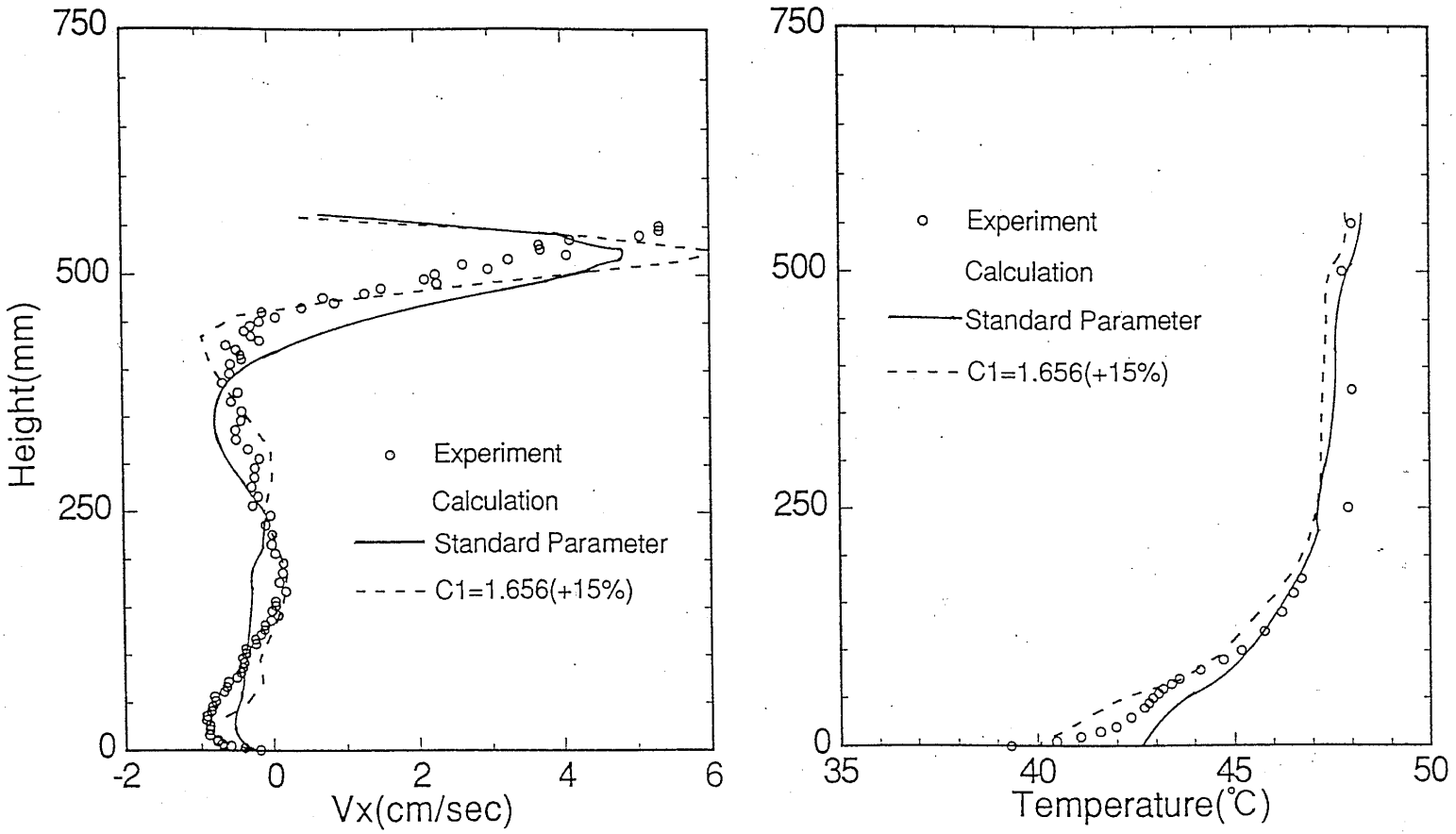

Fig. 3.3-4 Influences of Parameter C_1 in k-ε model on Velocity and Temperature Distributions along P1 Line in Case 1 using Method DKQ

(5) Calculated Results for Penetration flow

The penetration flow was predicted by the applied methods for Case 1. Table 3.3-2 gives a summary of the comparisons of the predicted penetration depths. Here, the experimental data were the maximum depths at which the penetration flow was detected with a frequency of at least 1/1000 cps as described in the section 3.2.

For Case 1, Method-DL1 using the laminar flow model overestimated the maximum penetration depth. Method-DKQ predicted the penetration flow. Penetration flow behaviors obtained from these methods were nearly stable in contrast to the experimental results. Method-DKQ used the turbulence models which used the modified model constant C_1. The temperature distribution calculated by Method-DKQ with the modified C_1 (1.656) is compared with that of an additional calculation with the standard constant C_1= 1.44 for Case 1 in Fig. 3.3-5. The penetration flow was not predicted by the k-ε model using the standard constants. This comparison shows that the constant C_1 had a large effect not only on the stratified flow but on the penetration flow.

The set of the calculations from Cases 1 to 4 could give the onset criteria of the penetration flow relative to the Re number. The Gr number was nearly constant and the Re number was varied as shown in Fig. 3.2-11. In the experiments, the onset condition of the penetration flow, Gr/Re^2= 0.55, was between Case 3 and 4. The predicted onset was between Case 2 and Case 3 by Method-DL1 and Method-DKQ. In other words, both calculations gave the penetration flow under a slightly higher Re condition as compared with the experimental results. These results were considered to be in good agreement with the experimental results.

To predict the penetration flow, turbulence models played an important role. The calculations without any turbulence models overestimated the depth of penetration. The actual penetration flow remained in the upper region because of the inertia of upward flow, loss of the negative buoyancy force due to the mixing with the upward hot flow, and shear stress between the penetration flow and the upward flow. The laminar model underestimated both shear stress and loss of the negative buoyancy force due to

Table 3.3-2 Prediction of Maximum Penetration Depth

		Case 1	Case 2	Case 3	Case 4
Measured Depth		5 cm	3 cm	1 cm	No*
No.	Method	Calculated Depth			
1	DL1	16.6 cm	3.5	No	No
2	DKQ	8.5	1.2	No	No

* : No penetration was observed.

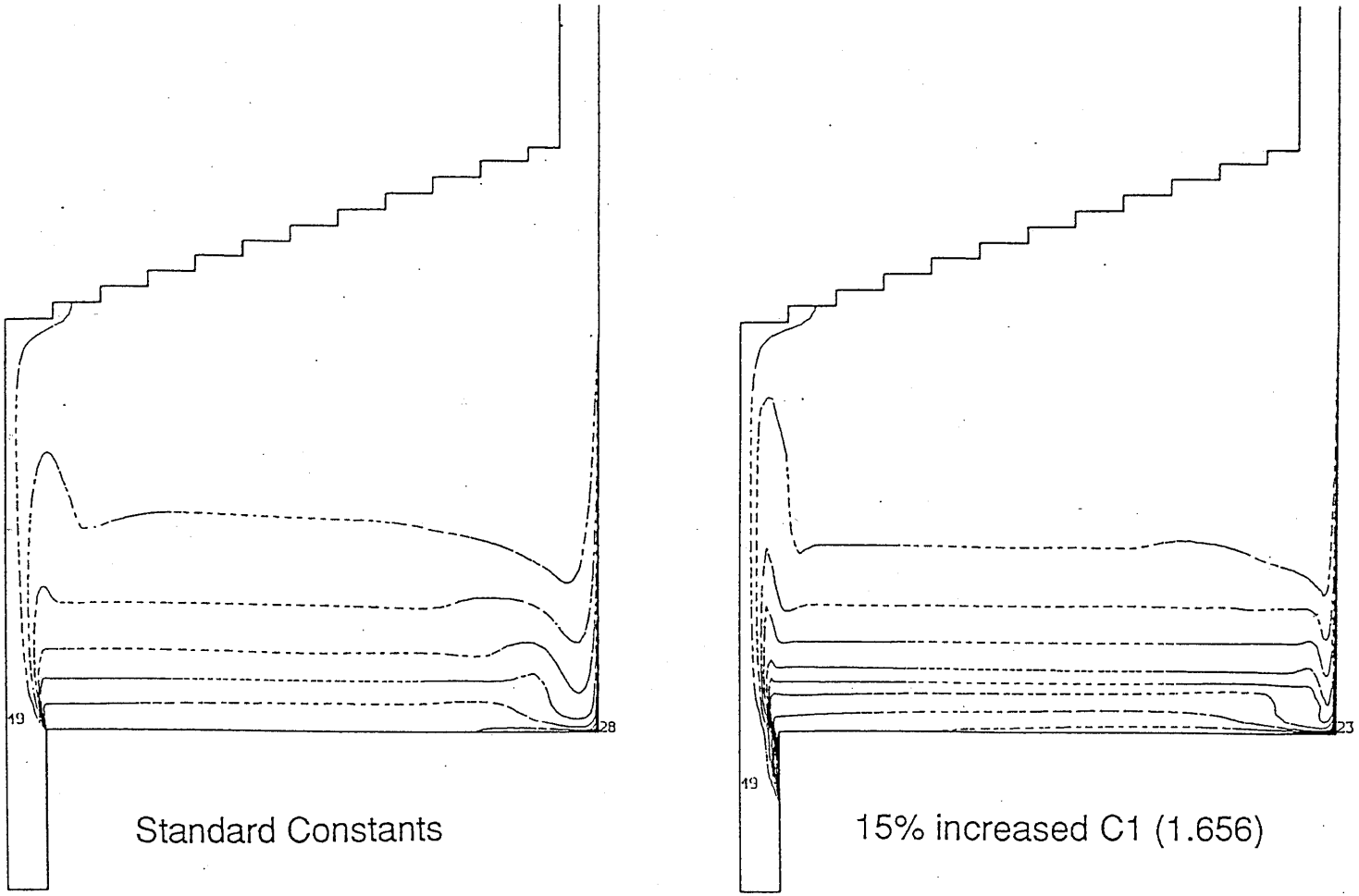

Fig. 3.3-5 Influences of Parameter C_1 in k-ε model on Temperature Distributions in the plenum and the upflow channel using Method DKQ

insufficient mixing. However, calculations with the standard k-ε model could not predict the penetration. The calculation with k-ε model using the modified model constant, C_1 predicted the penetration flow well. Here, C_1 is the coefficient of the production term of the dissipation rate. Thus, the increase of C_1 results in a decrease of turbulent kinetic energy and turbulent viscosity. The modified k-ε model produced less turbulent mixing than the original k-ε model. These results strongly suggest that the amount of turbulence mixing is central to the prediction of penetration flow phenomena.

(6) Summary

The penetration flow into subassemblies due to the negative buoyancy force was investigated using a simple water test apparatus. The thermal stratification in the upper plenum and the penetration flow of stratified cold fluid were realized in the experiment. It is recognized that Gr/Re^2 is one of key parameters for the onset of the penetration flow, and Re dependency is one of key parameters for penetration depth.

From the experimental analyses, the following conclusions were drawn:

(1) Plenum thermal hydraulics

- For higher order schemes of convection terms in the finite difference method, a turbulence model was required to avoid unphysical flow instability.
- An advanced turbulence model was desired to simulate stratified flow, which had a low Re number but still exhibited turbulent characteristics.

(2) Penetration flow

- The penetration flow was calculated by the numerical methods while the results showed wide variation on the onset condition as well as the penetration depth.
- The turbulent viscosity and turbulent mixing strongly influenced the penetration depth. Thus, improvement in turbulence models, especially for low Re and mixed convection flows, is important.

3.4 Sodium Experiment on Penetration flow

(1) Experimental Setup

The water experiments gave many insights on this phenomenon, however, influences of higher heat conduction and lower viscosity of sodium as compared with those of water were still not clear. Thus, sodium experiments (Kamide, 2009) were carried out for the penetration flow driven by the buoyancy force in order to investigate the onset condition and also the penetration depth in a subassembly.

Schematic of test section for the sodium experiment is shown in Fig. 3.4-1. The penetration flow phenomena are driven by buoyancy force and the flow velocity is so small. Thus influences of heat conduction in sodium should be taken into accounts to simulate the partial back flow into a channel. Pe number similarity was considered to model the channels, then nearly the same scale of the flow channels with those in a reactor were used in the sodium experiment.

Three parallel channels are connected to an upper plenum. Each of the channels has wire wrapped heater pins and simulates a fuel subassembly. The upper part of the channel has a hollow type neutron shielding and a handling head at the upper end. The diameter of flow channel in the upper neutron shielding is 80mm and nearly equal to that in a real reactor subassembly. One of the three subassemblies has 61-pin bundle, which simulate a blanket fuel subassembly. The pin diameter, pin pitch, and wire wrapping pitch were set nearly equal to those in a reactor. The outlet of the 61-pin subassembly is located at the center of the upper plenum. The other two subassemblies have 19-pin bundles. The heating length is 0.6m with flat profile of heat flux in each subassembly. The flat-to-flat distance of hexagonal flow area in each subassembly is 0.13m and also nearly equal to that in a real reactor.

In a reactor upper plenum, a dipped heat exchanger of DRACS is installed and provides low temperature sodium, which covers the top of the core during the decay heat removal operation. In the experiment, cold sodium is fed into the upper plenum via a bypass line from the subassembly inlet instead of the dipped heat exchanger. It means the temperature of the cold sodium in the bypass line is equal to the inlet temperature of the

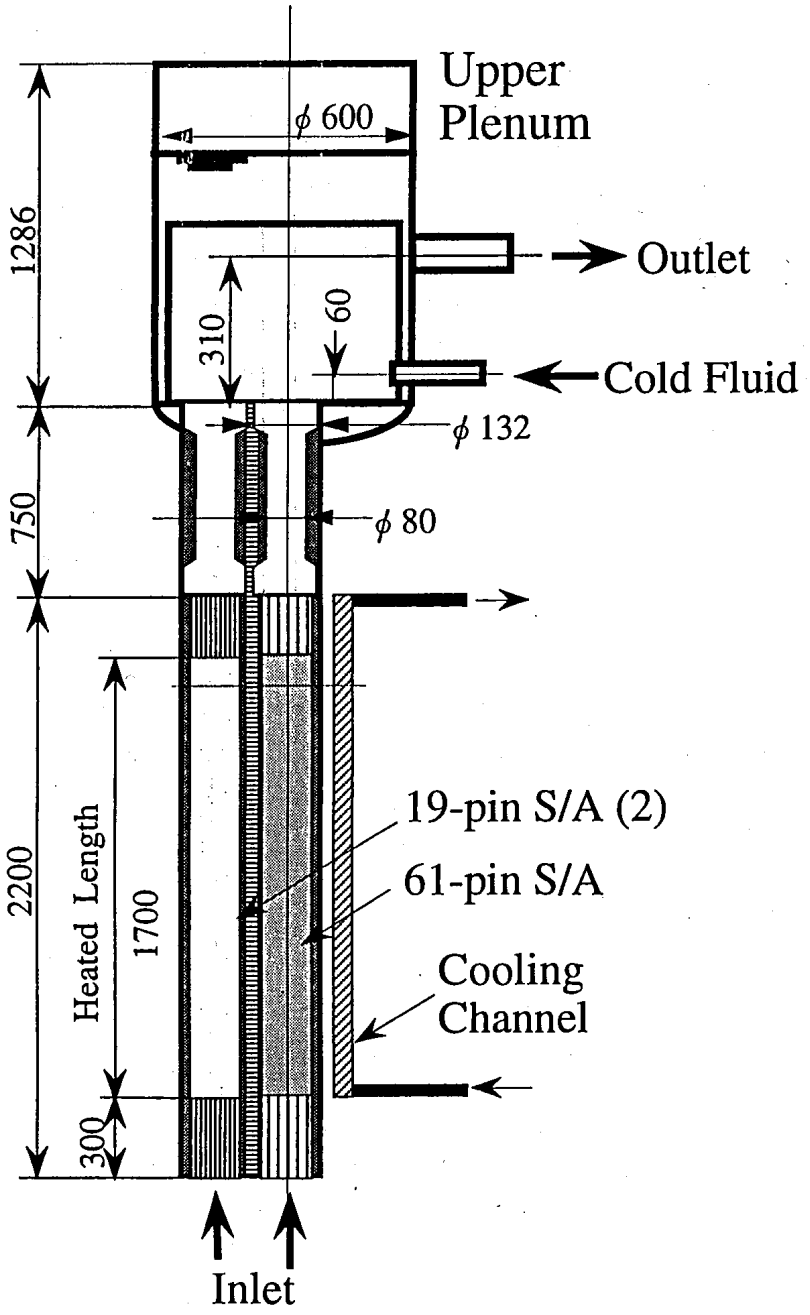

Fig. 3.4-1 Test Section of Sodium Experiment

subassemblies. The cold sodium provided by the bypass line is spread at the bottom of upper plenum and covers the top of the subassembly outlets. The larger flow rate in the bypass line results in the lower temperature in the upper plenum.

The cold penetration flow should be local phenomena in a subassembly and cold sodium above the subassembly outlet. Thus, these three channels and a cold bypass line can simulate the low power and low flow velocity channels covered by the stratified cold fluid in a reactor using full scale models of subassembly outlet and full temperature difference of sodium. It means that these experiments were carried out under Ri number similarity conditions.

(2) Measurement System

Temperatures in the test section are measured by thermocouples of 0.5mm diameter. Temperature measurement positions are shown in Fig. 3.4-2. In the handling head of the center subassembly, the temperatures are measured at inner wall surface so as to detect the cold fluid flow along the channel wall. The positions are set at two levels of 30 and 60mm from the subassembly outlet, and at circumferential angles of -30 to 90˚ and 180˚ (total of 6 angles). The angle of 90˚ corresponds to the direction toward the outlet of cold bypass line in the upper plenum.

Below the handling head, there is a hollow type neutron shielding of 520mm length. The diameter in the channel is reduced from 132 to 80mm in the neutron shielding. The temperatures in this neutron shielding are measured at three levels of 150, 410, and 670mm from the subassembly outlet on the wall surface and also at the channel center.

The signals of the thermocouples and electro-magnetic flow meters in the feed lines into the three subassemblies and the bypass line are recorded by a computer controlled digital data acquisition system. The data recording time and sampling frequency of the temperatures and flow rates were 300s with frequency of 10Hz or 10,000s with frequency of 2Hz.

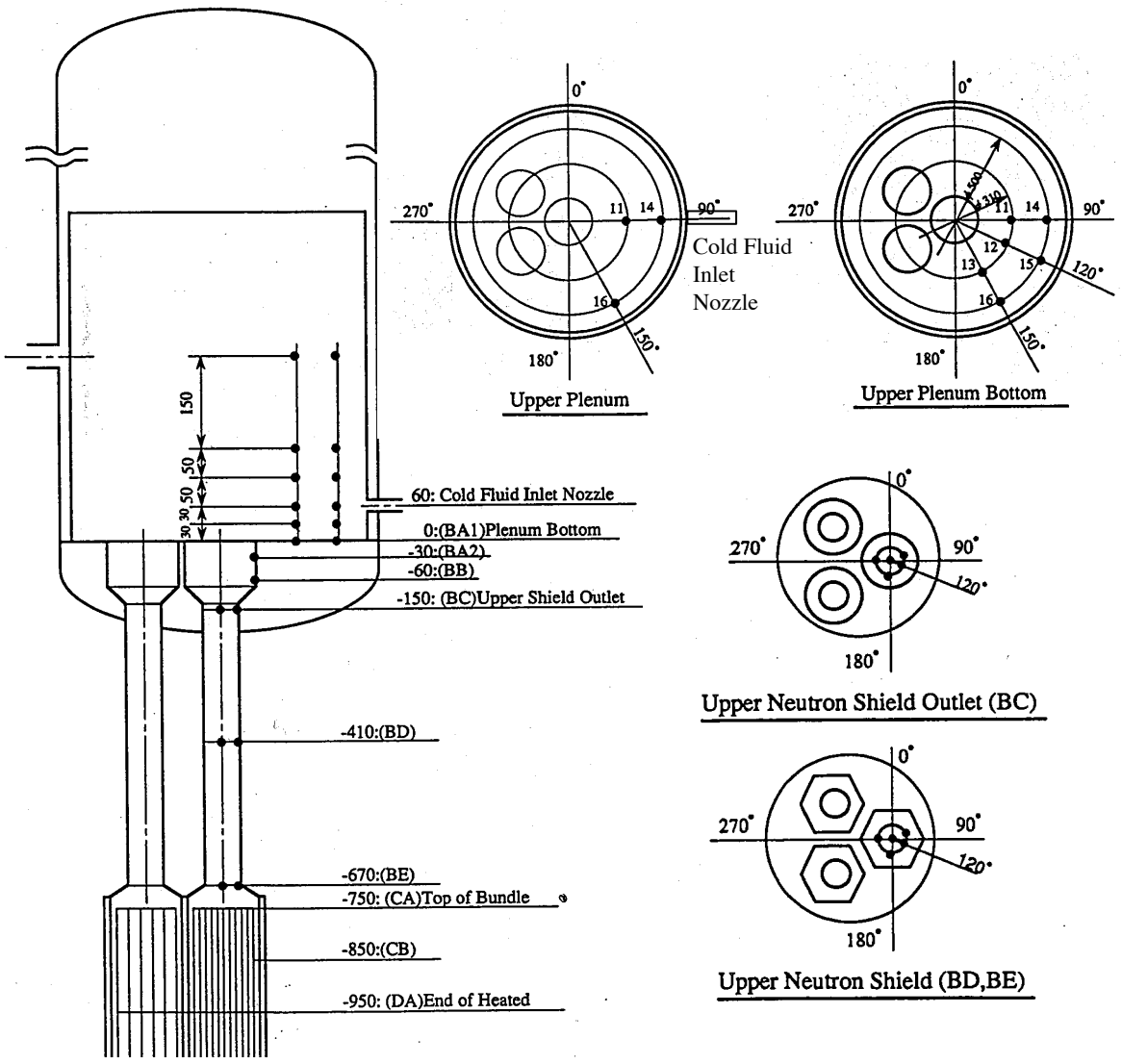

Fig. 3.4-2 Schematic of TC Positions in Test Section

The measurement error of the temperature is within 0.6˚C by relative calibration carried out at five levels from 250 to 450˚C. The flow meters were also calibrated by using duration time and volume between level meters during sodium drain in the upper plenum. The measurement errors of the flow meters were estimated to be within 0.1 l/min.

(3) Experimental Parameters

The sodium experiments were carried out with parameters of velocity in the subassembly and temperature difference between the upward flow at the end of pin bundle and bottom of the upper plenum. The velocity and temperature ranges were decided so as cover the reactor conditions. The penetration flow occurs easily in low velocity channels in general. Thus, the blanket fuel subassembly is significant in this study.

The decay heat in the subassemblies decreases with time. Here, 2% level of full power was assumed, it corresponded to nearly 1000s from the reactor shutdown. The natural circulation flow rate also depends on time and reactor design of component layout and pressure loss coefficient. The natural circulation flow rate in JSFR was predicted to be 2 to 3% of full power conditions in a water experiment (Ohyama, 2009). Here, 2% flow velocity is assumed as a reactor condition.

The three subassembly channels had identical heater powers and flow rates in the experiments. Maximum temperature difference was 140 ˚C in the parameter range, which was bounded by the heater power in the pin bundles. This temperature difference was larger by factor of 2 than the temperature difference at a typical blanket subassembly in DRACS case.

The velocity in the flow channel of neutron shielding was varied from 0.014 to 0.16 m/s. This velocity range corresponds to 1 to 11% of velocity in a blanket subassembly outlet under full power condition and 0.3 to 4% in a core fuel subassembly. The experiments were carried out under steady state conditions. The temperatures in the test sections were measured after 6 hours of operation so as to keep the steady state conditions. The

test matrix of the flow velocity in the neutron shielding channel, V, and the temperature difference between the plenum bottom and the pin bundle outlet, ΔT, had total of 37 cases, where ΔT was varied up to 140 ˚C.

(4) Experimental Results

The temperature distributions in the upper plenum are significant on a point of cold fluid source toward the subassembly outlet. Figure 3.4-3 shows vertical temperature distributions in the upper plenum in cases of low flow rate condition, i.e., 4 l/min (V= 0.014m/s) in each subassembly. The temperatures were measured at a mid point between the 61-pin subassembly outlet and the plenum wall in the direction toward the cold fluid outlet at the vessel wall (90˚). The temperatures are shown in three cases of cold fluid flow rate in the bypass line, zero, 10 and 15 l/min. In the zero flow rate case, the temperature distribution was nearly flat in the upper plenum. This temperature was nearly equal to the pin bundle outlet temperatures. The outlet temperature of the 61-pin bundle was estimated by the flow area weighted average of subchannel temperatures at the top of heated part of pin bundle. It was confirmed that the cold sodium did not reach this height in the pin bundle in all cases in the experiments as shown later. The plenum temperature was lower by 10 ˚C than the estimated subassembly outlet temperature. It is presumed that the reason of this difference is heat loss at the vessel wall of 430 ˚C.

Thermal stratifications were observed in cases of 10 and 15 l/min of the cold fluid flow rate. The stratification interfaces were located at the height of the cold fluid outlet at the plenum wall as shown in the figure. The temperatures at the plenum bottom in cases of 10 and 15 l/min were lower than that in the zero flow rate case by 95 ˚C and 130 ˚C, respectively and also lower than the pin bundle outlet temperatures by 102 ˚C and 140 ˚C, respectively. This large temperature difference between the plenum bottom and the hot flow in the subassembly causes the penetration flow into the subassembly.

Figure 3.4-4 shows the temperature trends in the case of V= 0.014m/s and ΔT=140˚C. The temperature at the top of the neutron shielding showed lager amplitude, 80˚C, of

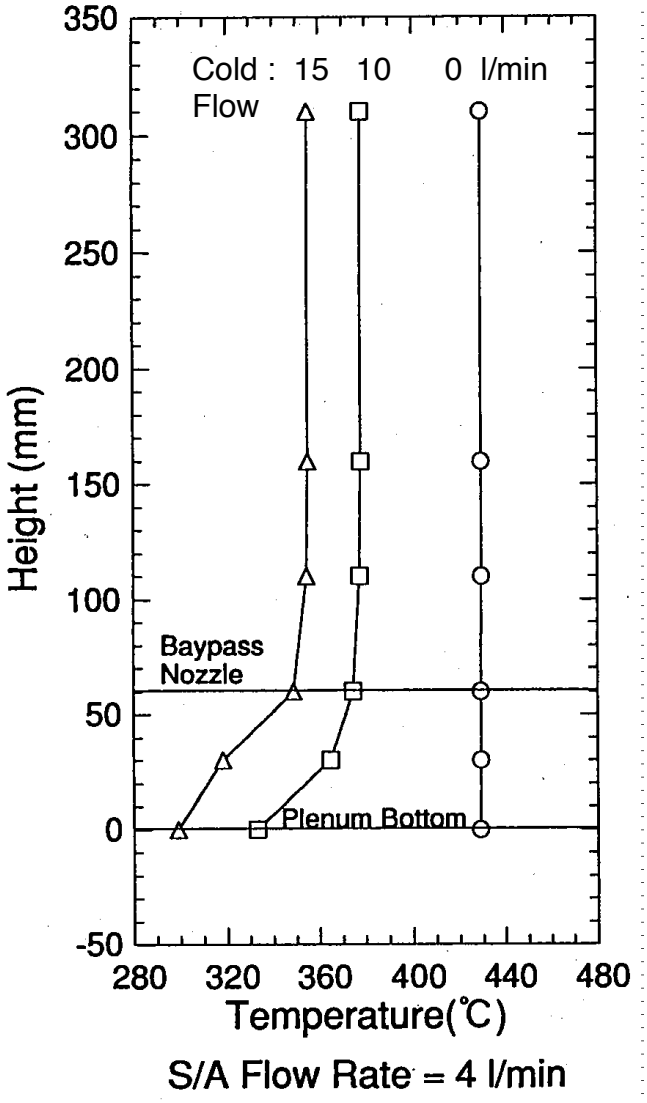

Fig. 3.4-3 Vertical Temperature Distributions in Upper Plenum

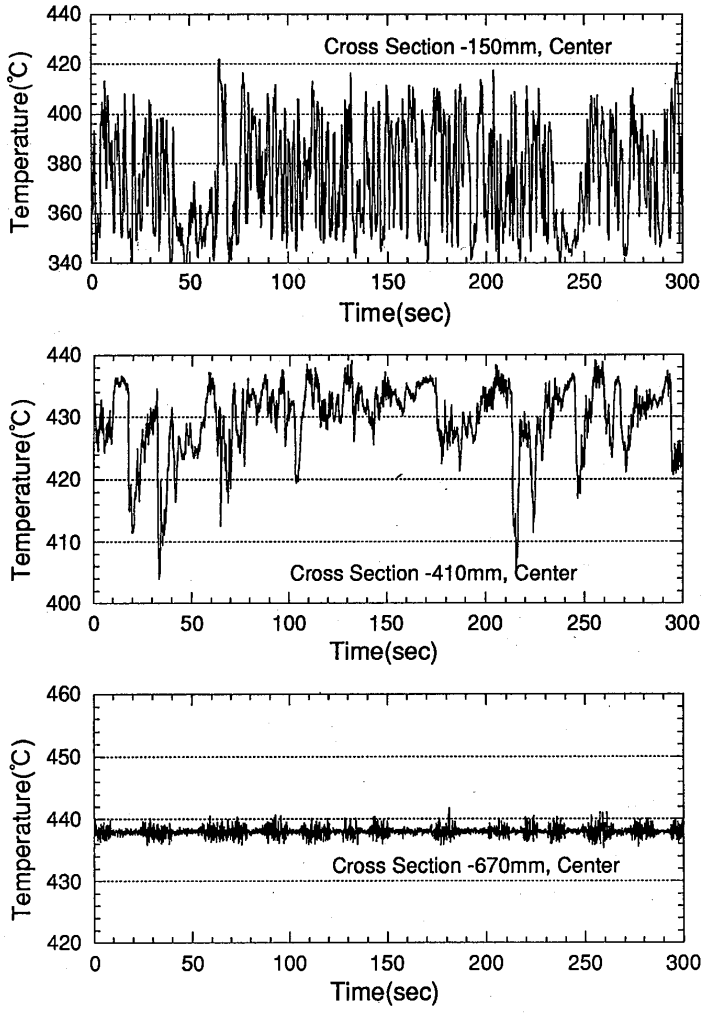

Fig. 3.4-4 Time Trends of Temperature in Neutron Shielding in Case of V=1.4cm/s, ΔT=140˚C

the fluctuation. Continuous lower temperatures with time periods of 10 to 20s were also registered. The cold downward flow would cover the center of the flow channel intermittently at this height.

At the middle height of the neutron shielding, the amplitude of low temperature spike decreased to 35 ˚C and frequency of the spike also decreased as compared with at the top of neutron shielding. However, this time trend means that large amount of cold fluid reached the middle height of the neutron shielding. On the other hand, no penetration flow was observed at the lower end of the neutron shielding where the temperature showed nearly flat trend except for the noise.

The penetration flow was detected by the temperature history at the neutron shielding. When the penetration flow reached the thermocouple position, the temperature trend showed the cold spikes as shown in Fig. 3.4-4. Thus it was needed to detect this cold spike. The procedure to detect the penetration flow in this experiment is as follows;

1) The temperature data of 10,000s with time interval of 0.5s were obtained in each case at the top and middle heights of the neutron shielding. Moving average was operated to the time trend data with a window size of 6 sampling data to reduce the influence of electric noise.
2) The maximum temperature (T^1_{max}) and standard deviation (σ_1) were obtained from the temperature data.
3) The temperature data less than (T^1_{max} - 4x σ_1) were excluded. Time averaged temperature (T^2_{ave}) was obtained from the residual data.
4) The temperature data larger than (T^2_{ave} - 2 x σ_1) were selected from the original data. Time averaged temperature (T^3_{ave}) was obtained from the selected data.
5) The criterion of lower temperature was set at (T^3_{ave} - 4 x σ_1).
6) The definition of the penetration flow was to detect the lower temperature than the criterion (T^3_{ave} - 4 x σ_1) in the time trend.

The detected penetration flow at the top of neutron shielding is plotted in a condition map of the velocity in the neutron shielding and the temperature difference, ΔT, between the plenum bottom and the pin bundle outlet as shown in Fig. 3.4-5. It is

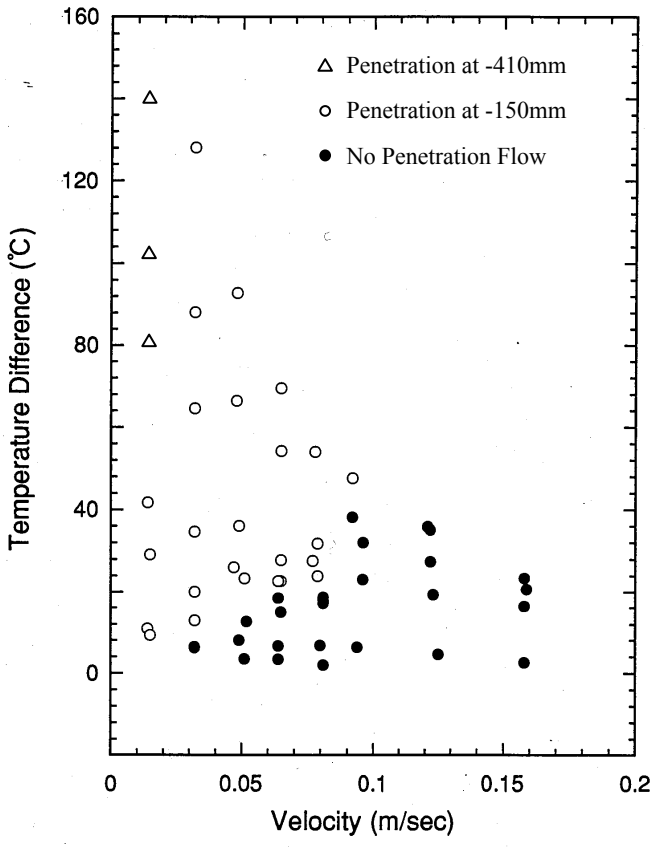

Fig. 3.4-5 Occurrence Map of Penetration Flow on Axes of V and ΔT

obviously seen that the lower velocity and the higher temperature difference resulted in the penetration flow.

The detected penetration flows at the middle height of the neutron shielding (-410mm) are also plotted in Fig. 3.4-5 as a triangle symbol. When the flow velocity was larger than 0.03 m/s, the temperature difference of 120 ˚C did not result in the penetration flow at the middle height of neutron shielding. It means that the penetration lengths were less than 0.26m from the top of neutron shielding in these cases. Further, the penetration flow did not reach the pin bundle when the flow velocity was 0.014 m/s and the temperature difference was 140 ˚C as shown in Fig. 3.4-4.

(5) Discussions

The onset conditions of the penetration flow were correlated with Gr and Re numbers, i.e., buoyancy force and inertial force in the water experiment. The occurrence map of penetration flow in the sodium experiment is plotted in log scale axes of Gr and Re numbers as shown in Fig. 3.4-6. The definitions of Gr and Re numbers are as follows.

$$Gr = \frac{g\beta\Delta T D^3}{\nu^2} \qquad \text{Re} = \frac{V D}{\nu} \qquad \text{(3-4).}$$

Here, representative length, D, is the hydraulic equivalent diameter of the flow channel. The definitions of ΔT and V are same as in the parameters of the penetration flow experiments. The regions where the penetration flow was detected and not detected are divided by a straight line on the map of log scale axes.

Several water experiments of the partial back flow into a channel are available to compare with this sodium experiment. Barakat, et al., carried out the water experiments using centrally heated annular channels connected to a cold upper plenum. The channel diameter was varied as an experimental parameter. Onset conditions of the penetration were obtained in these experiments. Figure 3.4-7 shows onset condition of the penetration flow on the log scale axes of Gr and Re in the sodium experiments together with the water experiments of Barakat (1992), and also the square

channel water experiment (COPIES) in the section 3.3. The onset conditions in the sodium experiments were obtained as the mid points between nearest pairs of detected and non-detected conditions in Fig. 3.4-6.

The onset conditions in the sodium experiment can be expressed by a straight line, Gr/Re^2=Constant, as well as in the water experiments. The constants varied among the experiments due to the difference of geometry and also the detailed definition of the penetration flow. However, the onset condition of the penetration flow can be predicted by the balance between the buoyancy force and the inertial force even in the sodium flows.

The sodium experiment showed that the penetration flow would occur at the top of neutron shielding in a reactor. However, the penetration length in the blanket subassembly will be less than 0.26m when the flow rate is larger than 2% of the full power condition and will not reach the pin bundle, when the flow rate is at 1% of the full power condition (0.014m/s in the upper neutron shielding).

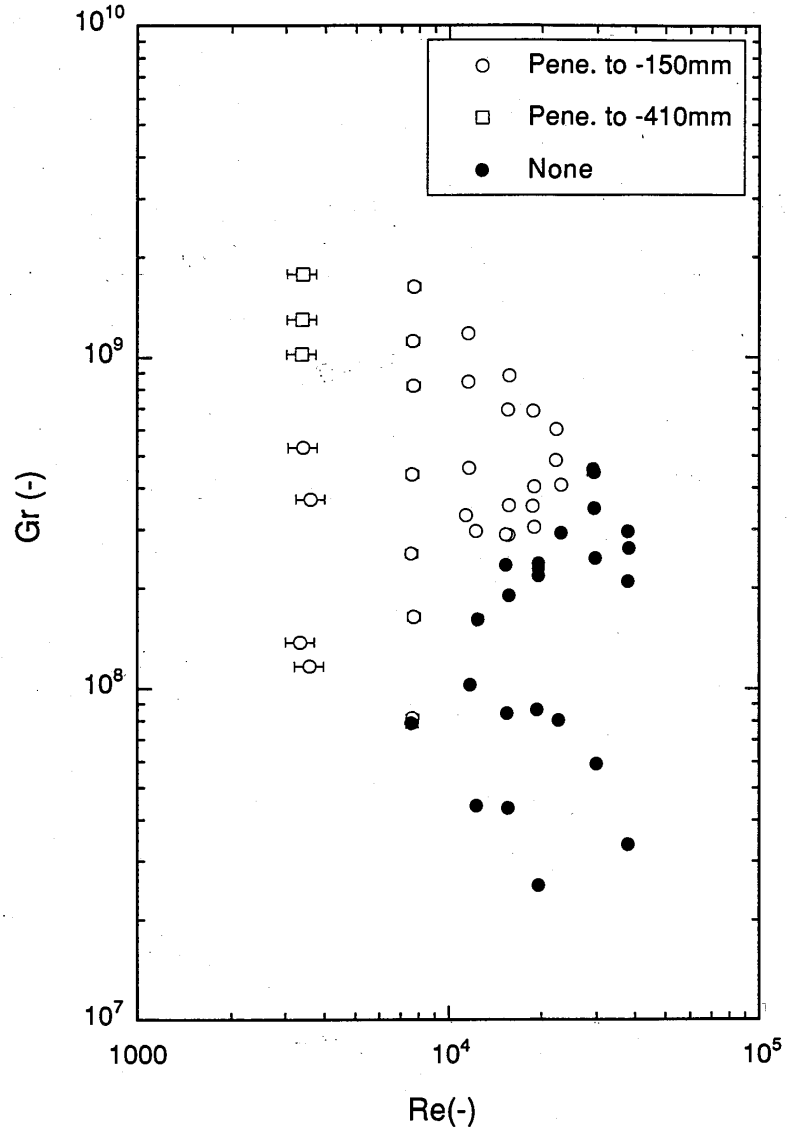

Fig. 3.4-6 Occurrence Map of Penetration Flow on Axes of Gr and Re

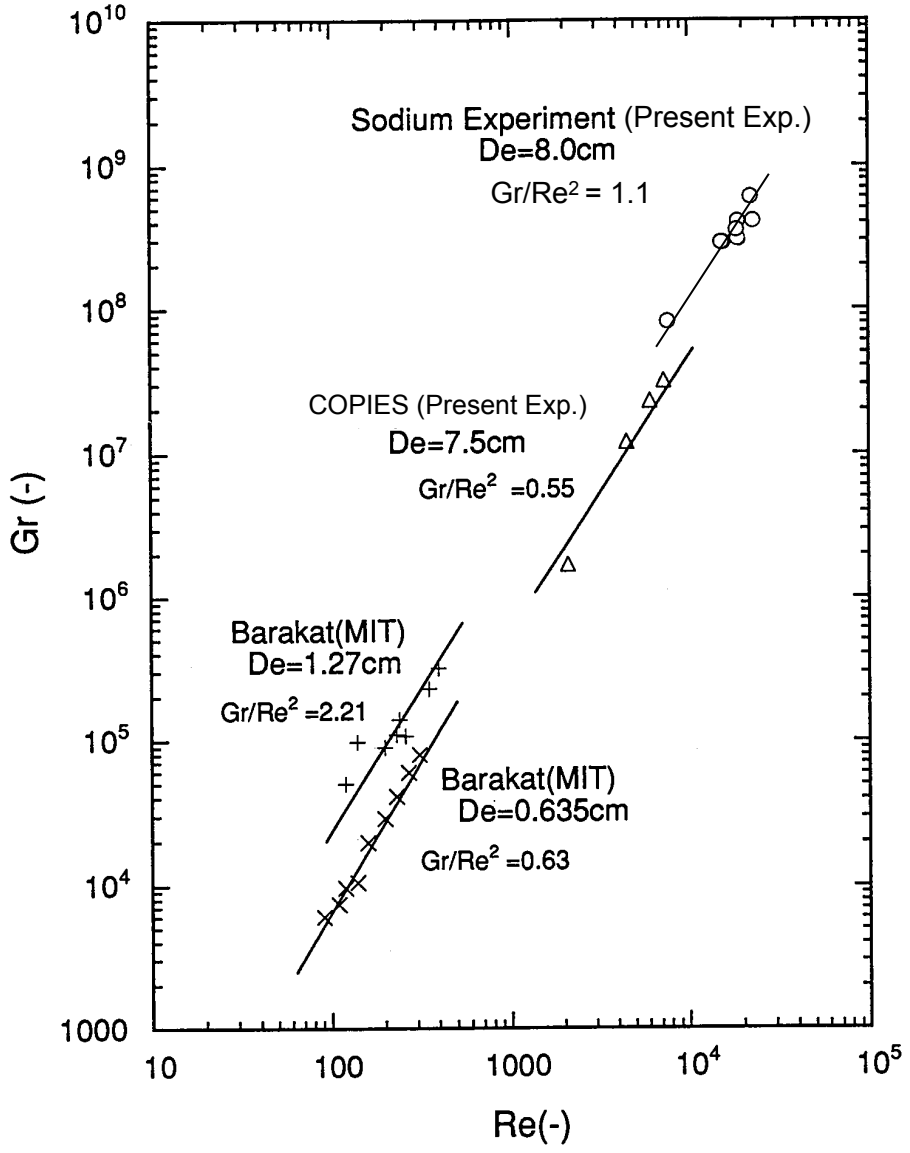

Fig. 3.4-7 Onset Condition of Penetration Flow

(6) Summary

Sodium experiments were carried out for the penetration flow into a low power subassembly due to negative buoyancy force during natural circulation decay heat removal. The subassembly geometry was modeled including the handling head and hollow type upper neutron shielding above the pin bundle in real dimensions. The diameter of the flow channel in the upper neutron shielding was 0.08m. Following findings were obtained through the experiments.

1) The onset conditions of the penetration flow in the sodium experiments can be expressed by a straight line, Gr/Re^2=Constant, as well as in the water experiments. Thus, the onset condition can be predicted by the balance between the buoyancy force and the inertial force even in the sodium flows.
2) The penetration flow was detected at the top of neutron shielding in a subassembly under low flow rate conditions of natural circulation in a blanket subassembly of a reactor. However, the penetration lengths in the upper neutron shielding were less than 0.26m when the flow rate was larger than 2% level of the full power condition of a blanket subassembly. Further the penetration flow did not reach the pin bundle, when the flow velocity was maintained at 0.014m/s in the upper neutron shielding (1% of the full power condition).

3.5 Conclusions

The penetration flow into subassemblies due to the negative buoyancy force was investigated using a simple water test apparatus and also a sodium test facility.

In the water experiment, the thermal stratification in the upper plenum and the penetration flow of stratified cold fluid were simulated by using a square shape channel connected to a slab geometry plenum. In the sodium experiment, three subassemblies were modeled including the handling head and hollow type upper neutron shielding above the pin bundle. The diameter of the flow channel in the upper neutron shielding was 0.08m and nearly equal to that in a reactor. The subassemblies were connected to an upper plenum where cold sodium can be provided.

Onset conditions of the penetration flow were obtained as a function of non-dimensional numbers of Gr and Re in the water experiment and the sodium experiment. It was recognized that Gr/Re^2 is a key parameter for the onset of the penetration flow both in the water and sodium experiments. It means that the onset condition can be predicted by the balance between the buoyancy force and the inertial force even in the sodium flows.

In the water experiment, Re dependency is one of key parameters for the penetration depth. The sodium experiments showed that the penetration flow occurred at the top of neutron shielding under low flow rate conditions of natural circulation in a blanket subassembly of a reactor. However, the penetration lengths in the upper neutron shielding were less than 0.26m when the flow rate was larger than 2% level of the full power condition of a blanket subassembly in a reactor. Further, the penetration flow did not reach the pin bundle, when the flow velocity was maintained at 0.014m/s in the upper neutron shielding (1% of the full power condition).

From the numerical simulations of the water experiments, the following conclusions were drawn:

(1) Plenum thermal hydraulics

- For higher order schemes of convection terms in the finite difference method, a turbulence model was required to avoid unphysical flow instability.
- An advanced turbulence model was desired to simulate stratified flow, which had a low Re number but still exhibited turbulent characteristics.

(2) Penetration flow

- The penetration flow was calculated by the numerical methods while the results showed wide variation on the onset condition as well as the penetration depth.
- The turbulent viscosity and turbulent mixing strongly influenced the penetration depth. Thus, improvement in turbulence models, especially for low Re and mixed convection flows, is important.

These calculations showed that the penetration flow due to the buoyancy force can be predicted by the multi-dimensional analyses where physical viscosity should be treated well accompanied with numerical viscosity according to the numerical schemes.

The sodium experiments using the full-scale subassembly model revealed that the buoyancy driven penetration flow would occur in the blanket subassemblies under natural circulation condition. However, the penetration depth will be limited in the upper neutron shielding and not reach the pin bundle when the flow velocity is larger than 1% level of the full power condition of a blanket subassembly in a reactor. This means that influence of the penetration flow phenomena would be limited on the thermal hydraulics during the natural circulation in a reactor core. Even though the influence is limited, this study on the penetration flow is still of importance to understand the thermal hydraulic phenomena in the core during natural circulation decay heat removal.

Nomenclature

Water Experiment:

A_c	surface area of the cold wall (m^2),
A_{in}	cross section area of the inlet channel (m^2),
D	hydraulic equivalent diameter of the inlet channel (m),
q"	heat flux through the cold wall used for the boundary condition (W/ m^2),
Q	total heat removed by cooling box (W),
T_{av}	averaged temperature of the channel inlet temperature and the temperature at the bottom of the P1 line in the plenum (˚C),
v_{av}	average velocity on the x-z plane (y = 0 mm) at the inlet channel (m/s),
v_z	averaged velocity at the channel inlet (m/s),
W	volumetric flow rate in the inlet channel (m^3/s),
β	thermal expansion rate of water at T_{av} (1/°C),
ΔT	the difference between the channel inlet temperature and the temperature at the bottom of the P1 line in the plenum (°C), and
ν	kinetic viscosity of water at T_{av} (m^2/s).

Sodium Experiment:

D	hydraulic equivalent diameter of flow channel (m),
g	gravity acceleration (9.8 m/s^2),
V	cross section averaged velocity in the flow channel,
β	thermal expansion coefficient of fluid (1/˚C),
ΔT	difference between the temperature at the plenum bottom and the pin bundle outlet temperature,
ν	kinetic viscosity of fluid (m^2/s).

Chapter 4. Inter-Wrapper Flow

Chapter 4. Inter-Wrapper Flow

4.1 Introduction

Natural circulation decay heat removal (NC/DHR) is one of the most important features of sodium-cooled fast reactors in terms of inherent safety. The evaluation of core thermohydraulics under natural circulation conditions is significant for the utilization of the passive safety features of fast reactors.

As the decay heat removal system, a direct reactor auxiliary cooling system (DRACS) is selected in JSFR (Japan Sodium-cooled Fast Reactor) and Japanese Demonstration Fast Breeder Reactor designs (DFBR, Ueta, 1999), where sodium/sodium heat exchangers (which are referred to as dipped heat exchangers, DHXs) are immersed in an upper plenum of the reactor vessel. Water experiments (Takakuwa, 1995) were carried out to study the characteristics of NC/DHR for Japanese DFBR. It was pointed out that reverse flow in radial reflectors is an important factor in the evaluation of core cooling capabilities during natural circulation. Under low flow rate conditions, i.e. natural circulation, core-plenum interactions may occur, particularly in a system with DRACS, e.g., reverse flow in non-heated channels, inter-subassembly heat transfer, and inter-wrapper flow. Sodium experiments (Kamide, 1994 and 1995) have been carried out by authors for inter-subassembly heat transfer.

When DRACS is operated, cold sodium is provided by the DHXs and a thermal stratification phenomenon occurs in the reactor upper plenum. This cold sodium penetrates into low power channels (the reverse flow in the radial reflector channels) and into the gap region between the subassemblies and enhances the natural convection in the gap region. The gap region is closed by a grid-plate at bottom and by a core barrel at side. Only the top of gap region is open to the reactor upper plenum through the subassembly spacer-pads. There is no leak flow from the high pressure plenum through the grid-plate during natural circulation decay heat removal. The natural convection in the gap between the wrapper tubes is referred to as inter-wrapper flow (IWF). Water experiments on the NEPTUN model (Weinberg, 1995 and 1995) have been carried out for NC/DHR in the European Fast Reactor (EFR) which features

DRACS. The fuel subassemblies were simulated by 253 circular tubes where 19-pin electric heaters were installed. IWF was observed in the experiments. It was found that IWF exerted a significant influence on the core thermal hydraulics and that it could remove more than 40% of the core heater power which simulated the decay heat.

In this study, sodium experiments for IWF under forced flow conditions were carried out. The influence of IWF on subassembly thermohydraulics was studied under a wide range of power and flow conditions which covered NC/DHR in a large size FBR. This study also focused on the influence of IWF on natural circulation flow in primary loop and transient characteristics of IWF after the scram. Sodium experiments were performed using the PLANDTL-DHX (Plant Dynamics Test Loop with DHX) test rig, composed of seven subassemblies, inter-wrapper gap, upper plenum with DHX, primary loop, intermediate heat exchanger (IHX) and secondary loop with air cooler as the final heat sink.

Two sets of sodium experiments were carried out. The first set consisted of steady state experiments (Kamide, 1997, 2001). Heat removal characteristics of IWF were studied under low flow rate and natural circulation conditions in the primary loop. The experiments were carried out under forced and natural circulation. The natural circulation test can reveal the influence of IWF on the loop flow rate via temperature distribution in the core. The second set consisted of transient experiments from forced to natural circulation (Kamide, 1997, Nishimura, 2000). The time constants for heat removal due to IWF and for the change of the loop flow rate due to IWF are of interest. Transient characteristics of core-plenum interactions were investigated with and without natural circulation in the IHX secondary loop.

As mentioned above, the PLANDTL-DHX sodium test rig has only seven subassemblies. Thus, natural convection along the sodium gaps in the entire core is not modeled. The reactor core has inner and outer core subassemblies, radial blanket subassemblies, and radial reflectors. It has a radial temperature profile due to the configuration of these subassemblies. IWF will develop according to this radial temperature profile and interact with each other. A water experiment was carried out

for this core scale IWF. In past studies, several water experiments were carried out for IWF. In the NEPTUN experiment, the subassemblies were modeled by using circular tubes and the gap region between the subassemblies had a relatively larger flow area and different geometry as compared with the zigzag shape between hexagonal wrapper tubes in a reactor. In this study a 1/12 sector core model was used where hexagonal shape subassemblies were modeled (Kamide, 2001, 2002). Flow visualization and temperature measurements were performed to investigate an overall flow filed of the IWF in a core.

Through the sodium experiments using the 7-subassembly model, the heat transfer between the IWF and the subassemblies is revealed. The water experiment of 1/12 sector model of a core is used to study an overall flow pattern in a core and also to verify a numerical simulation method which estimates the IWF of a reactor core.

4.2 Steady State Sodium Experiment

(1) Experimental Apparatus

In order to investigate IWF in the gap between subassemblies, a core model composed of seven subassemblies was installed in the PLANDTL-DHX facility. Figure 4.2-1 shows a horizontal cross section of the simulated core. The center subassembly has 37 electrically heated pins, each 8.3 mm in diameter, while the six outer subassemblies each have seven heater pins. The heater pins in the center subassembly simulate the core fuel pins of a reactor in full scale and thus include the spacer wires. The role of the outer subassemblies is to add thermal boundary condition to the center subassembly and to the gap flow between the subassemblies. Thermohydraulics inside the subassembly is investigated only in the center subassembly. The heated length is 1m and the axial power profile is modeled as a chopped cosine distribution. The upper and lower axial blankets of the fuel pin are modeled as non-heated parts. The flat-to-flat distance of the subassembly is approximately 1/2 the actual scale, which consists of 217 fuel pins. The subassemblies are modeled in actual scale in the axial direction, including upper axial reflectors. The thickness of the wrapper tubes is 4 mm which is the same as that in an actual reactor. The inter-wrapper gap filled with sodium is connected to an upper plenum. The width of the gap is kept constant by cylindrical rods measuring 7 mm in diameter and 30 mm in length. These spacer rods are set at the top and at the mid-level of the subassemblies. This spacer geometry permits the flow between the inter-wrapper gap and the upper plenum.

Figure 4.2-2 shows a PLANDTL-DHX flow diagram. The subassemblies are connected to the upper plenum, which has an upper inner structure (UIS) and the DHX. The primary loop has an intermediate heat exchanger (IHX), an electromagnetic pump, flow control valves, and a lower plenum. Sodium is provided by three lines into the center subassembly, the three outer subassemblies on the right side, and the remaining three subassemblies on the left side, respectively. The secondary loop of the IHX has an air cooler and a pump. As part of the decay heat removal system, PRACS (Primary Reactor Auxiliary Cooling System, see chapter 1) cooling coils are also installed on the primary side of the inlet plenum of IHX.

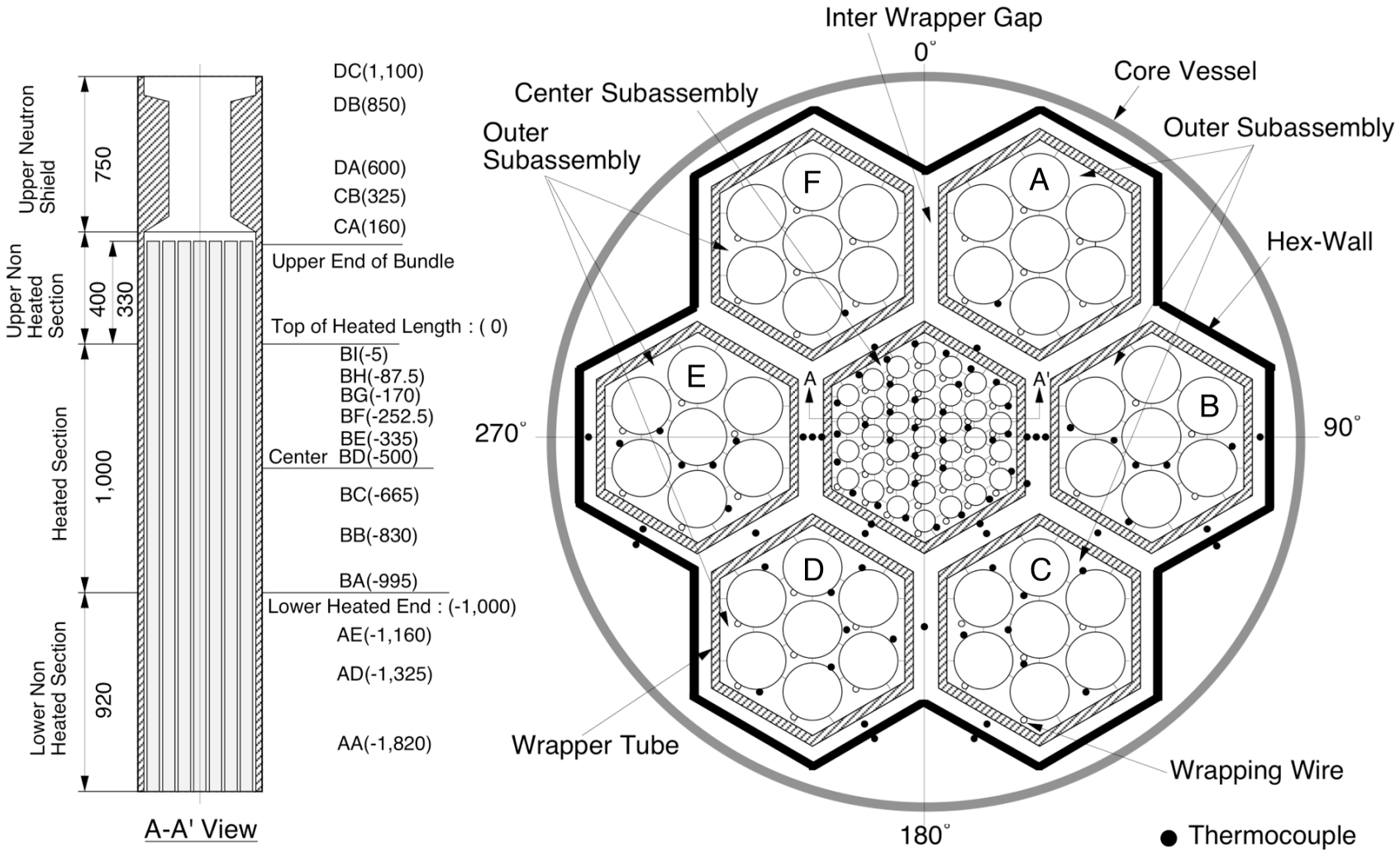

Fig. 4.2-1 Core Configuration of Seven-Subassembly Model

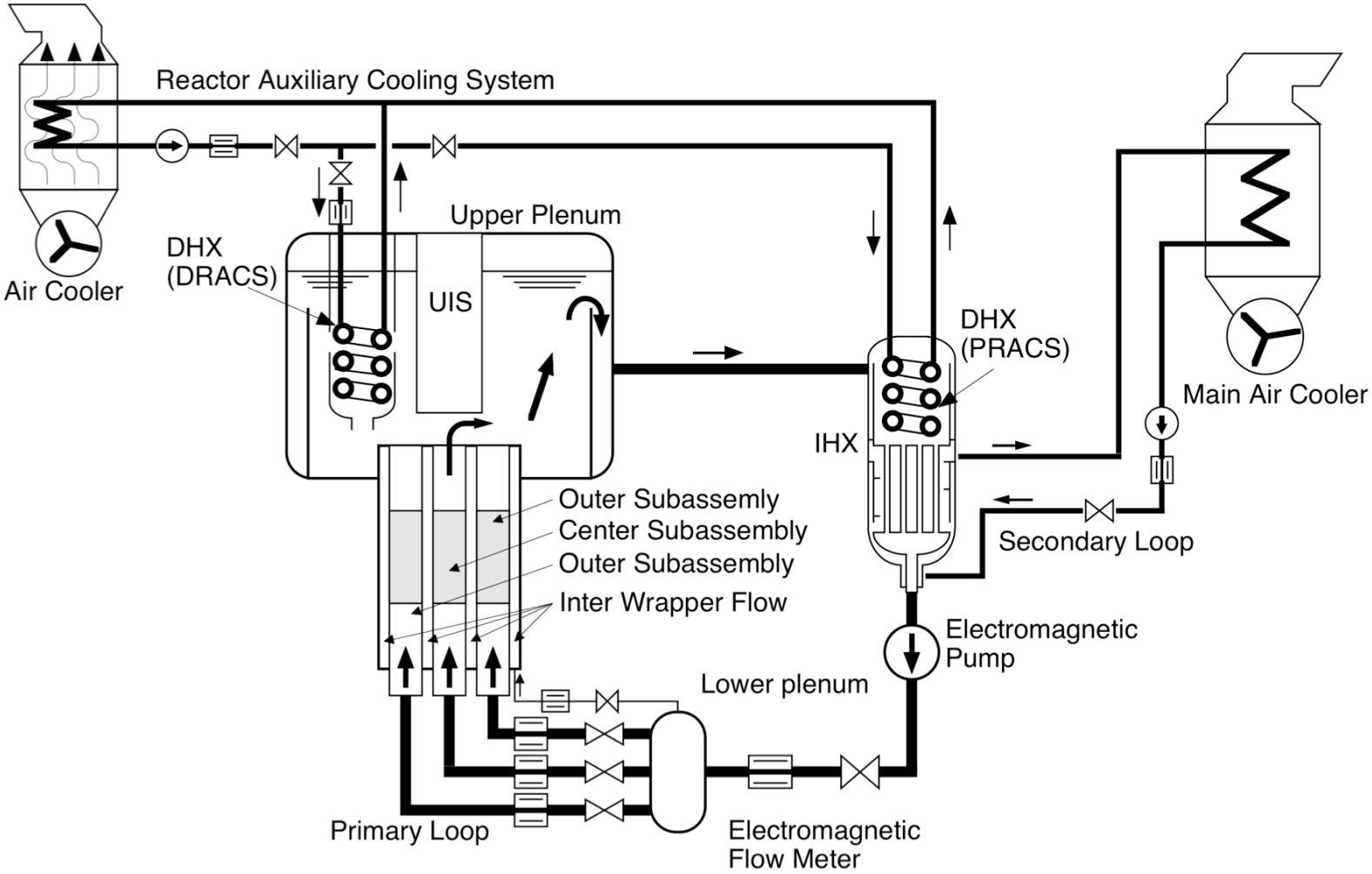

Fig. 4.2-2 Flow Diagram of PLANDTL-DHX

It is noted that the PRACS is one of the design choices for the decay heat removal system, while the DRACS is part of the reference design of the Japanese DFBR and JSFR. The DRACS or PRACS can be selected by valves in the secondary loop of the decay heat removal system. The major specifications of the PLANDTL-DHX facility are listed in Table 4.2-1.

The sodium temperatures in the core were measured by thermocouples of 0.3 or 0.5 mm diameter (see Fig. 4.2-1). Measurement accuracy was maintained by relative calibrations. A maximum flow rate of 1200 l/min was provided through the test section at constant temperature to maintain all thermocouples at identical temperature. Such homogeneous temperature data were recorded at seven temperature levels from 250 to 550˚C. Calibration constants were obtained from the least square method based on reference thermocouples, previously calibrated by hot bath. The maximum error among all thermocouples was 0.5˚C after calibration. The signals from the thermocouples, flow meters, and the electric power input of heater pins were recorded by 16-bit A/D converters at a sampling interval of 0.096s (~10 Hz).

(2) Experimental Parameters and Procedure

a. Forced Circulation Condition

The primary objective of this study was to assess the influence of IWF on core thermohydraulics. It is believed that IWF will influence long term transitions, including the third peak (at ~1000s after the scram) in temperature in the core due to the slow development of natural circulation in the primary loop. Examples of time histories of core temperatures and loop flow rates obtained in a water experiment (Ieda, 1991), where the DRACS and PRACS were installed in a pool type reactor model, are shown in Figs. 4.2-3 and 4.2-4 for a total blackout event. A third peak of core outlet temperature is seen in the DRACS case at ~3000s, and it is a slow transient. Therefore, steady-state sodium experiments, which simulate the natural circulation decay heat removal, were performed to investigate the basic characteristics of IWF.

Table 4.2-1 Major Specifications of PLANDTL-DHX

Simulated Core		
	Center S/A	Outer S/A
Number of Subassemblies	1	6
Flat to Flat Distance (m) of Hexagonal Flow Area	0.063	
Wrapper Tube Thickness (m)	0.004	
Inter-wrapper Gap Width (m)	0.007	
Number of Heater Pins	37	7
Pin Diameter (m)	0.0083	0.0208
Pin Pitch/ Diameter (-)	1.19	1.08
Hydraulic Equivalent Diameter (m)	0.0042	0.0059
Wire Diameter (m)	0.0015	0.0015
Wire Lead (m)	0.165	0.165
Heated Length (m)	1.0	1.0
Axial Power Profile	Chopped Cosine	
Loop		
Core, Maximum Power;	1.2 MW	
Main Pipe Diameter:	4 in.	
Maximum Flow rate:	1200 l/min.	
IHX:	Primary side is inside of tubes	

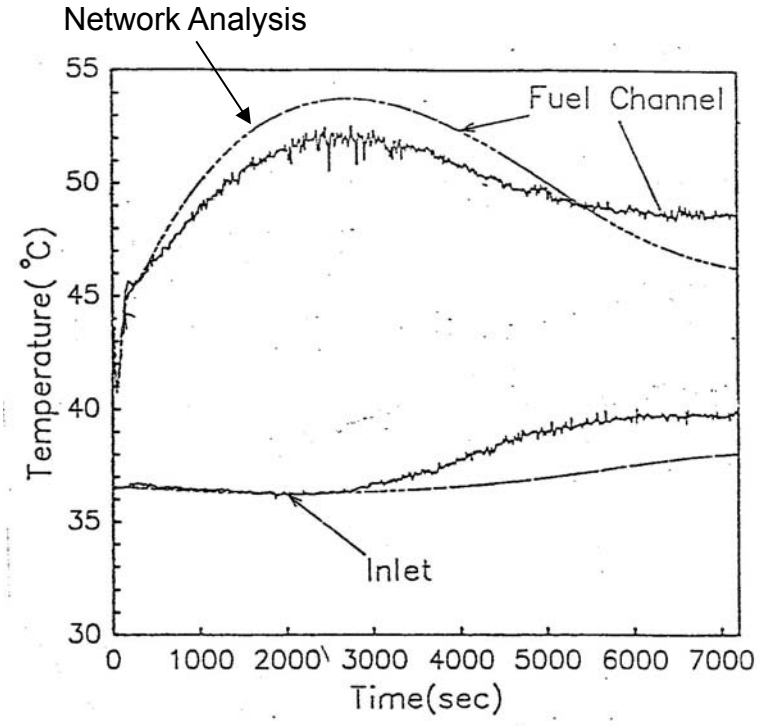

(a) DRACS

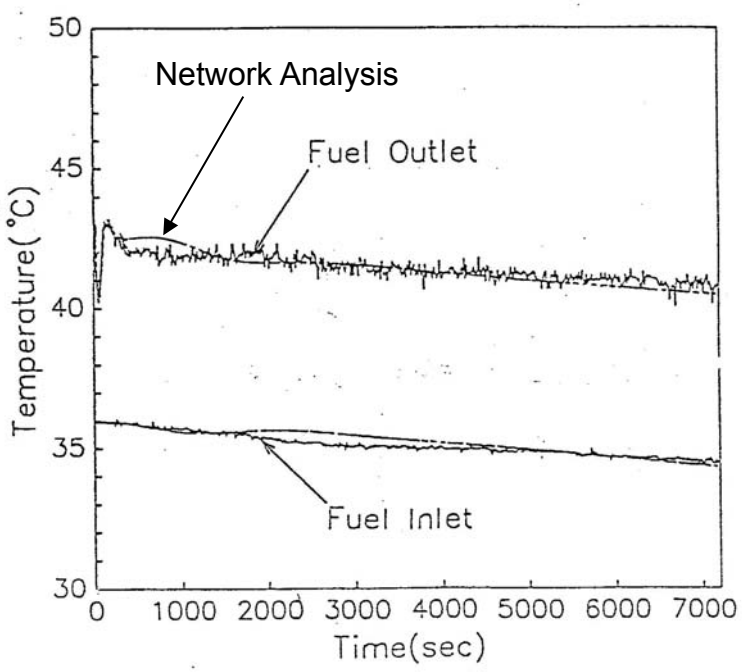

(b) PRACS

DELTA Experiments (Ieda, 1991)

Fig. 4.2-3 Core Inlet an Outlet Temperature Courses in Water Experiments featured with DRACS and PRACS

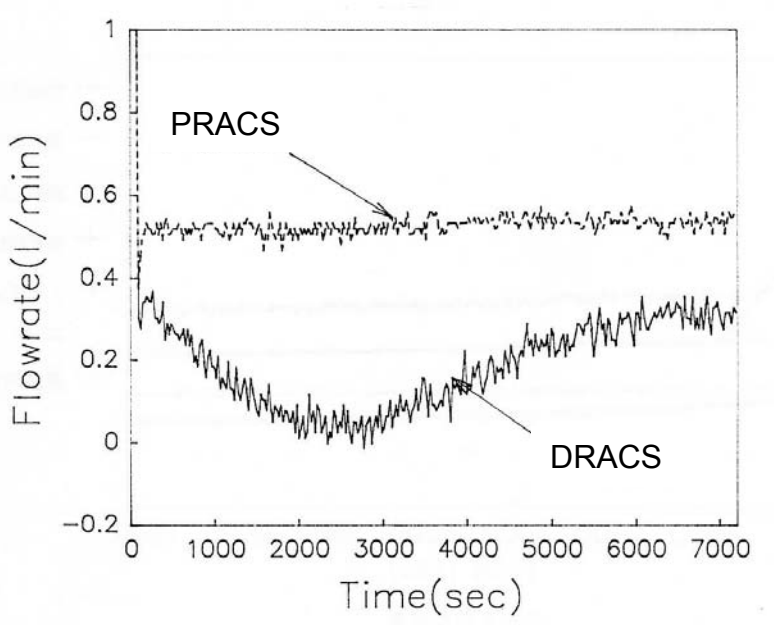

DELTA Experiments (Ieda, 1991)

Fig. 4.2-4 Comparison of Flow Rate Courses through a Core Subassembly between in DRACS and PRACS Cases

Comparisons between two situations, with IWF and without IWF, were conducted in order to evaluate IWF. The gap region between the subassemblies is closed at the bottom and open to the upper plenum at the height of the subassembly outlet. Thus, the sodium temperature difference between the inter-wrapper gap region and the upper plenum induces natural convection in the inter-wrapper gap, i.e., IWF. Thus, one of the experimental parameters was the choice of heat sink; that is, the DHX in the upper plenum or the IHX (the PRACS coil). When the IHX is selected, the upper plenum has the same sodium temperature as the outlet of the subassemblies. This means, then, that there is no temperature difference between the upper plenum and the core, and, therefore, no IWF phenomena.

The second parameter is the flow rate in the subassembly. The flow rate is determined by a balance between the natural circulation head and the flow resistances in both our model and actual reactors. In the experiments, however, the flow rates in the subassemblies were provided by a pump and actually covered a range equivalent to natural circulation conditions in reactors. This forced circulation option enabled us to set the same flow conditions between the cases using the DHX and the IHX. The flow rate was varied from 1% to 3% of the full flow condition in a reactor; that is, the flow velocity in the pin bundle of the center subassembly is set at 1% to 3% of that in a core fuel subassembly. In addition, extremely low flow conditions including zero flow rate in the subassemblies (valves in all feed lines were closed) were also examined in the cases using the DHX. The main experimental cases are Cases D2.6 to D0.0 and Cases P2.9 to P1.1 (see Table 4.2-2). The first character "D" indicates that the DHX is used and "P" indicates the IHX (the PRACS coil). The number "2.6" indicates that the flow velocity is 2.6% of the full power condition in a reactor. The Re number was defined in the 37-pin bundle using a hydraulic equivalent diameter in the bundle, the bundle average velocity and kinematic viscosity at average temperature along the heated length. The Re number was varied from 650 to 1900 in the flow conditions of 1 to 3%.

The heater power of the core was adjusted so that the heat flux at the pin surfaces in the center subassembly would be maintained at 1.5% of the full power conditions of a real reactor. As an additional parameter, the heater power level was varied from 1 to 2%.

Table 4.2-2 Experimental Parameters of Forced Circulation Experiments

Case Name[*1]	Power[*2] (kW)	(%)[*3]	Flow Rate[*2] (l/min)	(%)[*3]	Inlet Temp. to S/A (°C)	Heat Sink
D2.6	18.4	1.53	10.3	2.6	304	DHX (DRACS)
D1.9	18.3	1.53	7.6	1.9	303	DHX
D1.3	18.2	1.52	5.3	1.3	305	DHX
D1.0	18.1	1.51	4.0	1.0	308	DHX
P2.9	18.4	1.53	11.4	2.9	301	IHX (PRACS)
P2.2	18.5	1.54	8.7	2.2	305	IHX
P1.5	18.5	1.54	6.0	1.5	308	IHX
P1.1	18.4	1.53	4.5	1.1	305	IHX
D1.0a	18.4	1.53	4.2	1.0	277	DHX
D0.5	18.2	1.52	2.1	0.5	302	DHX
D0.0	18.5	1.54	0	0	-	DHX
D-F2P2	24.6	2.05	7.7	1.9	320	DHX
D-F1P2	24.2	2.02	4.2	1.0	305	DHX
D-F1P1	12.1	1.01	4.1	1.0	260	DHX

*1: D (DHX), P (IHX), F (Flow, %), P (Power, %)

*2: Value in Center Subassembly (same with that in other 6 subassemblies)

*3: Ratio to full power condition of a core fuel subassembly in a reactor

The heater power and flow rate in the subassemblies were set at the same values for each of the seven subassemblies using flow control valves in the feed lines between the lower plenum and the core. In order to simplify the phenomena in the core model, the valve openings of these flow control valves were set at a small value, i.e., flow redistribution between the subassemblies was suppressed. The inlet temperature of the core was set at a constant value (300˚C) in all experimental cases. The secondary circuit of the IHX was always closed by a valve. The experimental conditions are shown in Table 4.2-2. Steady-state condition was confirmed by noting a flat time trend in the upper plenum temperatures; typically, steady-state was attained in one day.

The data of temperature and flow rate were recorded for 300s at time intervals of 0.096s. The time-averaged data are discussed in the following sections.

b. Natural Circulation Condition

The influence of IWF on the primary loop flow was investigated by natural circulation experiments where no pump was operated in the primary loop. Experimental parameters were also selection of the heat sink, i.e., the DHX or IHX (the PRACS coil), and flow resistance in the primary loop which was controlled by an opening of the valve after the main pump (see Fig. 4.2-2). Comparison of thermohydraulics between the cases using the DHX and IHX will show influences of IWF on the primary loop flow rate. The natural circulation flow rate in an actual reactor will change during transient after the scram. Several water experiments (Ieda, 1991, Hoffmann, 1992) have shown that the primary loop flow rate decreases in a time range of 1000s (see Fig. 4.2-4) due to temperature increase in the IHX (decrease of the natural circulation head). In the experiments, the flow resistance in the primary loop (opening of the main valve) was varied to simulate such low flow rate situations. The influences of IWF were investigated under high and low flow rate conditions in the core.

A total of four experimental cases were carried out. The experimental conditions are listed in Table 4.2-3. The valve openings were set at 20% and 10% open position. Cases DN20 and DN10 are cases using the DHX with valve openings at 20% and 10%, respectively. Cases PN20 and PN10 are cases using the IHX with valve openings at

Table 4.2-3 Experimental Parameters and Results of Natural Circulation Experiments

	20% Valve Open		10% Valve Open	
Parameter	DRACS	PRACS	DRACS	PRACS
Case Name	DN20	PN20	DN10	PN10
Total Core Power	128 kW (1.5%*1)			
Inlet Temperature into Core	300 ˚C			
Flow Rate (l/min)				
Loop	29.2	38.1	15.4	24.6
Ratio (%)*1	1.04	1.36	0.55	0.88
Center S/A	5.0	5.4	3.8	3.6
Line-1	11.8	16.5	6.4	10.5
Line-2	12.4	16.2	5.2	10.5
Flow Redistribution*2				
Center S/A	1.20	0.99	1.73	1.02
Outer S/As	0.97	1.00	0.88	1.00
Highest Temperature				
Experiment	495˚C	473	498	570
Power/Flow*3	526˚C	474	729	569

*1 Ratio of experimental data to reactor rated condition

*2 Ratio of subassembly flow rate to 1/7th of loop flow Rate

*3 T_c in Eq. (4-2)

20% and 10%, respectively. The heater power in each subassembly was set at an identical value, 1.5% of full power conditions in an actual reactor with respect to the pin surface heat flux of the center subassembly. The flow control valves in the feed lines were set in a preliminary experiment so as to maintain flat flow distribution among all subassemblies at 2% flow rate of full power conditions in an actual reactor under forced convection and isothermal conditions. The valve openings were sufficiently large to allow flow redistribution between the subassemblies due to the temperature distribution across the core. The air cooler of the decay heat removal system was operated so as to keep the inlet sodium temperature of the core at 300 ˚C.

(3) Results of Forced Circulation Tests

a. Comparison between Cases using DHX and IHX

The vertical temperature distributions in the upper plenum are shown in Fig. 4.2-5 for Cases D1.0 and P1.1. The height 0mm corresponds to the core outlet level. The measurement position is at the mid-point between the vessel wall and the UIS wall, and circumferentially at an angle of 120˚ from the DHX position. Thermal stratification was seen in Case D1.0 due to the flow of cold sodium provided by the DHX. The temperature distribution in Case P1.1 was flat because there is no heat sink in the upper plenum.

The transverse temperature distributions at the top of the heated length, across the three subassemblies, along the 270˚-90˚ line (see Fig. 4.2-1) are shown in Fig. 4.2-6. In the cases using the IHX (P1.1 and 1.5), the lower flow rate resulted in a flatter temperature profile in the center subassembly. This is due to buoyancy-driven flow redistribution in the subassembly. The temperatures at the ends of the gap region (at -126 and 126mm) were nearly the same as the sodium temperatures at the wall subchannels in the center subassembly.

In the cases using the DHX (D1.0 and 1.3), the temperatures in the gap region were lower than the sodium temperatures at the wall subchannels in the center subassembly, and at the end of the gap regions in particular. This is due to IWF coming from the cold upper plenum (see Fig. 4.2-5). The temperature gradient in the center subassembly in each case using the DHX was steeper than in the case using the IHX which had nearly the same flow rate as the DHX case. This indicates that heat was removed by IWF through the wrapper tube wall.

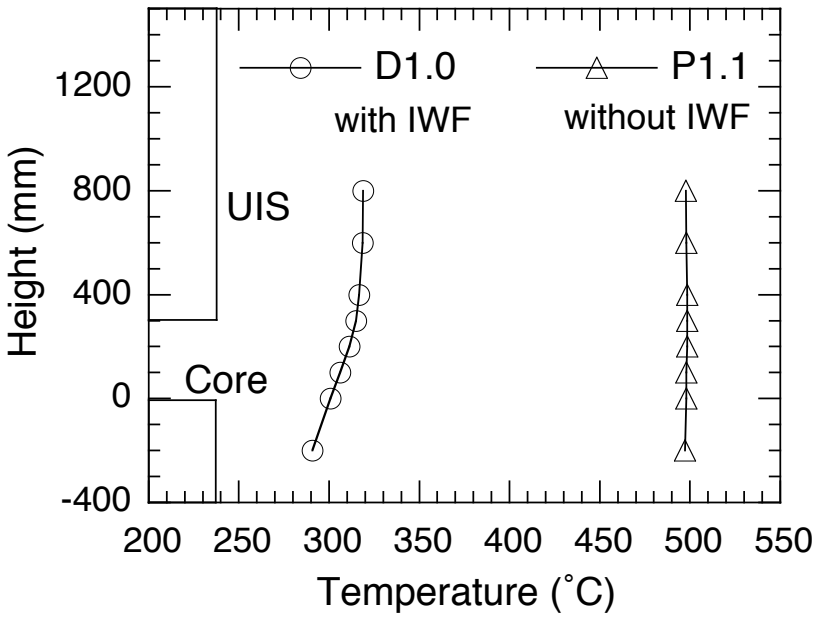

Fig. 4.2-5 Axial Temperature Distributions in Upper Plenum in Cases P1.1 and D1.0

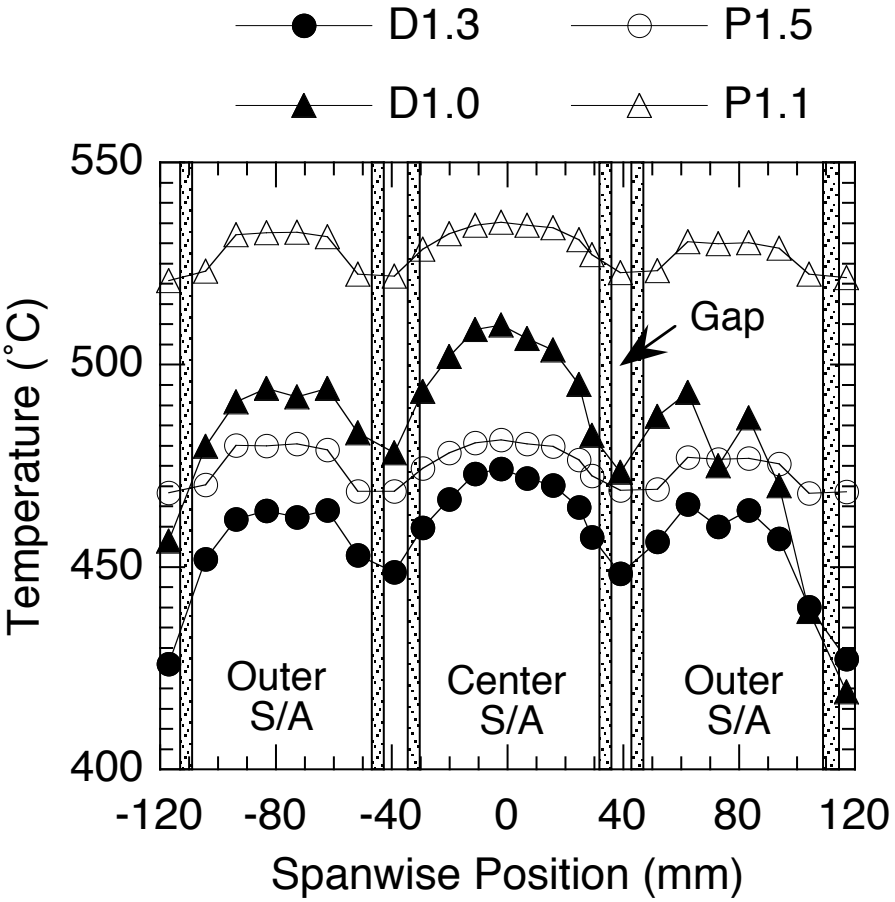

Fig. 4.2-6 Transverse Temperature Distributions at Top of Heated Length in Forced Flow Conditions

In general, the highest temperature in the core was registered in a subchannel around the center pin (the center subchannel) in the central subassembly as seen in Fig. 4.2-6. The axial temperature distributions along the center subchannel are shown in Fig. 4.2-7. The height of 0mm corresponds to the top of the heated length. In these cases using the IHX, the temperatures increased along the heated length and showed the maximum values at the top of the heated length. Mixing in the horizontal cross section and in the upper non-heated pin bundle caused a small temperature decrease. The temperature distribution in the upper reflector was nearly constant. On the other hand, in the cases using the DHX, the temperatures in the upper reflector decreased from the temperature at the top of the heated length due to IWF. This temperature decrease in the upper non-heated region reduces the natural circulation head and the flow rate in the primary loop equally. This will result in temperature increase in the core. This is a counter effect of IWF for NC/DHR and is discussed in the next section.

The hottest temperature in each case using the DHX was lower than that using the IHX, in which case nearly the same flow rate as the DHX case was given, due to the cooling effect of IWF. In Case D1.0, the highest temperature was not registered at the top of the heated length. In fact, heat removal through the wrapper tube wall exceeded the heat input at the end of the heated region, under 1% flow velocity in the subassembly, relative to the rated conditions of a real reactor.

The axial temperature distributions in the gap region are shown in Fig. 4.2-8 for Cases P1.1 and D1.0, respectively. In Case P1.1, the gap temperatures at both ends (at -126 and 126mm) were identical. The temperature distribution was similar to that along the center subchannel (see Fig. 4.2-7). In Case D1.0, the gap temperatures showed asymmetric characteristics at the two end positions and much lower temperature in the upper reflector region in contrast to the heated region. This temperature profile suggests the likely penetration of cold sodium into the right (90˚) end gap from the upper plenum. From here it penetrated into the gap region.

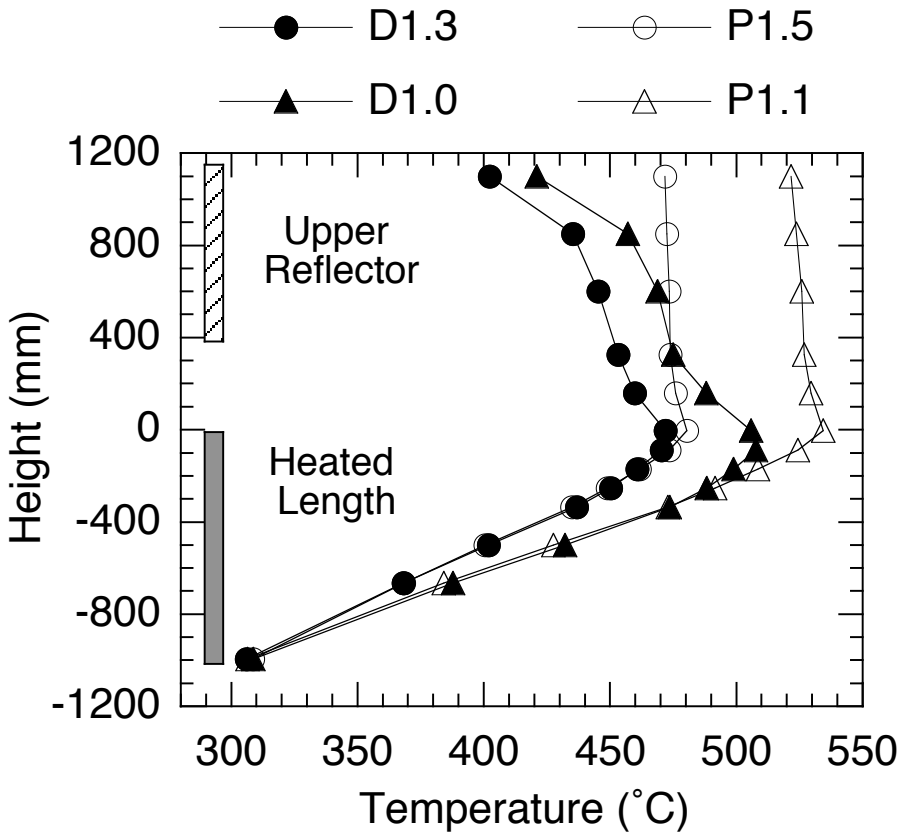

Fig. 4.2-7 Axial Temperature Distributions along Center Subchannel in Center Subassembly under Forced Flow Conditions

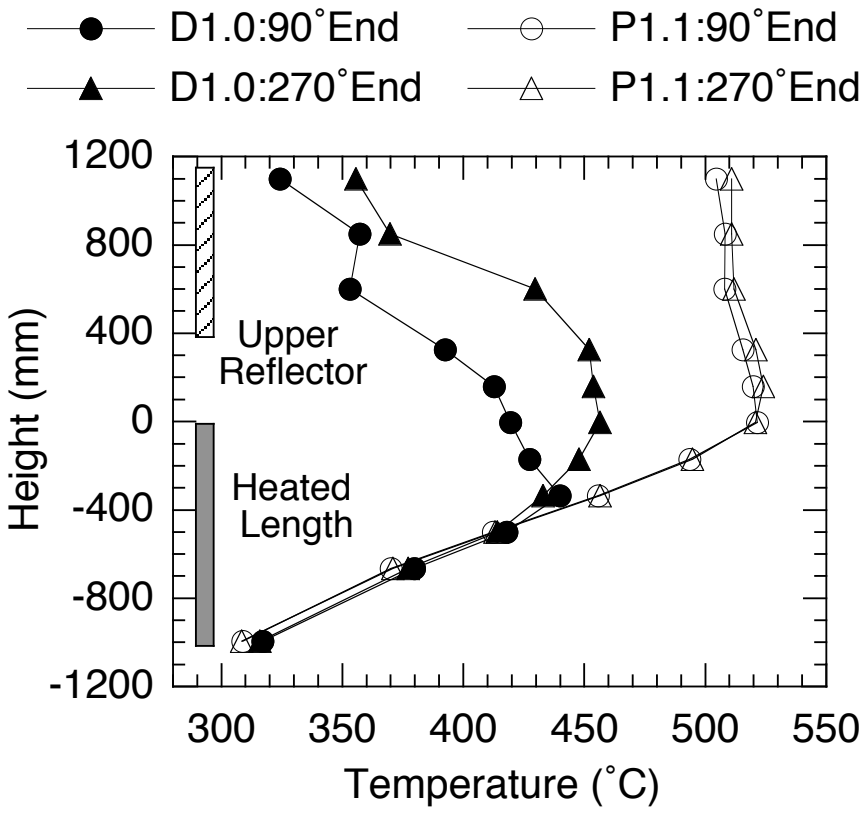

Fig. 4.2-8 Axial Temperature Distributions along Inter-wrapper Gaps at 90˚ and 270˚ Ends in Core Model under Forced Flow Conditions

b. Extremely Low Flow Conditions in Cases using DHX

Extremely low flow conditions in the subassemblies, including zero flow rate, were examined. The zero flow rate condition, in particular, simulates the situation where all primary circuits in a reactor are unavailable and decay heat is removed solely by in-vessel natural convections.

The axial temperature distributions along the center subchannel in the center subassembly are shown in Fig. 4.2-9. In Case D0.5, the upper 1/3 of the heated length showed a flat temperature profile due to heat removal by IWF. The temperature increase from the inlet was larger, by some 30˚C, in contrast to Case D1.0, as the flow rate in the subassembly was one-half that of Case D1.0 (heater power was identical). In Case D0.0, all feed lines into the subassemblies were closed by valves. The IWF could remove all heat generated in the subassemblies while maintaining the highest temperature below 600˚C. In the upper half of the heated length, the higher position exhibited a lower temperature than in the lower half. The highest temperature was registered at a position below the middle of the heated length where the power profile has a peak. A likely explanation for this heat sink trend is that the cold fluid in fact penetrates the gap regions from the upper plenum. Penetrating flow into the subassembly from the cold upper plenum can also function as a heat sink in the pin-bundle; however, it was observed only in the upper reflector, not in the pin-bundle. This penetrating flow was detected by temperature fluctuations caused by mixing between the falling cold sodium and rising hot sodium.

The transverse temperature distributions at the top of the heated length are shown in Fig. 4.2-10. In Case D0.0, a steep and asymmetric temperature distribution was seen in the center subassembly. This was caused by asymmetric flow in the inter-wrapper gap and natural convection in the subassembly. Figure 4.2-11shows the transverse temperature distributions in Case D0.0 during an extended time interval at the height where the highest temperature was registered. The temperature profiles were nearly identical during 1500s, a clear indication that natural convection in the subassemblies was stable.

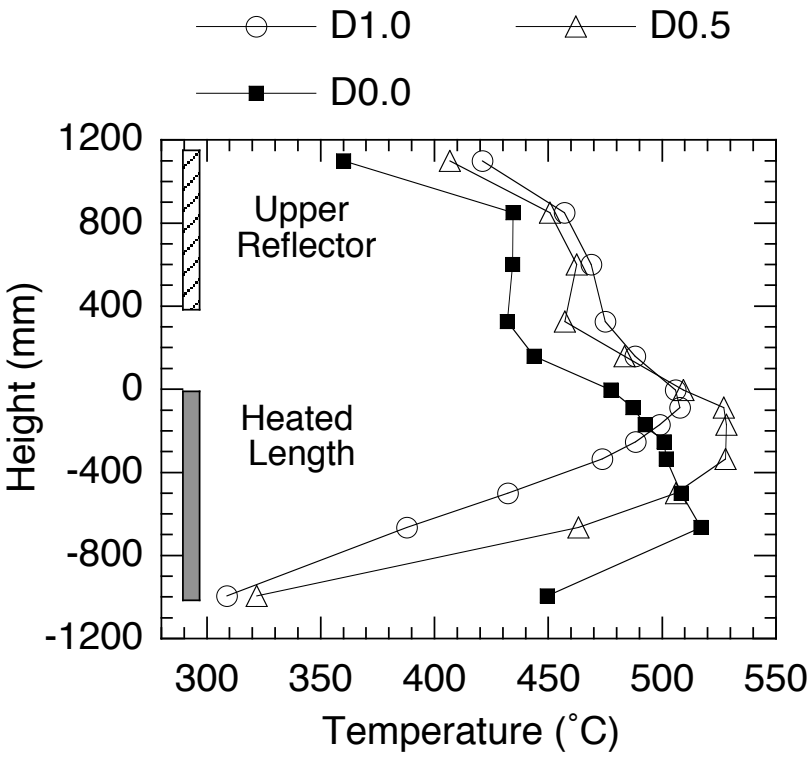

Fig. 4.2-9 Axial Temperature Distributions along Center Subchannel in Low Flow Cases under Forced Flow Conditions

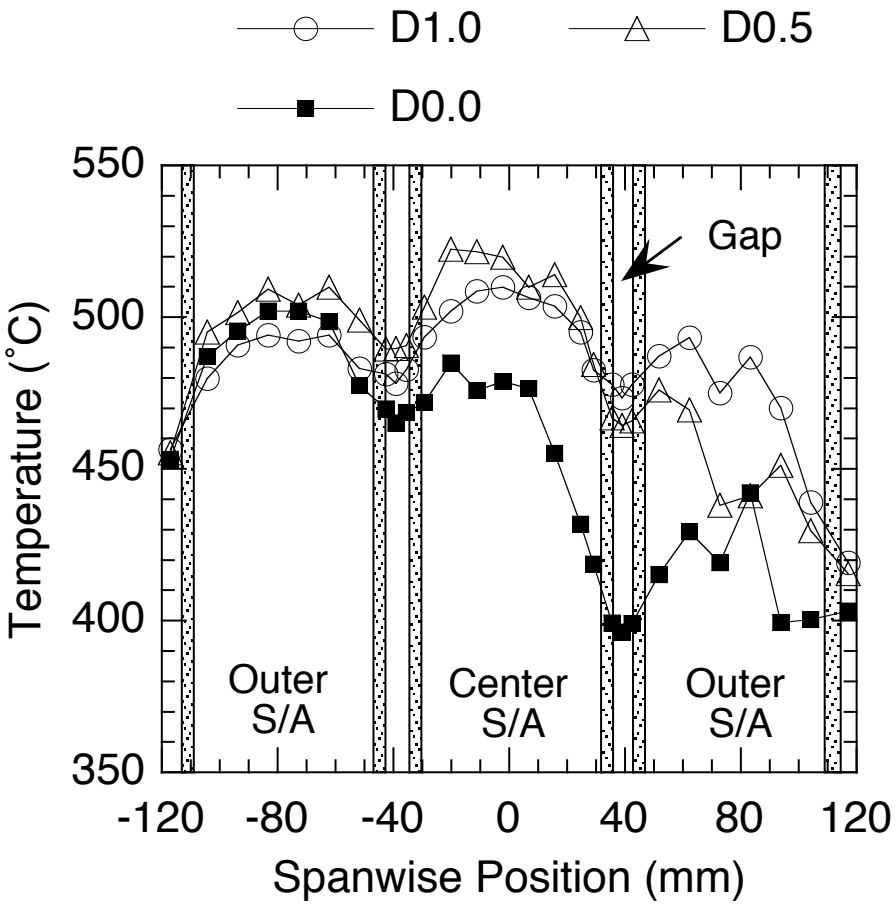

Fig. 4.2-10 Transverse Temperature Distributions at Top of Heated Length in Low Flow Cases under Forced Flow Conditions

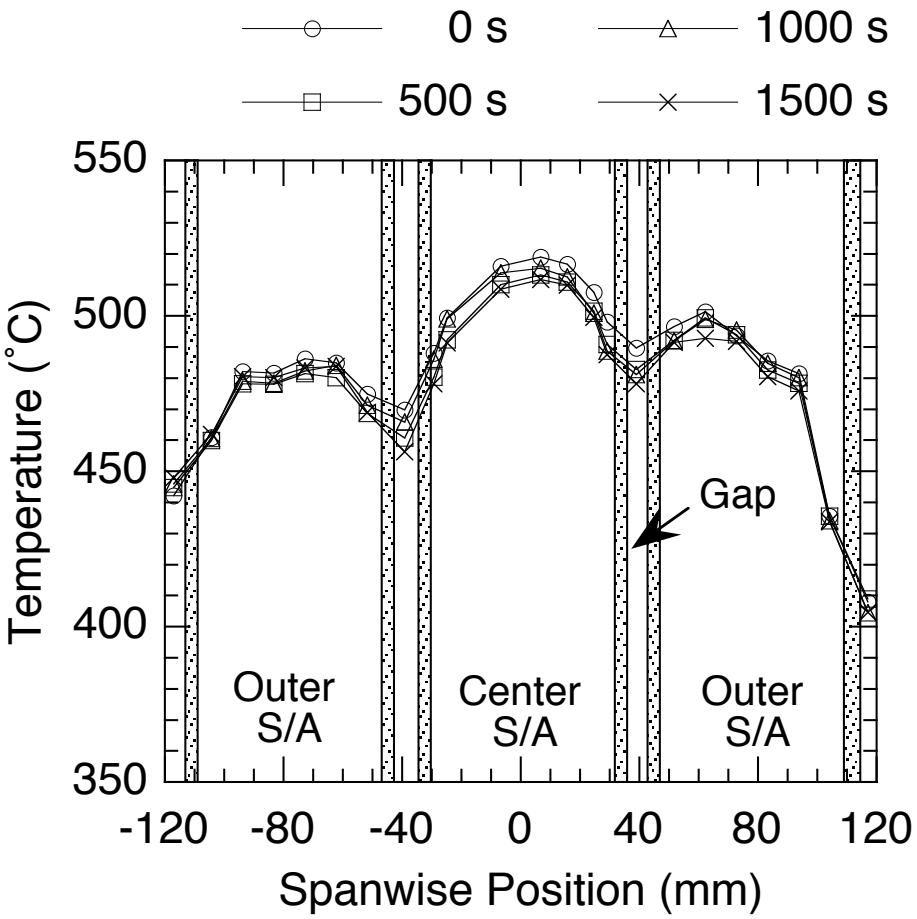

Fig. 4.2-11 Transverse Temperature Distributions at the Hottest Height in Case D0.0

The cooling effects of IWF were observed in the experiments. Figure 4.2-12 shows the influence of IWF on the highest temperature in the core in cases of the core power at 1.5% (see Table 4.2-2). The temperature increase at the peak point from the core inlet was normalized by the average temperature increase based on the flow rate and the heater power in the subassembly as follows,

$$T^* = \frac{T_{peak} - T_{in}}{\Delta T_{Q/F}}$$
$$\Delta T_{Q/F} = \frac{Q}{\rho Cp A_b V_b} \qquad (4\text{-}1).$$

In the cases without IWF (using the IHX), the non-dimensional peak temperature tended to reach unity as the flow rate decreased because of flow redistribution in the subassembly, i.e., the flow rate in the hot subchannels increased due to buoyancy force. In the cases with IWF (using the DHX), the non-dimensional temperature decreased from unity as the flow rate decreased. The influence of IWF was significant when the flow rate in the subassembly was less than 1%. The IWF could maintain the temperature increase in the core at only one-half value, which was estimated under adiabatic conditions at the wrapper tube wall and 0.5% flow velocity. This indicates that IWF can remove 50% of the heater power in the center subassembly.

(4) Results of Natural Circulation Tests

The influence of IWF on the natural circulation flow in the primary loop is discussed here. The measured flow rates in the primary loop and in the subassemblies are shown in Table 4.2-3. The loop flow rate in Case DN20 corresponds to 1.04% of full power conditions in an actual reactor and is smaller by a factor of 0.77 than Case PN20. One of the reasons for this is that the temperature in the upper plenum, when considered in terms of an upward flow path from the core outlet to an outlet nozzle, was lower (lower natural circulation head) in the cases using the DHX than in cases using the IHX. The loop flow rate in Case DN10 was reduced by factor of 0.53 from Case DN20. In contrast to this, the loop flow rate in Case PN10 decreased by factor of 0.65 from Case PN20. The reason for this relatively larger flow reduction in the cases using the DHX is the temperature drop in the core due to IWF.

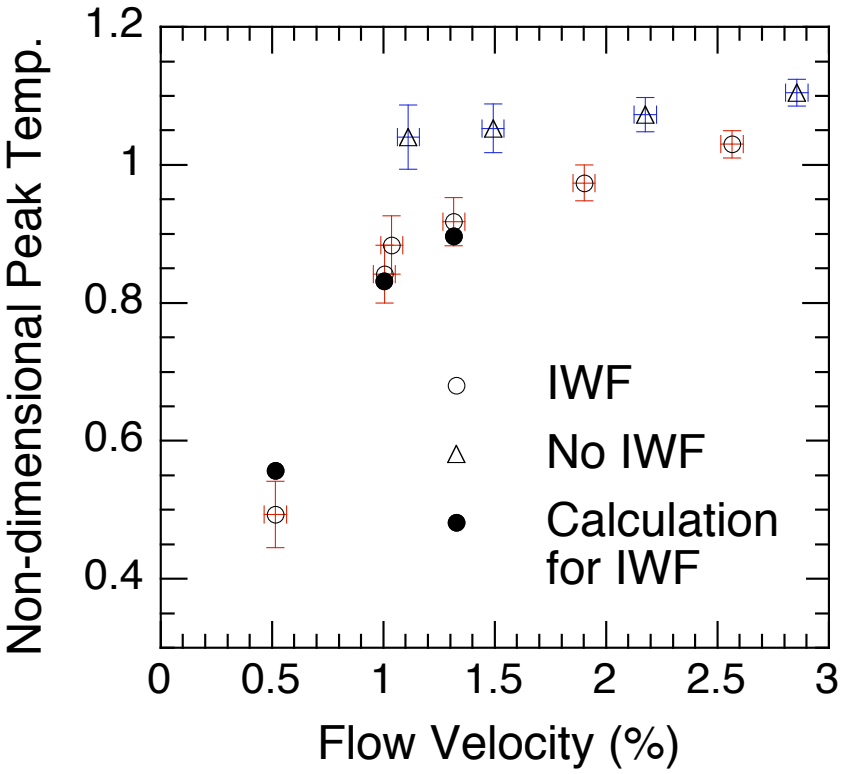

Fig. 4.2-12 Non-dimensional Peak Temperatures under Forced Flow Conditions

Flow distributions in the core were flat in the cases using the IHX, while the flow rates in outer subassemblies were smaller than that in the center in cases using the DHX. This tendency escalated in the cases with 10% valve opening. The flow redistribution in cases using the DHX resulted from the space dependent cooling effect of IWF.

Figure 4.2-13 shows transverse temperature distributions in the core at the top of the heated length in Cases DN10 and PN10. In the case using the DHX, the outer subassemblies show lower temperatures than the center subassembly in spite of the lower flow rates as shown before. This is due to the stronger cooling effect of IWF in the outer region of the core, where cold sodium penetrates into the outer gap region from the upper plenum. On the other hand, flow redistribution, from the outer subassemblies to the center subassembly, reduces the temperature in the center subassembly, for which direct cooling effect by IWF is weak because the temperature in the inner gap flow has already been increased by the heat from the outer subassemblies.

The highest temperature in the core was registered at subchannels around the center pin (center subchannels) in the center subassembly. Figure 4.2-14 shows the axial temperature distributions along the center subchannels in the center subassembly. In the cases using the DHX, the temperatures in the upper reflector decreased relative to the temperatures at the top of the heated length. This temperature decrease in the upper non-heated region reduced the natural circulation head and, consequently, the flow rates in the subassemblies. A larger temperature reduction in Case DN10 as compared to Case DN20 resulted in a larger decrease of the loop flow rate compared to the cases using IHX. In Case DN10, the temperature gradient in the upper half of heated length was small and nearly zero at the top of heated length. The highest temperature in the core in Case DN10 was lower than that in Case PN10, even though the loop flow rate was smaller by factor of 0.63. Thus the strong cooling effect of IWF is evident.

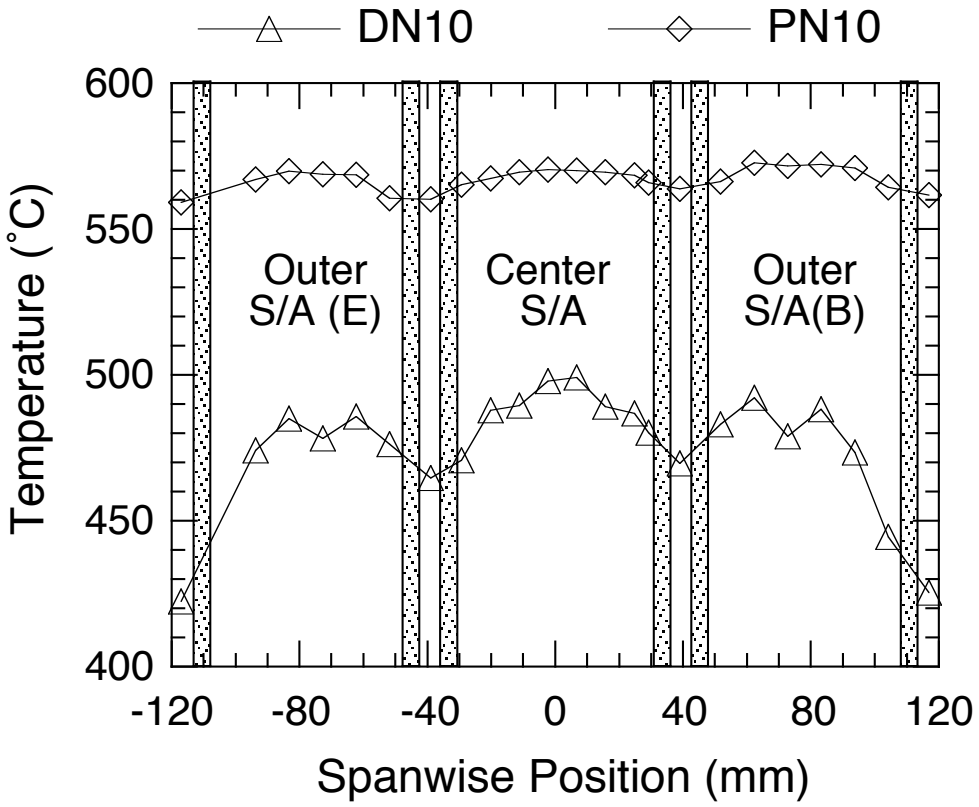

Fig. 4.2-13 Transverse Temperature Distributions at Top of Heated Length under Natural Circulation Conditions

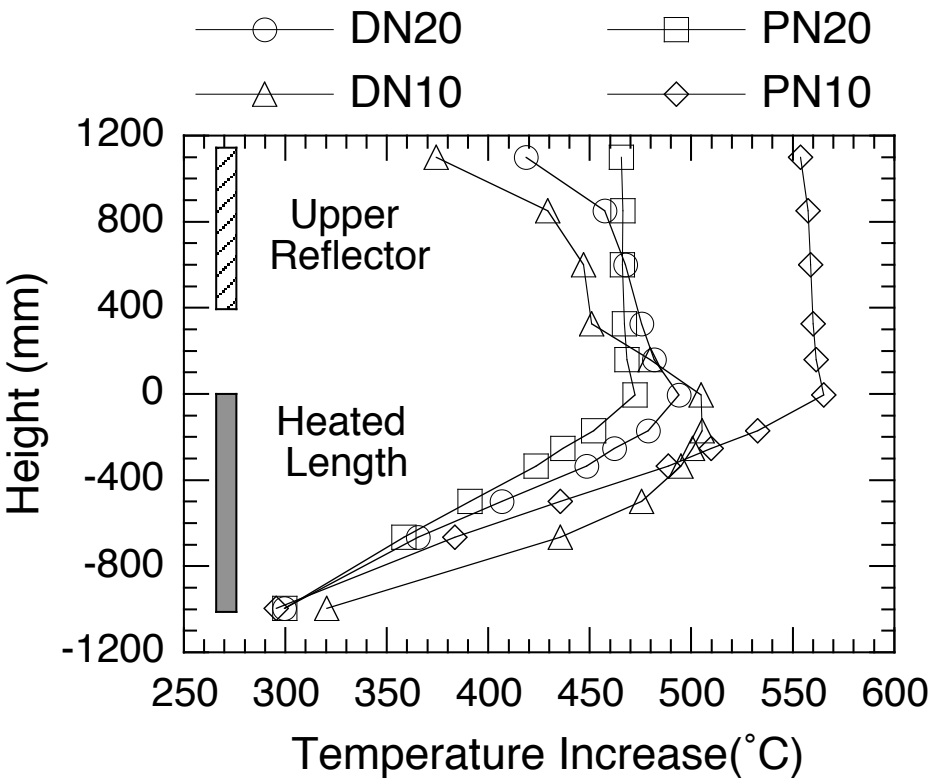

Fig. 4.2-14 Axial Temperature Distributions along Center Subchannel under Natural Circulation Condition

Figure 4.2-15 shows a density-height curve along the flow path through the center subassembly and the primary loop in Case DN10. The area enclosed by the loci of points in the clockwise direction corresponds to a positive natural circulation head, and the area in the counter clockwise direction corresponds to a negative head. A positive head was formed only in the core region. There was a negative head area in the upper plenum due to the cold sodium provided by the DHX. IWF cooled the upper non-heated section in the core (see Fig. 4.2-14) and reduced the positive head area in the core region. If the upper non-heated section were not cooled, the natural circulation head would increase. The hypothetical increase of the head is shown in the figure as a hatched area. The amount of potential head increase is approximately 120 Pa, an amount corresponding to 18% of the total natural circulation head in Case DN10. That is, IWF decreased the natural circulation head by 18%.

The highest temperatures in the core are compared with the average temperature obtained from the ratio of core power to loop flow rate in Table 4.2-3. The measured highest temperature in Case DN20 was higher by 20˚C than that in Case PN20 due to the lower loop flow rate. However, the temperature was, in reality, 30˚C lower than the calculated temperature, T_c, based on the power and flow ratio. Here,

$$T_c = T_{in} + \Delta T_{Q/F} \qquad (4\text{-}2).$$

This means in effect that IWF more than compensates the temperature increase resulting from a lower flow rate. When the valve in the primary loop was closed to 10%, the recovery due to IWF (231˚C) exceeded the influence of the flow reduction due to a decrease in the natural circulation head in the upper plenum and in the core (see Fig. 4.2-15). The highest temperature in the core in Case DN10 was some 70˚C lower than that in Case PN10, which has no reduction of natural circulation head.

The experimental data thus shows that the negative influence of IWF on the natural circulation flow rate in the primary loop was not as large as the beneficial cooling effect on the core. In spite of an 18% loss of the natural circulation head, a reduction by 231 ˚C was obtained at the hottest point in the core as compared with a situation of no heat removal through the wrapper tube wall.

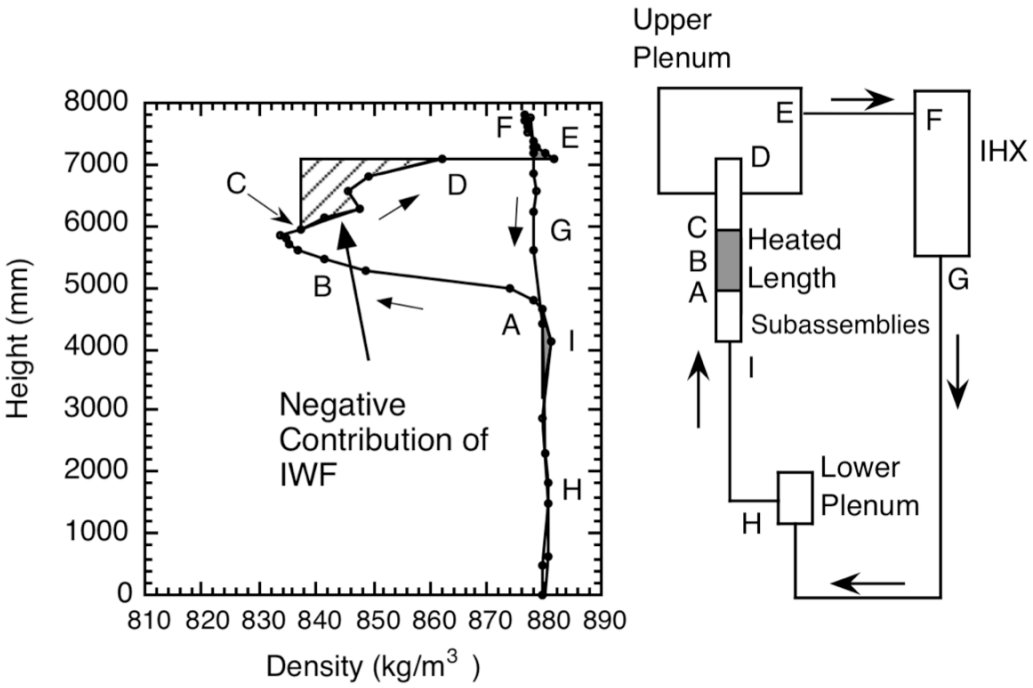

Fig. 4.2-15 Density-Height Curve along Primary Circuit in Case DN10

(5) Discussion

The experiments revealed that the highest temperature in the simulated core could be reduced by IWF, especially under low flow conditions. Here, a non-dimensional parameter for this cooling effect by IWF is introduced. The cooling effect can be described as a function of the ratio of the heat removal by IWF to the heater power (Q),

$$\frac{Heat(IWF)}{Q} \propto \frac{\rho Cp A_g V_g \Delta T_{Q/F}}{\rho Cp A_b V_b \Delta T_{Q/F}} = \frac{A_g V_g}{A_b V_b} \qquad (4\text{-}3).$$

Here, temperature increase in IWF was assumed to be proportional to the average temperature increase ($\Delta T_{Q/F}$) in the subassembly based on the flow rate and heater power in the subassembly. In the steady state condition of natural circulation, the outlet temperature of the upper plenum equals to the inlet temperature of the core because there is no heat sink in the primary loop. The temperature of penetrating flow into the gap region between the subassemblies equals the mixing temperature in the upper plenum and, consequently, the core inlet temperature. The exiting flow from the gap between the subassemblies will have the same temperature as the core outlet because of the low flow rate in the gap region and the complete heat exchange between the gap flow and the flow inside subassemblies. Thus, the temperature increase in the gap flow will be same as that in the core (in the subassemblies).

The flow velocity in the gap region associated with IWF (V_g) was estimated by a balance between the buoyancy force and the pressure loss,

$$g \rho \beta \Delta T_{Q/F} L = \frac{L+R}{D_g} f \frac{1}{2} \rho V_g^2 \qquad (4\text{-}4).$$

Here, the temperature difference for the buoyancy force was assumed to be $\Delta T_{Q/F}$. L and R are core height from the mid plane in the core and core radius, respectively. An experimental analysis using three dimensional thermal hydraulic code (see Chapter 5.) showed that the IWF flow velocity was 0.1 to 0.5 m/s (Reynolds number; 4,000 to

20,000). This suggests that the flow regime of IWF is turbulent. The Blasius equation could then be used as a friction factor,

$$f = 0.316\mathrm{Re}^{-1/4} \tag{4-5}.$$

A non-dimensional parameter was deduced from Eqs. (4-3), (4-4), and (4-5) such that,

$$\frac{Heat(IWF)}{Q} \propto C\frac{Gr^{4/7}}{\mathrm{Re}} \tag{4-6},$$

where

$$C = \frac{A_g D_b}{A_b D_g}\left(\frac{L}{L+R}\right)^{4/7},$$
$$Gr = \frac{g\beta\Delta T_{Q/F} D_g^3}{\nu^2}, \quad \mathrm{Re} = \frac{V_b D_b}{\nu} \tag{4-7}.$$

Figure 4.2-16 shows the relation between this parameter, C $Gr^{4/7}$/Re, and the non-dimensional highest temperature in the simulated core measured in the forced circulation experiments. The peak temperatures obtained from the three-dimensional calculations (see Chapter 5) are also shown. The core power range in the experiments is 1 to 2% of the reactor full power condition and the flow rate through the core is 0.5 to 3%. These variations cover the range of natural circulation conditions in an actual reactor core. The highest temperature could be plotted on a straight line not only in cases at the 1.5% power level, but also in cases at the 1 and 2% power levels. This provides evidence that the non-dimensional parameter, C $Gr^{4/7}$/Re, is suitable for estimating the cooling effects of IWF.

As for the non-dimensional parameter, C $Gr^{4/7}$/Re, turbulent flow regime was assumed in the gap region between the subassemblies based on the flow velocity range obtained by a numerical simulation. Influence of this flow regime assumption is confirmed below. When the flow regime in the gap region is laminar flow, the friction factor of laminar flow in a parallel flow channel can be used in stead of Eq. (4-5),

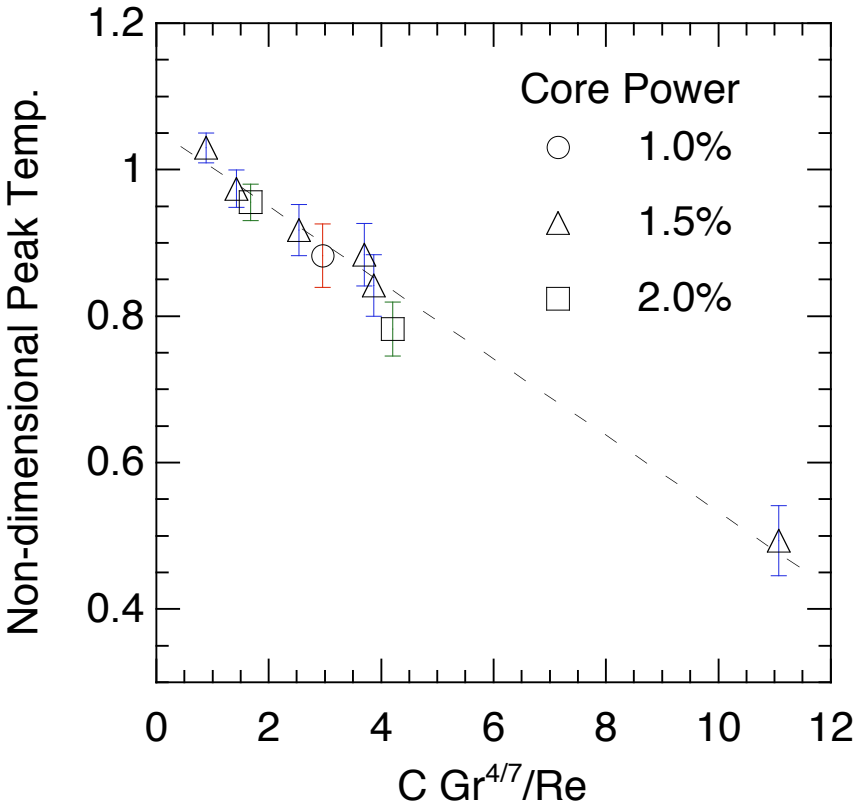

Fig. 4.2-16 Non-dimensional Peak Temperatures correlated with Dimensionless Number

$$f = \frac{96}{\mathrm{Re}} \qquad (4\text{-}8).$$

Then, a new non-dimensional parameter of IWF is deduced as follows,

$$\frac{Heat(IWF)}{Q} \propto C' \frac{Gr}{\mathrm{Re}}$$
$$C' = \frac{A_g D_b}{A_b D_g}\left(\frac{L}{L+R}\right) \qquad (4\text{-}9).$$

The definitions of Gr and Re are the same as in Eq. (4-7). The difference between the two non-dimensional parameters is the characteristic of Gr number, (4/7) for the turbulent flow and the unity for the laminar flow.

Figure 4.2-17 shows comparison of the non-dimensional peak temperatures between the Non-dimensional parameters of Eqs. (4-7) and (4-9), that is between the turbulent and the laminar flow regimes. The data of peak temperatures are correlated with the non-dimensional parameter in the laminar flow case as well as in the turbulent flow case. However, the linearity of the data on the non-dimensional parameter is better in the turbulent flow case than in the laminar flow case.

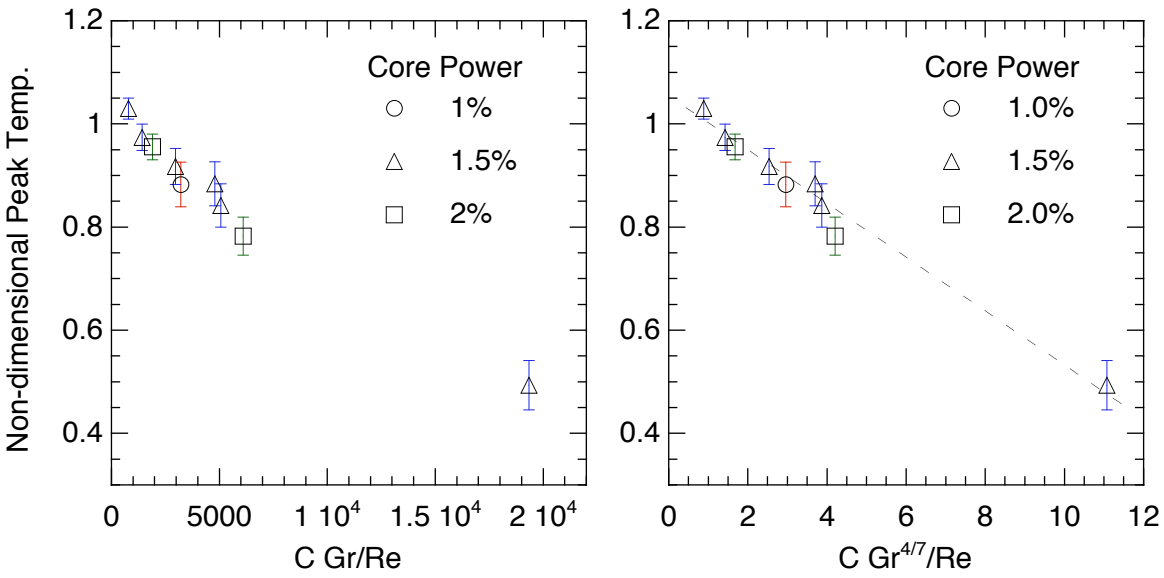

Laminar Flow: $f = \frac{96}{\mathrm{Re}}$ Turbulent Flow: $f = 0.316\mathrm{Re}^{-1/4}$

Fig. 4.2-17 Comparison of Non-dimensional Peak Temperatures between Non-dimensional Parameters based on Turbulent Flow and Laminar Flow Regimes

(6) Summary

Thermohydraulic experiments in a sodium facility were carried out in order to investigate IWF during natural circulation decay heat removal in fast reactors. The reactor core geometry was simulated by seven subassemblies. The temperature fields in the simulated core were measured under forced circulation and steady-state conditions with zero to 3% flow velocity in the subassemblies relative to the full power conditions of an actual reactor. The influence of IWF on natural circulation flow in the primary loop was also examined by conducting model experiments under natural circulation conditions. The following conclusions were reached from the experiments:

- When IWF occurred, the gradient of the transverse temperature distribution in the subassembly tended to increase. The axial position corresponding to the maximum temperature was, in fact, lower than the top of the heated length. These points should be considered in order to estimate the maximum temperature, which is influenced by the heat transfer through the wrapper tube wall.

- IWF can reduce the peak temperature in the subassembly. The cooling effect was significant when the flow velocity in the subassembly was less than 1% relative to rated conditions in a reactor. A new non-dimensional parameter, $C\ Gr^{4/7}/Re$, was introduced to characterize estimates of the cooling effects.

- The flow rate under natural circulation in the primary loop was also reduced by IWF; however, the cooling effect was relatively larger than the negative influence via the flow reduction when the primary flow rate was less than 1% of reactor rated conditions.

- The cooling effect of IWF was more evident in the outer subassemblies and weaker in the center subassembly. However, an indirect cooling effect due to IWF was seen in the center subassembly via the flow redistribution from the outer subassemblies to the center subassembly.

4.3 Transient Sodium Experiment

(1) Experimental Condition

As mentioned above, IWF exerts significant influence on core thermohydraulics. It has two major effects; 1) heat removal through the wrapper tube and 2) reduction of loop flow rate via the temperature decrease in the core, especially in the upper non-heated region. Decay heat removal should be maintained during transient from the scram. Thus, the time constants of these two effects are of importance. The core thermal hydraulics including IWF was investigated in transitions with a decrease of primary flow rate in a heat transport system with a DRACS. Two cases of transient experiments from forced to natural circulation were carried out. The operating condition of the secondary circuit of an IHX was selected as an experimental parameter. This brings a drastic change of natural circulation flow rate in the primary circuit. One is Case-Ref, where natural circulation in the IHX secondary loop is maintained during entire time of transient. The other is Case-Stop, where the natural circulation is stopped at a certain time.

The power and flow trends in the core are shown in Fig. 4.3-1. Since the pin bundle geometry in the subassembly is modeled in full scale, the time scale in the experiments was set to be the same as the reactor time. These curves simulated a transition from forced to natural circulation in the reactor and were identical between the two cases. Under the initial condition, the flow velocity and the average pin surface heat flux in the center subassembly were 0.6 m/s and 15 W/cm^2, respectively. They correspond to approximately 12% of the rated flow and power (full power conditions) in a reactor. The heater powers and the flow rates were identical among all subassemblies. The power transient in the experiments started at zero seconds and was controlled to simulate a power-to-flow ratio in the reactor within 30s. Thereafter, the power curve in the experiment traced the decay heat curve. The primary flow was reduced along the coast down curve, halving time of 7s, and the pump stopped at 61s from the scram. Thereafter, the natural circulation started. The Re number in the 37-pin bundle was changed from 7,000 to 600 (at 1% flow of full power condition) in this transient.

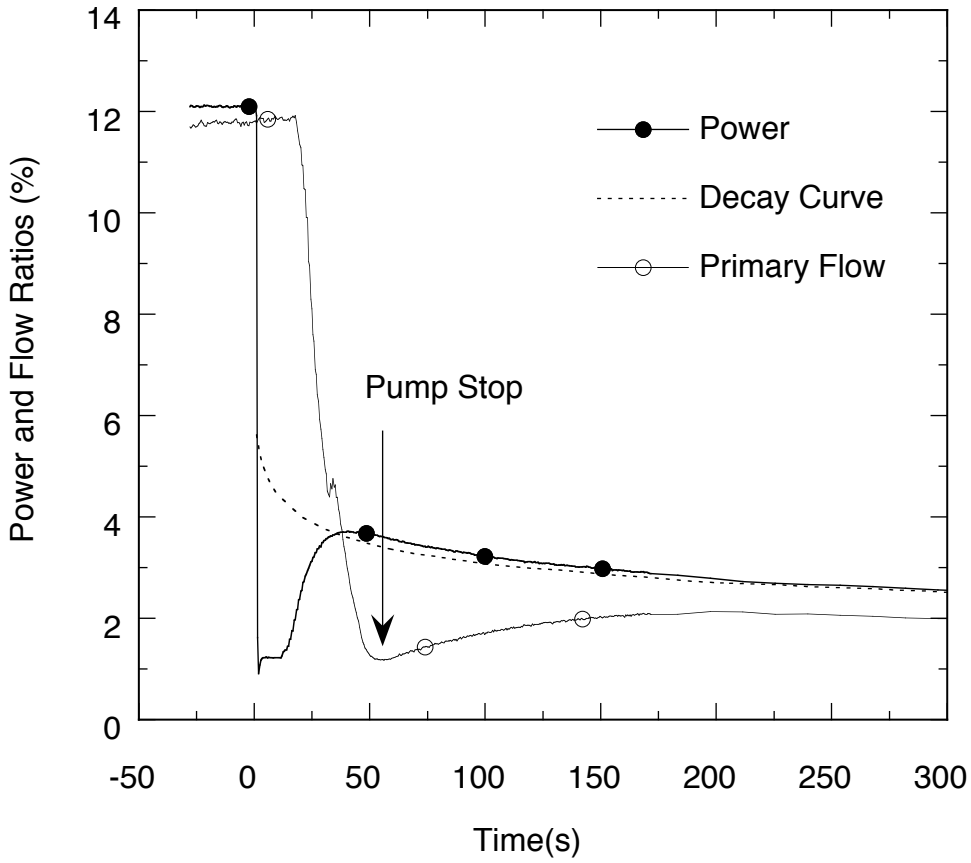

Fig. 4.3-1 Power and Flow Courses in Transient Experiments

As for the operation of the DRACS, a pump in the DHX secondary circuit and a blower in the air cooler started at 50s. These forced convections in the DRACS were continued until the end of the experiments. Under the initial condition, the heat in the core was removed by the main air cooler in the IHX secondary circuit. The flow rate in the IHX secondary circuits was coasted down in the same way as that in the primary circuit, and the pump and the blower of the main air cooler stopped at 60s. Dampers in the main air cooler were still open and natural draft was effective in the air side. In Case-Ref, natural circulation in the secondary circuit of the IHX was continued until the end of the experiment. In Case-Stop, a valve in the IHX secondary loop was closed at 2400s, and then the dampers were closed. This indicates that the natural circulation in the IHX secondary circuit was stopped at 2400s. In a reactor, when the steam generators stop during the scram transitions, the heat sink in the secondary loop of the IHX is lost and the natural circulation flow rate is decreased. Case-Stop simulated such flow rate reduction in the IHX secondary side.

(2) Experimental Results

Figure 4.3-2(a) shows the experimental results of flow trends in the primary loop in Cases-Ref and -Stop with a power curve during 7000s from the scram. Figure 4.3-2(b) shows the flow rate in the IHX secondary loop and the temperature histories at inlet and outlet of the IHX primary side in Case-Stop. The natural circulation in the primary loop started at 61s and achieved a peak flow rate at 200s. Thereafter, the flow rate decreased as the outlet temperature of the IHX increased. In Case-Stop, the IHX outlet temperature increased at 2400s due to the stopping of natural circulation in the secondary loop. This temperature increase resulted in a significant reduction of the primary flow rate. On the other hand, the primary flow rate in Case-Ref was kept at nearly 1% due to the continuous cooling in the IHX. These results show that the natural circulation in the primary loop strongly coupled with heat removal in the IHX secondary side.

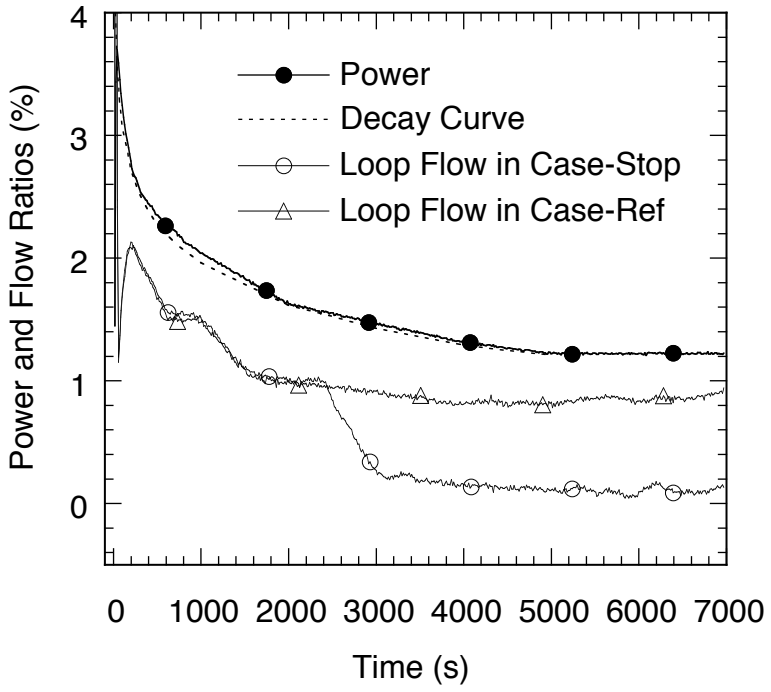

(a) Power and Flow Rate in Primary Loop

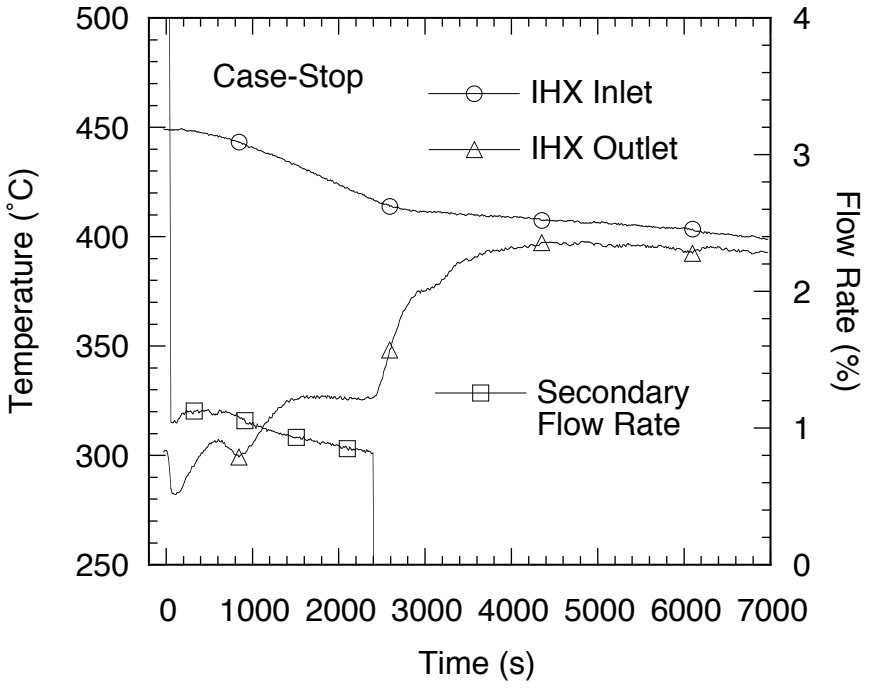

(b) IHX Temperatures and Flow Rate in Secondary Loop in Case-Stop

Fig. 4.3-2 Natural Circulation Flow Rates in Primary and Secondary Loops

The density-height curve in the primary loop in Case-Stop is shown in Fig. 4.3-3 at 3600s. The negative head region (gray area) was formed in the downstream piping of the IHX. This negative head reduced the natural circulation flow rate in the primary loop. The PLANDTL-DHX test facility has piping at a lower position than the core inlet height in the downstream piping from the IHX. Such low pipe configuration is not seen in a reactor design. One of the reasons for the low flow rate in the primary loop after 2400s registered in the experiment is this piping layout. Relative volume of the upper hot plenum per subassembly in the experiments is larger than in the reactor. This maintains the IHX at a high temperature and causes a low natural circulation head for a longer period of time compared with the reactor. Thus, the flow reduction would be not significant in the reactor. We can consider the low primary flow rate in the experiment an extreme condition for decay heat removal.

Figure 4.3-4 shows the flow courses in Case-Stop through the center subassembly and in two feed lines, Line-1 and Line-2, each connected to three outer subassemblies. Figure 4.3-5 shows the temperatures at inlet and outlet of Subassemblies-B and -C (see Fig. 4.2-1) connected to Line -1 in Case-Stop. The flow trends show that the reverse flow occurred in Line-1 from 3000 to 5000s. At 3000s, the inlet temperature increased rapidly and outlet temperatures decreased, and these temperatures reversed at 4800s in Subassembly-B. The same phenomena were registered in Subassembly-A. Such temperature inverse was not registered in Subassembly-C. In the subassemblies connected to Line-2, the temperature reverse was registered only in Subassembly-F. These results indicate that cold sodium entered from the upper plenum and flowed downward in Subassemblies-A, -B, and -F. The reversed flow was fed into the upward flow channels via the lower plenum. That is, the reverse flow through the subassemblies can serve as a flow path in addition to the primary loop.

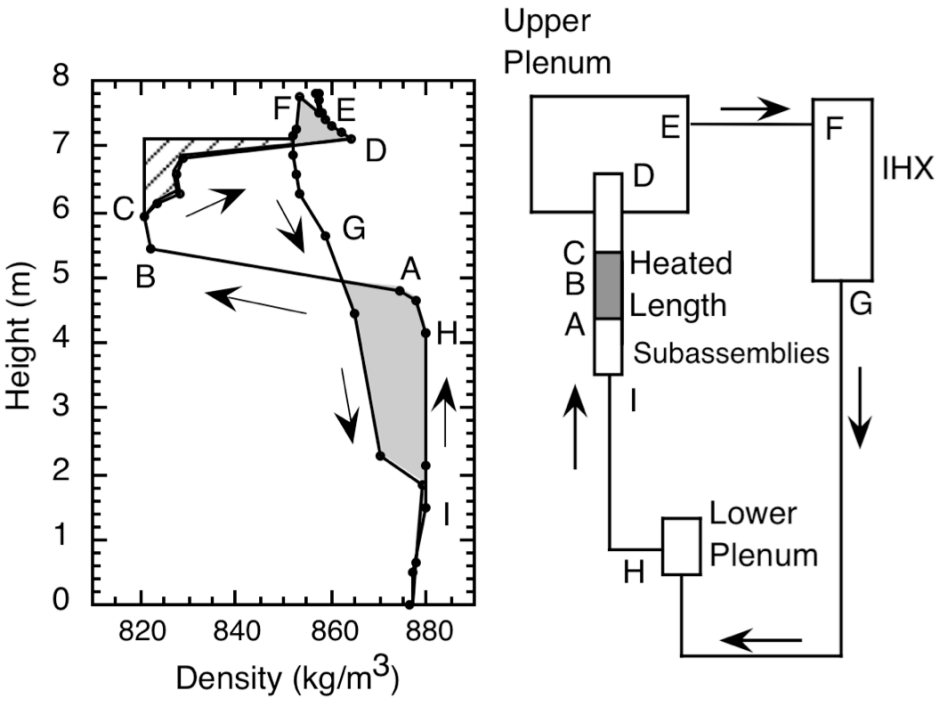

Fig. 4.3-3 Density-Height Curve in Case-Stop at 3600s

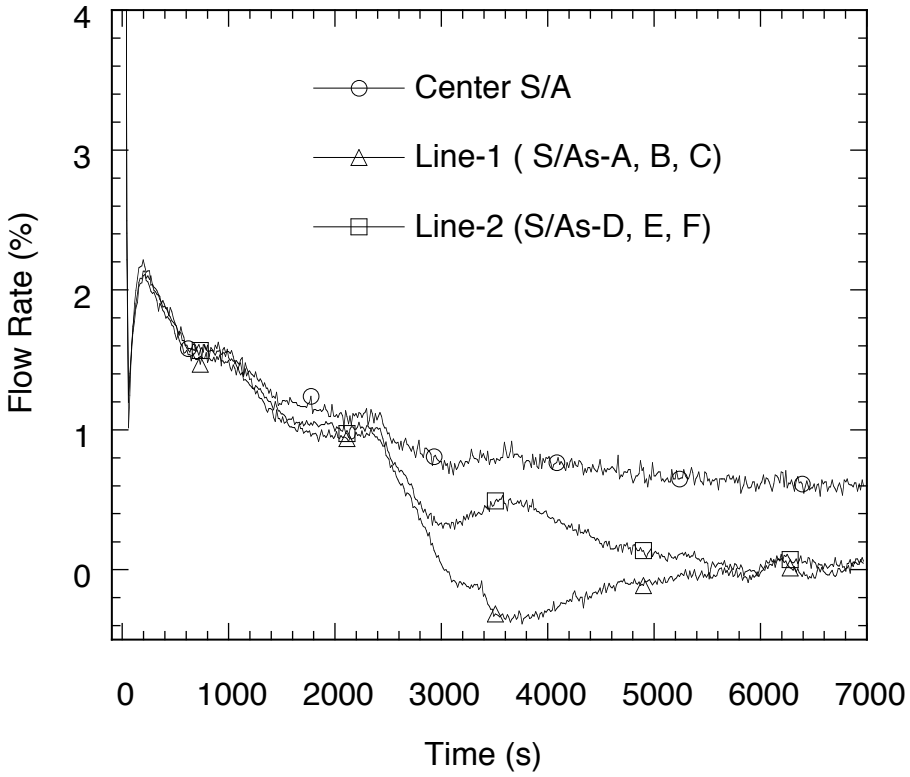

Fig. 4.3-4 Natural Circulation Flow Rates in Subassemblies in Case-Stop

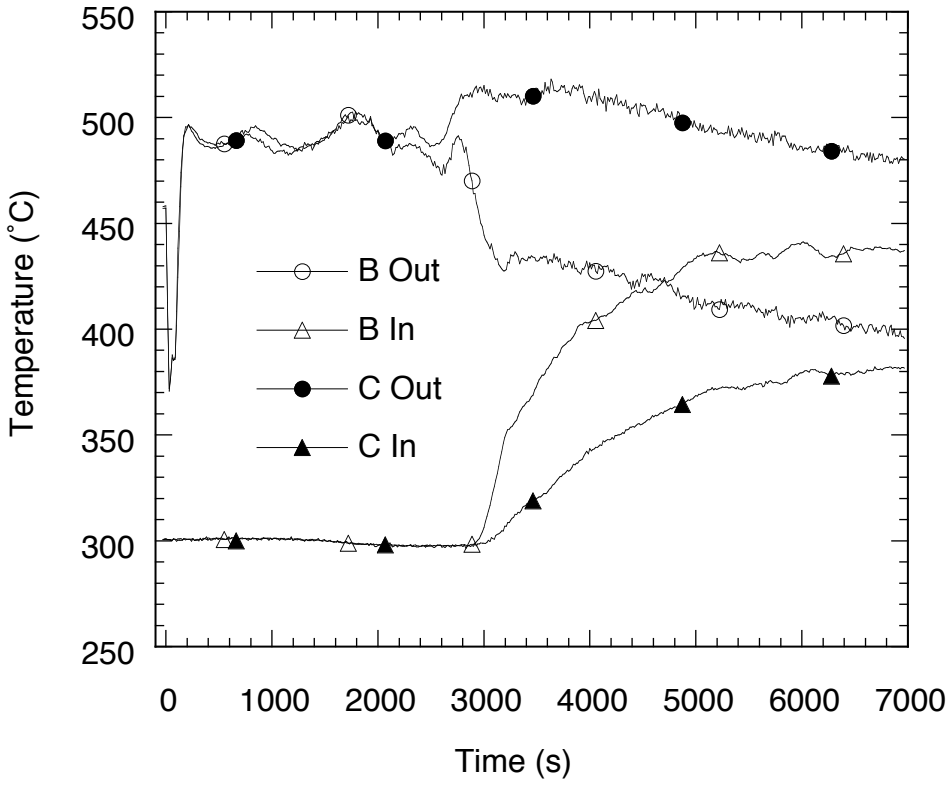

Fig. 4.3-5 Temperature Trends at Inlet and Outlets of Subassemblies B and C in Case-Stop

Temperature trends of the center subchannel in the center subassembly at the end of heated length and of the core inlet in Cases-Ref and -Stop are shown in Fig. 4.3-6. The highest temperature in the core was registered at the end of heated length in Case-Stop. The center subchannel temperature decreased monotonously in Case-Ref after 2000s due to the decay of heater power. On the other hand, in Case-Stop, the temperature at the top of the active heated length increased during 2400 to 3600s due to the decrease of primary flow rate and also the increase of inlet temperature. However, the peak temperature in Case-Stop was higher by only 50˚C than that in Case-Ref although the loop flow rate in Case-Stop was less than 20% of that in Case-Stop.

Figure 4.3-7 shows the axial temperature distributions along the center subchannel in the center-subassembly at 2800 and 3600s. In Case-Ref, the temperature increased along the heated length at both time points. The temperature profile in the upper half of heated length, however, was flat at 3600s in Case-Stop. This indicates that the heat in the subassembly was removed through the wrapper tube in the upper half region.

Transverse temperature distributions along the 270˚-90˚ line (see Fig. 4.2-1) at the top of the active heater are shown in Fig. 4.3-8 at 2800 and 3600s. The temperature gradient in the center-subassembly in Case-Stop was larger than that in Case-Ref at 2800s due to the larger heat removal through the wrapper tube. At 3600s, the temperature at the right hand side in the center-subassembly showed a sharp fall in Case-Stop. This temperature profile may result from strong heat transfer through the right side wall. Low temperature in Subassembly-B (right hand side) was seen at 3600s. This is due to the cold reverse flow from the upper plenum. These data show that the center-subassembly was cooled by the inter-wrapper flow and the inter-subassembly heat transfer to the reverse flow channels after 2400s.

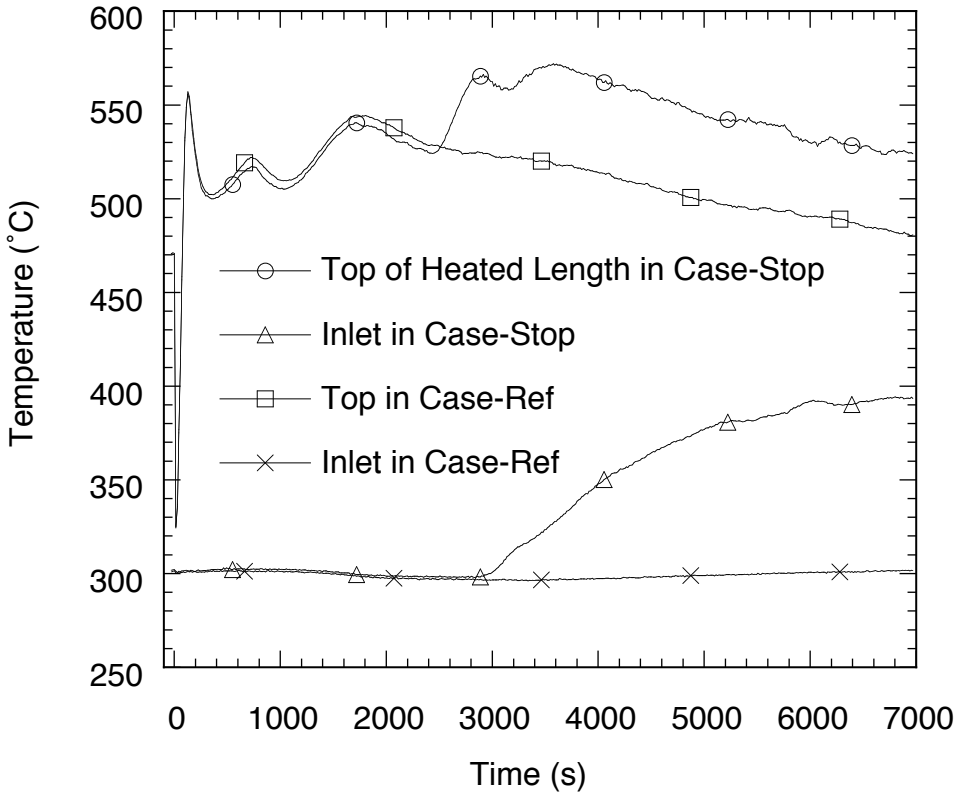

Fig. 4.3-6 Temperature Trends at Inlet and Top of Heated Length in Center Subchannel in Cases-Ref and -Stop

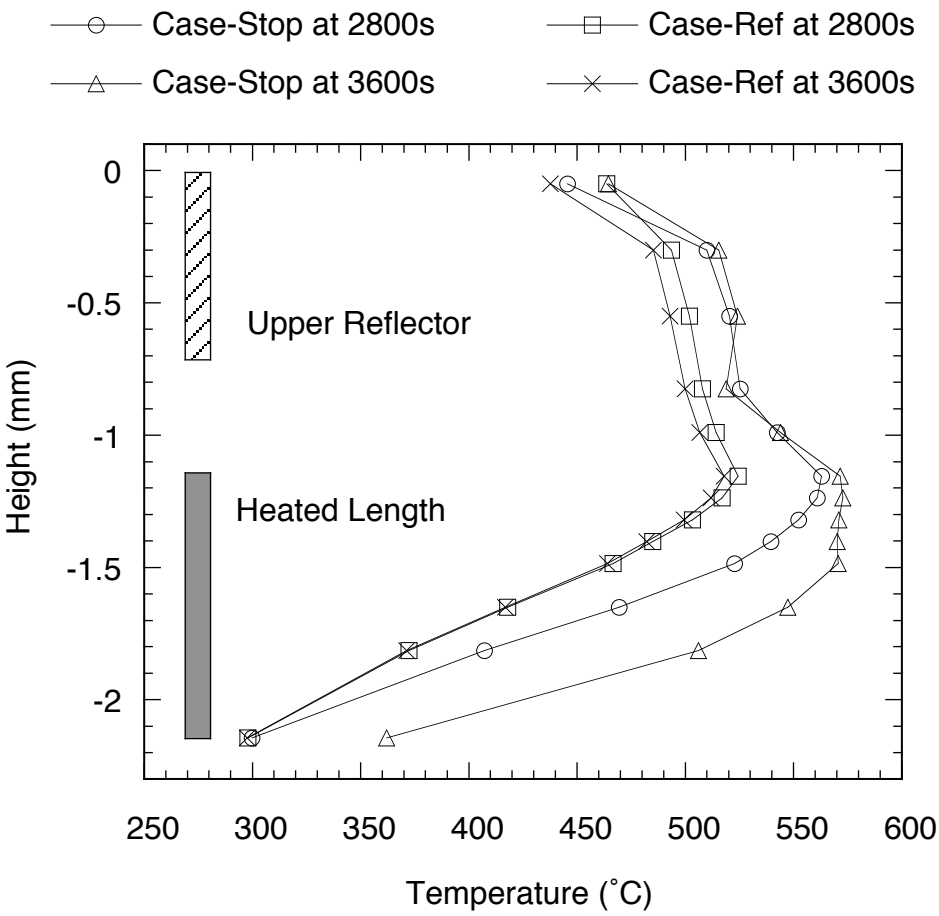

Fig. 4.3-7 Axial Temperature Distributions along Center Subchannel in Cases-Ref and -Stop

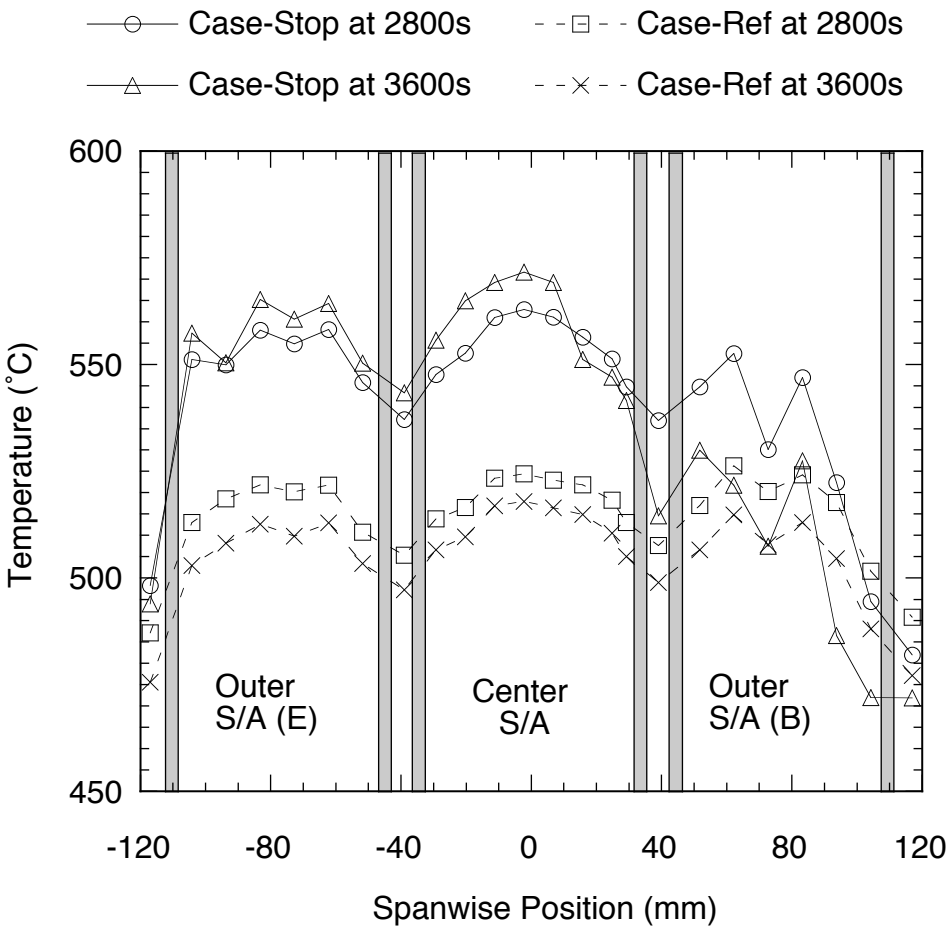

Fig. 4.3-8 Transverse Temperature Distributions at Top of Heated Length across Core Region in Cases-Ref and -Stop

Figure 4.3-9 shows the time histories of the highest temperature in the core and the average temperature obtained from the core power and loop flow rate. In Case-Ref, the registered temperature was lower by approximately 20˚C than the calculated temperature, Tc, based on power and flow ratio and assumption of quasi steady state. This is due to the cooling effect of IWF. In Case-Stop, the calculated temperature increased to beyond 800˚C at 2800s due to the reduction of the loop flow rate. However, the measured highest temperature was below 570˚C during the entire period. In addition, the calculated temperature from the flow rate and power in the center subassembly is also shown in Case-Stop. The measured data were still below the calculated values after 3000s. The reasons to maintain the highest temperatures at lower value are the cooling effect of IWF and the heat transfer to the reverse flow subassemblies.

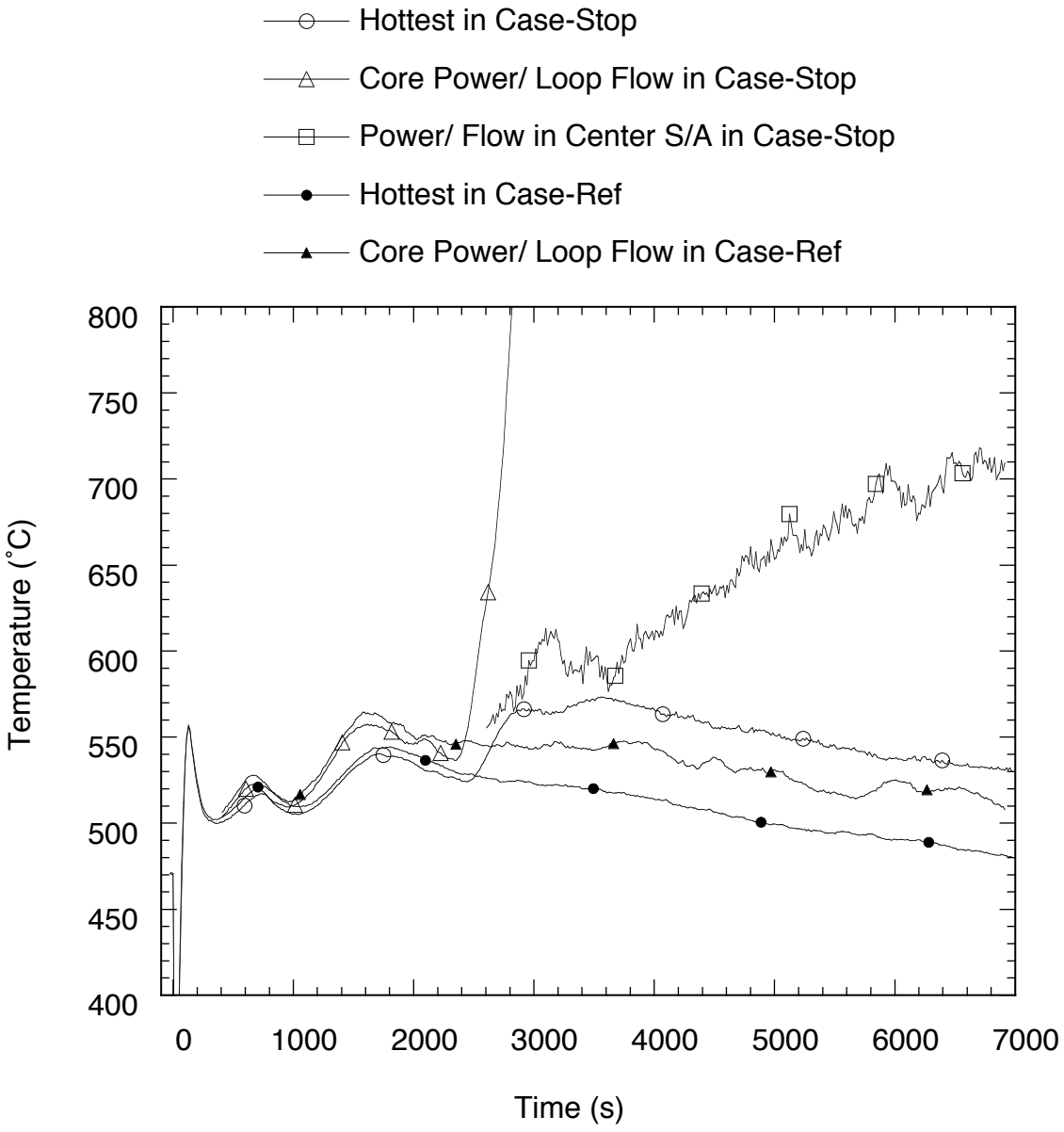

Fig. 4.3-9 Highest Temperature Courses in Experiments and Calculated Data from Power and Flow Rate

(3) Discussions

a. Influence of IWF on Loop Flow Rate

In Case-Stop, the natural circulation flow rate in the primary loop was reduced and not recovered after the closure of the IHX secondary loop. The flow decrease was caused by the temperature increase in the IHX primary side and the existence of low temperature sodium in the upward inlet piping toward the core (downstream piping from the IHX). The flow recovery was delayed by the extremely low flow rate via the transport delay in the piping from the upper plenum to the core. When the primary loop was filled with the cold sodium from the upper plenum where the DHX is operated, the natural circulation head and the flow rate recovered. In fact, the primary flow rates were sufficiently larger in the steady state cases in section 5.2, i.e., Cases-DN10 and -DN20 as compared with the flow rate after 3000s in Case-Stop.

During the low flow period in Case-Stop, IWF contributed to the cooling of the core, as shown in the previous section. The influence of IWF on the loop flow rate was not large. Figure 4.3-3 shows that reduction of natural circulation head due to IWF cooling in the core was less than 20% of the positive head. On the other hand, IWF had a limited effect on core thermal hydraulics in Case-Ref, where the primary flow rate was maintained at approximately 1% of the full power conditions in the reactor in spite of the low temperature condition in the upper plenum, which was the same as Case-Stop. This indicates that the core-plenum interactions, i.e., IWF, flow reverse in the subassemblies, and the inter-subassembly heat transfer provide on-demand cooling of the core and have no significant draw back when the core is sufficiently cooled by the primary flow.

b. Limitation of Subassembly Model

It was shown that IWF had the potential to cool the core in the case of low flow rate conditions. This cooling function will depend on the geometry of the core, e.g., size of the subassemblies and the spacer pad shape between the subassemblies. The simulated core consists of seven subassemblies, and each subassembly has 71mm of flat-to-flat distance, which is nearly 1/2 of the 217-pin subassemblies in a large scale fast reactor. The spacer pad is not simulated. Several cylinders are installed in the core as spacers

between the subassemblies instead of the spacer pad. On the point of heat transfer area, the wrapper tube size is an important factor in determining heat removal due to IWF. An area parameter can be defined as a perimeter length of wrapper tube divided by pin number. This area parameter is 6.6 mm/pin for the PLANDTL-DHX center subassembly and 2.4 mm/pin for a large scale reactor. The parameter in the test facility is larger by a factor of 2.8 than that in a large scale reactor. This indicates that the subassemblies in the PLANDTL-DHX are more sensitive to IWF than those in an actual reactor. However this excess is less than a factor of 3.

As for the pad geometry, the spacer cylinders in the simulated core allow vertical flow through the pad. In reactors, the pad geometry has flexibility in design. A button type pad can also allow IWF. It should be noted that such permeable pad geometry allows IWF under the full power conditions. Hot sodium in the upper plenum can penetrate into the gap region between subassemblies in a reactor with a low-baffle type UIS due to the radial pressure gradient across the core top. We have to take account of such IWF during full power operation when the permeable pad geometry is selected.

Impermeable pad geometry is selected in the reference design of JSFR and in the Japanese DFBR. However, flow holes through a core former are also available as a flow path for IWF, in addition to the permeable pad. The core former is a support structure between the core barrel and the outermost subassemblies, i.e., neutron shielding. The flow holes in the core former can form flow paths in downward and upward flows between the upper plenum and the inter-wrapper gap region. In this design, IWF during full power operation would be suppressed. Many design choices will be available for the utilization of IWF for decay heat removal. The effects of these designs are examined in Chapter 5.

(4) Summary

Transient sodium tests were carried out for natural circulation decay heat removal. An investigation of thermal hydraulics in the core during natural circulation was carried out by sodium test loop, PLANDTL-DHX, which simulated the primary loop, core (seven-subassembly), the IHX, the secondary loop, and also a decay heat removal system using a dipped heat exchanger in the upper plenum. The simulated core has cylindrical spacers between the subassemblies to allow the natural convection from the upper plenum into the subassembly gaps.

The following conclusions were obtained from the experimental results:

- IWF could remove the heat from the subassemblies even in a transition from forced to natural circulation.

- In a case of sudden decrease of the primary flow rate, IWF functioned to remove the heat in time.

- Core-plenum interactions, i.e., IWF, reverse flow, and the inter-subassembly heat transfer can cool the core on demand and have no significant negative influences on core thermal hydraulics in the case of sufficient core flow rate.

4.4 Core Scale Water Experiment

(1) Test Apparatus

A water experiment, TRIF (Test rig of inter-wrapper flow), has been carried out to investigate the flow field of IWF in the whole core. The PLANDTL-DHX sodium experiment revealed the cooling characteristics of IWF in the seven-subassembly partial core model. However, the reactor core has several regions, e.g., inner core and radial reflector. The flow field of IWF in the core will depend on such a core matrix. In a simple assumption, it is predicted that cold sodium in the bottom of the reactor upper plenum flows downward in the outermost radial reflector region and flows up in the inner core region. The TRIF experiment was planned to clarify the flow and temperature fields of IWF in the whole core.

Figure 4.4-1 shows a schematic of the reactor vessel model of TRIF. A 1/12 (30˚) sector of the reactor core and upper plenum is modeled. The model scale of the core is 1/1. The flow field of IWF is of interest in this experiment. Flow visualization and particle image velocimetry (PIV) were used to obtain the flow field in complex geometry (Kimura, 2000). For the visualization, no heater pin is installed inside of the subassemblies and flow through the subassembly is not simulated. The wrapper tube of the subassembly is made of transparent resin. Glass heater panels, coated by tin-oxide and electrically heated, are set on the wrapper tube wall to simulate heating by the core fuel subassemblies. This subassembly model enables clarification of the flow in the gap region between the subassemblies from outside of the reactor core model. Non-heated subassemblies are set in outer region of the core to simulate radial reflectors. The flat to flat length of hexagonal subassembly is 0.152m and the gap width between the subassemblies is 0.006m. The heated length of the glass heater is 0.94m. Button type spacer pads are set on the wrapper tube wall, and the pad is used to maintain the pitch of the subassembly arrangement. This geometry of the spacer pad permits vertical flow through the pad position, i.e., fluid exchange between the gap region in the core and the upper plenum. Four cooling panels are immersed in the upper plenum to simulate the DHX. Cold water provided by the cooling panel flows into the gap region between the heated subassemblies, and IWF occurs.

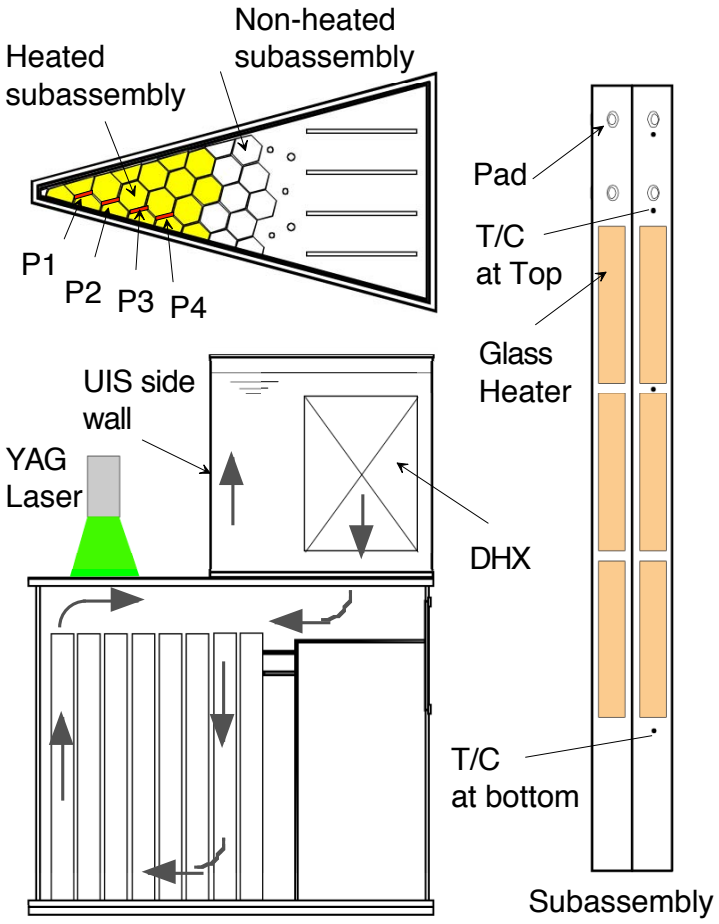

Fig. 4.4-1 Schematic of TRIF Experimental Apparatus

The temperatures were measured by thermocouples at lower end, middle height, top of heated region and handling head height on the wrapper tubes. The estimated error of temperature measurement was less than 0.4˚C.

The velocity fileds in the gap region between the subassemblies were measured by PIV. Detail of the measurement technique using PIV was reported in the reference (Kimura, 2000). The velocity vectors are time averaged values of 60 data during 2s. The maximum velocity was 0.04m/s and the estimated measurement error was less than 0.002 m/s.

(2) Flow Field of IWF

Experimental conditions were as follows. Heat flux at each of the heater panels on the subassembly walls were set 2,090 W/m^2 and kept constant. Total heater power in the core was 9.73kW. The flow rate into each of the cooling panel was 20 l/min and inlet temperature was 12.4˚C. The total of removed heat of the cooling panel was 8.86kW and heat balance was 91%.

A schematic of the visualized flow pattern is shown in Fig. 4.4-1. Water in the upper plenum was cooled by the DHX and stratified in the bottom. The cold water penetrated into the inter-wrapper gap in the outer non-heated region in the core. At the bottom of core, radial flow toward the center of the core was observed. In the inner region of the core, upward flow was observed.

The velocity field of IWF in the gap region is shown in Fig. 4.4-2. The velocity vectors were measured in the gaps of P1 to P4 in the heated region of the core (see Fig. 4.4-1). The radial component of velocity was small in these gap regions. The upward flow velocity of IWF increased as it flowed upward. The upward flow velocity in the inner gap was larger than that in the outer gap. The major flow velocity was around 0.02 m/s at the middle height of heated length. The estimated Re number was 240. The flow pattern and magnitude of flow velocity of IWF were grasped in the geometry of the button type pad.

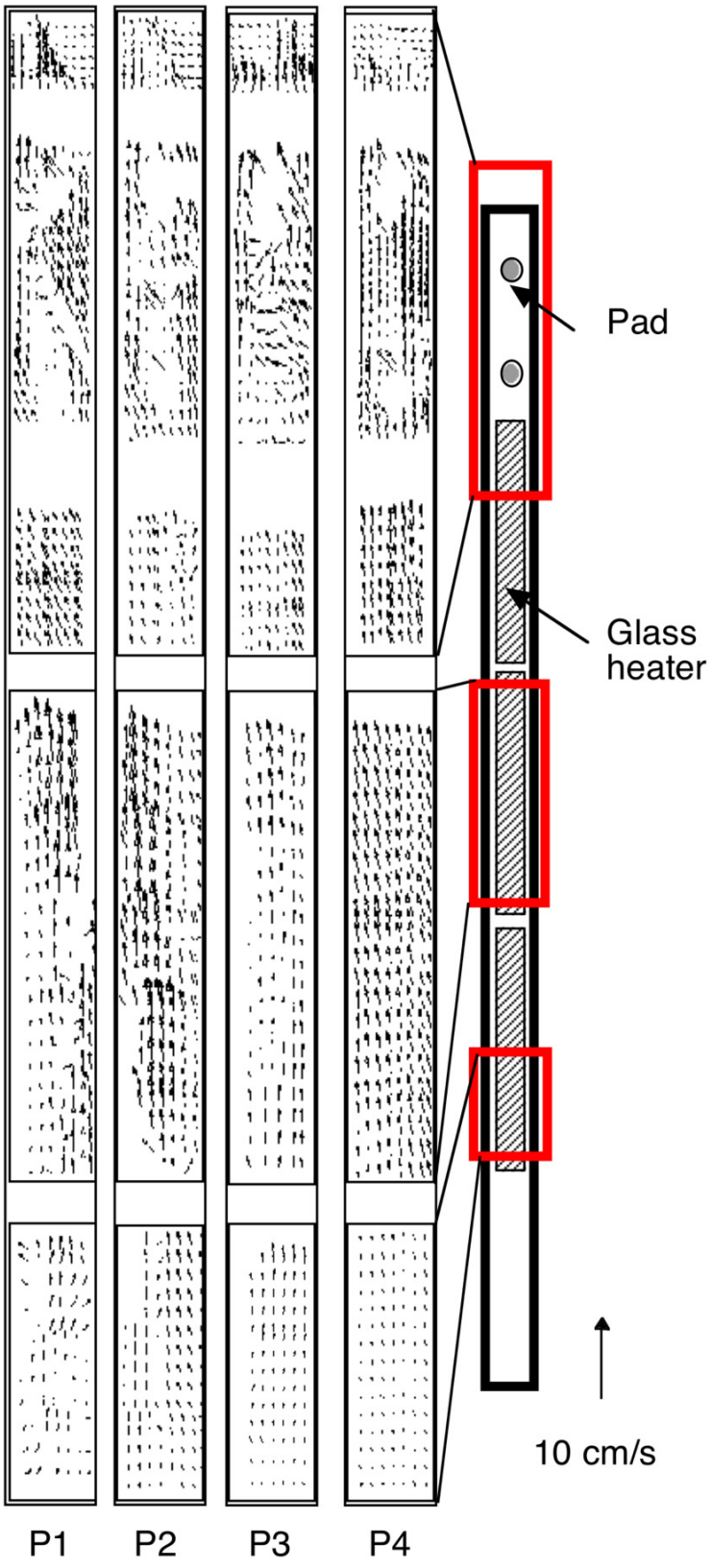

Fig. 4.4-2 Velocity Field in Inter-Wrapper Gap Region

(3) Summary

A water experiment was carried out to investigate IWF in a whole core. A 1/12 sector of a reactor core was modeled by a hexagonal configuration of core fuel subassemblies and radial shielding. The flow field in the gap region was grasped and a data set was obtained for the verification of a numerical simulation method.

4.5 Conclusions

Sodium and water experiments revealed that the inter-wrapper flow (IWF) has a significant potential to remove the decay heat in the core when a DRACS is used as the decay heat removal system. When the flow rate through the core is reduced to less than 1% of the full power condition, IWF will be a major heat removal path. A new non-dimensional parameter, $C\ Gr^{4/7}/Re$, was deduced and it was shown that this number could characterize estimates of such cooling effects.

In case of high IWF cooling, thermal hydraulics in the subassemblies become complex to produce a recirculation flow. Further, IWF reduces the temperature in the upper non-heated part of the subassembly, and this results in the decrease of the natural circulation head. Although these drawbacks were considered, the transient sodium experiments showed that IWF could reduce the highest temperature in the subassemblies.

The water experiment showed the core scale flow pattern in the inter-wrapper gap so as to cover the space limitation of the seven-subassembly sodium experiments.

Nomenclature

A: flow area, m^2

C: geometric constant, dimensionless

Cp: specific heat of sodium, J/kg K

D: hydraulic equivalent diameter, m

f: friction factor, dimension less

g: acceleration of gravity, m/s^2

Gr: Grashof number, dimension less

L: length between the top of a subassembly and the middle of heated length, m

Q: heater power in a subassembly, W

R: radius of core region, m

Re: Reynolds number, dimensionless

T*: non-dimensional peak temperature in the core, dimensionless

T_{in}: inlet sodium temperature of the core, ˚C

T_{peak}: peak temperature in the core, ˚C

T_c: calculated temperature ($T_c = T_{in} + \Delta T_{Q/F}$), ˚C

V: flow velocity, m/s

β: coefficient of thermal expansion of sodium, 1/K

$\Delta T_{Q/F}$: average temperature increase based on heater power and flow rate in a subassembly, ˚C

ν: kinematic viscosity, $m^{2/}s$

ρ: density of sodium, kg/m^3

Subscripts:

b: in a pin bundle of subassembly

g: in a gap between subassemblies

Chapter 5. Whole Core Analysis of NC/DHR

Chapter 5. Whole Core Analysis of NC/DHR

5.1 Introduction

Here, a prediction method for the natural circulation phenomena in a whole core using AQUA code (Maekawa, 1990) is developed to investigate core scale thermal hydraulic phenomena, which are not confirmed in the small or partial model experiments. The prediction method considers each subassembly in a reactor core and models the gap region between the subassemblies and the upper plenum in a reactor vessel. This modeling enables us to calculate IWF, thermal interaction between IWF and flow in the subassemblies, intra-flow redistribution in each subassembly, inter-subassembly heat transfer due to radial temperature distribution across the core, and the inter-subassembly flow redistribution in the core. That is an overall simulation method based on the findings of the experiments and the simulation method of multi-subassembly system.

This prediction method was verified through the experimental data of a sodium test using a seven-subassembly core model (Kamide, 2001) and the water test, which simulated IWF using a 1/12 sector model of a reactor core. Thermal coupling between IWF and temperature distribution in the subassemblies was shown in the seven-subassembly sodium experiment. The calculation method was examined for temperature decrease in the subassembly due to IWF. In the water experiment, the velocity profile of IWF in the core was obtained by using flow visualization and particle image velocimetry. The calculated velocity profile was compared with the experimental data.

The prediction method was applied to natural circulation decay heat removal (NC/DHR) of a 600 MWe class fast reactor in order to investigate thermal hydraulic phenomena in the entire core (Kamide, 2002). The parameters of the calculations are geometry of the inter-subassembly spacer pad, which maintains the pitch of the subassemblies, and the flow guide for IWF, which delivers the cold fluid into the core. Key functions required for simulation methods to predict the highest temperature in the reactor core are also discussed through an analysis of thermal hydraulic phenomena.

5.2 Multi-dimensional Analysis Method: Brick-subassembly Model

The thermohydraulic phenomena considered in a reactor vessel during natural circulation are as follows:

1) thermal stratification in the reactor upper plenum, whereby cold sodium provided by DHXs stratifies in lower part of the upper plenum,
2) IWF, the gap flow between the subassemblies,
3) penetration flow into the subassemblies from the stratified upper plenum,
4) inter-subassembly heat transfer, the radial heat transfer across the core,
5) flow redistribution among the subassemblies due to buoyancy force.

During the natural circulation, flow rate through the core is so small that the highest temperature in a subassembly is affected by the heat transportation through the wrapper tube wall due to IWF and inter-subassembly heat transfer. The inter-subassembly flow redistribution flattens the radial temperature distribution across the core. The penetration flow occurs when negative buoyancy force is larger than the inertia force of upward flow in a subassembly (Kamide, 1996). However, the penetration flow will remain in a neutron shielding above the pin bundle and influences will be limited as shown in chapter 3.

The three-dimensional thermohydraulic analysis code AQUA is used to predict the above-mentioned phenomena in the core and the upper plenum. AQUA is the code developed in-house based on the finite difference method in Cartesian or cylindrical coordinates. The thermohydraulic conditions in the inter-wrapper gap regions is connected to the upper plenum, which is a source of cold sodium, and is additionally coupled with the flow in the subassemblies. Transverse temperature gradient in the subassembly becomes pronounced due to heat removal through the wrapper tube wall. These temperature gradients thus influence the heat transfer between the subassemblies and the gap regions as shown in chapters 2 and 4. Therefore, three regions; 1) the inter-wrapper gap, 2) the upper plenum, and 3) the subassemblies, have been analyzed together. Further, each of the subassemblies has two layers of the wall subchannel region and the inner subchannel region.

The scales of the flow (representative length) in these regions are quite different; 3 mm in a fuel pin bundle, 12 mm in gap region, 2 m in the upper plenum. Full simulation of the geometry with wide variation of the length scale, which needs significantly large computer resources, is beyond the scope of our purpose. A prediction method with adequate refinement is needed on the point of engineering or technical application to estimate the highest temperature in the core.

The horizontal mesh scheme for the core section is shown in Fig. 5.2-1. The Cartesian coordinate system is used to model the above-mentioned three regions together. The calculation domain is a sector model for 1/12 of the core. The hexagonal shape of the subassembly is converted to a rectangular shape while maintaining the perimeter of the wrapper tube facing the gap region, which corresponds to the heat transfer area between the subassembly and the gap region. IWF in the gap region removes heat from the subassemblies. In the horizontal plane of the gap region, one section has hot upward flow and the other section has cold downward flow. Thus, the relative position between an element of the gap region and a side of hexagonal wrapper tube is maintained in the mesh scheme to simulate the heat flow between IWF and the subassemblies.

In the subassembly region, the meshes facing the wrapper tube are modeled as the wall subchannels and the inner meshes are modeled as the inner subchannels. This manner of classifying subchannels is known to be useful for simulating the flow and temperature field in a subassembly using a staggered half-pin mesh arrangement (Kamide, 1998, Nishimura, 2000 as shown in chapter 2). The total flow area in each mesh type is set equal to that in the subassembly by using a porous body model. The fraction of heater power in each mesh is also set in the same manner. Flow resistance coefficients at the wall and inner subchannel regions are set based on the correlations developed for subchannel analyses by Cheng (1986). The width and flow area of the gap region are identical to the actual geometry.

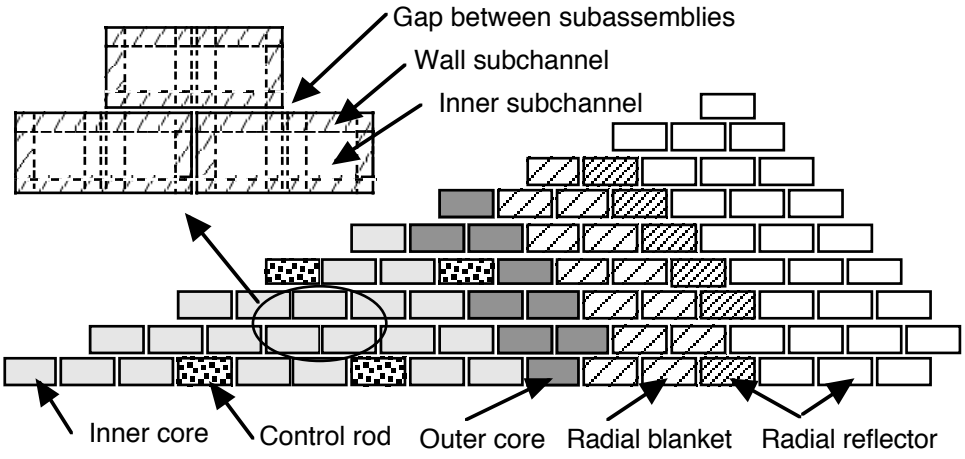

Fig. 5.2-1 Mesh Scheme for Subassemblies and Core Matrix

Figure 5.2-2 shows a vertical cross section of the core and the upper plenum. At the height of the core outlet, the subassembly regions and the gap region are connected to the upper plenum region. All subassemblies including control rod channels are connected to a high pressure plenum at the bottom. A low pressure plenum, to which the radial reflector and control rod channels are connected in the ordinary way, is neglected for the sake of creating a simplified model. There is no flow connection between the gap region and the high pressure plenum. The DHX is also modeled in the upper plenum region. Boundary conditions are as follows: flow rate, temperature into the high pressure plenum, decay heat in each subassembly, and flow rate and inlet temperature in the secondary loop of the DHX. A first-order upwind scheme is used for convection term differencing and a laminar flow model is applied because of the simple mesh modeling in the core for the actual complex geometry (e.g., wire wrapped fuel pin bundle). The above-mentioned method of calculation is referred to as a brick subassembly model.

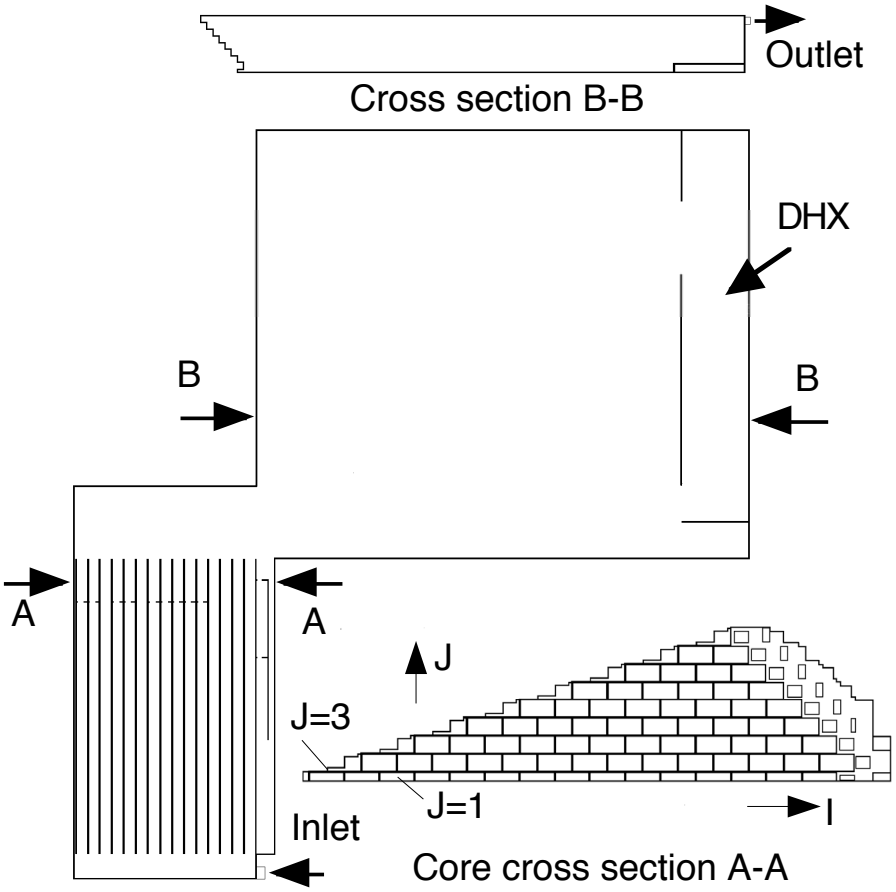

Fig. 5.2-2 Mesh Scheme for Core and Upper Plenum

5.3 Validation Based on Experiments

(1) Cooling Effects of IWF on a Subassembly

Thermal interaction between IWF and flow in the subassemblies has been investigated in sodium experiments using the PLANDTL-DHX facility (Kamide, 2001, Nishimura, 2000) as shown in chapter 2. The brick subassembly model was applied to the sodium experiment (Kamide, 2002). Here, some comparisons between experiments and calculations are shown to validate the modeling for thermal interaction.

The mesh scheme used for the calculations is shown in Fig. 5.3-1. At the height of the core outlet, the subassembly regions and the gap region were connected to the upper plenum region. DHX was also modeled in the upper plenum region. Boundary conditions were as follows: flow rate, inlet temperature, heater power in each subassembly, and flow rate and inlet temperature in the secondary loop of the DHX.

The simulations were carried out for Cases D1.3, D1.0, and D0.5 in the forced circulation experiments described in section 4.2. The transverse temperature distributions at the top of the heated length in Case D0.5 are shown in Fig. 5.3-2. The temperature increases from the inlet are plotted. The simulation predicted well the low temperature at the right end gap, which is due to cold penetration flow from the upper plenum. In the center subassembly, the temperature decreases near the wrapper wall, which were due to heat removal through the wall, were also simulated. The maximum temperature between the experiment and simulation was in agreement to within 50˚C. If the additional heat removal, i.e. by IWF, were not taken into account, the average temperature increase at the heated end based on the flow rate and heater power in the subassembly would have been 510˚C.

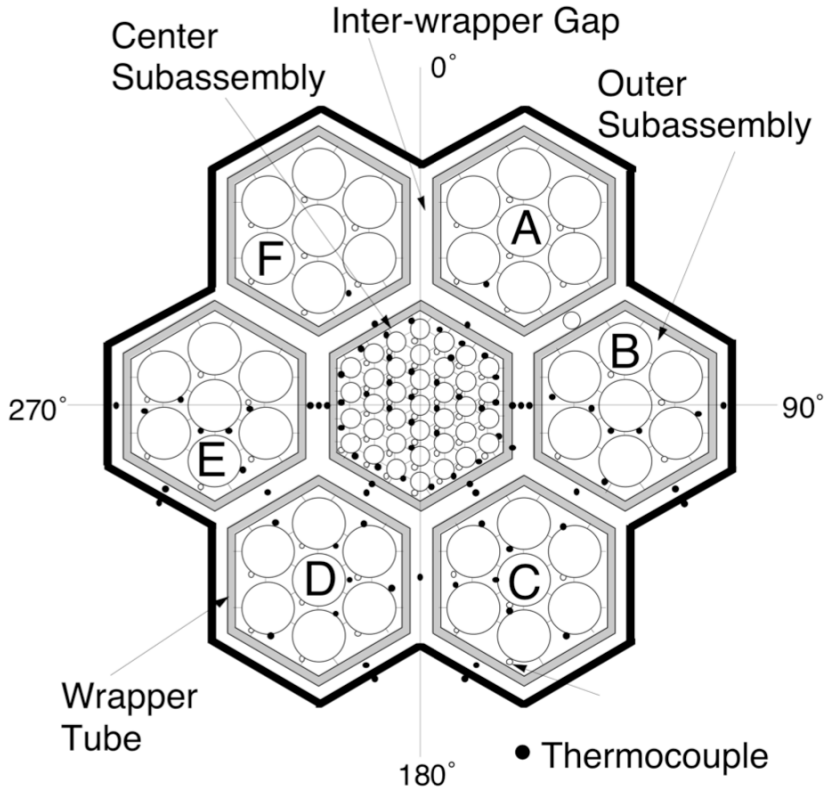

(a) Seven-Subassembly Core

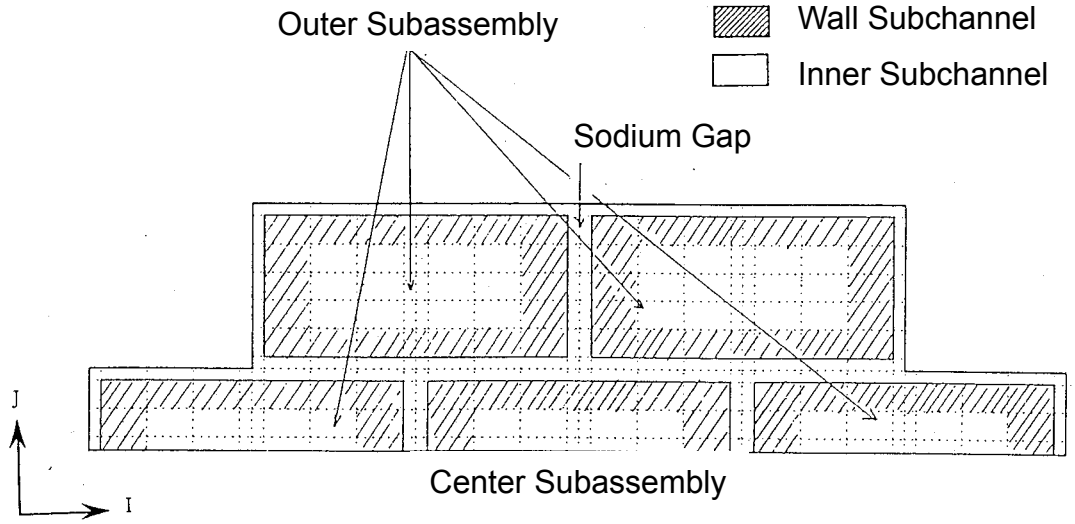

(b) Mesh Arrangement of Core Cross Section

Fig. 5.3-1 Mesh Scheme of Core Cross Section
for Seven-Subassembly Model

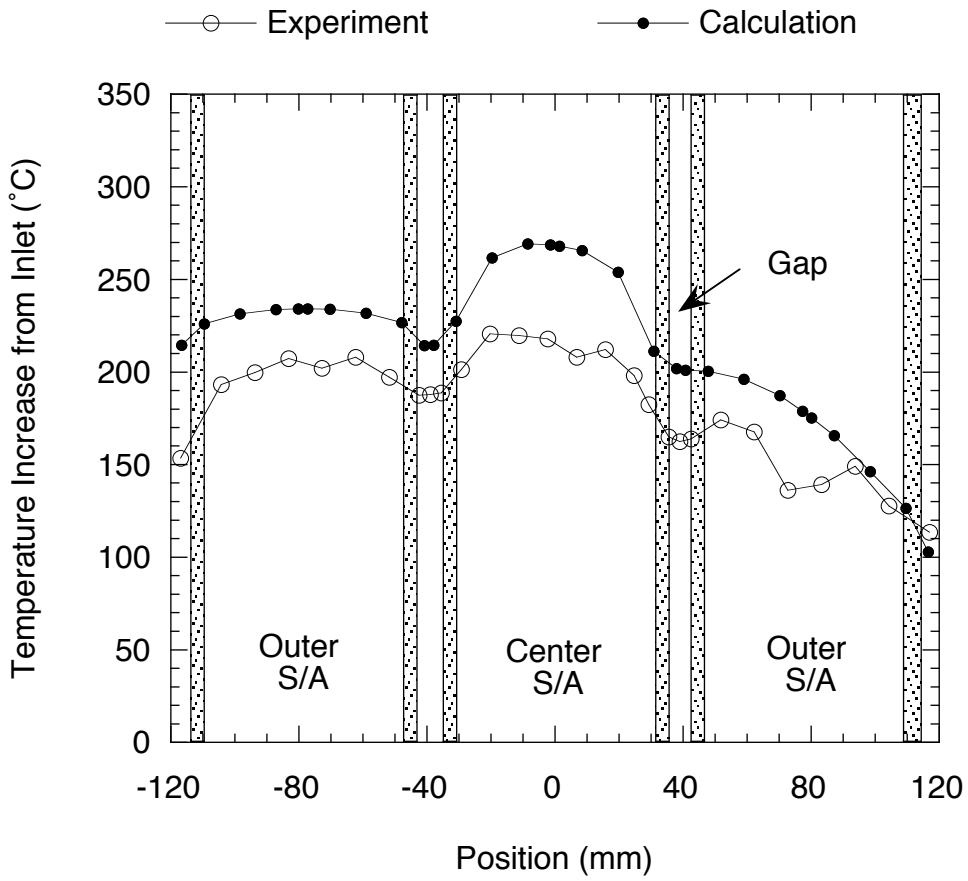

Fig. 5.3-2 Transverse Temperature Distributions at Top of Heated Length in Case D0.5 and Calculation

The axial temperature distributions along the center subchannel are compared in Fig. 5.3-3. In the cases with 1% flow velocity, the predicted results were in good agreement with the measured data. In the cases with 0.5% flow velocity, the temperature decrease in the upper region of heated length could not be simulated. Heat removal by IWF was underestimated in the analysis, for extremely low flow conditions. Figure 5.3-4 shows axial temperature distributions along the gap region in Cases D1.0 and D0.5. The 90˚ and 270˚ ends correspond to both ends in the gap region along the 90˚-270˚ line shown in Fig. 5.3-1. In Case D1.0, temperature decreases in the upper region of the heated length were simulated at both the 90˚ and 270˚ ends. However, the calculation in Case D0.5 simulated the temperature decrease at the 90˚ end only. This indicates that the cold penetration flow was underestimated at the 270˚ end in Case D0.5. In case of extremely low flow rate through the subassemblies, the temperature inside the subassembly increases. This resulted in a higher temperature in the calculation at the center subchannel in Case D0.5, as shown in Fig. 5.3-3. The sodium in the inter-wrapper gap region will be heated by the subassemblies and the influence of buoyancy force will increase in such case. The simulation of IWF presents greater difficulty under lower flow rate conditions in the subassemblies.

Figure 5.3-5 shows non-dimensional peak temperature in the center subassembly. The horizontal axis is the non-dimensional parameter of IWF heat removal deduced in section 4.2 as follows:

$$\frac{Heat(IWF)}{Q} \propto C\frac{Gr^{4/7}}{\mathrm{Re}},$$

where

$$C = \frac{A_g D_b}{A_b D_g}\left(\frac{L}{L+R}\right)^{4/7},$$

$$Gr = \frac{g\beta\Delta T_{Q/F} D_g^3}{\nu^2}, \quad \mathrm{Re} = \frac{V_b D_b}{\nu}.$$

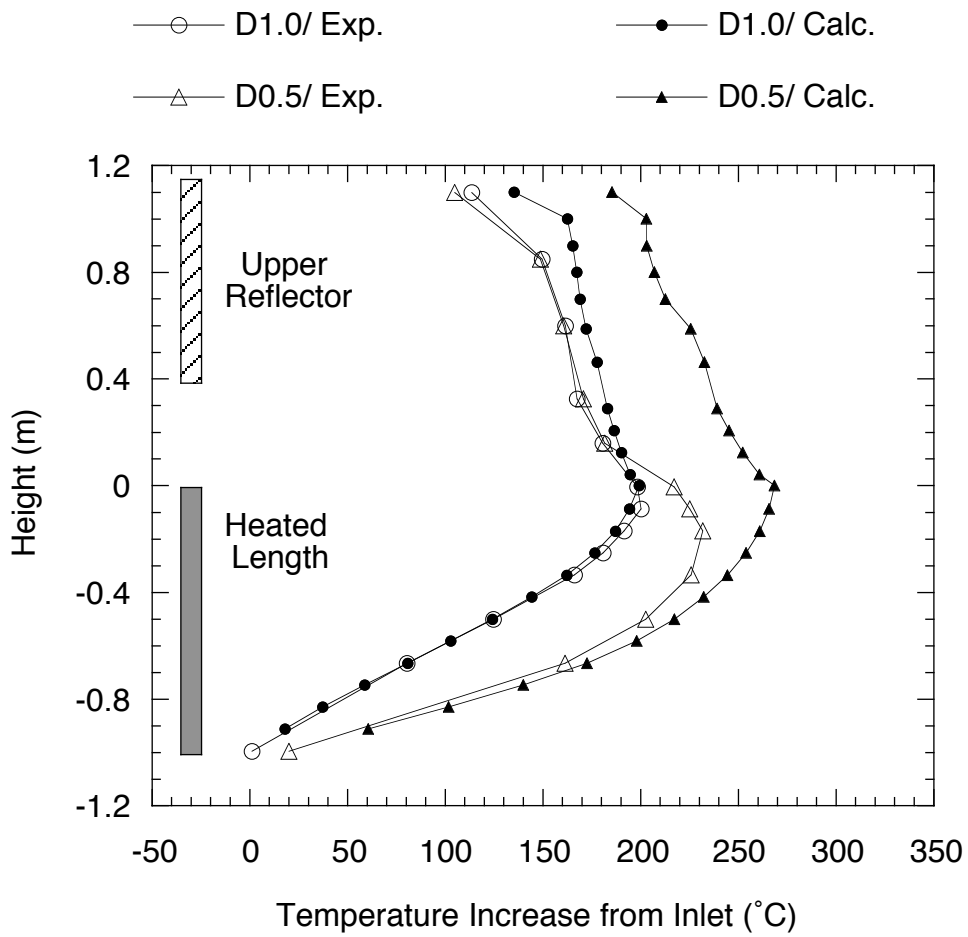

Fig. 5.3-3 Axial Temperature Distributions along Center Subchannel in Cases D0.5 and 1.0 and Calculations

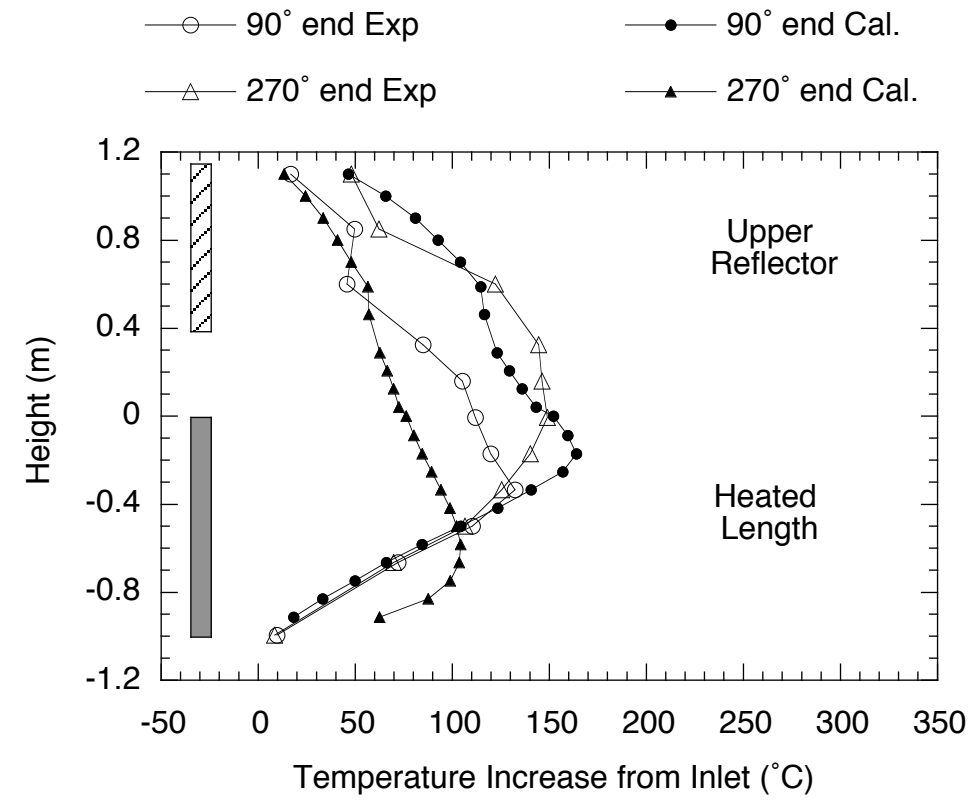

(a) Case D1.0

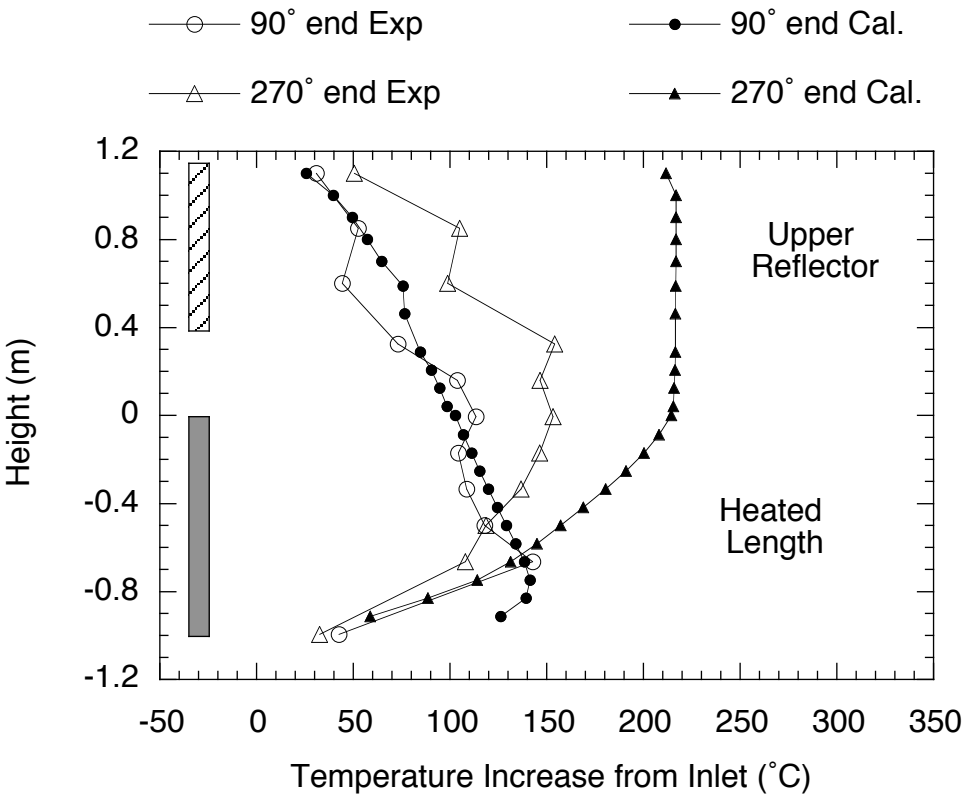

(b) Case D0.5

Fig. 5.3-4 Axial Temperature Distributions along Inter-Subassembly Gap Regions in Cases D0.5 and 1.0 and Calculations

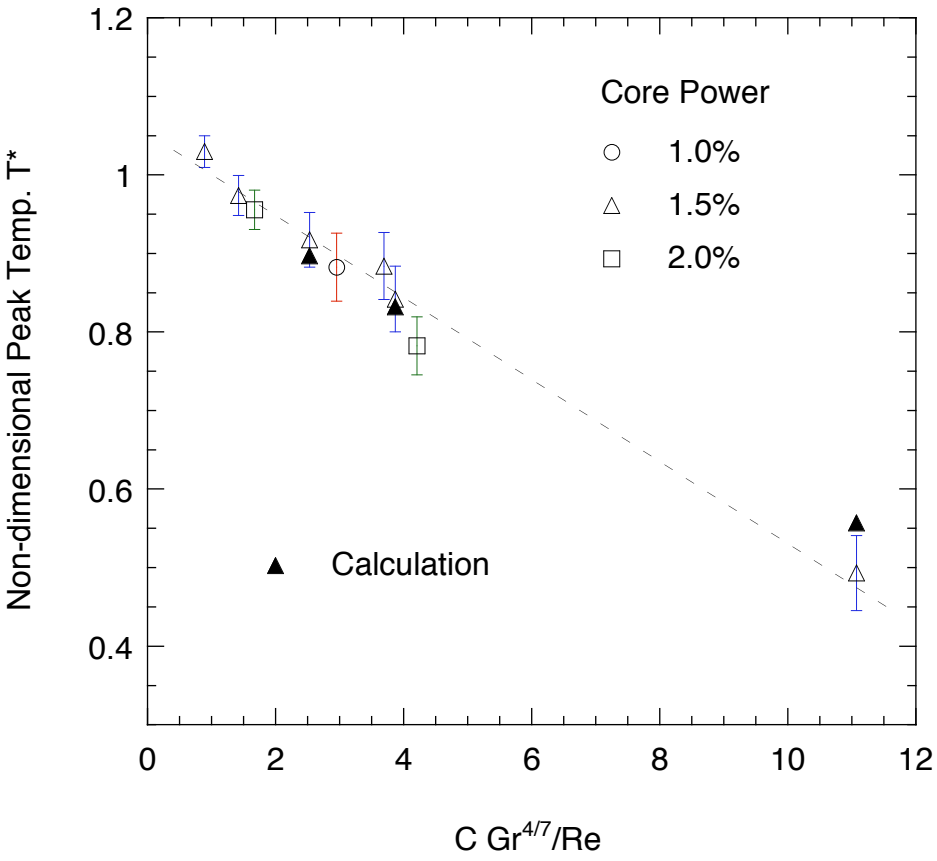

Fig. 5.3-5 Non-Dimensional Peak Temperatures in Experiments and Calculations

The loop flow rate in the experiment was maintained at a constant by a pump. The non-dimensional peak temperature, T^*, was obtained according to the following equations (see section 4.2):

$$T^* = \frac{T_{peak} - T_{in}}{\Delta T_{Q/F}},$$

$$\Delta T_{Q/F} = \frac{Q}{\rho Cp A_b V_b}.$$

Here, T_{peak} is the highest temperature in the core, T_{in} is the inlet temperature into the core, Q is heat input in a subassembly, V_b is the section averaged flow velocity in the pin bundle, and C_p is the specific heat of sodium.

ΔT corresponds to the average temperature increase under adiabatic conditions at the wrapper tube wall. Thus, (1-T*) indicates the heat removal ratio of IWF (heat removal through the wrapper tube) to the heater power in the center subassembly. When the non-dimensional parameter of IWF heat removal, $Gr^{4/7}/Re$, was increased, the quantity of heat removal via IWF was larger. The calculated value of T* was in good agreement with the experimental results within the measurement accuracy, which was decided by flow meter accuracy in lower range.

When the flow velocity ratio was less than 1.5%, the non-dimensional temperature became smaller than unity. The non-dimensional temperature was 0.5 when the velocity ratio was 0.5%. This indicates that IWF removes 50% of heater power in the center subassembly. The calculated data was in good agreement with the experimental results within the measurement error, which resulted from flow rate measurement in the subassembly.

The experimental analyses revealed that the brick-subassembly model calculation could simulate temperature decrease in the gap region between the subassemblies and the decrease of the peak temperature in the subassembly. The heat transportation via IWF was well calculated by this numerical simulation model.

(2) Verification of Flow Field of IWF based on Water Experiment

Thermal interaction between the intra-subassembly thermal hydraulics and natural convection in the inter-wrapper gap region was investigated by using the seven-subassembly sodium experiment and numerical analyses. However, natural convection in the inter-wrapper gap is governed by whole core temperature distribution, not at a local three or seven subassembly scale. The water experiment, TRIF, was carried out to examine such core-scale natural convection in the gap region. Here, the brick-subassembly model is applied to the TRIF experimental analyses to evaluate its applicability to natural convection in a whole core region. The mesh scheme of the test section is shown in Fig. 5.3-6.

Velocity and temperature fields in the gap region of the TRIF experiment were calculated using the AQUA code and the brick subassembly mesh scheme. The calculated temperature and velocity fields in a vertical cross section of J=3 are shown in Fig. 5.3-7. The horizontal mesh arrangement to simulate the core is also shown in Fig. 5.3-7. This cross section (J=3) includes the gaps of P1 to P4 where flow field was measured. The calculated flow pattern was in good agreement with the visualized pattern; however, the radial flow component in the heated subassembly region of the core was larger than measured velocity vectors (see Fig. 5.4-2). Figure 5.3-8 shows a comparison of vertical velocity components between experiment and calculation in the gap of P1 (see Figs. 4.4-1 and 5.3-7). The measured data were scattered depending on their transverse position in the gap. The calculated distribution of flow velocity traced the trend of experimental data.

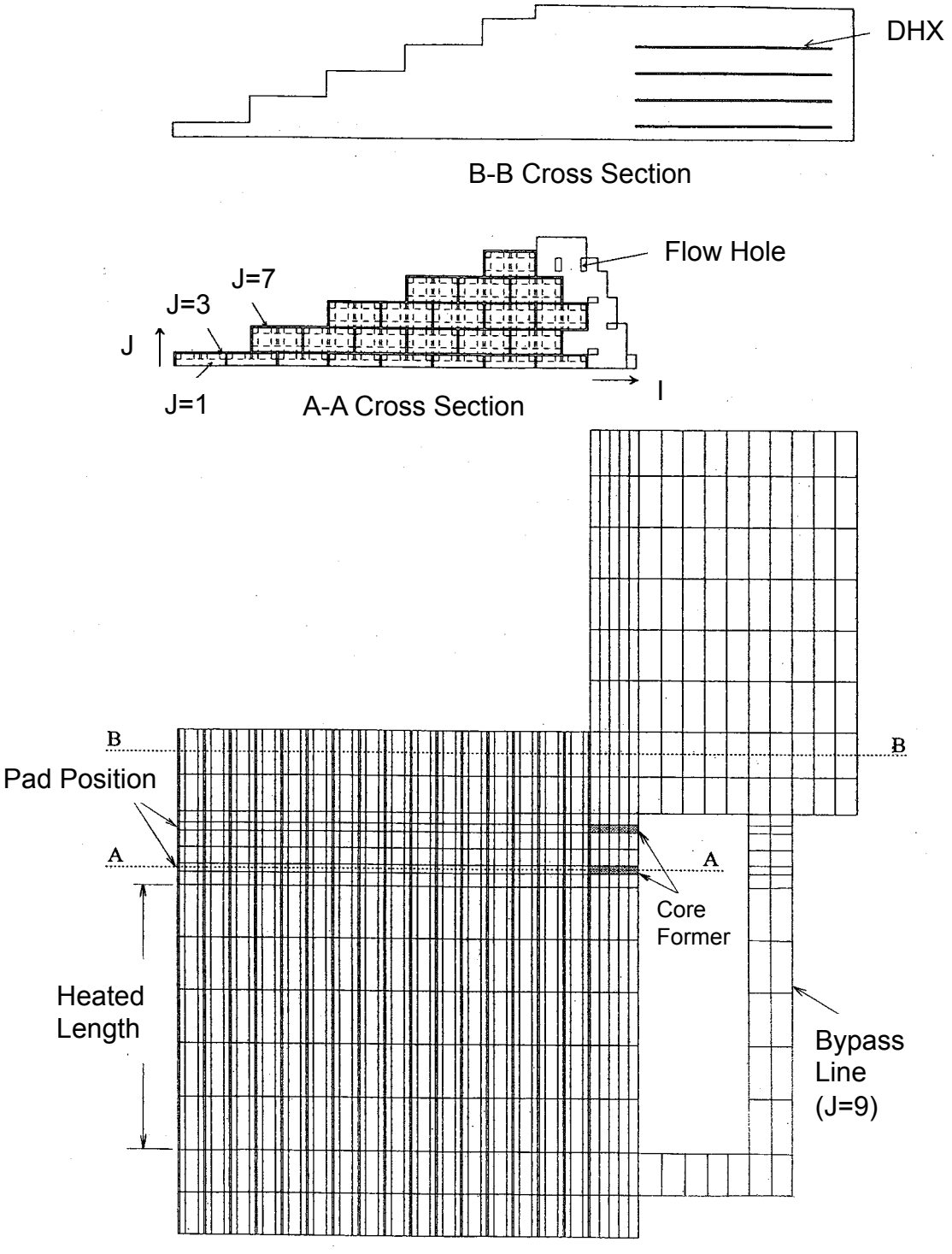

Fig. 5.3-6 Mesh Scheme of TRIF Test Section

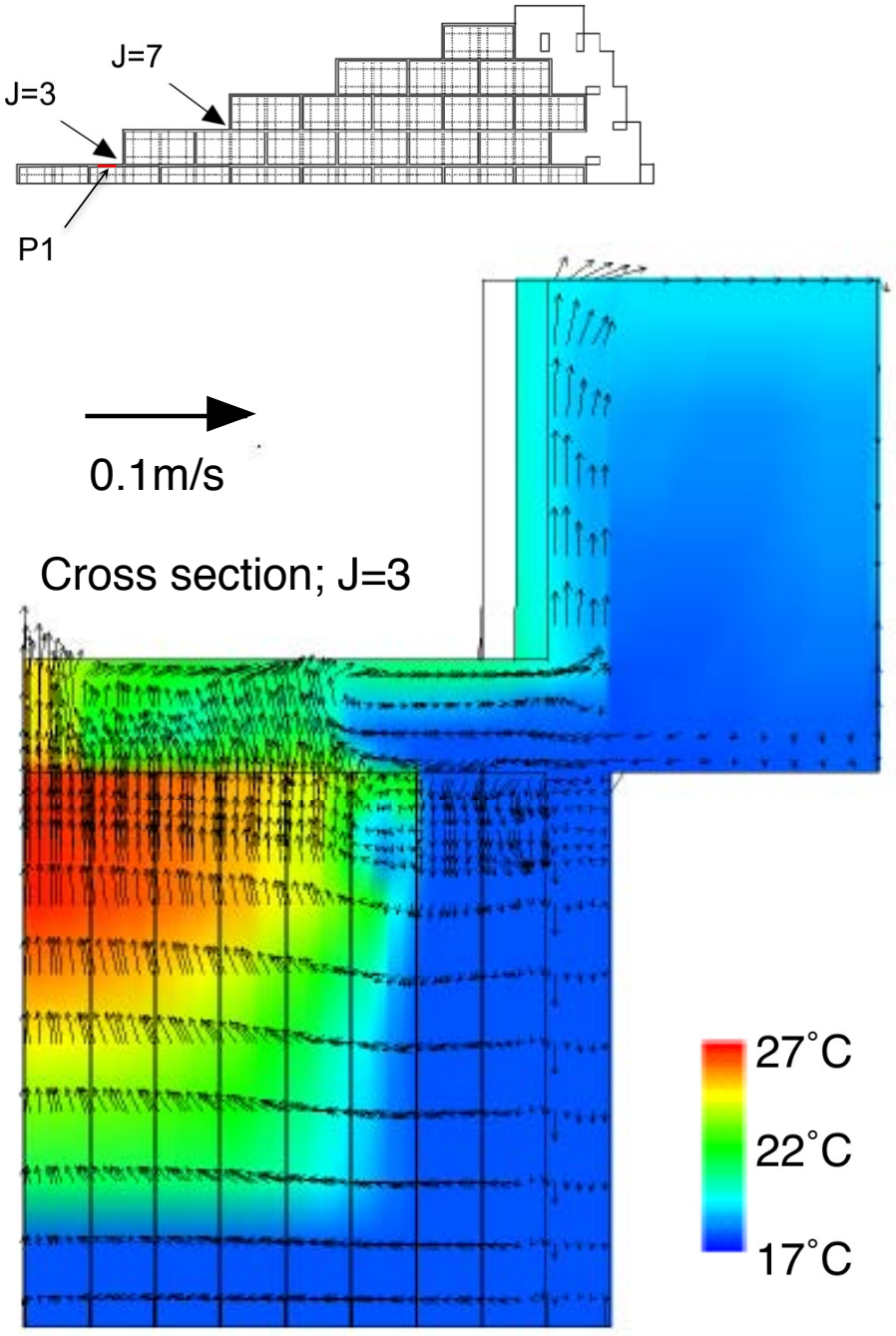

Fig. 5.3-7 Calculated Temperature Contour and Velocity Field on Vertical Cross Section in TRIF and Mesh Scheme at Core Cross Section

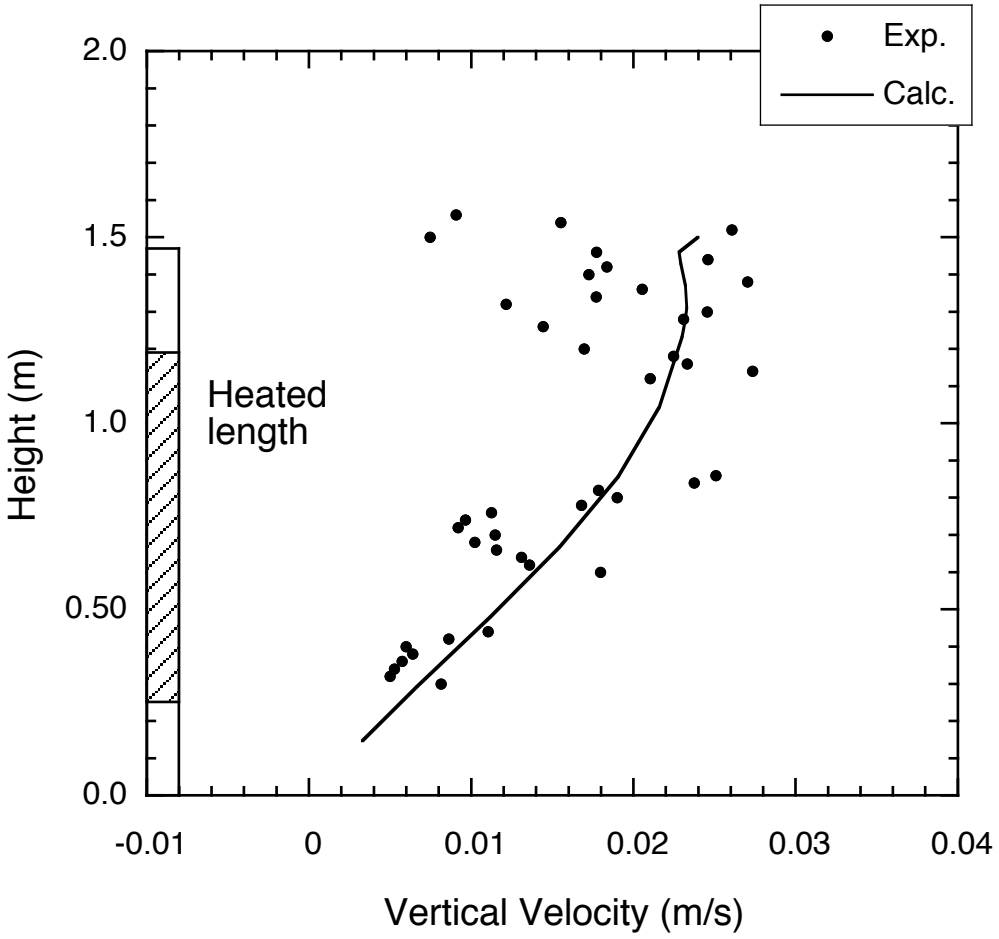

Fig. 5.3-8 Comparison of Vertical Distributions of Vertical Velocity Component in Gap Region between Experiment and Calculation

Temperature distributions are also compared between the experiment and calculations. Figure 5.3-9 shows radial temperature distributions in vertical cross sections of J=3 and 7 (see Fig. 5.3-7). Parametric calculations were carried out for the vertical flow resistance coefficient at the inter-subassembly spacer pad. In the nominal case, the resistance coefficient was obtained according to the change of flow area through the pad position. The resistance coefficient was varied in a range of 0.5 to 2.0 as compared with the nominal case. As shown in the figure, the radial temperature distribution at the top of heated length was influenced by flow resistance through the pad position. The case of higher resistance showed comparatively better agreement with the experimental results than the nominal case. The vertical velocity distributions in three calculated cases are also compared in Fig. 5.3-9. The region of upward flow expanded in the outer space of the heated subassembly region when the flow resistance increased. The higher flow resistance will reduce convective flow rate in the gap region. Thus, the requirement for the flow area of cold downward flow is reduced. This change in the boundary between the hot upward flow and cold downward flow results in good agreement with the measured temperature distribution in the case of higher flow resistance.

The calculations showed reasonably good agreement of temperature distributions with the measured data. It is also shown that the flow and temperature fields of IWF are sensitive to flow resistance through the pad position.

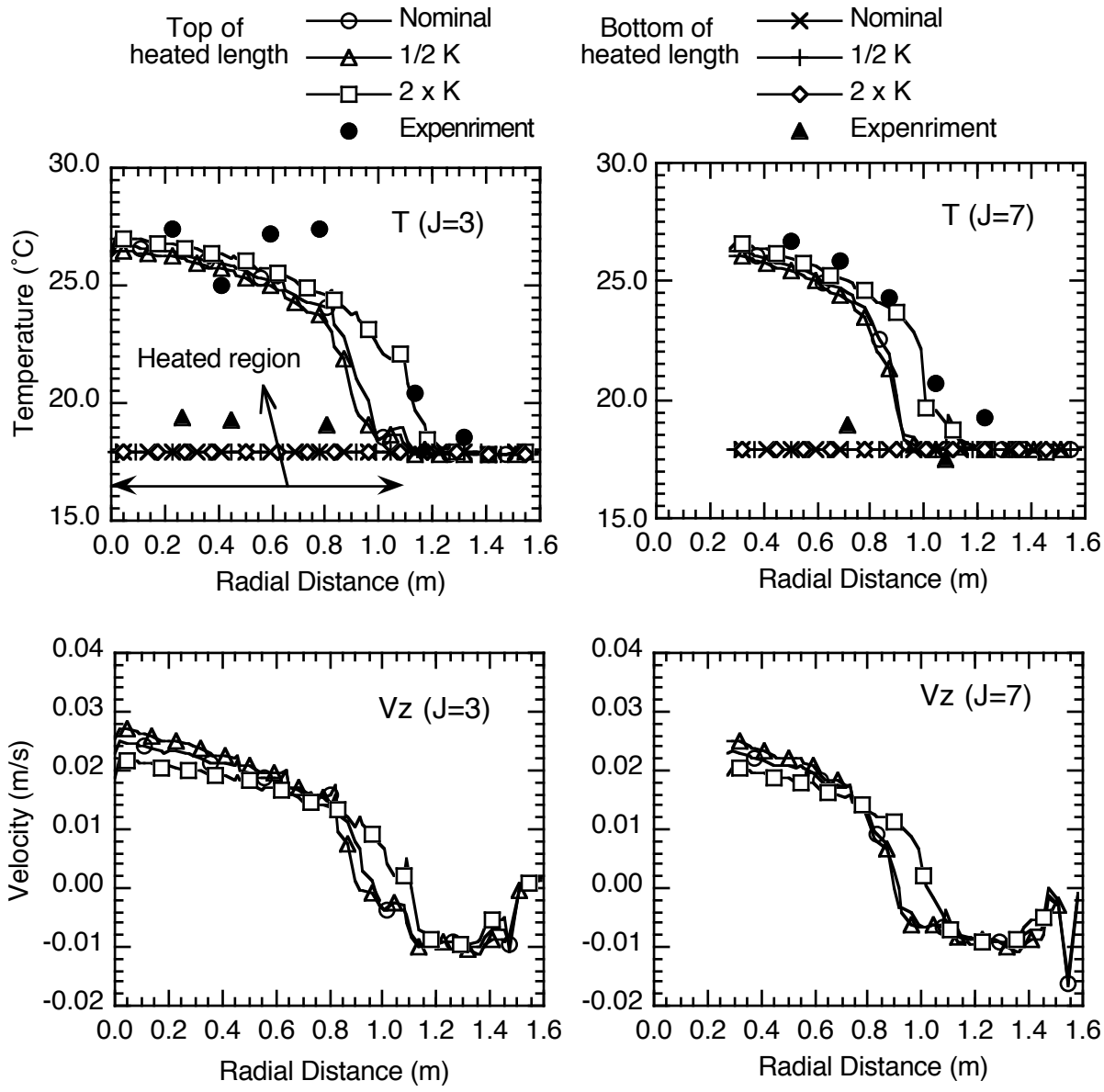

Fig.5.3-9 Radial Distributions of Temperature and Vertical Velocity Component along J=3 and 7

5.4 Whole Core Analyses of 600MWe Class Reactor

(1) Boundary Conditions

Prediction analyses (Kamide, 2002) were carried out for thermal hydraulic phenomena in an entire core under natural circulation conditions. The core matrix and mesh arrangement are shown in Figs. 5.2-1 and -2, respectively. The calculational conditions are listed in Table 5.4-1. The reactor core has inner and outer cores, a radial blanket, and radial reflector. Flow rate into the lower plenum was a boundary condition and set at 1% of full power conditions, which corresponds to a level of natural circulation flow rate in a reactor.

Inter-subassembly spacer pad shape is a calculational parameter. The reference case has a band-type pad, which does not allow vertical flow through the pad position. The other is a slit type, which allows fluid exchange between the inter-wrapper gap region and the upper plenum (Watanabe, 1999). The slit-type pad is illustrated in Fig. 5.4-1. Geometry of core former, which is a plate and covers the region between the outermost subassemblies and the core barrel, is also changed as a calculational parameter. In a reference case, the core former closes the flow path between the core barrel and the reactor upper plenum together with the band-type pad. Flow guide through the core former is added to allow fluid exchange between the gap region in the core and the upper plenum as shown in Fig. 5.4-1. Several ducts penetrate through the core former, which allow downward flow from the upper plenum and prevent mixing with hot fluid in the higher section of the gap region. This duct will help to provide the cold fluid directly to the inter-wrapper gap region to remove the decay heat. Several flow holes are also set in the core former to release the hot fluid from the gap region to the upper plenum. The total of the three cases, closed pad, slit pad, and flow guide, were calculated. The calculated cases are summarized in Table 5.4-2.

Table 5.4-1 Calculated Conditions

Item	Data
Time control	Steady state calculation
Decay heat level	1.7% of full power condition
Loop flow rate	1.0 % of full power condition
Core inlet temperature	450˚C

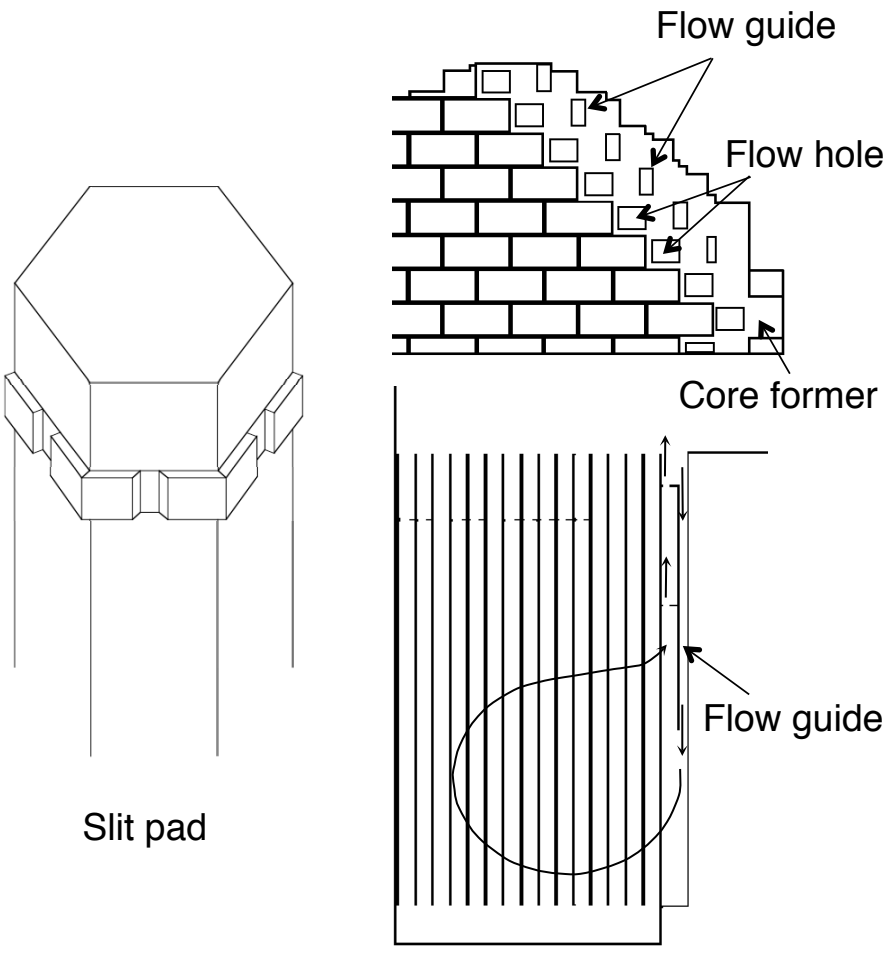

Fig. 5.4-1 Geometry of Subassembly Pad and Flow Guide

Table 5.4-2 Calculated Cases

Case	Geometry
Closed pad	Pad: closed type Core former: closed
Slit pad	Pad: slit type Core former: closed
Flow guide	Pad: closed pad Core former: open

(2) Calculational Results

Figure 5.4-2 shows the calculated temperature and velocity fields in a vertical cross section through the gap region (J=3, see Fig. 5.2-2) in the closed and the slit pad cases. Flow velocity of IWF in the slit pad case was larger than that in the closed pad case, and the temperature along the inner core region in the slit pad case was lower than that in the closed pad case. Cold downward flow from the upper plenum was seen in the radial reflector region in the slit pad case. It decreased the temperature in the gap region.

Radial temperature distributions across the subassemblies (J=1, see Fig. 5.2-2) at the top of active core fuel are compared among the three cases in Fig. 5.4-3. The slid pad case showed the lowest temperature in the core region among the three cases. The temperature gradient in each subassembly was larger in the slit pad case than the closed pad case, especially in the inner core region. This indicates that the decay heat is removed by IWF through the wrapper tube in the slit pad case. The outer core subassembly had steep distribution in all cases. This is due to the inter-subassembly heat transfer to the adjacent blanket subassembly, which is much colder than the outer core subassembly. This outer core subassembly showed the highest temperature in the core in each case. One of the reasons is flow redistribution in the core, which is shown in Fig. 5.4-4.

The vertical axis of Fig. 5.4-4 is relative flow rate in the subassembly normalized by the loop flow rate. The flow rate in the inner core region increased compared with that under full power conditions. The excess flow rate was provided by reverse flow in the radial blanket region and the radial reflector region. However, the flow rate in the outer core region was comparable with that under full power conditions. This relatively low flow rate resulted in the highest temperature in the outer core subassembly in Fig. 5.4-3. Partial reverse flow (recirculation flow) was seen in the subassembly due to the low flow rate. Further, cold radial flow in the gap region, above the pad position and coming from the upper plenum, could cool the upper part of the outer core subassembly, which is located in the outermost layer in the core fuel subassemblies. These cooling effects via the cold fluid from the DHX reduced the

temperature in the upper non heated part of the outer core subassembly. Such temperature decrease also reduced the natural circulation head and the flow rate in the subassembly. Thus, the outer core subassemblies could not gain the additional flow rate.

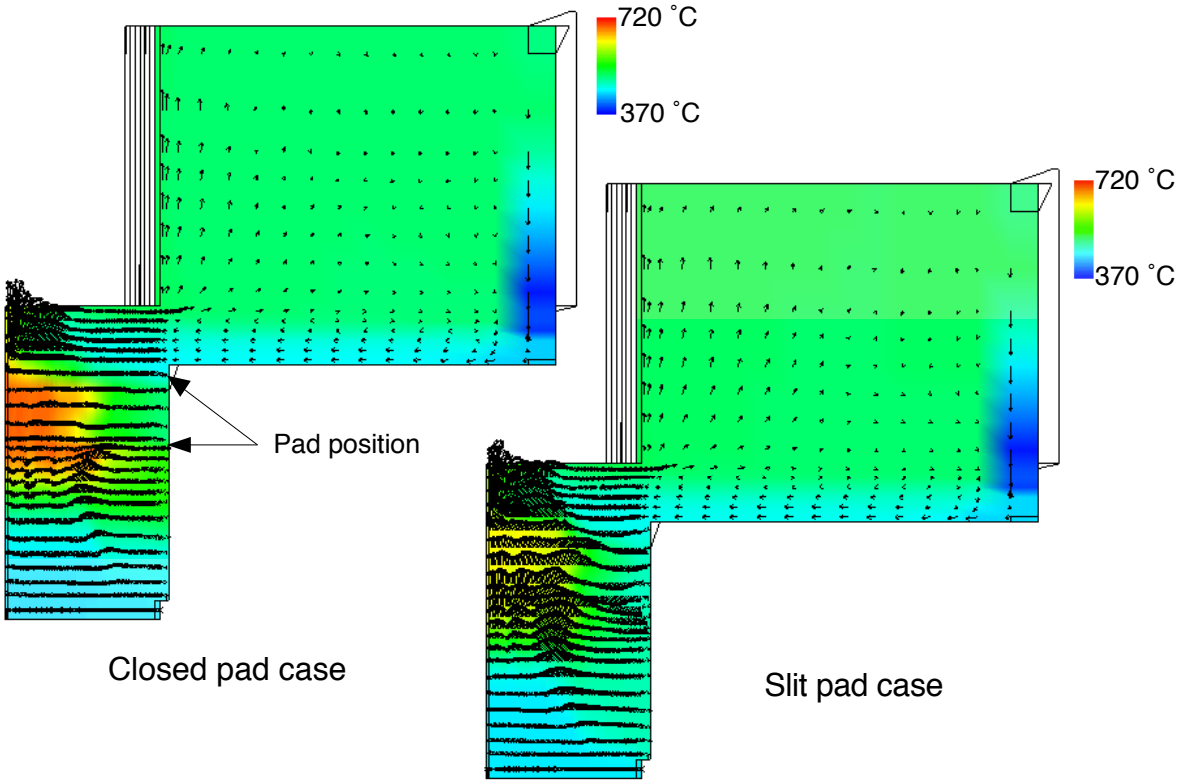

Fig. 5.4-2 Calculated Velocity and Temperature Fields in Gap Region (J=3) in a Reactor Core

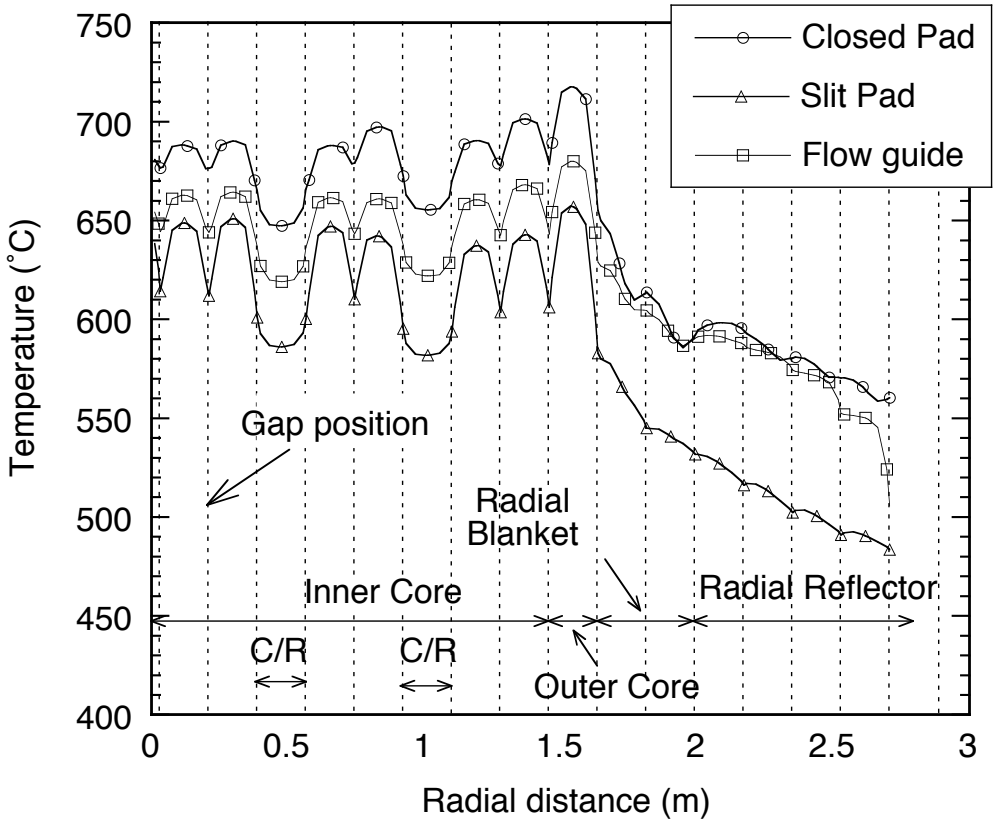

Fig. 5.4-3 Radial Temperature Distributions across the Subassemblies at Top of Active Core

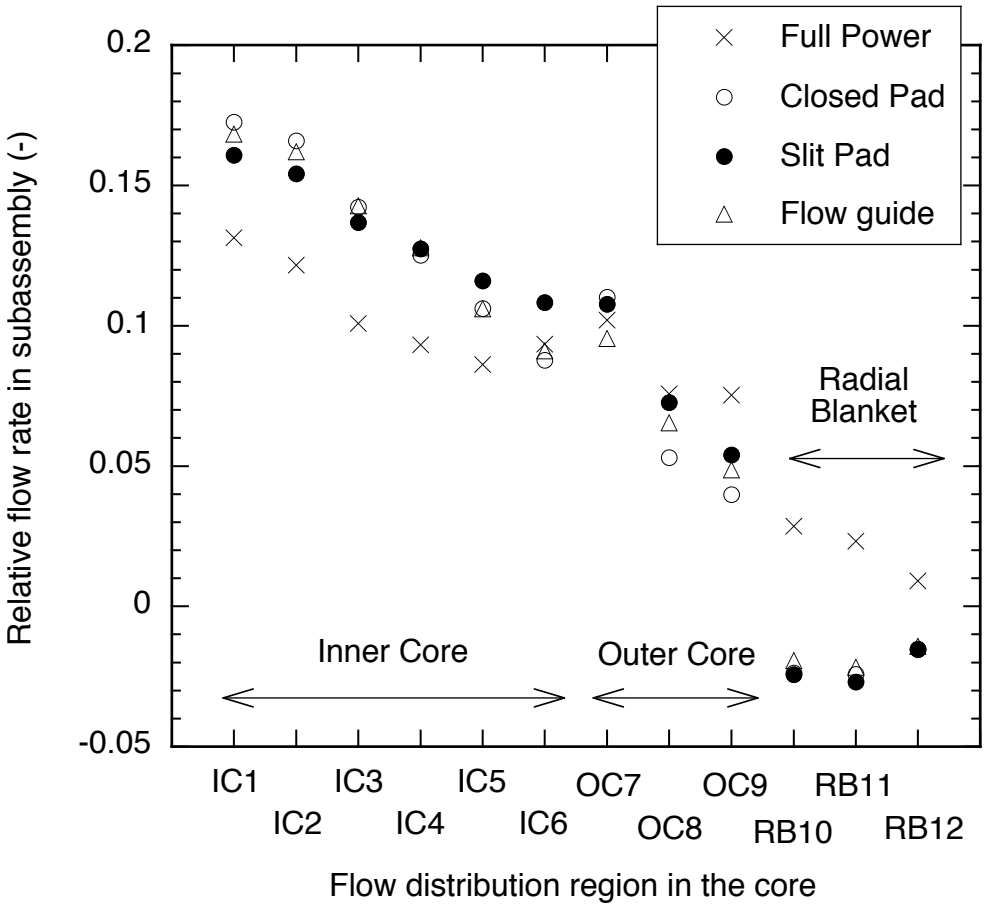

Fig. 5.4-4 Flow Redistribution under Natural Circulation Condition

(3) Discussions

a. Heat removal by IWF

Figure 5.4-5 shows non-dimensional peak temperature, T*, in each subassembly along the J=1 array. The definition of the non-dimensional temperature is the same as Eq. (4.1). T* is relative peak temperature as compared with the average temperature increase based on the power and flow rate in each subassembly.

In the closed pad case, T* in the outer core subassembly (OC7) and the outermost subassembly (IC5) in the inner core showed 0.9 to 0.8. These subassemblies had higher temperature in the core (see Fig. 5.4-3) and were cooled by the inter-subassembly heat transfer and IWF. In the inner core subassemblies, T* showed around 1.1. This resulted from heat transportation from the outer core subassemblies to the inner core subassemblies via IWF (see Fig. 5.4-2). In the slit pad case, the T* in the inner core subassemblies showed 0.8. This indicates that IWF cools the inner core subassemblies by 20% of the decay heat. In the outer core subassembly, it reached nearly 40%. The non-dimensional temperature in the flow guide case was higher than that in the slit pad case by 5 to 10%. However, the flow guide functioned to utilize IWF to reduce the core temperatures.

b. Key phenomena during natural circulation

It was revealed by the prediction analyses that IWF had significant influence on core thermohydraulic conditions. The highest temperature in the core was decreased by IWF in the case of the slit-type pad. The radial temperature profile in the core was affected by the flow redistribution, caused by buoyancy force, in the core. In the outer subassemblies, the buoyancy force was reduced by the penetration flow (partial reverse flow from the upper plenum) in the upper axial reflector and IWF via the temperature decrease in the upper non heated part in the subassemblies. The inter-subassembly heat transfer also reduced the temperature in the outer core subassembly due to the large temperature difference between the outer core subassemblies and the radial blanket subassemblies.

These phenomena were coupled with each other. Thus, a precise prediction method

should have the capability to consider all phenomena together. The following points are to be modeled:

1) IWF,

2) inter-subassembly heat transfer,

3) flow redistributions in a subassembly and among subassemblies.

Transverse temperature distribution in the subassembly, i.e., temperature dip in the wall subchannel, is also significant in the simulation of heat removal through the wrapper tube by IWF and the inter-subassembly heat transfer.

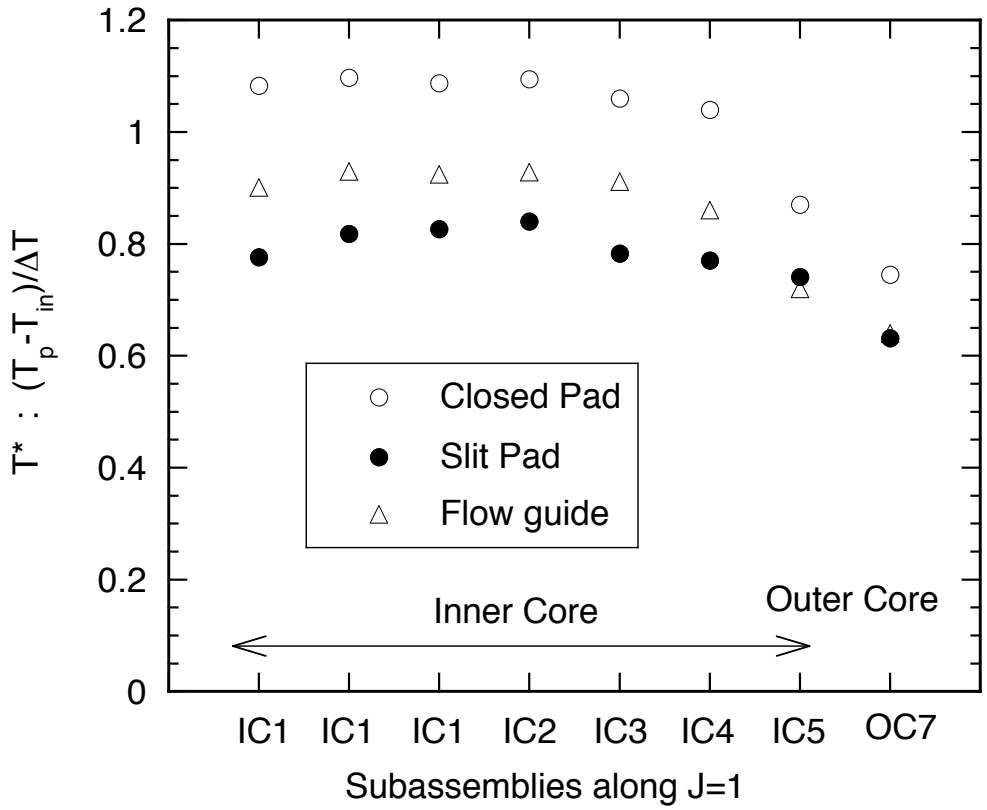

Fig. 5.4-5 Radial Distributions of Non-dimensional Peak Temperature in the Subassemblies along J=1

5.5 Conclusions

A multi-dimensional calculation using the brick-subassembly model based on the finite difference method was developed to investigate the thermal hydraulics in an entire core during natural circulation. The calculational method models the subassemblies, the gap region between the subassemblies, and the upper plenum together to simulate the gap flow between the subassemblies (inter-wrapper flow, IWF). The subassembly is modeled in a rectangular mesh scheme which considers the structure of inner and wall subchannels. It can simulate temperature decrease in wall subchannel region when IWF cools the subassembly through the wrapper tube.

The calculational method was verified through the water and sodium experiments on the points of the flow field of IWF and the temperature decrease in the subassemblies, respectively. The parametric calculations showed that the vertical flow resistance coefficient in the gap region through the pad position should be set carefully.

Prediction analyses using this method were performed for a 600 MWe class fast reactor core which features the direct reactor auxiliary cooling system (DRACS). Inter-subassembly spacer pad and flow guide through the core former exerted a significant influence on IWF and, consequently, on the highest temperature in the core. The slit in the pad enhanced IWF and significantly reduced the highest temperature in the core as compared with that in the closed core barrel using the band-type pad and the closed core former. The radial temperature profile in the core was affected by the inter-subassembly flow redistribution, caused by buoyancy force. The inter-subassembly heat transfer also reduced the temperature in the outer core subassembly due to the large temperature difference between the outer core subassemblies and the radial blanket subassemblies.

It is also pointed out that the prediction methods of thermal hydraulic phenomena in a core during natural circulation should model IWF, the inter-subassembly heat transfer and the flow redistribution in the core.

Chapter 6. Discussions

Chapter 6. Discussions

In this chapter, the obtained findings are summarized in the categories of experiments and simulation methods. Then, core thermal hydraulics in a reactor of design study is predicted based on these findings. Further, feedback to the reactor design and requirements of the evaluation method are discussed.

6.1 Obtained Insights

The significant insights obtained in this study are depicted in this section. These insights should be considered in an evaluation method of the core thermal hydraulics during the natural circulation.

6.1.1 Phenomena Identified

First, identified phenomena in the multi-subassembly experiments are listed below.

1) Flow redistribution in a subassembly

- ✓ Temperature distribution is flattened in a subassembly by the flow redistribution.
- ✓ Temperature flattening was represented by a peaking factor of normalized highest temperature in the cross section. The peaking factor was well correlated by a buoyancy parameter, i.e., Gr*/Re.
- ✓ Decrease of the temperature peaking due to the flow redistribution was observed even in the second peak after a scram and also correlated with the buoyancy parameter.

2) Inter-subassembly heat transfer

- ✓ The inter-subassembly heat transfer reduced the temperature at the center subchannel even in a large subassembly although the heat was removed through the outermost wrapper tube wall.
- ✓ The highest temperature was reduced by the inter-subassembly heat transfer even in the second peak after a scram.
- ✓ The wall subchannel temperature changed drastically as compared with the section averaged temperature when the heat flux of the inter-subassembly heat transfer was large.

- ✓ Thus, the heat flux of the inter-subassembly heat transfer should be correlated with the wall subchannel temperature in the subassemblies, NOT the bundle averaged temperature.
- ✓ The wall subchannel temperature was correlated with the buoyancy parameter and a ratio of the heat flux through the wrapper tube wall to the fuel pin surface heat flux.

3) Penetration flow into a subassembly

- ✓ Penetration flow was intermittent phenomena driven by the negative buoyancy force
- ✓ Onset condition of the penetration flow was represented by a critical value of Gr/Re^2 in water experiments.
- ✓ Onset condition in sodium was also correlated with Gr/Re^2. The correlation was obtained in a sodium experiment, where an upper plenum and a subassembly were modeled (Kamide, 2009).
- ✓ Influence of the penetration flow would be limited because of the short penetration length revealed in the sodium experiment (Kamide, 2009).

4) Inter-wrapper flow (IWF)

- ✓ Heat removal of IWF would decrease the center subchannel temperature even in a large size bundle as well as the inter-subassembly heat transfer.
- ✓ This temperature reduction effect of IWF was well represented by a non-dimensional parameter, $Gr/Re^{7/4}$
- ✓ IWF reduced the highest temperature of a core in a transient event.

6.1.2 Simulation Methods

A numerical simulation method was developed based on a three-dimensional code for thermal hydraulics in a multi-subassembly system where the heat was transferred between the subassemblies. The features of the simulation method are listed below.

- ✓ A staggered half-pin mesh arrangement is applied, which is equivalent to a subchannel mesh scheme.
- ✓ The wall and internal subchannels are treated separately in the mesh arrangement by using Cheng and Todreas correlations of pressure loss coefficients.

- ✓ Each of the subassemblies is modeled in a computational domain by using a multi-region model. The heat transfer between the subassemblies is considered across the computational domains.

The application of this simulation method to the multi-subassembly experiments showed that the temperature distributions flattened by the flow redistribution and distorted by the heat flux through the wrapper tube wall were well predicted.

6.2 Whole Core Analysis of Thermal Hydraulics

Multi-dimensional simulation method of an entire core in a reactor vessel was developed based on the experimental insights of IWF obtained by the seven-subassembly model and also the simulation method of a multi-subassembly system. Specifications of the simulation method are as follows:

- ✓ Subassemblies in a core, inter-wrapper gap, and reactor upper plenum system are modeled in a computational domain.
- ✓ The wall and internal subchannel areas are separately modeled by a simplified mesh scheme in each subassembly.

The validation analyses showed the good agreements of the temperature profiles in the subassemblies and also in the core barrel with the 7-subassembly sodium experiments and also the core scale water test.

This entire core simulation method was applied to a prediction analysis of decay heat removal in a 600 MWe class fast reactor. Insights obtained by the application analysis are listed below.

- ✓ IWF has significant effect to reduce the highest temperature in a large scale core during natural circulation.
- ✓ Flow path through the spacer pads on the subassembly walls is a key parameter of IWF. The slit in the pad has significant effect to enhance the IWF cooling.
- ✓ The radial temperature profile in the core was affected by the flow redistribution, caused by buoyancy force, in combination with IWF in the core. The flow rates through the subassemblies strongly cooled by IWF are redistributed into the high temperature subassemblies in the core.
- ✓ The inter-subassembly heat transfer also reduced the temperature in the outer core subassembly due to the large temperature difference between the outer core subassemblies and the radial blanket subassemblies.
- ✓ A combination of an inter-wrapper gap model, which considers IWF and inter-subassembly heat transfer, and the multi-area subassembly model, which treats the wall and internal subchannels separately, were significant to simulate the core thermal hydraulics. These modeling points should be considered in a simulation method of the core thermal hydraulics.

6.3 Feedbacks to Reactor Design and Evaluation

Several insights of phenomena in a core under natural circulation and the simulation method of an entire core were obtained in this study. At this moment a 1,500MWe class reactor, Japan Sodium-cooled Fast Reactor (JSFR), was designed and developed by Japan Atomic Energy Agency (Ichimiya, 2007, Kotake, 2010). Here, thermal hydraulic phenomena under natural circulation decay heat removal in the JSFR are predicted based on the design features of JSFR and experimental insights obtained in this study. Further, several points to be considered in the design study are discussed.

6.3.1 Design Features of JSFR

Decay heat removal system of JSFR is shown in Chapter 2. Here significant points for the core thermal hydraulics are listed:

- ✓ Single heat exchanger of DRACS (DHX) is dipped in the reactor upper plenum.
- ✓ Column type upper internal structure (UIS) is adopted. The core flow can pass through the UIS. The UIS has a slit in radial direction at far side from the DHX.
- ✓ 600 of core fuel subassemblies are housed in a core barrel.
- ✓ Band type pad is used as the subassembly spacer on a wrapper tube wall. Thus gap at the spacer pad is limited, but still exists due clearance for the subassembly exchange and local disorder of subassembly arrangement.
- ✓ The sole DRACS operation is assumed in case of beyond design base events.

6.3.2 Predicted Characteristics of Core Thermal Hydraulics Related to JSFR Features

The design features mentioned above will bring unique phenomena in the core. Such phenomena are presumed based on the insights obtained in this study.

Hot flow from the core fuel subassemblies will get together toward the core center and rise through the column type UIS composed of permeable baffle plates. Thus, surrounding fluid in the bottom of reactor upper plenum will flow toward the core and cover the outer region of the core. Asymmetric arrangement of the heat exchanger and

also asymmetric flow velocity filed in the UIS will bring low temperature fluid above the core locally near the DHX. Such local cold region above the core may result in asymmetric natural convection in the core barrel, i.e., IWF. This asymmetric flow pattern of IWF will influence the thermal bowing of the subassemblies and increase the gap width between the subassembly spacer pads. Such local increase of gap width will enhance asymmetric IWF further.

The sole DRACS operation results in lower natural circulation flow rate because of temperature increase in the IHX of downward flow path. In this case, IWF will take a significant role to decrease the highest temperature in the core.

6.3.3 Feedbacks to Design Approaches of JSFR

IWF will occur even if the band type spacer pad is employed in the core due to limited and uncontrolled small gap at the pads. On the other hand, heat removal due to IWF will be required in case of the sole DRACS operation.

These facts will bring other design approaches to utilize IWF effectively. One of ideas is that slit in the band type spacer pad will permit small amount of flow through the pads not in local region but the entire region of the core. It will help to reduce asymmetric temperature filed in the inter-wrapper gap. Further, it would enhance IWF and the heat removal capability in the reactor vessel, if the core temperature increased during the sole DRACS operation (Kamide, 2002).

6.3.4 Role of Evaluation Method and Required Functions

The evaluation method of core thermal hydraulics is significant to design and optimize the flow path of IWF in a core during natural circulation. According to this study on the core thermal hydraulics, following phenomena were of importance and should be considered in the evaluation of the highest temperature in a core:

- ✓ Flow redistributions in a subassembly and also in a core
- ✓ Inter-subassembly heat transfer
- ✓ Inter-wrapper flow

These phenomena depend on each other and should be modeled together in the

evaluation method, when the IWF path in a core is designed.

The inter-subassembly heat transfer is closely related with the flow redistribution in a subassembly. The heat flux between the subassemblies was decided by not the subassembly average temperatures but the wall subchannel temperatures at face to face walls. Further, the multi-subassembly sodium experiments showed that the wall subchannel temperatures were influenced significantly by the heat flux of the inter-subassembly heat transfer and also by the flow redistribution in subassembly. Thus, the wall subchanels at each side of a hexagonal tube and internal subchannel should be modeled separately in a subassembly model. This modeling is also the minimum requirement to consider the flow redistribution in the subassemblies.

IWF consists of complex flow network, i.e., gap region between the subassemblies in a core barrel and partially separated by the spacer pads on the subassemblies, and finally connected to the reactor upper plenum through the spacer pad gaps. The gap flows between the subassemblies also exchange the heat with the wall subchannels in each subassembly through the wrapper tube wall. The experimental results showed that the wall subchannel temperatures were decreased drastically by the heat removal of IWF as compared with the internal subchannel temperatures. This heat removal was asymmetric in a core and different at each side of a subassembly. These insights lead the modeling of IWF should consider each flow path of the inter-wrapper gaps and geometrical correlation with the sides of hexagonal wrapper tubes.

The brick subassembly model using a three dimensional thermal hydraulics code proposed in the Chapter 5 is one of answers to model the inter-wrapper gap, flow structure in each subassembly, and geometrical correlations of the gap and the subassemblies.

The negative buoyancy force of the cold fluid provided by DHX in the reactor upper plenum is significant driving force of IWF in a hot core barrel. Thus thermal stratification in the reactor upper plenum should be correctly predicted to estimate this negative buoyancy force. Further this upper plenum must be connected with the

complex gap flow region in a core. These flow paths are spread over the entire core and flow directions (downward or upward) at the paths will change according to the positions and time.

Such complex modeling is difficult for a kind of one-dimensional network model. Thus, a multi-dimensional code is one of solutions to model the complex flow paths of IWF and thermal stratification in the reactor upper plenum.

6.3.5 Evaluation Method to be Applied

According to these considerations of the core thermal hydraulics, followings are the required features and functions of the evaluation method;

- ✓ Wall subchannels and internal subchannels are modeled separately in each subassembly.
- ✓ Each flow path of the inter-wrapper gaps is modeled so as to keep geometrical correlation between the flow paths and the sides of hexagonal wrapper tubes.
- ✓ The reactor upper plenum is modeled to simulate thermal stratification due to the cold sodium provided by DHX.
- ✓ The reactor upper plenum is connected with the inter-wrapper gap region through the spacer pad clearances.

The brick-subassembly model with a reactor upper plenum using a multi-dimensional code is one of methods satisfying these requirements. Applicability of this modeling was demonstrated in Chapter 5. Design study of the flow path through the spacer pads will be useful to optimize the heat removal capacity of IWF in a reactor.

6.4 Summary

In this chapter, several significant insights obtained in this study were summarized and needs of a multi-dimensional simulation method were confirmed as an evaluation method of the core thermal hydraulic phenomena under natural circulation conditions. Further, feedback for a design study of 1,500 MWe class sodium-cooled reactor was pointed out. Especially, utilization of IWF as a heat removal path was proposed for a beyond design event where DRACS was solely used as the decay heat removal system. Additional role of the evaluation method is to optimize such designs of IWF enhancement. Finally, required features and functions of the evaluation methods to be applied to the core thermal hydraulic phenomena under natural circulation were summarized.

Chapter 7. Summary and Conclusions

Chapter 7. Summary and Conclusions

7.1 Summary

Natural circulation is of importance for decay heat removal after the shutdown of a reactor from the viewpoint of passive safety. Several sodium and water experiments on core thermal hydraulics under natural circulation conditions of a sodium-cooled fast reactor were carried out to understand the buoyancy driven phenomena and to develop estimation methods.

The core is composed of several types of subassemblies that have their own thermal power and flow resistance coefficients. This leads buoyancy-induced flow redistribution in the core under low flow rate conditions of natural circulation. Further, the radial temperature distribution across the core brings heat transfer between the subassemblies. Such heat flow through the wrapper tube is considerably large under low flow rate conditions through the subassembly. The sodium gap between the subassemblies creates natural convection according to the radial temperature distributions in the core. This inter-wrapper flow can transport the heat from the core center to the peripheral regions.

These findings suggest us that thermal hydraulic phenomena in an FBR core should be treated with a multi-subassembly or an entire core system. The phenomena to be resolved were as follows:

- ✓ Flow redistributions in a subassembly (Chapter 2.)
- ✓ Inter-subassembly heat transfer (Chapter 2.)
- ✓ Buoyancy-induced penetration flow into a subassembly (Chapter 3.)
- ✓ Inter-wrapper flow (IWF) (Chapter 4.)

Further thermal hydraulics in the entire core was predicted by a whole core calculation, which was developed based on experimental findings in this study in Chapter 5. Feedbacks to design of Japanese Sodium-cooled Fast Reactor, JSFR, were discussed in Chapter 6. Each of the chapters is summarized below.

Chapter 2:

The subassembly thermal hydraulics were investigated by the three-subassembly model and the seven-subassembly model using sodium as a working fluid. The experiments focused on flow redistribution and inter-subassembly heat transfer under NC/DHR conditions including transient from forced to natural circulation. The three-subassembly model simulated a blanket fuel subassembly of 61-pin bundle in real dimensions and also the boundary between the blanket fuel subassemblies and the core fuel subassemblies. The seven-subassembly model simulated the core fuel subassembly of 37-pin bundle surrounded by six subassemblies as a partial model under the steady state conditions and the scram transient conditions.

The peaking factor (P_f), normalized highest temperature at a cross section, was obtained in the steady state and transient experiments. Radial heat transfer between subassemblies was coupled with the wall subchannel temperatures. Thus, the wall subchannel factor (W_f) was defined to estimate the wall subchannel temperature from the average cross section temperature by using the analogy of the peaking factor (P_f). Characteristics of intra-subassembly thermal hydraulics were grasped under the steady state conditions and the scram transient conditions:

1) Influence of intra-subassembly flow redistribution
   - The transverse temperature distribution was flattened by the flow redistribution, even if inter-subassembly heat transfer occurred and during the scram transient including the second peak.
   - The influences on P_f and W_f correlated well by a modified buoyancy parameter, Gr*/Re, in the blanket and also core fuel pin bundles under steady state conditions of NC/DHR. The obtained correlation with Gr*/Re was independent of the axial position in the subassembly.
   - The P_f decreased from 1.2 to 1.05 during the transitions from the 12% velocity condition to 2% of the full power condition in a core fuel subassembly. The P_f

was nearly 1.08 at the second peak during the scram transition.

- The P_f correlation using Gr*/Re obtained from the steady state experiments could be applied to the estimation of the transient behavior.

2) Influence of inter-subassembly heat transfer

- The inter-subassembly heat transfer reduced the highest temperature, even in a full size pin bundle of the blanket core fuel subassembly.
- Influence of inter-subassembly heat transfer on W_f and P_f correlated well using the wall heat flux ratio ($q"_{w/p}$).
- Under the conditions of a large negative $q"_{w/p}$ and high Gr*/Re, W_f decreased extremely.
- The inter-subassembly heat transfer had significant effect on the reduction of the hottest temperature in a subassembly during the transition including the second peak in a core fuel subassembly model.

The three-dimensional calculation method was applied to the experimental analyses of the three-subassembly model tests. The multi-region model and the staggered half pin mesh arrangement were used. The correlations of axial flow resistance developed for subchannel analysis codes were applied in the wall subchannel region and the inner subchannel region separately.

The applied method could accurately simulate the transverse temperature distributions in the multi-subassembly system, including P_f and W_f under mixed convection conditions influenced by inter-subassembly heat transfer. These facts showed that the modeling of the staggered half pin mesh arrangement and the axial flow resistance coefficients at the wall subchannel and the inner subchannel regions was adequate for the simulation of subassembly thermal hydraulics under natural circulation conditions.

Chapter 3:

The penetration flow into subassemblies due to the negative buoyancy force was investigated using a simple water test apparatus and also a sodium test facility.

In the water experiment, the thermal stratification in the upper plenum and the penetration flow coming from stratified cold fluid were simulated by using a square shape channel connected to a slab geometry plenum. In the sodium experiment, three subassemblies were modeled including the handling head and hollow type upper neutron shielding above the pin bundle. The diameter of the flow channel in the upper neutron shielding was 0.08m and nearly equal to that in a reactor. The subassemblies were connected to an upper plenum where cold sodium can be provided.

Onset conditions of the penetration flow were obtained as a function of non-dimensional numbers of Gr and Re in the water experiment and the sodium experiment. It was recognized that Gr/Re^2 is a key parameter for the onset of the penetration flow both in the water and sodium experiments. It means that the onset condition is decided by the balance between the buoyancy force and the inertial force even in the sodium system.

The sodium experiments showed that the penetration lengths in the upper neutron shielding were less than 0.26m when the flow rate was larger than 2% level of the full power condition of a blanket subassembly in a reactor. Further, the penetration flow did not reach the pin bundle, when the flow velocity was maintained at 0.014m/s in the upper neutron shielding (1% of the full power condition).

From the numerical simulations of the water experiments, the following conclusions were drawn:

- The penetration flow was calculated by the numerical methods while the results showed wide variation on the onset condition as well as the penetration depth.
- The turbulent viscosity and turbulent mixing strongly influenced the penetration depth. Thus, improvement in turbulence models, especially for low Re and mixed convection flows, is important.

These calculations showed that the penetration flow due to the buoyancy force can be predicted by the multi-dimensional analyses where physical viscosity should be treated well accompanied with numerical viscosity according to the numerical schemes.

The sodium experiments using the full-scale subassembly model revealed that the penetration depth would stay in the upper neutron shielding and influence of the penetration flow phenomena would be limited on the thermal hydraulics during the natural circulation in a reactor core.

Chapter 4:

Thermal hydraulic experiments in a sodium facility were carried out in order to investigate IWF during natural circulation decay heat removal in fast reactors. The reactor core geometry was simulated by seven subassemblies. The temperature fields in the simulated core were measured under steady-state conditions with zero to 3% flow velocity in the subassemblies relative to the full power conditions of an actual reactor. Following conclusions were reached from the experiments:

- When IWF occurred, the gradient of the transverse temperature distribution in the subassembly tended to increase. The axial position corresponding to the maximum temperature was, in fact, lower than the top of the heated length. These points should be considered in order to estimate the maximum temperature, which is influenced by the heat transfer through the wrapper tube wall.

- IWF can reduce the peak temperature in the subassembly. The cooling effect was significant when the flow velocity in the subassembly was less than 1% relative to rated conditions in a reactor. A new non-dimensional parameter, $C\,Gr^{4/7}/Re$, was introduced to characterize estimates of the cooling effects.

- The flow rate under natural circulation in the primary loop was also reduced by IWF; however, the cooling effect was relatively larger than the negative influence via the flow reduction when the primary flow rate was less than 1% of reactor rated conditions.

- The cooling effect of IWF was more evident in the outer subassemblies and weaker in the center subassembly. However, an indirect cooling effect due to IWF was seen in the center subassembly via the flow redistribution from the outer subassemblies to the center subassembly.

Further, transient sodium tests were carried out for natural circulation decay heat removal. The test loop, PLANDTL-DHX, simulated the primary loop, core (seven-subassembly), the IHX, the secondary loop, and also a decay heat removal system using a dipped heat exchanger in the upper plenum. The simulated core has cylindrical spacers between the subassemblies to allow the natural convection from the upper plenum into the subassembly gaps.

The following conclusions were obtained from the experimental results:

- IWF could remove the heat from the subassemblies even in a transition from forced to natural circulation.
- In a case of sudden decrease of the primary flow rate, IWF functioned to remove the heat in time.
- Core-plenum interactions, i.e., IWF, reverse flow, and the inter-subassembly heat transfer can cool the core on demand and have no significant negative influences on core thermal hydraulics in the case of sufficient core flow rate.

A water experiment was carried out to investigate IWF in a whole core. A 1/12 sector of a reactor core was modeled by a hexagonal configuration of core fuel subassemblies and radial shielding. The flow field in the gap region was grasped and a data set was obtained for the verification of a numerical simulation method.

Chapter 5:

A multi-dimensional calculation using the brick-subassembly model based on the finite difference method was developed to investigate the thermal hydraulics in an entire core during natural circulation. The calculational method models the subassemblies, the gap region between the subassemblies, and the upper plenum together to simulate the gap flow between the subassemblies (inter-wrapper flow, IWF). Each subassembly is modeled in a rectangular mesh scheme which considers the structure of inner and wall subchannels. The peripheral length of each subassembly is set equal to that of the hexagonal shape of the wrapper tube to simulate the heat exchange area and heat flux between the subassemblies and the inter-wrapper gap. The calculational method was verified through the water and sodium experiments on the points of the flow field of IWF and the temperature decrease in the subassemblies, respectively.

Prediction analyses using this method were performed for a 600 MWe class fast reactor core which features the direct reactor auxiliary cooling system (DRACS). Inter-subassembly spacer pad and flow guide through the core former exerted a significant influence on IWF and, consequently, on the highest temperature in the core. The slit in the pad enhanced IWF and significantly reduced the highest temperature in the core as compared with that in the closed core barrel using the band-type pad and the closed core former. The radial temperature profile in the core was affected by the inter-subassembly flow redistribution, caused by buoyancy force. The inter-subassembly heat transfer also reduced the temperature in the outer core subassembly due to the large temperature difference between the outer core subassemblies and the radial blanket subassemblies.

Chapter 6:

The significant insights obtained in this study were summarized and needs of a multi-dimensional simulation method were confirmed as an evaluation tool of the core thermal hydraulic phenomena under natural circulation conditions. Further, feedback for a design study of 1,500 MWe class sodium-cooled reactor was pointed out. Especially, utilization of IWF as a heat removal path was proposed for a beyond design event where DRACS was solely used as the decay heat removal system. One of ideas

is that slit in the band type spacer pad will permit small amount of flow through the pads not in local region but the entire region of the core. It will help to reduce asymmetric temperature filed in the inter-wrapper gap. Further, it would enhance IWF and the heat removal capability in the reactor vessel, if the core temperature increased during the sole DRACS operation.

Additional role of the evaluation method is to optimize such designs of IWF enhancement. Finally, required features and functions of the evaluation methods to be applied to the core thermal hydraulic phenomena under natural circulation were summarized.

7.2 Concluding Remarks

1) Experiments on Thermal Hydraulic Phenomena in Core

Three-subassembly sodium experiments under natural circulation conditions showed a decrease of the highest temperature even in a full size subassembly due to lateral heat flux through the wrapper tube, i.e., inter-subassembly heat transfer. This heat removal by inter-subassembly heat transfer and the transverse temperature profile in the subassembly, especially at the wall subchannels, influenced each other. A wall subchannel factor was defined to indicate distortion of the wall subchannel temperature as compared with the section average temperature as well as peaking factor, which was well used as a non-dimensional peak temperature. The experiments showed that the temperature profile in the subassembly depended on buoyancy force and heat flux at the wrapper tube wall due to inter-subassembly heat transfer. A buoyancy parameter of Gr*/Re was deduced to consider buoyancy force with the functions of temperature increase and flow velocity in a subassembly. Height from the lower heated end and hydraulic equivalent diameter were used as the representative lengths to define the non-dimensional parameter, Gr*. As for the heat flux at the wrapper tube wall, a wall heat flux ratio was defined as a ratio of the heat flux at the wrapper tube wall to that at the pin surface. The influences of the flow velocity, the temperature increase in the subassembly, and the inter-subassembly heat transfer on the transverse temperature profile in the subassembly were obtained by the three-subassembly sodium experiment. These influences on the peaking factor and the wall subchannel factor were well correlated by Gr*/Re and the wall heat flux ratio.

Seven-subassembly sodium experiments were performed to clarify influences of the inter-wrapper flow (IWF) and transient phenomena of the flow redistribution in a subassembly with the inter-subassembly heat transfer. In the transient experiments from forced to natural circulation, the peaking factor was reduced according to the velocity decrease during the transitions from forced flow condition, even in the timing that the highest temperature was registered. This transient peaking factor was well correlated by the empirical relationship of the steady state peaking factor and Gr*/Re. The inter-subassembly heat transfer also reduced the peak temperature in the transient.

The dipped heat exchanger of DRACS provides cold sodium into the reactor upper plenum and creates thermal stratification. A basic water experiment and a sodium experiment were carried out on a penetration flow of this cold fluid into a hot upward flow channel due to negative buoyancy force. The water experiment showed that the penetration flow occurred intermittently under steady state conditions, triggered by instability at hot and cold fluid interface. Onset conditions of the penetration flow were obtained with parameters of the temperature difference and the upward flow velocity in the water experiment and the sodium experiment. They were well correlated with a non-dimensional parameter of Gr/Re^2. Temperature distributions in the stratified layer and the onset conditions of the submerged flow in the water experiment were applied to the experimental analyses in order to obtain adequate numerical schemes and turbulence models of the three-dimensional analyses. The sodium experiments showed that the penetration flow occurred at the top of neutron shielding under low flow rate conditions of natural circulation in a blanket subassembly of a reactor. However, the penetration lengths in the upper neutron shielding were less than 0.26m when the flow rate was larger than 2% level of the full power condition of a blanket subassembly in a reactor. Further, the penetration flow did not reach the pin bundle, when the flow velocity was maintained at 0.014m/s in the upper neutron shielding (1% of the full power condition).

It was shown that the sodium temperature in the inter-wrapper gap region decreased due to inter wrapper flow (IWF), when the dipped heat exchanger of the DHRS was operated in the upper plenum above the subassemblies. The highest temperature in the subassemblies was reduced by IWF, i.e., heat removal through the wrapper tube wall. A non-dimensional parameter of $Gr^{4/7}/Re$ was derived to represent this heat removal by IWF, and the decease of the highest temperature in the subassemblies due to this IWF was well correlated with the $Gr^{4/7}/Re$.

Further, transient sodium tests were carried out for IWF. IWF could remove the heat from the subassemblies even in a transition from forced to natural circulation. In a case of sudden decrease of the primary flow rate, IWF functioned to remove the heat in time. Core-plenum interactions, i.e., IWF, reverse flow, and the inter-subassembly

heat transfer can cool the core on demand and have no significant negative influences on core thermal hydraulics in the case of sufficient core flow rate.

A water model experiment was performed to clarify IWF in a whole core. A 1/12 sector of the core, the reactor upper plenum, and the dipped heat exchanger were modeled. Flow pattern and temperature distributions in the gap region of the entire core were obtained utilizing parameters of the wall heat flux on the subassemblies. Downward flow in the outer non-heated subassembly region and upward flow in the core center region were confirmed.

2) Numerical Simulations for Multi-Subassembly System:

Numerical simulation methods are of importance the prediction and estimation of phenomena in a reactor. Several simulation methods were developed and validated based on the sodium and water experiments. A three-dimensional thermal hydraulics code, AQUA, was applied to the flow redistribution in a subassembly and inter-subassembly heat transfer. The pin bundle was modeled by the staggered half-pin mesh arrangement and the flow resistance coefficients based on the Cheng and Todreas correlation. The inter-subassembly heat transfer was simulated by a multi-subassembly mesh scheme using a multi-region model and heat conduction between the adjacent regions (subassemblies).

Applicability to flow redistribution in a full-size subassembly and to inter-subassembly heat transfer under steady state conditions was examined based on three-subassembly experiments in which flow rates, heater pin powers, and temperature difference between the adjacent subassemblies were varied. Transverse temperature profiles in the subassemblies were in good agreement between experiments and analyses, even in the case of high heat flux conditions at the wrapper tube wall and local recirculation along the cooled wall. Peaking and wall subchannel factors were also well predicted by the numerical analyses over a wide Gr*/Re parameter range.

Multi-dimensional analysis method was applied to thermal stratification and submerged flow into the upward flow channel. The higher-order differential scheme of the

momentum and lower viscosity resulting from the adequate turbulence model predicted the cold penetration flow into the hot upward flow channel. It was shown that the penetration flow could be predicted by the multi-dimensional analyses where physical viscosity should be sufficiently taken into account accompanied with numerical viscosity according to the numerical schemes.

3) Whole Core Analysis of Natural Circulation:

The brick-subassembly model with the reactor upper plenum using the finite difference method code, AQUA, was developed to investigate core-scale thermal hydraulics, i.e., the inter-wrapper flow, the flow redistributions in each subassembly and among the subassemblies, and the inter-subassembly heat transfer in an entire core. Each of the subassemblies is divided into the wall subchannel layer and inner subchannel layer in a square shaped mesh scheme. The brick-subassembly model was verified through the core scale water and seven-subassembly sodium experiments.

Prediction analyses using the brick-subassembly core model were performed for a 600 MWe class fast reactor which featured the direct reactor auxiliary cooling system (DRACS) to investigate the core-scale thermal hydraulic phenomena. The spacer pad geometry of the subassembly and flow guide through the core former exerted a significant influence on IWF and, consequently, on the highest temperature in the core. A slit in the spacer pad enhanced IWF and reduced the highest temperature. The radial temperature profile in the core was affected by the inter-subassembly flow redistribution and the inter-subassembly heat transfer.

4) Feedbacks to Reactor Design from This Study

The feedbacks to a design study of JSFR were pointed out based on findings of this study. Especially, utilization of IWF as a heat removal path was proposed for a beyond design-base event where DRACS was solely used as the decay heat removal system. One of ideas is that slit in the band type spacer pad will permit small amount of flow through the pads not in local region but the entire region of the core. It would enhance IWF and the heat removal capability in the reactor vessel, if the core temperature increased during the sole DRACS operation.

References

References

Arul, A. John, Kumar, C. Senthil, Athmalingam, S., et al., Reliability analysis of safety grade decay heat removal system of Indian prototype fast breeder reactor, Annals of Nuclear Energy, 33, pp.180-188 (2006).

Barakat, A.I. and Todreas, N.E., Mixed Convection Buoyancy-Induced Backflow in a Vertical Single Rod Channel Connected to an Upper Plenum, Proc. 4th Inter. Topical Meeting on Nuclear Reactor Thermal-Hydraulics Volume 2, p. 746, Karlsruhe, F.R. Germany, Oct. (1989).

Chang Jong-Eun, Suh Kune Y., Hwang Il Soon, Natural circulation capability of Pb-Bi cooled fast reactor: PEACER, Progress in Nuclear Energy, Vol.37, Issues 1-4, pp.211-216 (2000)

Cheng, S., and Todreas, N.E., Hydrodynamic models and correlations for bare and wire-wrapped hexagonal rod bundles - Bundle friction factors, subchannel friction factors and mixing parameters, Nucl. Eng. & Des. **92**, 227 (1986).

Davis Cliff B., Kim Dohyoung, Todreas Neil E., Kazimi Mujid S., Core power limits for a lead-bismuth natural circulation actinide burner reactor, Nuclear Engineering and Design, Vol.213, No.2-3, pp.165-182 (2002).

Eguchi, Y., Takeda, H., Koga, T., Tanaka ,N., and Yamamoto, K., Quantitative prediction of natural circulation in an LMFR with a similarity law and a water test, Nuclear Engineering and Design, Volume 178, Number 3, pp. 295-307 (1997).

Engel, F.C., Markley, R.A., The effects of radial heat flux gradients and flow regimes on the peak sodium temperature rise in wire wrapped rod bundles, Proc. ANS Top. Mtg. on Advance in Reactor Physics & Core Therm. Hydr., NUREG/CP0034, Vol.2, p.566 (1982).

Farrar, B., Lefe`vre, J.C., Kubo, S., et al., Fast reactor decay heat removal: approach to the safety system design in Japan and Europe, Nuclear Engineering and Design **193** 45–54 (1999).

Favet, D., et al., Natural circulation tests on SPX 1, ANS Intern. Fast Reactor Safety Meeting, Snowbird, UT, USA, Vol.4, Aug. 12-16 (1990).

Feldman, E.E., Mohr, D., Chang, L.K., et al., EBR-II Unprotected Loss-of-Heat-Sink Predictions and Preliminary Test Results, Nuclear Engineering and Design **101** 57-66 (1987).

Fraikin, M.P. and Portier, J.J., et al., Application of a k-ε turbulence model to an enclosed buoyancy driven recirculating flow, Chem. Eng. Commun. Vol. 13, pp.289-314, (1982).

Gry, W., Friedel, G., et al., FBR Decay Heat Removal System Design and Safety Studies, Proceedings of International Fast Reactor Safety Meeting, Snowbird, Utah, USA, p.543, Aug. (1990).

Hennies, H.H., Leduc, J., and Goddard, S.C., Development of Fast Reactors in Europe, Proc. Int. Conf. on Fast Reactors and Related Fuel Cycles, Kyoto, Japan, Oct. 28-Nov. 1, Vol.1, pp.1.2-1 ~11, Atomic Energy Society of Japan (1991).

Hoffmann, H., Marten, K., Weinberg, D., and Kamide, H., Thermohydraulic Model Experiments on the Transition from Forced to Natural Circulation for Pool-Type Fast Reactors, Nuclear Technology, Vol.99, No.3, p.374 (1992).

Hoffmann, H., Weinberg, D., et al., Scaled Model Studies of Decay Heat Removal by Natural Convection for the European Fast Reactor, Proceedings of NURETH-6, Grenoble, France, p.54, Oct. (1993).

Huebel, H., Koehler, M., Lange, L., Design of The Primary Containment for Pool and Loop Arrangements of LMFBRS, Nuclear Engineering and Design **27**, 139-154 (1974).

IAEA, LMFR core and heat exchanger thermal hydraulic design: Former USSR and present Russian approaches, IAEA-TECDOC-1060 (1999).

IAEA, VIENNA, Natural Circulation in Water Cooled Nuclear Power Plants: Phenomena, Models, and Methodology for System Reliability Assessments, IAEA-TECDOC-1474 (2005).

IAEA, Fast Reactor Database, http://www.iaea.org/inisnkm/nkm/aws/frdb/index.html (2006).

Ichimiya, M., Mizuno, T., and Kotake, S., A Next Generation Sodium-Cooled Fast Reactor Concept and Its R&D Program, Nuclear Engineering and Technology, Vol.39 No.3 (2007).

Ieda, Y. and Hayashi, K. et al., Thermohydraulic Study on Natural Circulation Decay Heat Removal for a Pool-type LMFBR, Proc. Inter. Conf. on Fast Reactors and Related Fuel Cycles, Volume II, p. 16.9-1, Kyoto, Japan, Oct. (1991).

Jerng, D.W. and Todreas, N.E., Mixed Convective Flow Penetration in Vertical Channels, Proc. 5th Inter. Meeting on Reactor Thermal Hydraulics, p.1720, Salt Lake City, USA, Sep. (1992).

Kamide, H., Ieda, Y., et al., Multi-bundle sodium experiments for thermohydraulics in core subassemblies during natural circulation decay heat removal operation , Proc. Int. Working Group on Fast Reactors specialists' meeting on Evaluation of Decay Heat Removal by Natural Circulation, O-arai, Japan, IWGFR/88 p.127 (1993).

Kamide, H., Ieda, Y., et al., Core-plenum thermohydraulics under decay heat removal by natural circulation - Sodium experiments for seven-subassembly model-, Proc. Int. Top. Mtg. on Sodium Cooled Fast Reactor Safety, Obninsk, Russia, Vol. 4, p.6-64 (1994).

Kamide, H., et al., "Inter-subassembly heat transfer during natural circulation decay heat removal of FBRs - Multi-subassembly sodium experiments -," Proc. 3rd JSME/ASME Joint Int. Conf. on Nucl. Eng., Kyoto, Japan, April 23-27, Vol.1, p.23 (1995).

Kamide, H., Kobayashi, J., Ieda, Y., and Ninokata, H., Benchmark exercise for multi-dimensional thermohydraulic analysis codes - Buoyancy driven penetration flow phenomena and thermal stratification -, Journal of Hydraulic Research, Vol.34, No.3, p.317-344 (1996).

Kamide. H., Hayashi, K., Isozaki, T., and Momoi, K., Investigation on Inter-Wrapper Flow in Fast Reactors during Natural Circulation Decay Heat Removal, -

Seven-subassembly Sodium Experiments -, Proc. Int. Mtg. on Advanced Reactors Safety (ARS '97), Orlando, Florida, Vol. 2, pp.1141-1149 (1997).

Kamide, H., Hayashi, K., and Momoi, K., Experimental Study of Core Thermohydraulics in Fast Reactors during Transition from Forced to Natural Circulation – Influence of Inter-Wrapper Flow -, Proc. 8th Int. Top. Mtg. on Nuclear Reactor Thermal Hydraulics (NURETH-8), Kyoto, Japan, Vol. 2 pp.922-931 (1997).

Kamide, H., Hayashi, K., and Toda, S., An Experimental Study of Inter-subassembly Heat Transfer during Natural Circulation Decay Heat Removal in Fast Breeder Reactors, Nucl. Eng. & Des., Vol.183, p.97-106 (1998).

Kamide, H., Hayashi, K., Isozaki, T., and Nishimura, M., Investigation of core thermohydraulics in fast reactors - Interwrapper flow during natural circulation, Nucl. Tech., Vol.133, p.77-91 (2001).

Kamide, K., Nagasawa, K., Kimura, N., and Miyakoshi, H., Evaluation Method for Core Thermohydraulics during Natural Circulation in Fast Reactors - Numerical Predictions of Inter-Wrapper Flow -, Proc. 9th Int. Conf. on Nuclear Engineering (ICONE-9), Nice, France, CD-ROM (2001).

Kamide, H., Nagasawa, K., Kimura, N., et al., Evaluation Method for Core Thermohydraulics during Natural Circulation in Fast Reactors, JSME International Journal Series B Fluids and Thermal Engineering, Vol. 45, No. 3, pp.577-585 (2002).

Kamide, H., Kobayashi, J., and Hayashi, K., Sodium Experiments of Buoyancy Driven Penetration Flow into Low Power Subassemblies in a Sodium Cooled Fast Reactor during Natural Circulation Decay Heat Removal, Proc. of The 13th International Topical Meeting on Nuclear Reactor Thermal Hydraulics (NURETH-13), Ishikawa, Japan, September 27-October 2, N13P1145 (2009).

Kimura, N., Miyake, Y., et al., Noise Reduction Techniques for the Particle Image Velocimetry -Application to an Experimental Study on Natural Convection in a Fast Reactor Core-, ICONE-8, Baltimore, MD, USA, April 2-6, ICONE-8405 (2000).

Kobayashi, J., Tokuhiro, A., Kamide, H., Ohshima, H., and Ieda, Y., An Experimental Investigation on Penetration of Buoyancy-Driven Cold Liquid into A Vertical Channel

with Hot, Forced-Flow, Nuclear Engineering and Design, Vol.177, Issues 1-3, pp.91-104 (1997).

Koga, T., Takeda, H., Moriya, S., et al., Natural circulation water tests for top-entry loop type LMFBR. Proc. 6th Int. Topical Meeting on Nuclear Reactor Thermal Hydraulics, Grenoble, France, pp.1302–1308 (1993).

Kotake, S., Sakamoto, Y., Mihara, T., et al., Development of Advanced Loop-Type Fast Reactor in Japan, Nucl. Tech., Vol.170, pp.133-147 (2010).

Luangdilok, W., and Todreas, N.E., Wall-cooling-induced mixed-convection flow recirculation in a vertical square-array multi-rod channel, Proc. 4th Int. Top. Mtg. on Nucl. Reac. Thermal-Hydraulics, Karlsruhe, F.R.Germany, Vol.2 p.1332 (1989).

Launder, B.E. and Spalding, D.B., The numerical Computation of Turbulence Flows, Comp. Methods Apple. Mech. Eng., Vol. 3 p. 269, (1974).

Maekawa, I., et al., Numerical diffusion in single-phase multi-dimensional thermal-hydraulic analysis, Nucl. Eng. & Des. Vol.120, p.323 (1990).

Modi, V. and Torrance. K.E., Experimental and Numerical Studies of Cold Inflow at the Exit of Buoyant Channel Flows, Journal of Heat Transfer, Volume 109, pp.392-399, (1987).

Naohara, N., Akutu, Y., et al., Study on Thermohydraulic Characteristics of Pool-type FBR Decay Heat Removal, Proceedings of International Fast Reactor Safety Meeting, Snowbird, Utah, USA, p.503, Aug. (1990)

Namekawa, F., Luangdilok, W., et al., Buoyancy and radial power skew effects on wire-wrapped rod bundle thermal hydraulics in an LMFBR fuel assembly, Proc. 3rd Int. Top. Mtg. on Reactor Thermal Hydraulics, Vol.2 16.J-1 (1985).

Nayak, A.K., Vijayan, P.K., Saha, D., Venkat Raj, V., and Aritomi, M., Study on the stability behavior of a natural circulation pressure tube type boiling water reactor, Nuclear Engineering and Design, Vol.215, Issues 1-2, pp.127-137 (2002).

Ninokata, H., Current practice in fast reactor safety thermohydraulic analysis, Proc. 3rd International Topical Meeting on Reactor Thermal Hydraulics, Keynote, Vol. 2, pp. 12.A-1 - 9, Newport, October (1985).

Ninokata, H., A Subchannel Analysis Code ASFRE-III and its Application to a Local Blockage Experiment in a Wire-Wrapped Pin Bundle, Proceedings of 14th Meeting of the Liquid Metal Boiling Working Group, Brasimone, Italy, p.287, Apr. (1991).

Nishimura, M., Kamide, H., Hayashi, K., and Momoi, K., Transient experiments on fast reactor core thermal-hydraulics and its numerical analysis Inter-subassembly heat transfer and inter-wrapper flow under natural circulation conditions, Nucl. Eng. & Des., Vol.200, p.157-175 (2000).

Ohyama, K., Watanabe, O., Eguchi, Y., Koga, T., et al., Decay Heat Removal System by Natural Circulation for JSFR, Proc. of Int. Conf. on Fast Reactors and Related Fuel Cycles (FR09), 08-21P, Kyoto, Japan, Dec. 7-11 (2009).

Rehme, K. and Trippe, G., Pressure Drop and Velocity Distribution in Rod Bundles with Spacer Grids, Nuclear Engineering Design, Vol.62, pp.349-359 (1980).

Ro, T.S., and Todreas, N.E., Porous body approach for wire-wrapped rod bundle analysis, Proc. 3rd Int. Top. Mtg. on Nucl. Power Plant Therm. Hydr. & Operation, Seoul, South Korea, A4.A-3 (1988).

Rodi W., Turbulence Models for Environmental Problems, Prediction Methods for Turbulent Flows, Hemisphere Publishing Corporation (1980).

SAKAI Takaaki, ENUMA Yasuhiro, IWASAKI Takashi, System analysis for decay heat removal in lead-bismuth-cooled natural-circulation reactors, Nuclear Technology, Vol. 145, No.3, pp. 287-297 (2004).

Satoh, K and Miyakoshi, H., Study of Decay Heat Removal by Natural Circulation - Transition from Forced to Natural Circulation Flow -, Proc. 4th Inter. Topical Meeting on Nuclear Reactor Thermal-Hydraulics, Volume 1, p. 378, Karlsruhe, F.R. Germany, Oct. (1989).

Sawada, M., Arikawa, H. and Mizoo, N., Experiment and Analysis on Natural Convection Characteristics in The Experimental Fast Reactor Joyo, Nuclear Engineering and Design, **120** 341-347 (1990).

Schubert, B.K, Dynamic simulation of the air-cooled decay heat removal system of the German KNK-II experimental breeder reactor, Brookhaven National Lab., Upton, NY (USA), NUREG/CR—3910 (1984).

Schulz, T.L., Westinghouse AP1000 advanced passive plant, Nuclear Engineering and Design, Vol.236, Issues 14-16, pp.1547-1557 (2006).

Sienicki J.J. and Moisseytsev A.V., SSTAR Lead-Cooled, Small Modular Fast Reactor for Deployment at Remote Sites - System Thermal Hydraulic Development, Proc. of ICAPP '05, Seoul, KOREA, May 15-19, Paper 5426 (2005).

SOROKIN Georgy, NINOKATA Hisashi, SOROKIN Alexander, ENDO Hiroshi, and IVANOV Eugeny F., Experimental and numerical study of liquid metal boiling in a system of parallel bundles under natural circulation conditions, Journal of Nuclear Science and Technology, vol.43, no.6, pp.623-634 (2006).

Stehle, H., Damm, G., and Jansing, W., Large scale experiments with a 5MW sodium/air heat exchanger for decay heat removal, Nuclear Engineering and Design, **146**, pp.383-390 (1994).

SUBKI Muhammad Hadid, WATANABE Noriyuki, ARITOMI Masanori, et al., Multi Parameters Effect on Thermohydraulic Instability in Natural Circulation Boiling Water Reactor during Startup, Proc. of ICONE11, ICONE11-36077 (2003).

SUZUTA Tadahiko, MAKIHARA Yoshiaki, NAITO Takashi, et al., Development of Integrated Modular Water Reactor : Standalone Safety System, Proc. of National Symposium on Power and Energy Systems, Vol.2002, No.8(20020614) pp. 563-566 (2002).

Takahashi, M., Sofue, H., Iguchi, T., Matsumoto, M., et al., Study on Pb-Bi natural circulation phenomena, Progress in Nuclear Energy, Vol.47, Issues 1-4, pp.553-560 (2005).

Takahashi Minoru, Uchida Shoji, and Kasahara Yoshiyuki, Design study on reactor structure of Pb–Bi-cooled direct contact boiling water fast previous reactor term (PBWFR), Progress in Nuclear Energy, Vol.50, Issues 2-6, pp.197-205 (2008).

Takakuwa, T., et al., Development of Multi-dimensional Natural Circulation Evaluation Code for Japanese DFBR, Proc. 3rd JSME/ASME Joint Int. Conf. on Nucl. Eng., Kyoto, Japan, April 23-27, Vol.1, p.513 (1995).

Toda, S., Ieda, Y., et al., Transverse temperature distribution in a multi-subassembly test section simulating natural circulation decay heat removal in the LMFBR, Proc. Int. Conf. on Design and Safety of Advanced Nuclear Power Plants, Tokyo, Japan, p.26.1-1 (1992).

Ueta, M., Inagaki, T., Shibata, Y., Tarutani, K., and Okada, K., The Development of Demonstration Fast Breeder Reactor (DFBR), Proc. 3rd JSME/ASME Joint Int. Conf. on Nucl. Eng. (ICONE-3), Kyoto, Japan, April 23-27, Vol.2, pp.771-776, Japan Society of Mech. Eng. (1995).

Watanabe, O. and Kubo, S., Study on natural circulation evaluation method for a large FBR (III) -(2) An evaluation of IWF promoted concept for natural circulation, Proc. of 1999 fall meeting of the atomic energy society of Japan, F7, (in Japanese) (1999).

Weinberg, D., Hoffmann, H., Hain, K., Hofmann, F., and Dueweke, M., Experimental and theoretical program to study the natural circulation decay heat removal system of the SNR-2, Proc. of Int. Conf. on Design and Safety of Advanced Nuclear Power Plants, Tokyo, Japan, Vol.3, pp.26.2/1-7, October (1992).

Weinberg, D., Hoffmann, H., Rust, K., Frey, H.H., Hain, K., Leiling, W., and Hayafune, H., Summary Report of NEPTUN Investigations into the Transient Thermal Hydraulics of the Passive Decay Heat Removal, FZK report FZKA 5666, Forshungszentrum Karlsruhe, Germany (1995).

Weinberg, D., et al., Transient NEPTUN Experiments on Passive Decay Heat Removal, Proc. 3rd JSME/ASME Joint Int. Conf. on Nucl. Eng., Kyoto, Japan, April 23-27, Vol.1, p.519 (1995).

Weissenfluh, T.v., Sigg, B., et al., Survey of SONACO 37-pin bundle experiments, Proc.

4th Int. Top. Mtg. on Nucl. Reac. Thermal-Hydraulics, Karlsruhe, F.R.Germany, Vol.2, p.1339 (1989).

Willrodt, U., Verifications of the design calculations of the immersed cooler system during the start-up tests of SNR-300, Nuclear Engineering and Design, **113**, 121-130 (1989).

Yamaguchi, A., et al., Plant wide thermal hydraulic analysis of natural circulation test at Joyo with MK-II irradiation core, Proc. 4th Int. Top. Mtg. on Nuclear Reactor Thermal-Hydraulics, Karlsruhe, F.R. Germany, Vol.1 p.398 (1989).